DOCTOR OF PHILOSOPHY

Design and modelling of optimal driveline control strategy for an electric racing car with rear in-line motors

Guo, Meng

Award date:
2015

Awarding institution:
Coventry University

DESIGN AND MODELLING OF OPTIMAL DRIVELINE CONTROL STRATEGY FOR AN ELECTRIC RACING CAR WITH REAR IN-LINE MOTORS

Meng Guo

A thesis submitted in partial fulfilment of the

requirements of the Coventry University

for the degree of Doctor of Philosophy

August 2015

Abstract

Interest in electric vehicles (EVs) has increased rapidly over recent years from both industrial and academic viewpoints due to increasing concerns about environmental pollution and global oil usage. In the automotive sector, huge efforts have been invested in vehicle technology to improve efficiency and reduce carbon emissions with, for example, electric vehicles. Nowadays, the safety and handling of electric vehicles present new tasks for vehicle dynamics engineers due to the changes in weight distribution and vehicle architecture. This thesis focuses on one design area of the electric vehicle – torque vectoring control – with the aim of investigating the potential benefits of improved vehicle dynamics and handling for EVs.

A full electric racing car kit developed by Westfield Sportcars based on an in-line motors design has been modelled in ADAMS with typical subsystems, and then simulated with computer-based kinematic and dynamic analyses. Thus, the characteristics of the suspensions and the natural frequencies of the sprung and unsprung masses were found, so that the model was validated for further simulation and investigation. Different architectures of the EVs, namely the in-line motors and the in-wheel motors, are compared using objective measurements. The objective measurements predicted with kinematics, dynamics and handling analyses confirm that the architecture of the in-line motors provides a superior dynamics performance for ride and driveability. An Optimal Driveline Control Strategy (ODCS) based on the concept of individual wheel control is designed and its performance is compared with the more common driveline used successfully in the past. The research challenge is to investigate the optimisation of the driving torque outputs to control the vehicle and provide the desired vehicle dynamics. The simulation results confirm that active yaw control is indeed achievable.

The original aspects of this work include defining the characteristics and linearity of the project vehicle using a novel consideration of yaw rate gain; the design and development the Optimal Driveline Control Strategy (ODCS); the analysis and modelling the ODCS in the vehicle and the comparison of the results with conventional drivelines. The work has demonstrated that valuable performance benefits result from using optimal torque vectoring control for electric vehicle

Contents

Index for Figures

Index for tables

Annotations

A_x	Longitudinal acceleration
A_y	Lateral acceleration
b	Longitudinal distance of body mass centre from front axle
c	Longitudinal distance of body mass centre from rear axle
f	Natural frequency
k	Path curvature
K_s	Spring stiffness
kw	Stiffness of equivalent spring at the wheel centre
m	Mass of a body
v_x	Longitudinal velocity
v_y	Lateral velocity
F_x	Longitudinal tractive or braking tyre force
F_y	Lateral tyre force
F_z	Vertical tyre force
F_D	Drag force
A_f	Front axle slip angle
a_r	Rear axle slip angle
β	Side slip angle
δ	Steer or toe angle
ω	Yaw rate
ω_d	Demanded yaw rate
ω_{err}	Yaw rate error
ω_{fns}	Front axle no-slip yaw rate
ΔT	Difference in driving torque

Abbreviations

ALSD	Active Limited-Slip Differential
AYC	Active Yaw Control
ATVC	Advanced Torque Vectoring Control
AWD	All Wheel Drive
ADAMS	Automated Dynamic Analysis of Mechanical Systems
DOF	Degrees of Freedom
EV	Electric Vehicles
GRG	Generalized Reduced Gradient
IC	Internal Combustion
LSD	Limited-Slip Differential
LQG	Linear Quadratic Gaussian
ODCS	Optimal Driveline Control Strategy
RWD	Rear-Wheel-Drive
SC	Speed Compensation
YRE	Yaw Rate Error
Yaw Rate Gain	YRG

Acknowledgement

I would like to express my gratitude to all those who gave me the possibility to complete this thesis. I want to thank Coventry University for giving me permission to commence this thesis in the first instance. I have furthermore to thank my second supervisor, Dr Gary Wood, who encouraged me to go ahead with my thesis. Also I would like to thank Mr Damian Harty for his assistance over the period of the research study.

I am deeply indebted to my director of study Professor Mike Blundell, who gave me huge support and helped me throughout the research project and in writing up of the thesis.

Especially, I would like to give my special thanks to my family whose love enabled me to complete this work.

1. Introduction

1.1 Pollution and fuel consumption

Fossil oil is the most important natural resource to support the world economy. Although recent estimates vary, there is absolutely no doubt that global concerns about the finite nature of our oil-based energy reserves are well founded (Hirsch, Bezdek et al. 2005). Global energy demand from all sources is expected to increase by 1.3 percent per year on average from 2005 to 2030 (ExxonMobil 2007).

Apart from the shortage of oil supply, the concerns in growth of emissions and pollutions have been discussed every day. In fact, the transportation sector accounts for about 21 percent of current global fossil fuel CO_2 emissions to the atmosphere-second only to emissions from power production (IPIECA 2004). According to the Technology Strategy Board (TSB), in the UK it is estimated that transport accounts for 24% of the UK's carbon emissions. Road transport accounts for 80% of this figure (IME 2009). However, the big challenge to the automotive industry is to be responsive to both legislation-reducing emissions and the market-growing consumer demands.

1.2 Developing electric vehicles

There has been a massive resurgence of interest in electric vehicles (EVs) over the past decade. Many observers now see them as the long-term solution to reducing vehicle emissions and CO_2 usage in comparison to alternative approaches such as hybrid vehicles, fuel cells or biofuels. The public perception of electric vehicles has changed dramatically – and recently announced vehicles such as the Tesla roadster and Chevrolet Volt have reinforced the idea that they are now becoming seriously competitive products. Not long ago, electric vehicles were still seen as niche products – and associated more with 'milk float' technology rather than a viable passenger transport alternative (Chan and Chau, 2001; Husain 2003; Larminie and Lowry 2003).

Massive advances have occurred in battery technology – although the progress has been gradual and sustained, so that it has not commonly been perceived as a major breakthrough. The vehicle range available with modern battery sets – such as Lithium Ion – is now typically of the order of 200km, which makes electric vehicles widely acceptable for much urban use. The high cost of the batteries is still a problem and despite a relentless downward price trend, the battery sets are often supplied on a leasing arrangement rather than a straightforward purchase.

As the electric vehicle market continues to grow, the chassis engineers will place increasing emphasis on searching for dynamics control due to the new architecture used on the electric vehicle. This process of continual improvement is central to vehicle development of safety and handling, and has occurred for example, over recent decades with vehicle dynamics. The industry has achieved ride comfort and safety figures that were considered impossible twenty years ago. Of all the green solutions, battery electric cars have the best dynamics control, individual wheel control, of both conventional cars and hydrogen fuel-cell cars. Also the driving efficiency is high, for example, with 1 MWh of electricity, an EV can drive 5525 km; while using the same amount of electricity to generate hydrogen and to drive a fuel cell car, the distance is reduced to 1790 km (Randall, 2009).

The electric vehicle as a main test platform for this research focuses on one area of interest in which dynamics control gains may be achievable for electric powertrains with individual control motors. As is known, it is commonly argued that one of the distinct advantages of an electric motor as a motive unit is its torque characteristic; it can deliver maximum torque from zero speed and throughout the low speed range – typically up to around 2000 rev/min. Then, the available maximum torque reduces with speed along the motor's maximum power curve. This is a much better characteristic than that associated with internal combustion engines, which cannot deliver useful torque at low speeds and because of their relatively narrow torque and power bands, must be used with multispeed transmissions in order to deliver tractive power to the vehicle in a suitable form. Typical electric motors have another desirable feature – their maximum intermittent power is considerably higher than their rated continuous power. The limiting factor is usually related to controlling the

amount of heat build-up. Consequently, good acceleration times can be achieved providing they are only used for relatively short periods – a situation which fortunately is typical of normal driving.

1.3 Aim and objectives

The proposed research is focused on active yaw control for electric racing vehicles. Due to this research being based on an industrial project from Westfield Sportcars, the company is starting to investigate and develop a full electric racing vehicle that is called – the Westfield i-Racer. The Westfield engineers have developed the world's first electric race car kit that can be built at home, while also supporting the requirement of sport racing with zero emissions vehicles.

Initially, the project vehicle with typical sub-systems such as suspension, steering and driveline system were modelled and assembled so that the requirements of the vehicle dynamics simulation could be fulfilled. A model audit was needed to ensure a rigorous system was used in the following research. The audit involved calculating the mass and inertia properties for the vehicle body and all the components in the sub-systems, as well as finding the central of mass position for the vehicle body and the characteristics of the spring and damper in the following section. The tyre-sourced data is based on the Pacejka 89 version, with the manufacturer's coefficients and the tyre model being run on a computing-based tyre test rig to indicate all characteristics of the tyre.

When building the project vehicle in computer-based software, the accuracy of the simulation results relies on the accuracy of the model and the vehicle parameters used to build the model. Hence, there are several methods available to validate the vehicle model, such as kinematic and dynamic manoeuvres. In order to verify the performance of the suspension system, a range of characteristics were determined through simulation of a quarter vehicle model. The full vehicle model was analysed in a number of ways that provided information to support the following investigations. Also, the steady-state cornering manoeuvre was used to define the basic driving characteristics of the project model.

A main difference in architecture for the conventional vehicles is the position of the Internal Combustion (IC) engine, which can be located at the front, the middle or the rear of the vehicle; thus influencing the mechanical, such as the Rear-Wheel-Drive (RWD) or the All-Wheel-Drive (AWD). A novel architecture for the electric vehicle driveline was designed that has the freedom to move the motors to a single location in the vehicle, for example, by mounting the motors within individual wheels. In addition, the electric motors can also be located in the middle of the chassis at the front, rear or both axles. The recent conformity in electric vehicle architecture, with high driving eff/iciency of in-wheel motors now on the market, has led to some complacency in viewing any other architecture. Westfield Sportcars, a producer of the in-line motors, has commissioned a series of wide-ranging studies into the effects of vehicle performance. However, a comparison will be introduced that includes a ride comfort check and drivability check studies using the ADAMS model. These studies provide a comprehensive overview of the implications of in-wheel and in-line motors in this particular racing model.

Finally, the most important part of this investigation is to develop and design a novel Torque Vectoring control strategy. In the literature, active intelligent control systems for achieving vehicle stability and handling have been developed and implemented to enhance the safety and performance of the driven vehicle. Some enhancements, such as the Active Steering System and the Electronic Stability Program, can help the driver to retain control of their vehicles when the grip between road surface and tyre is lost. In previous investigations, ABS based Stability Control Systems have been the principal implementation to accomplish the safety requirements with adverse road conditions. However, the vehicle speed is degraded while the Stability Control System implements braking force on four wheels individually to improve the correct position of the vehicle body. Moreover, the Torque Vectoring (TV) system can be designed to improve the vehicle handling qualities and avoid the vehicle speed decrease, or in other words the ‘fun-to-drive’ aspect. Thus, torque vectoring can be used to influence the driver experience.

A new control strategy, that is called Optimal Driveline Control Strategy (ODCS), will be design and/ developed. The ODCS involves three levels of control: Desired

Dynamics Behaviours, Secondary Control and Advanced Torque Vectoring Control, more details of which will be represented in the following section. Reviewing the basic principles for TV control on the conventional driveline helps to understand how those control strategies on the pure electric vehicle can be implemented. The configuration of the ODCS algorithm is clearly shown and each level of control is explained in detail.

The project vehicle model will be taken into the typical vehicle dynamic simulations, by running the vehicle model through the steady state cornering and lane change manoeuvres. The results will be analysed and compared against the project model running with the different driving modes, assuming the model has the conventional drivelines, namely Open and Limited Slip Differentials on the rear axle, so that these will be simulated for the same manoeuvres.

2 Literature Review

2.1 Introduction

The previous work on Vehicle Dynamics Control, Direct Yaw Control, Torque Vectoring and the vehicle dynamics control strategies of Electric Vehicles (EVs) are reviewed here. The definitions and classifications for a Final Drive Unit are summarised and the main tools for vehicle dynamics analysis are introduced. For control strategies, the current situation and the future trends are analysed. Torque vectoring for electric vehicles has received a substantial amount of attention and several different designs have been proposed over the past decade. The important dynamics control strategies for electric racing vehicles, a crucial feature in optimizing performance and overall performance, are reviewed.

2.2 Electric Vehicle

Vehicle industries and governments around the world appear to have a high level of interest in electric vehicles, an interest which is growing at a substantial rate. In the past, commercial vehicles powered by the Internal Combustion engine became available at the end of the 19^{th} century; while at the same time, an electric vehicle broke the world land speed record in 1899, becoming the first car to exceed one mile per minute. At that time, there were three propulsion systems: the electric motor, the IC engine and the steam engine. Comparing the size and complexities of these devices, the electric motor was a clear winner; however, it used original lead acid batteries for the energy storage, which have 300 times lower capacity than that of the specific energy of the gasoline-driven vehicle.

Based on the global requirement to reduce emissions, both political and technological sectors have currently been experiencing a resurgence of interest in electric vehicles supported by emerging battery technologies. Investigations are mainly focused on energy density, improved specific energy and rechargability properties. The electric motor has a great advantage in torque characteristic, which

means the motor can provide a more desirable spread of torque over the vehicle speed range compared to that of the IC engine, and also electric vehicle architecture provides the shortest driveline in contrast to conventional vehicles.

Currently, the most popular design approach for electric vehicle is to connect the motor to the driven wheels directly, with some designs requiring a transmission unit between the motor and the wheels. In general, the characteristics of the current electric motor have two regions – intermittent peak torques and operating torques that are comparatively lower; the high torques can provide desired acceleration from very low speeds, and the top speed is constrained by the continuous torques. Normally, the transmission unit with a fixed gear is used to control the top speed. In addition, there is another area of interest in the case of an electric vehicle, which is to investigate how to control the efficiency of the electric motor, so that particular capacities of the motor are required, namely low speed with high torque, direct-drive and excellent torque-power densities.

In a similar fashion, plug-in electric vehicle have also become a very topical subject. For example, the ‘i MiEV’ from Mitsubishi Motors has been commercially produced and 200 of these vehicles have been put into the UK for test driving. Using the on-board charger, the vehicle can be charged with a 100 V or 200 V power source in the home. The range over one of the driving cycles, for one charge is 160 km, which is enough for most commuting applications. For example, in the United States, half of U.S. households have a daily mileage of less than 30 miles per day; 78% of daily work commuters travel 40 miles or less (Babik 2006).

2.3 Drivetrain Designs

2.3.1 Conventional mechanical drivetrains

An “Open” differential drives the wheels to rotate at different speeds while balancing the torques between them. A limited slip differential allows for unequal torque distribution between the wheels, but with a fixed kinematic relationship, and the torque can only be transferred from the wheel spinning faster to the wheel spinning

slower. A torque vectoring system, while retaining the ability to function as a simple differential, incorporates a means to vary the kinematic ratio across the differential, thus affecting the torque distribution between the wheels. Torque vector is defined as the torque difference between the two output torques.

During cornering, the vehicle wheels rotate at different speeds. The differential is equipped to rotate both the driven wheels with identical torque but different angular velocity. For this device, the capability to transfer torque and rotation is through three shafts, one input two outputs. This is found in most vehicles, which allows each of the driven wheels to rotate at different speeds, while supplying equal torque to each of them. When cornering, the inside wheel is rolling in a smaller circle than the outside wheel and without the differential, the inside wheel is spinning and the outside wheel is dragging. This scenario may cause problematic and unexpected handling, more tyre wear, and damage to (or possible failure of) the entire drivetrain.

2.3.2 Drivetrains for electric vehicle

Novel concepts of electric vehicle layouts are gaining more and more importance. The first generation of fully electric vehicles was based on the conversion of internal combustion engine driven vehicles into electric vehicles, by replacing the drivetrains, while keeping the same driveline structure; that is, one electric motor drive, which is located centrally between the driven wheels, and a single-speed mechanical transmission including a differential. Such a design solution is going to be gradually substituted by novel vehicle architecture, based on the adoption of individually controlled electric powertrains, with the unique possibility to improve the vehicle dynamics control because of their intrinsic high and independent controllability. The active control of electric powertrains allows the regulation of the distribution of the driving torques in order to achieve desired steady-state and transient vehicle dynamics characteristics. At the same time, if implemented through in-wheel motors, these architectural solutions allow an improvement of the overall vehicle packaging as less space is required by the powertrain.

Current electric vehicle research is investigating different powertrain configurations, constituted by one, two, three or four electric motors with different performance in

terms of vehicle dynamics behaviour and energy saving targets (Novellis, Sorniotti, Gruber,2012 and Rinderknecht, Meier,2010) . The possible architectures are shown in Figure 2-1 (Ehsani, Gao et al.2004), from which it can be seen that mainly two types of transmissions are used on electric vehicles: multi-gear transmission and single-gear transmission. Currently, single gear transmissions are used on most EVs. For example, on the Gulliver U500 design from Tecnobus, the transmission is a single gear with a fixed ratio of 1:4.37. For configurations like Figure 2-1 (a) and (b), an electric propulsion motor replaces the IC engine of a conventional vehicle drive train. The multi-gear transmissions here were originally designed for an engine, not especially for electric motors. It is perhaps surprising, but there is very little published research on the potential benefits from connecting the motor to driven wheels directly by using driving shafts, it can save major components in the transmission system reduce the weight of entire vehicle and improve driving efficiency.

Figure 2-1 Possible EV configurations (Ehsani, Gao et al. 2004)

2.4 Vehicle dynamics control

In recent years, several researchers have invested time in, and effort on, the improvement of vehicle dynamics control, generally focusing on agility, stability, reliability and linearity to improve handling. These requirements have been applied to new designs of electric and hybrid vehicles. A Limited-Slip Differential (LSD) is based on the open differential with a type of gear arrangement that allows the wheels to have differences in angular velocity and the driving torque. In order to provide increased stability, alternative control systems are then considered without the disturbance of brake-based stability control programmes. A Limited-Slip Differential uses the electronic controller to transfer torque between the driven wheels. Controlled torque transfer between the driven wheels can generate a yaw moment that is able to improve the stability of vehicle; and due to the wheel torque being redistributed without any speed reduction, this improvement in stability is less intrusive than a brake-based stability control programme.

In general, active steering systems can help the driver to face a critical driving situation. Zhang (2008) presented a paper that described a multi-body vehicle dynamic model with an active steering system using a fuzzy logic control strategy. The multi-body vehicle dynamic model was built in ADAMS and the dynamic performance of the vehicle could be accurately predicted. The methodology of control included active front steering and rear wheel steering by wire, to which active steering at the front axle involved a modified steering angle added to the driver input, and the rear wheel steering was controlled by wire. This combination was effectively used to control both body-slip angle and the yaw rate. The controllers used in the active front and rear steering control were based on a set of fuzzy logic rules to adjust the body-slip angle and the yaw rate. Optimization of the fuzzy logic control in both the active front and rear steering system was also represented. Thus, the simulation results indicated that active front and rear steering using a fuzzy control logic strategy enabled improved handling and stability of the vehicle comparing the four-wheel steering with front wheel steering only.

Modification of the vehicle dynamics can also be achieved by controlling the distribution of lateral forces using the combinations of front and/or rear steering

angles in four-wheel steer by wire (Ackermann and Sienel, 1993, Ackermann et al., 1995, Kohen and Ecrick, 2004 and Vilaplana et al., 2005). Moreover, the improvement of the vehicle safety capability for emergency avoidance, using the optimization of both the direct yaw control and active steering control is another research area of interest (Mokhiamar and Abe, 2002).

According to these previous works, the control designs are only for the development of the yaw stability control algorithm. The control is based on a model with the desired vehicle response. The model is a basic vehicle model that can be used to calculate the desired yaw rate based on the steering input, vehicle speed and road surface. Moreover, the Limited-Slip Differential designs generate a required torque to transfer across the axle depending on the error between the desired and actual yaw rate of the vehicle. The error is fed through a feedback controller, but the Limited-Slip Differential only develops the yaw moment in the under-steer condition. Also Four-Wheel Steer and Active steering systems have same limitation.

2.4.1 Direct Yaw Control

Due to unusual external conditions there can be unexpected dangerous behaviours in vehicle yaw dynamics, such as unexpected side-wind force, different road surface texture on left-right wheels, and emergency avoidance. Moreover, under-steer may degrade the handling performance in cornering manoeuvres and cause discomfort to the human driver. There are, however, a few solutions available in recent years to solve these issues, and the task is still to carry out intensive research activities in both practical and analytical studies (see e.g. Börner and Isermann, 2006, Colombo, 2005, Gaspar et al., 2005). In this case the purpose of the study was to modify the vehicle dynamics and exploit the best combinations in longitudinal and lateral tyre forces. Also, using the uneven longitudinal driving force on the left and right sides can control the yaw rate. This approach involved different technologies, for example, Anti-Lock Braking System (ABS) and Electronic Stability Program (ESP) (Zanten, 2000 and Zanten, 1995) or torque vectoring control using active differentials (Assadian and Hancock, 2005, Colombo, 2005 and Gerhard, 2005).

Assadian, Hancock and Best (2010), describe some developments on mechanical limited slip differentials which provide a low cost traction solution. However, their passive nature means that mechanical limited slip differentials cannot adapt to different conditions and their yaw moment generation potential cannot be used for vehicle handling or stability control. Active limited slip differentials are becoming popular as they are able to exploit this potential and also achieve a better traction compromise due to their ability to adapt to different scenarios. The development of a control algorithm for an Active Limited-Slip Differential (ALSD) fitted to a RWD sports saloon vehicle. The ALSD uses a wet friction clutch unit to transfer the torque across the driven axle, and a driven actuation system with an electric motor controls the clamping force on the clutch unit through a ball and ramp device.

However, the Limited-Slip Differentials use the wet clutch unit to provide a controlled left-and-right torque distribution on the front or rear axle, and four-wheel torque distribution, thus resulting in improved traction control and yaw stability control performance without being intrusive for the driver. The case speed is equal to $\omega_c = (\omega_1 + \omega_2)/2$ and the clutch always transfers the torque from its faster to its slower shaft. The direction of torque transfer is determined by the difference in the wheel speed across the axle. It is restricted to over-steer compensation only when being used as a yaw stability control device, since only an under-steer torque can be generated.

Active Yaw Control (AYC) and Super-Active Yaw Control developed by Mitsubishi Motors (Ushiroda,2003) based on an active differential to modify the torques at the driven wheels are reviewed in this section. These products were designed and implemented in the series of the Mitsubishi Lancer Evolution cars, which used a planetary gear-set, also being used in several Mitsubishi concept models, to support a greater torque distribution than that of the existing systems.

The simulation results, as shown in Figure 2-2, show that the maximum cornering performance is obtained by using an AYC model without limitations on torque transfer. This concept is based on a left-and-right torque vectoring system and the driving torque is optimally controlled depending on the vehicle conditions. A comparison of the vehicle with and without the AYC is presented in this paper; and

each of the curves shows the maximum lateral acceleration during the cornering manoeuvre for a given acceleration in the longitudinal direction. It is clear to see that the acceleration region of the optimally controlled AYC vehicle is 25% larger than that of the vehicle with only AYC. The torque transfer for the optimally controlled AYC is 1.8 times larger than the torque transfer amount with AYC alone. Thus, the increment in the amount of the torque transfer offers a target for which the authors in this research have identified potential methods to achieve.

Figure 0-2 Acceleration cornering performance (USHIRODA 2003)

Three different torque vectoring strategies which summarise the strategies explained in above the research have been implemented: i) constant torque distribution (referred to as the baseline vehicle); ii) torque proportional to the wheel vertical load; iii) torque distribution which allows achieving the same longitudinal slip ratio at each wheel.

2.4.2 Torque Vectoring System

Torque vectoring control can have a major impact on the general driving experience. Most of the time the driver operates the vehicle in steady-state, or slowly varying conditions, at lateral acceleration levels as below 0.5 g (Pacejka, 2006). During these sub-limit conditions, the continuous yaw moment control can significantly improve the vehicle cornering response. As recently pointed out in (Crolla, 2012),

“despite the significant volume of theoretical studies of torque-vectoring on vehicle handling control, there is no widely accepted design methodology of how to exploit it to improve vehicle handling and stability significantly.” To address this issue, novel tools for the design of torque vectoring control systems have to be proposed and assessed.

Vehicle steady-state cornering response is usually assessed in terms of its understeer characteristic, where the dynamic steering wheel angle is the difference between the actual steering wheel angle and the kinematic steering wheel angle (Gillespie, 1992). In general, in a passenger car, the dynamic steering wheel angle increases monotonically and nearly linearly up to a value of lateral acceleration of about 0.5 g for high friction conditions. Correspondingly, the understeer gradient of the vehicle is nearly constant. Beyond this linear region is non-linear and tends to an asymptotic value corresponding to maximum lateral acceleration when the tire friction limits are reached. In contrast to vehicles without torque vectoring control, where the specific understeer characteristics are determined by the tyre properties, geometrical and inertial parameters and the suspension elasto-kinematics (Reimpell, 2001 and Milliken, 2002), the understeer characteristics of a vehicle equipped with a TV system can be designed to achieve almost any desired response. For example, the understeer gradient in the linear part of the characteristic could be imposed. Also, the width of the linear region could be increased, or the maximum lateral acceleration could be altered, with the constraints dictated by tyre friction limits (Zorzutti, 2007).

In addition to the advantages during pure cornering manoeuvres, continuous TV control has the potential to improve the handling response of a vehicle while braking or accelerating. Despite the significant influence of accelerating and braking, the understeer characteristics for non-zero longitudinal acceleration are normally not considered and analysed. This restriction mainly results from limitations imposed by the typical vehicle dynamics simulation techniques or testing procedures used to derive the zero longitudinal acceleration cornering response plots, namely, skid-pad tests or ramp-steer manoeuvres.

Yaw control is effective in order to realise the active safety philosophy that makes the likely occurrence of an accident small; and the yaw control technology by using brake based systems has been developed in a large number of products. As a next step, direct yaw control can be achieved using the right-and-left torque vectoring control. This system can directly control the yaw moment acting on a vehicle by vectoring the torques between wheels on either side with minimum energy loss. Therefore, the strong point of this system is to be able to improve the stability of the vehicle from the normal condition to the high marginal condition seamlessly (Ikushima,1995).

Figure 0-1 Vectoring torque acting on rear right and left wheels (Sawase and Ushiroda, 2007)

A concept is shown in Figure 2-3; the torque flow between the right and left wheels can be controlled by a device, so that it can make on one side of the driving forces small, and the other side driving forces large. The difference in the longitudinal driving torque generated on the right-and-left wheels can control the yaw moment that acts on the vehicle, even if the engine torque and/or braking force are applied.

//Figure 0-2 Effect of torque vectoring (Sawase and Ushiroda, 2007)

Figure 2-4 shows the relation between the tyre maximum friction force, the driving force, and the maximum cornering force of the right and left wheels during cornering. When the vehicle is cornering to the left, lateral acceleration causes the left tyre maximum friction force R_l (shown as the radius of the tyre maximum friction circle) to decrease and the right tyre maximum friction force R_r to increase. Therefore R_l is smaller than R_r. The left tyre maximum friction force is the same R_l and the left driving force D assumes an equal state in the case of a vehicle without torque vectoring, as shown in Figure 2-4 (A). In this state, the right wheel can only generate the maximum cornering force C_{mr} in (A), because the right tyre maximum friction force R_r is bigger than the right driving force D. The left driving force is D - $\Delta D/2$ and the right driving force is $D + \Delta D/2$, so that the left wheel can generate the maximum cornering force, $C_{ml'}$ and the right wheel can generate the maximum cornering force $C_{mr'}$. The right and left wheels' total maximum cornering force difference between a vehicle with torque vectoring and one without torque vectoring by ΔC_m, is expressed by the following equation,

$$\Delta C_m = C_{ml'} + C_{mr'} - C_{mr} = \{R_l^2 - (D - \frac{\Delta D}{2})^2\}^{\frac{1}{2}} + \{R_r^2 - (D + \frac{\Delta D}{2})^2\}^{\frac{1}{2}} - (R_r^2 - D^2)^{\frac{1}{2}} \quad (2.1)$$

In this equation, when ΔD is increasing from zero, ΔC_m becomes maximum value at

$$\Delta D = D(R_r - D)/2(D + R_r) \quad (2.2)$$

Thus, it is shown that a torque vectoring increases the total maximum cornering force.

The calculated influence of the right-and-left torque vectoring control in the different types of driveline, namely, the front wheels only, the rear wheels only, and both front and rear wheels in FWD, RWD, and AWD vehicles is represented. The effect is evaluated by calculating the vehicle dynamics limit, the maximum acceleration and the cornering ability. The right-and-left vectoring torque, which is needed to increase the vehicle dynamics limit, is also calculated. Also, the application to the front wheels is more effective for FWD vehicles. On the other hand, the application to the rear wheels is more effective for RWD and AWD vehicles.

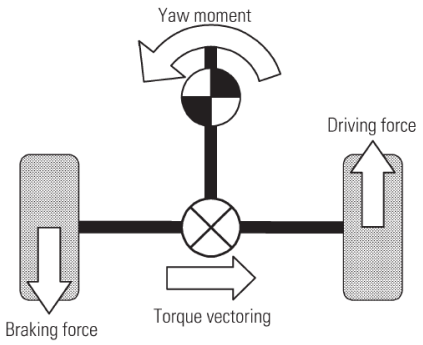

Figure 0-3 Left-Right Torque Vectoring Concept

Figure 2-5 shows the concept of left-and-right torque vectoring control in which this approach has the braking force applied to the left wheel and the same magnitude of the driving force applied on the right wheel. Thus, it is able to control the yaw rate directly as required at any time, and the control is without any constraints from the level of the engine torque, and any conflicts between the torque vectoring control and the operation of the driver.

Figure 0-4 Schematics of recent torque vectoring systems (Wheals, 2004)

Figure 2-6 shows a comparison between the Ricardo Torque Vectoring systems and alternatives such as the Mitsubishi EVO VIII device and the Mimura device:

- All designs provide permanent drive to the wheels via a differential when the actuation system is inactive.

- The Ricardo design uses two brakes whereas the Mitsubishi and Mimura designs both use two clutches. It describes a single brake design.
- The Mitsubishi and Mimura designs both use joined planet gears within the geared stage that force a speed difference between the outputs.
- The Ricardo Torque Vectoring™ device uses joined sun gear, which requires the use of additional annulus gears which are not required by the other designs.

2.5 Handling Control for electric vehicles

Electric vehicles can have different topological layouts with in-wheel or on-line motor drives. This design flexibility, combined with the possibility of continuous modulation of the electric motor torque, allows the implementation of advanced torque-vectoring (TV) control systems. In particular, based on the individual wheel torque control, novel TV strategies aimed at enhancing active safety (Kang, 2011, Nam, 2012 and Jonasson, 2011) and 'fun-to-drive' qualities (Gruber, 2013) in all possible driving conditions can be developed. Indeed, by directly controlling the yaw moment through the actuation of electric drivetrains, a TV system extends the safe driving conditions to greater vehicle velocities during emergency transient manoeuvres than a conventional vehicle dynamics control system based on the actuation of the friction brakes (Tseng, 1999, Doumiati, 2011). Different electric vehicle layouts are currently analysed for the demonstration of TV control strategies, including multiple individually controllable drivetrains (Xiong, 2009, Wang, 2009, Akaho, 2010, Tabbache,2011, Chen,2013) or one electric motor per axle coupled with an open mechanical differential or a TV mechanical differential.

Torque Vectoring control structures are usually organized according to a hierarchical approach as shown in Figure 2-7. A high-level vehicle dynamics controller generates a reference vehicle yaw rate, which is adopted by a feedback controller in order to compute the reference tractive or braking torque and yaw moment. The feedback controller is either based on sliding mode (Canale, 2005, Ferrara, 2009), linear quadratic regulation (Zanten, 2000), model predictive control (Chang, 2007) or robust control (Yin, 2007) . A feedforward contribution, M_Z^{FF} , for example based on maps, can be also included, as shown in Figure 2-7, in such a way that the control

yaw moment is given by $M_Z^{TOT} = M_Z^{FF} + \Delta M_Z^{FB}$, where the feedback term ΔM_Z^{FB} compensates the inaccuracies, the disturbances or the variation of the vehicle parameters (such as vehicle mass, position of the center of gravity, etc…) considered for the derivation of the feedforward maps.

Figure 2-7 Functional schematic of a typical TV controller for a FEV with multiple individually controllable drivetrains also illustrated in (Xiong, 2009 and Wang,2009).

At a lower level, the objective of the control allocation is to generate appropriate commands for the actuators in order to produce the desired control action in terms of traction or braking torque and yaw moment. When the number of actuators is larger than the number of reference control actions, the control allocation problem can be solved by minimizing an assigned objective function. This is achieved with simplified formulas based on the vertical load distribution (Tanaka, 1992 and Mutoh, 2012) or with more advanced techniques such as weighted pseudo-inverse control allocation (Tabbache, 2011 and Yim,2012), linear matrix inequality (Fallah, 2013) or quadratic programming with inequality constraints (Tjonnas, 2010). The optimization algorithms most commonly employed for on-line control allocation schemes are active set, fixed point and accelerated fixed point. The published methods are shown to be successful, but their application and analysis are limited as their tuning is carried out through the optimization of the vehicle performance during specific maneuvers (Naraghj, 2010) and not the full range of possible operating conditions. More importantly, the effect of the possible alternative formulations of the objective functions for control allocation on the overall performance is not explored in the literature.

For example, Kim (2007) designed a new control algorithm for the stability enhancement in which an electric vehicle with four-wheel-drive used the rear in-wheel motor driving, regenerative braking control, and electrohydraulic brake (EHB)

control. The control algorithm is based on a fuzzy-rule-based control that can minimize the errors of the body-slip angle and the yaw rate. A co-simulation of ADAMS and Simulink was used in this research, in which the vehicle was modelled in ADAMS with the suspension system, tyres, and steering system to describe the dynamic behaviour of the vehicle. Moreover, the driveline components of the given vehicle with the control algorithm, such as the motor, engine, transmission and battery, were modelled in MATLAB Simulink, and again only the chassis elements modelled in ADAMS. The simulation results showed that the combination of the rear motor driving and regenerative braking can improve the stability performance and the driving efficiency of the vehicle.

Also**,** Shino and Nagai (2001) have investigated the use of direct yaw rate control using a brake-based system to distribute the driving torque, thus improving the vehicle dynamics of electric vehicles. Based on **their** research, the design used the architecture of the electric vehicle with in-wheel motors that can implement the control strategy to the vehicle to fulfil the requirements of the control performance. Fundamentally, the control strategy based on a model following controller is able to impel the vehicle to follow the desired dynamics. The control strategy included a feed-forward body-slip angle regulator and the feedback control for the yaw rate. The vehicle with the new control strategy has been simulated in several computer-based manoeuvres to test the performance of the control. The validations clearly showed the dynamic behaviours of the electric vehicle have been enhanced, particularly in the handling and stability; also the improvement can be seen when the vehicle has been put through the different conditions of the road surface.

Pinto, Aldworth and Watkinson (2011) carried out research to develop a yaw motion control system based on torque vectoring with twin rear electric motors, with the main objective of enhancing the driving dynamics of a hybrid vehicle without compromising requirements on low emissions, safety or driver feedback. The distinct advantages of the system are investigated with simulation tools and verified with field measurements on MIRA’s prototype Hybrid 4-Wheel Drive Vehicle.

Figure 0-5 Wide lane change at 70km/h (L Pinto, Aldworth and Watkinson, 2004)

The result of the testing, which measured the yaw rate, hand-wheel angle, side-slip velocity, lateral acceleration and estimated side-slip angle are measured in a typical evasive manoeuvre, is shown in Figure 2-7. Results show effective under-steer compensation, enhanced agility, increased cornering speed, improved yaw damping, and a possibility to negotiate tight corners with drifts controlled by the driver's steering input. The high yaw authority is compensating under-steer, the possibility of enforced optimal yaw tracking in sub-limit driving, and the high potential for ease of integration with an existing ESC system. It makes the system suitable not only for sport applications but also for enhancing the everyday driving manoeuvrability of standard compact and subcompact vehicles. In its simplest version, it can be retrofitted to a standard FWD vehicle, together with a relatively small battery, and it can also be used to provide drivability functions such as launch support and 4WD mode, or it can be fully integrated into a proper hybrid power-train management system.

2.5.1 Driver Model

In many situations it can be beneficial to do analysis of the driver using a virtual representation. For real vehicle tests you can replace the driver with a steering robot, this being superior to the human in precision and repeatability for pre-defined control of the vehicle. If the driver is replaced with computer models, this allows the processing of large batches of tests in desktop computer simulation programs. For the driver input to the vehicle model you can use either open loop pre-defined steering or driver models, which more accurately represent the human driver and their limitations.

One of the first recognised model based driver descriptions is to be found in an early article (Gibson and Crooks, 1938). McRuer is one author who has had great influence on control-theory-based pilot models and driver model development, e.g. in (Westbrook,1959, McRuer and Wier 1967, and McRuer, 1980). Other authors (Fiala,1966, Mitschke, 1972, and Allen,1987) who have pioneered the development of driver models. In the early eighties, MacAdam presented his work on optimal control, which provided a much appreciated method for predicting vehicle movement which allowed good path following. Sharp and Casanova (2000) have among other things contributed with mathematical model and optimal control model development (Sharp and Valtertsiotis, 2001). Another driver modelling approach was given by Cole, who has studied neuro-muscular activities in the driver's steer control and implemented this research in driver models (Pick and Cole, 2003).

Driver models have been utilised in a number of different applications in the automotive field, such as safety, handling and fuel consumption. Driving safety is an important area of interest since the inception of the first vehicles, and driver models are now being used to improve safety. An understanding of driver behaviour when alert is needed, so that deviation from this type of behaviour may indicate that the driver is performing in an impaired state. As an example of this the frequency of steering correction (Paul) can be used as an indicator of fatigue. Similar driver model applications related to safety include predicting when an unsafe driver state may occur due to tiredness, distraction or impairment. In (Onken) a driver model is used to compare predictions with data from a computer vision system to decide whether

there is adequate distance from the car ahead and provide a warning if it is deemed to be a dangerous situation.

When simulating vehicle performance over a drive cycle, it is important to consider the effect of driver behaviour on the fuel consumption and emissions. The regulations of the New European Driving Cycle (NEDC) stipulate that the velocity profile is followed within a tolerance band to allow for the reaction time and sensitivity of the driver. Compared to a closed loop PID controller historically used in simulation to closely follow the velocity profile these driver deviations will have an effect on fuel consumption and emissions (Froberg, 2008 and McGordon, 2011). These deviations occur despite the use of professional test drivers with great experience of the cycle to be followed. The research into the motivations for particular driving behaviour can be extended to categorise certain types of behaviour into a driving style and analyse how particular styles affect traffic flow (Treiber, 2013), accident rates (Lajunen, 1997), and fuel consumption and emissions (Holmn,1998). Average acceleration and standard deviation of acceleration are used in (Langari, 2005) to identify driving style, categorised as calm, normal or aggressive using a fuzzy logic based system. Similarly the derivative of acceleration, known as jerk, is used in (Murphey, 2009) to classify driving style as calm, normal or aggressive.

In order to model driver performance and to determine if a driver's behaviour can be considered appropriate, any deviation from desired behaviour can be viewed as an error. Driving errors have some relation to vehicle safety. Driving errors can occur at all 3 levels of the driver behaviour and are classified as either being slips/lapses or mistakes (Parker, 2007). At the knowledge-based performance level of driver behaviour errors are considered to be mistakes, these errors occur due to incorrect or limited knowledge of the driving situation which results in the wrong course of action taken by the driver. At the rule-based level errors are also classified as mistakes, generally these errors are the result of misapplying a certain rule to the given situation. Finally at the skill-based level, errors are regarded as slips or lapses.

In order to quantify any errors certain measures are required. Several methods for time related measures are discussed by Horst (2007) who differentiates between methods that can be used for either lateral control. For lateral control of the vehicle the most heavily discussed measure is the Time-to-Line Crossing which, as the

name suggests, gives the amount of time before a vehicle crosses the line marking a lane and wanders over into another lane. To calculate the Time-to-Line Crossing, the lateral position, heading angle and speed are used. The driver has control over these parameters through the steering angle.

2.5.2 Importance of control strategy

The design of control strategies for active or semi-active differentials is needed to improve the handling performances of a vehicle (Cheli, Giaramita, Pedrinelli, 2005, Resta, Teuschl, Zanchetta, Zorzutti, 2005, Cheli, Pedrinelli, Resta, Travaglio, 2006). The purpose of this section is to discuss recent investigations (since 2000) and conclude the current control strategy for the torque vectoring system. The discussion will focus on knowledge of the control and the effectiveness for both situations of simulation and practice.

Figure 0-6 Control strategy for brake-based torque vectoring (Sabbioni, Kakalis and Cheli, 2010)

Some researchers (Sabbioni, Kakalis and Cheli, 2010) have made an enhancement in the performances of present control systems, which is by adding a Cybe™ Tyre into a Brake Torque Vectoring control strategy. The function of brake-based torque vectoring is to apply differential braking to the vehicle driven wheels in order to generate a yaw moment and in a simultaneous adjustment of the throttle valve to

avoid undesired speed reductions. The research has been developed by using validated numerical models and carrying out a series of test-runs. The additional information is able to exploit the potentialities of a control strategy oriented at enhancing the vehicle handling performance, and it can ensure control action robustness and vehicle safety under several road conditions such as dry, wet, snow, ice. In Figure 2-8, depending on the manoeuvres at steady-state and transient, the control logic identifies the braking torque and the eventual adjustment of the throttle valve needed in order to improve vehicle handling.

Kaiser, Holzmann, Chretien and Korte (2011) designed a vehicle model with 14 degrees of freedom, and the two individual electric motors mounted at each wheel centre can apply the positive and negative torque. This means it is possible for the driven wheels to be accelerated and braked independently. As is known, the driving torque from the electric motors has an extreme high level of quick response and accuracy for actuating the driving wheels (Milehins, Cheng, Chu, and Jones, 2010). In their paper, a control strategy for hybrid electric vehicle with torque vectoring control has been presented.

In Kang's paper, an optimal torque vectoring strategy for 4WD electric vehicles (EV) has been described in order to enhance vehicle manoeuvrability and lateral stability with the vehicle rollover prevention (Kang, Yi and Heo, 2012). They designed the 4WD EV driving with an in-line motor at a front driving shaft and in-wheel motors at the rear wheels, and the driving control algorithm involves three parts: a supervisory controller, an upper-level controller and an optimal torque vectoring algorithm. At the first level of control, the determinations such as the control functions, operation region of control and desired behaviours can be made, and the upper-level controller calculates the magnitude of driving force and yaw rate to follow the desired behaviours. The optimal torque vectoring algorithm determines actuator commands. The optimal torque vectoring algorithm is developed to map the desired driving force and the yaw rate to the actuators, taking into account the actuator constraints. Also, a wheel slip controller is designed to keep the slip ratio at each wheel below a limit value.

Figure 0-7 Schematic diagram of the driving control algorithm (Juyong Kang, Yi kyongsu and Hyundong Heo, 2012)

In order to describe the overall control architecture in their research simply, Figure 2-10 proposes a schematic diagram of the driving control algorithm, in which a control algorithm is designed to improve vehicle manoeuvrability and lateral stability. The control architecture involves three control levels, namely the supervisory controller, the upper-level controller and the optimal torque vectoring algorithm. The first level of control is to determine the control mode and desired behaviours, and the upper-level controller is able to minimize yaw rate error and modify the driving force. As follows, the inputs from upper-level control and wheel slip control are applied to the optimal torque vectoring algorithm.

2.6 Concluding remarks

Interest in the Electric Vehicle has increased rapidly over recent years, from both industrial and academic viewpoints. Research and development efforts have been focused on developing new concepts and low cost systems, but this has proved difficult primarily because of high battery costs. The current design trends in the improvement of the vehicle dynamics have been summarised. Historically, the role of the active yaw control in the overall development of vehicle dynamics control technology has commonly been the main area of focus. Active steering control and braking-based stability control have actually played the main crucial roles in

controlling the yaw moment of vehicles and ensuring good safety, driveability and manoeuvrability. It is concluded that it has been an area of rapidly changing technology over the past decade. But perhaps more importantly, this is certain to continue over the next decade.

The overall conclusion about the current mechanical drivelines is that whilst the first generation, open differential has proved to be adequate in the earlier passenger car sector, the limited-slip differential is set to have the ability to transfer the driving torque from the faster wheel to the slower wheel. Focusing on left-and-right torque vectoring systems, several types of torque vectoring differentials were reviewed. For the electric vehicle, the effect of direct yaw control on the vehicle performance and driving safety has not yet received much attention in the current research.

As mentioned previously, there are many different control strategies that have been used to solve the dynamics issues of the electric vehicle, but the overall designs can be summarised in only three generic types that are likely to have a future in the short to medium term:

i) Close-Loop Control – still the most important method being used in practical and prototype control systems.
ii) Multiple Controllers – useful applications which enable the enhancement of the performance.
iii) Optimization – to define the optimal performance and integrate into the close-loop control system design.

Almost all this recent work reviewed here has used standard vehicles and only investigated understeer characteristics as a basis for comparisons. Whilst there are good reasons to justify this, it nevertheless raises a driving response concern of whether the industry is designing cars around arbitrarily selected conventional Torque Vectoring control strategies using a full electric vehicle – rather than around architectures of electric vehicle, Linearity and efficient control strategies demands. There remains further scope for research into handling issues – in the lateral acceleration limitation and direct yaw control associated within racing conditions. A significant goal of benefit to the industry would be a better understanding of the

subjective/objective correlation of handling. There are three steps used to implement the torque vectoring control: defining reference model, close-loop control, and optimising the output. In this research, the close-loop control with PID controller and Generalized Reduced Gradient (GRG) algorithm are chosen as the methodologies most suitable for further investigation and implementation.

3. Modelling Electric Vehicle in ADAMS

3.1 Introduction

Vehicle design and development relies greatly on computer simulation to study general trends before investing heavily in actual experimental testing. Testing typically requires multiple vehicles, numerous sets of tyres and expensive instrumentation to confirm the performance of a new design. After all this, there is still a possibility that the results will show that the desired performance cannot be obtained, leading to further expense. To alleviate the expenses associated, a model is first created and simulations are run, to make sure that the design is foundational and that one may indeed go ahead and invest in the experimentation.

In this Chapter, the project vehicle with typical sub-systems such as suspensions, steering and driveline systems will be modelled and assembled so that the requirements of the vehicle dynamics simulation can be fulfilled. A model audit is needed to ensure a rigorous system model can be used in the following research. The audit involves calculating the mass and inertia properties for the vehicle body and all the components from the sub-systems, as well as finding the centre of mass position of the vehicle body and the characteristics of the springs and dampers. The tyre-sourced data is based on the Pacejka 89 version of the Magic-Formula tyre model, with the manufacturer's coefficients and the tyre model being run on a computer-based tyre test rig to indicate all characteristics of the tyre.

3.2 Project Vehicle

Due to the research being based on an industrial project from Westfield Sportcars, the company is starting to investigate and develop a full electric racing vehicle that is called the Westfield i-Racer (shown in Figure 3-1). The Westfield engineers have developed the world's first electric race car kit that can be built at home, while also supporting the requirement of a sports or racing vehicle with zero emissions.

The main specifications of the Westfield i-Racer are reasonably similar to those of typical wingless sprint cars. The Westfield i-Racer is short 3.6 metres in length and 1.635 metres in width but not slim as midget racing cars. Moreover, the Westfield i-Racer is heavier than a Formula One car with a limited weight of 770 kg, because of the 200 kg of lithium iron phosphate batteries that have to be carried with the vehicle.

Figure 3-1 Architecture of Westfield i-Racer

3.2.1 Driveline

The Westfield i-Racer, equipped with two YASA-750 electric motors, has a neoteric architecture of which the two in-line motors are located on the rear axle connected to each of the rear wheels, as shown in Figure 3-2. The YASA motors are specially designed for sports car and racing applications, thus the low speed with high torque, direct-drive and excellent torque-power densities are the particular capacities of the motors and the motors has been used in several applications and industries. Specifically, the motor has the high torque (Peak torque 800Nm/ Continuous 400Nm)

and high power (Peak power at 700v is 200kw and continuous 75kW) with a range of revolution speed 0-4000rpm. These characteristics make it very suitable for diesel generation and direct-drive applications. However, there are some limitations of the project vehicle, such as the top speed being constrained to 115 mph and also each motor being limited to 45kw.

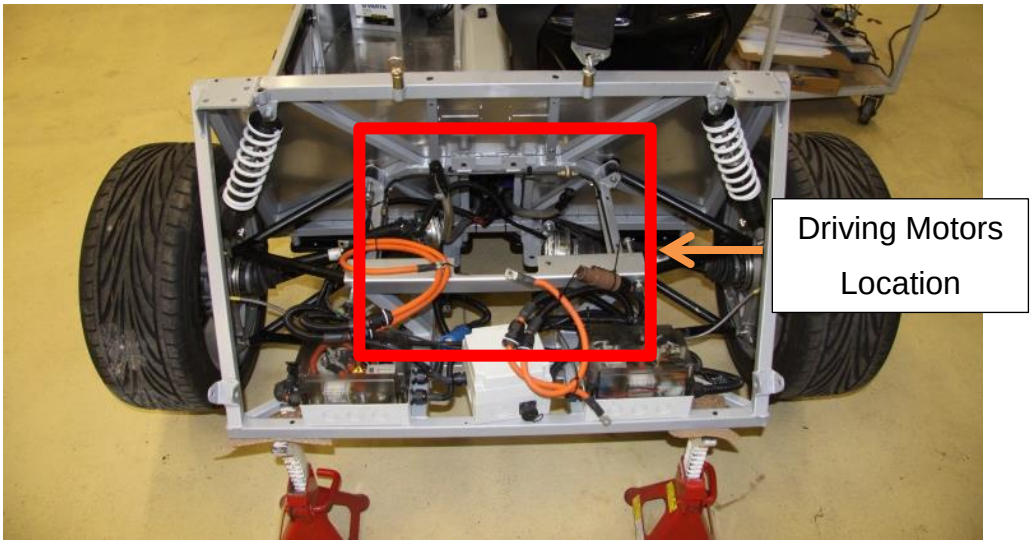

Figure 3-2 The position of the electric motors

An innovative modular design of the batteries has an energy capacity of 23 kWh, including up to eleven sealed Lithium Ion Phosphate units (48V), which contribute to the handling of the project vehicle, and which also can meet the stringent safety standards, as shown in Figure 3-3. Particularly, the operational range of the project vehicle is expected to be 50-60 miles so that the racing time is about 25 minutes.

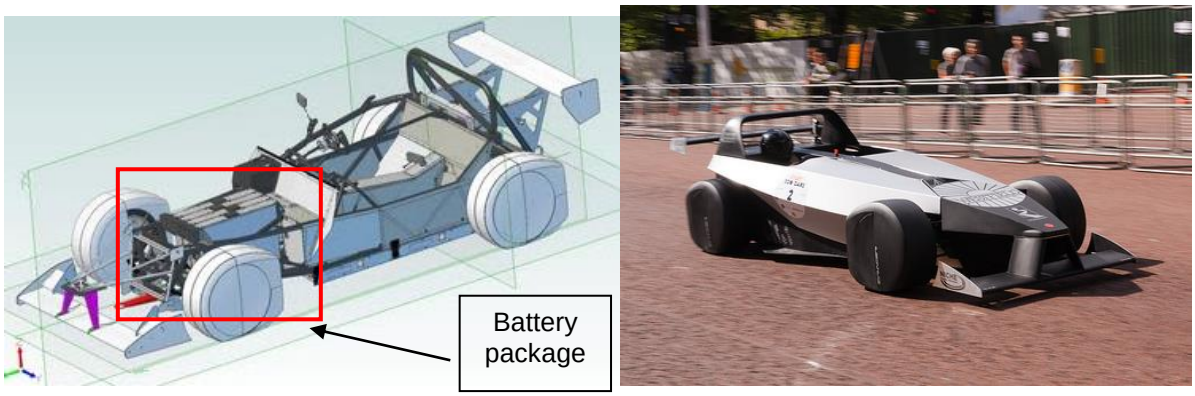

Figure 3-3 The position of the battery package

3.2.2 Chassis and Suspension system

Westfield Sportcars have completed a 'light-weighting' project working with tubing specialist Reynolds Technology, creating a new car chassis and wishbone by replacing much of the traditional mild steel with alloy tubing as used in Tour de France race bicycles, as shown in Figure 3-4.

Figure 3-4 The pictures for the chassis and suspensions

The design team chose to reduce the weight of the chassis and the wishbones by examining the possibility of using new thin-walled alloy tubing developed by Reynolds in place of the mild steel tubes used previously, as shown in Figure 3-5.

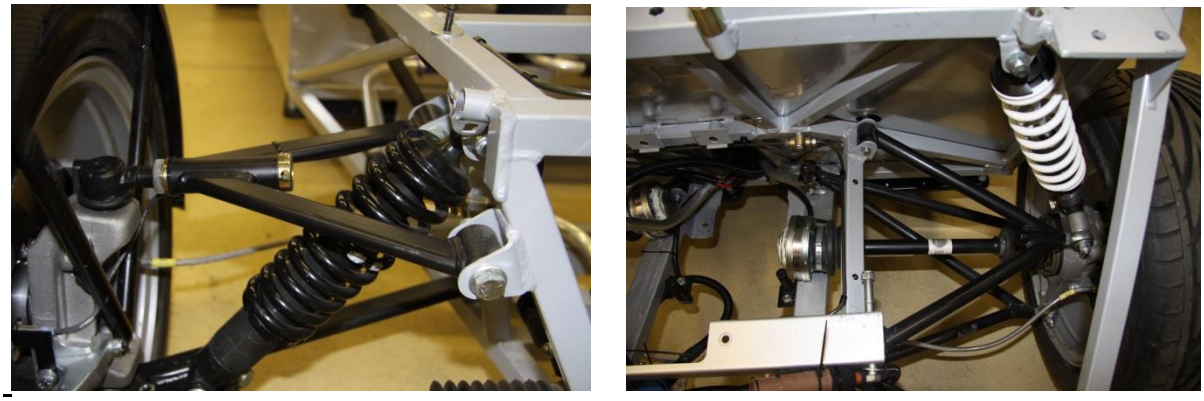

a) Front b) Rear

Figure 3-5 The pictures of the front and rear suspensions

3.3 Modelling project vehicle

In this section, the main systems will be modelled and assembled in computing-based software – ADAMS that can allow a number of vehicle subsystems to be modelled and simulated, namely the driveline, chassis and vehicle body. The modelling of a road as an element is also included to constitute the entire vehicle model; and modelling the suspension system is the most important part in this process.

The overall vehicle model is prepared using the Automated Dynamic Analysis of Mechanical Systems (ADAMS) tool from MSC.Software. ADAMS is a widely used tool for computing the large amplitude non-linear dynamic behaviour of systems such as ground vehicles. For this exercise, the ADAMS/Car environment was not used in order to make the modelling practices more transparent – the extensive use of templates and “sealed up” run-time procedures can sometimes make it difficult to understand the exact performance of the model when using the “Car” environment.

The process which has been used for modelling is planned to easily make some modifications later in the design. So, using the graphical user interface of ADAMS/View to create the full project vehicle as shown in Figure 3-6, the starting point is to create hard points to indicate the different key locations of the subsystems. As follows, these hard points are used to create the linkages; then the different joints are added to connect the components together to finalize the system. Finally, all the components of the project model have the mass and inertia properties.

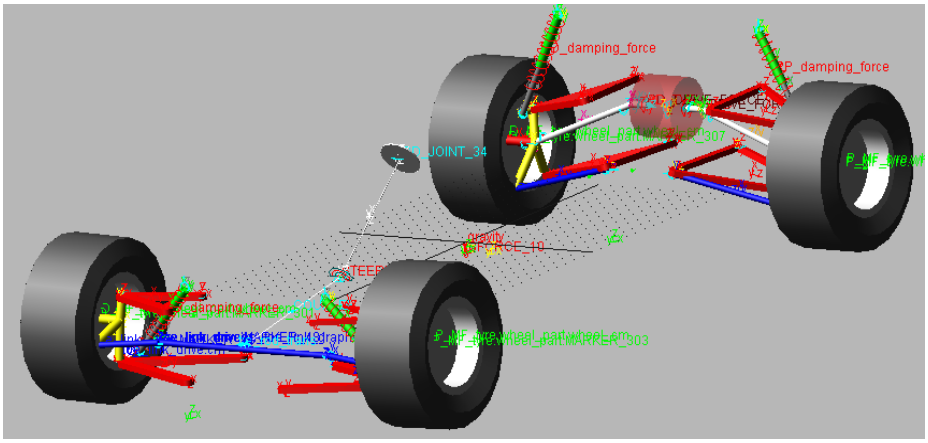

Figure 3-6 Westfield i-Racer model in ADAMS/View

In the following section, a model audit is carried out so that it can ensure that the model is more reliable and precise. More discussions are involved in this section and the auditing aspects of the model are listed as below:

- Sprung mass (The vehicle body)
- Centre of Mass Position (The vehicle body)
- Inertial Properties (All the components)
- Un-sprung Mass
- Spring and Damper Characteristics
- Modal Solution
    - Total Degrees of freedom
    - Eigen Solution

3.3.1 Vehicle Body

The first concern for describing the full vehicle is to define the data set of the vehicle body, namely the centre of mass position, the inertia properties and the masses, to fulfil the requirements of the vehicle dynamics simulation. In this particular vehicle model, the mass data of the vehicle body includes the mass of the body frame as well as the additional masses of the Front Battery Module, Motors, Bracket, Coolant and Controllers, and a passenger may even be added. Based on the project vehicle with a conventional architecture, a summary of the main data collections will be exhibited, namely that of the suspension geometry and the structure of the vehicle body. The original geometric data was captured using a single point Faro arm measuring device in the Coventry University Workshop, and all the dimensions of all the systems such as the suspensions, the springs and dampers, and the body were then processed using ADAMS to collate all of the data and achieve the single point data, as required for the computer simulations.

The mass of the Westfield i-Racer model was measured in the Coventry University Laboratory. It is important to note that the battery pack module, the complete rear motor controller unit and the vehicle body panels, as additional masses to the mass of the full vehicle, were assessed. The front, rear and full vertical loads are measured so that the mass and the centre of mass position in the longitudinal are be

defined. Here is a method to attain the centre of mass height, which is to lift the rear axle of the vehicle so the vehicle centreline from front to rear creates a certain angle. A diagram of this is shown in Figure 3-7; reproduced with permission from Milliken.

Figure 3-7 The method for locating vehicle centre of mass height (Milliken, 1955)

The solution for vehicle height is given by equation (3.1).

$$h = R_l + \left(\frac{W_F * l - W * b}{W * \tan\theta}\right) \tag{3.1}$$

R_L is the radius of the front tyre, *W* is the total weight of the vehicle, and W_F is the weight of the front of the vehicle during the test. The above method gave the centre of mass height at 232 mm above the road surface. Using this approach, where the total masses of the vehicle were the summation of the major components, the mass centre position can also be found by using the method described above.

The inertia properties of the vehicle body need to be determined because the dynamics of an actual vehicle are significantly affected by the yaw moment of inertia I_{ZZ}. This data generated mainly focused on two main areas in the mass of the chassis and four wheels. There is a detailed model to represent the mass and inertia properties for the body that involves the overall masses of an approximate chassis, battery Module and a motor controller which is provided by Westfield Sportcars, as shown in Figure 3-3 above.

3.3.2 Suspension System

A completed suspension system as a most important system of the full vehicle model will be established. In order to achieve a suspension model representing the one installed on the actual vehicle, the use of powerful multi-body systems analysis programs can be used. In the following discussion, modelling of a double wishbone suspension system at both the front and rear of the vehicle is referred to as a Linkage Model. Thus, the components of the suspension as rigid bodies can be modelled in detail and the actual front and rear suspensions as shown in Figure 3-8.

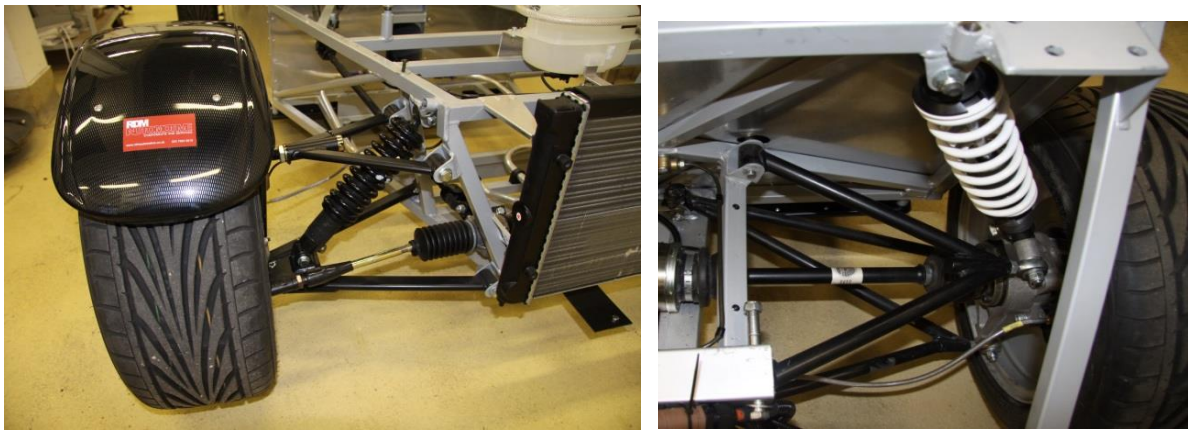

Figure 3-8 The actual front and rear suspensions

The SAE coordinate system is used while modelling the vehicle, with x backward, y to the right, and z downward. The origin is located directly below the centre of the vehicle body geometry. SI units are used, i.e. metres for length, Newtons for force, kilograms for mass and seconds for time. The data for the hard point locations are measured by using a single point Faro arm-measuring device in the Coventry University Laboratory. Table A5.1 lists the hard point coordinates of the right front side suspensions hard points. The left side hard points are coded as mirror images of the right points on the x-z plane. Hard-coding the left side as a mirror image of the right makes it simpler to make changes in the suspension geometry, as changing the coordinates of a point on the left side automatically maintains the symmetry of the right side. Table A5.2 lists the hard point coordinates for the rear left suspension. Here again the left side is hard coded as the mirror image of the left. The tables can be found in Appendix 5.

The linkages of the suspension are generated by using the various shapes of the rigid body in the Tool-box. The hard points were defined as being used to locate the positions of each suspension linkage and to generate the completed suspension geometry. The main components of the suspension are modelled separately and linked to each other through the joints. Figure 3-9 shows the front and rear suspension model in ADAMS/View. To clarity and simplify, the graphics of the Westfield i-Racer body are modelled as a dummy part that has the same mass and inertia properties as the body.

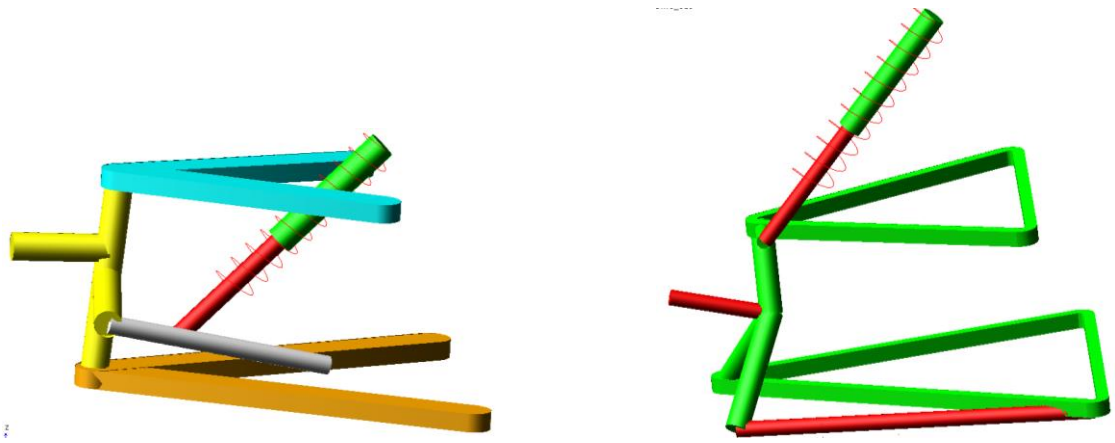

a) Front suspension model b) Rear suspension model

Figure 3-9 Front and rear suspension model in ADAMS/View

The Westfield i-Racer employs a double wishbone suspension on the front driving axle and a deformed double wishbone suspension on the rear driving axle. For each suspension, upper and lower A-shape arms and wheel knuckle are created as parts. Bushings are used to connect the two A-shape control arms to the sub-frame, and the control arms are linked to wheel knuckle by using spherical joints. The reason for using the bushings there is to introduce some steering compliance, so that the bushings as modelled have extremely high stiffness in the longitudinal and vertical directions, and are comparatively soft in the lateral direction. Again, all the components have their own mass and inertia properties.

The spring and damper configurations are created initially using the internal ADAMS commands so that a spring damper unit can be generated automatically. The springs are modelled by using a linear single component force that acting between the upper and lower mounting points of the strut. The force is used to define by a constant stiffness value with spring deflection. Westfield provided nonlinear damper data that is modelled using a single component force acting between the same mounting points as the spring. The nonlinear damping force is defined by a 2D curve with deformation velocity along the x axis and force on the y axis as shown in Figure 3-10.

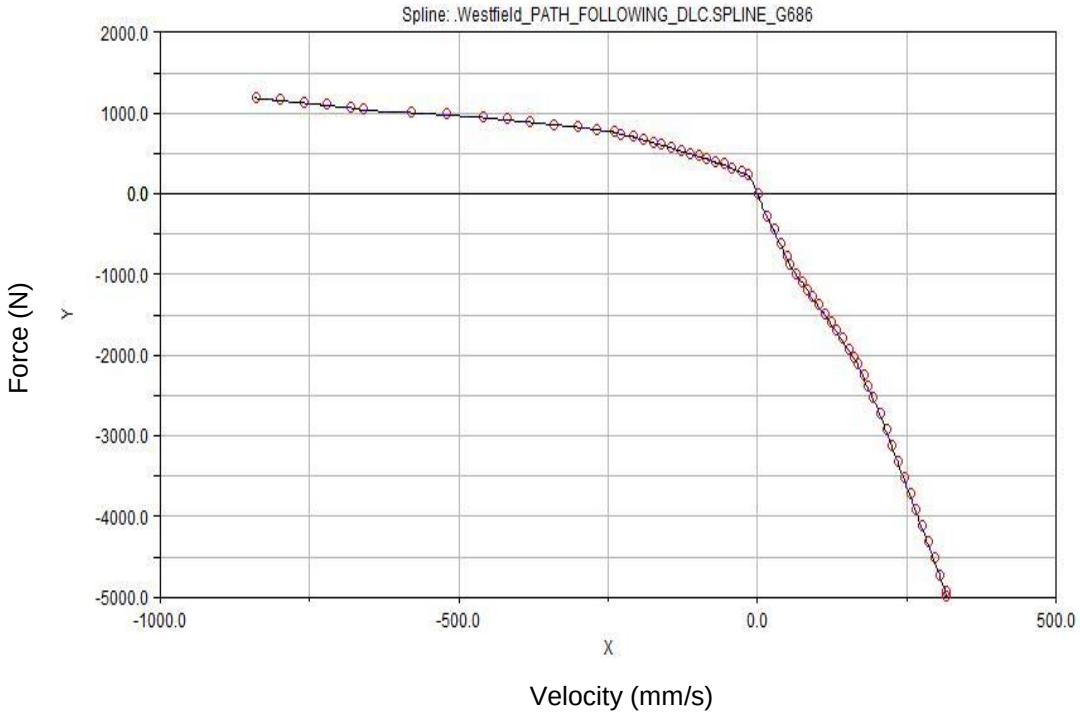

Figure 3-10 The 2D curve for the nonlinear damper

The purpose of the software to model the suspension structure is now well established and will be discussed further in the next chapter. The results from this type of analysis are mainly geometric and allow the outputs to be plotted graphically, such as the camber angle or roll centre position against the vertical wheel movement. The double wishbone suspension model can be simplified to represent connecting the A-shape control arms to the sub-frame. Modelling the suspension in this manner is necessary to calculate the degrees of freedom (DOF) for both the front and rear suspension systems.

Part	6 × 6 =36
Spherical	4 × -3 = -12
Revolute	2 × -5 = -10
Translation	1 × -5 = -5
Hook	2 × -4 = -8
	ΣDOF = 1

Hence, the calculation as shown above is an example showing that the motions of all six parts at the front suspension have been constrained by using different types of joints, as shown in Figure 3-11. Note that the type of the joint has to be chosen correctly in its location to attach the two parts together; otherwise the additional or incorrect numbers of degrees of freedom may cause the suspension system failure, or movement in the wrong direction. Also, the revolute joints that connected the wishbones to the frame will be replaced by bushings when using the full vehicle model for handling simulations.

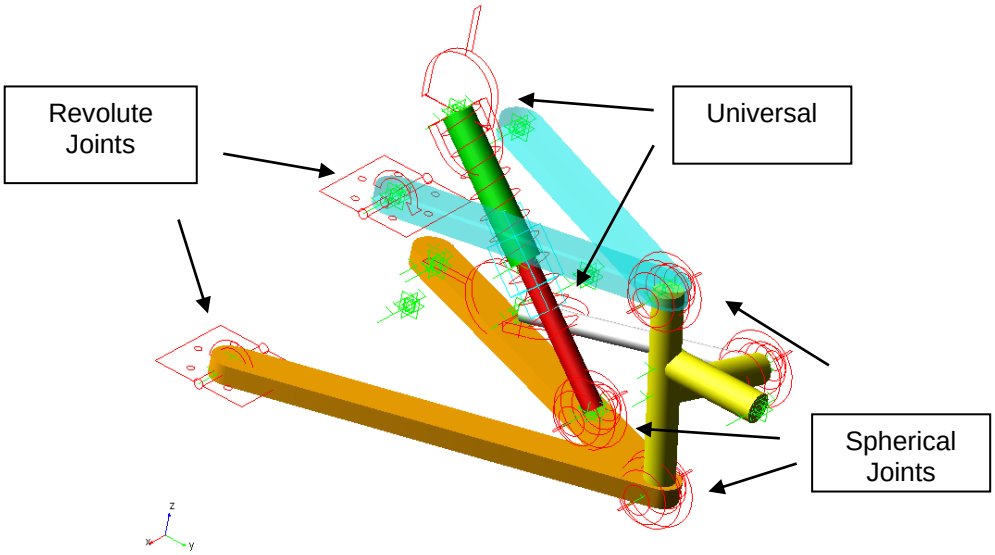

Figure 3-11 The parts connected by the correct joints

3.3.3 Steering System

The configurations of the steering system based on linkages and steering gearboxes are available for both cars and trucks. The steering system in the following sections is modelled by using a conventional Rack-Pinion system. Modelling a steering system on the actual vehicle can be represented as shown in Figure 3-12. Basically, a cylinder is used to model the steering column connects to the vehicle body by using the revolute joint, which the axis of the joint should align along the line of the column. The motion or torque inputs of the steering control are applied at this revolute joint to manoeuvre the vehicle model. Using a translational joint connecting the steering rack to the vehicle body is represented, and the rack is linked to the tie rods by using two universal joints. The steering ratio can be implemented into this system by using a coupler statement that can convert the rotation of the steering wheel inputs to the translation movement of the steering rack.

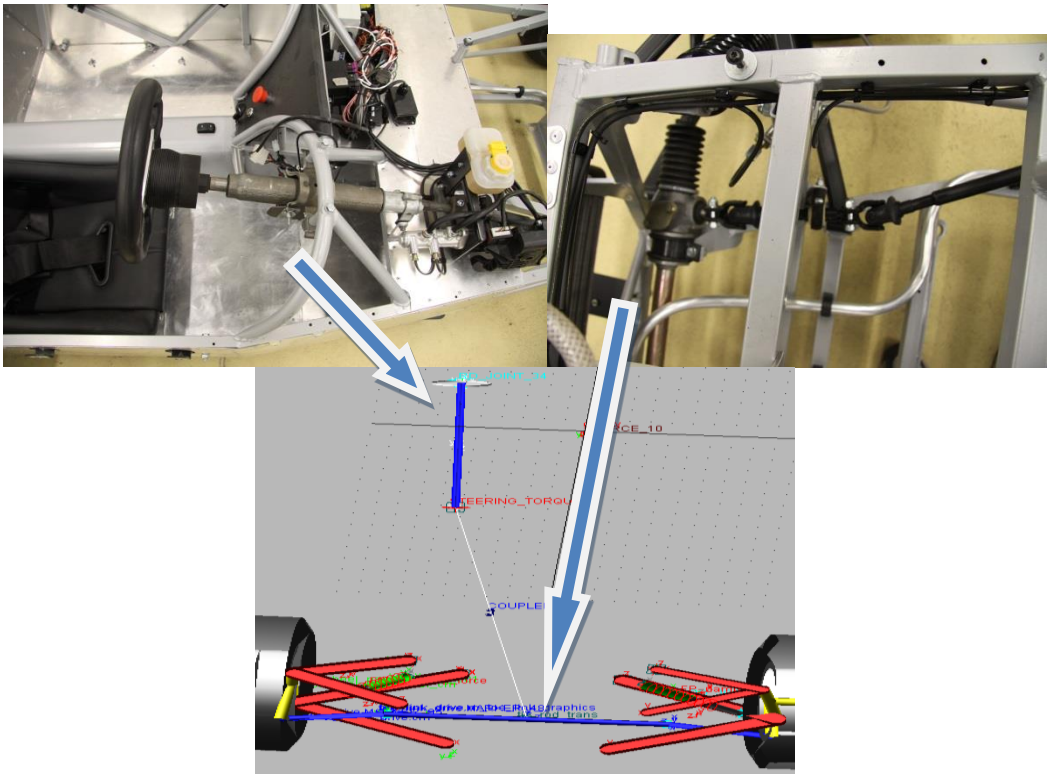

Figure 3-12 Modelling steering system in ADAMS

When starting the vehicle dynamics analysis, the steering ratio is always an important parameter for the model design; the relationship between the turning the steering hand wheel and the steer change at the front wheels has to be known. This coupler is based on a ratio where one degree of the steering column input generates the 0.18mm translational motion of the steering rack. This relationship is utilized to connect the two tie rods at the front suspension, and then control the steer angle at the wheels. Using a variable statement can measure out the steer angle of the front wheels. A steering ratio can be determined by a common fashion, degree-to-degree, which is the 22 degrees of hand wheel inputs relating to 1 degree of front wheel steering, as shown in Figure 3-13. In both the linkage model and the real vehicle, the steering ratio would vary when the wheels move in the motion of the full bump and rebound, or the vehicle rolls.

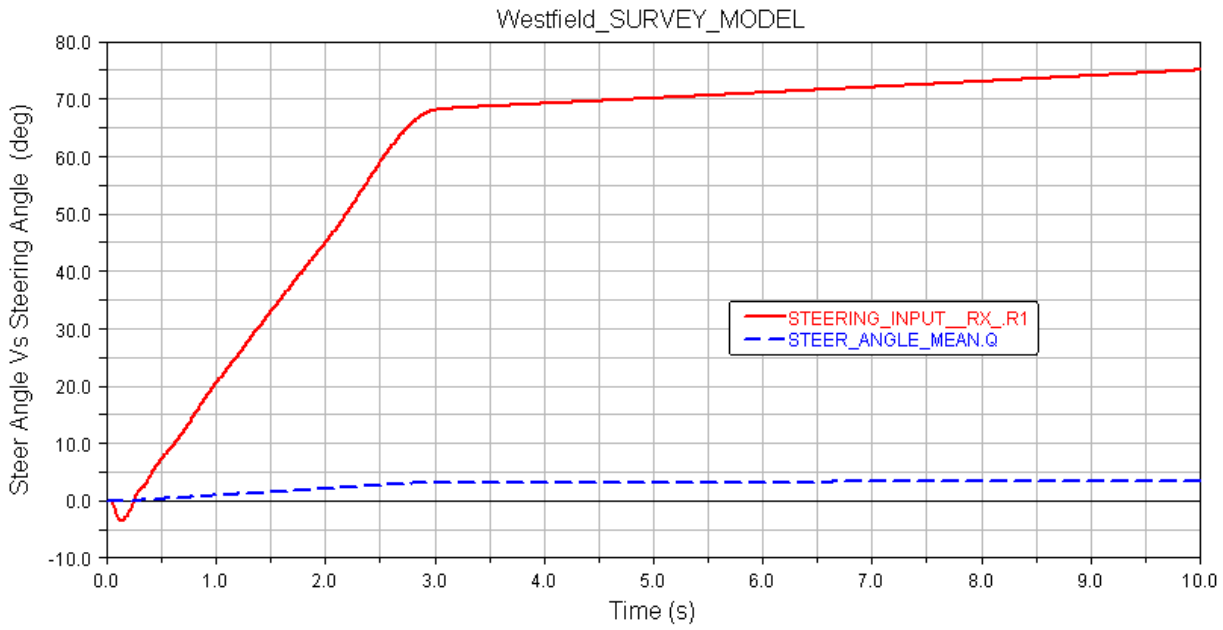

Figure 3-13 The steering ratio for Westfield i-Racer model

3.3.4 Aerodynamic Effects

Some classic assessments of aerodynamics in existing text books (Milliken and Milliken, 1995; Gillespie, 1992) that corresponds to the vehicle dynamics is introduced. As is known, when the air flows through the vehicle body, forces and moments can be produced because of the friction and pressure distribution between the air and the body surface. Thus, the forces in the longitudinal, lateral and vertical directions along with the moments in roll, pitch and yaw will arise in the same reference frame as that of the vehicle body.

In this simulation, the project vehicle moves only in the $X\,Y$ plane so that it is going to require at least the formulation of a longitudinal force F_x, a lateral force F_y. The direction of the project vehicle will be changed during the manoeuvre, hence it is going to be necessary to model the forces as components in the body-centred axis system located at the mass centre. The magnitude of the aerodynamic forces can be calculated out by using the equation 3-2 as shown below:

$$F_D = \frac{1}{2}\rho V^2 C_D A \tag{3-2}$$

Where

C_D = the aerodynamic drag coefficient

ρ = the density of air

A = the frontal area of the vehicle

V = the velocity of the vehicle in the direction of travel

Using this equation, there are only two forces that were applied within the model to exert the effects on both the longitudinally and laterally direction of the vehicle. An expected drag coefficient of 0.4 is used for the EV, and the rest of the data, such as the frontal area of the vehicle, was included from the Westfield Sportcars. Figure 3-14 shows that the aerodynamic drag forces act on the vehicle body when turning a corner.

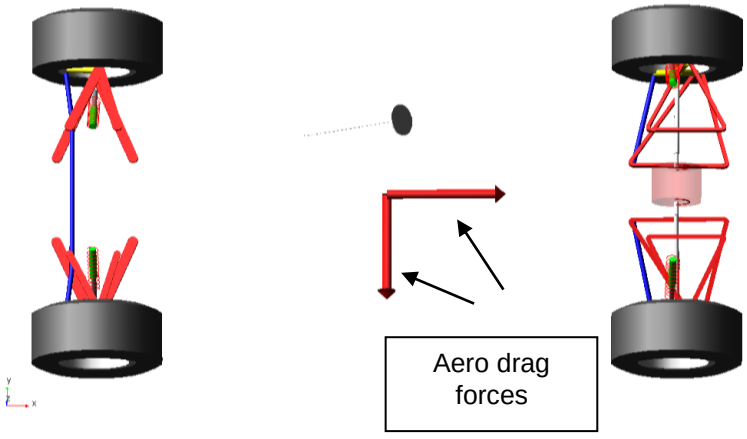

Figure 3-14 Aerodynamic drag forces in the lateral and longitudinal direction

3.3.5 Driveline Modelling

According to the position of the electric motors, the project vehicle is a typical rear-drive car, and the pair of electric motors is mounted in the centre of the rear axle, that is, a so-called 'In-line' motors electric vehicle. This type of architecture has been used in a few designs for racing purposes, such as the Delta E-4 coupe and the Le Mans Electric. Figure 3-15 b) shows the motors can be directly connected to the drive-shaft without any transmission system, such as gearbox and differential; thus the driveline has been shortened and the higher driving efficiency of the powertrain can be improved.

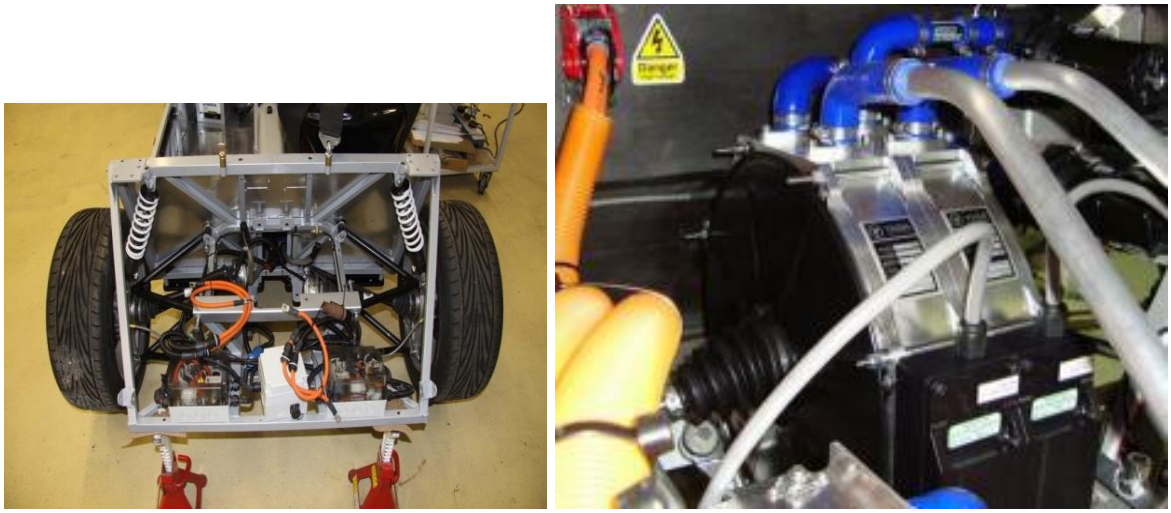

a) The position of the motors b) The electric motors on the rear axle

Figure 3-15 The motors position of the project vehicle

However, this new driveline will be modelled in this section, as shown in Figure 3-16. Based on the architecture of the project vehicle with the in-line motors, modelling the driveline consists of creating two new parts: a cylinder for the twin electric motors, and two columns for the drive-shafts. And those parts are constrained by using a few type joints, for example, the cylinder (twin motors) is attached on the vehicle body using a fixed joint, and linked to the columns (drive-shafts) using two constant velocity joints. The constant velocity joints are typically used to model the drive-shafts connections. There are no extra degrees of freedom available on this driveline.

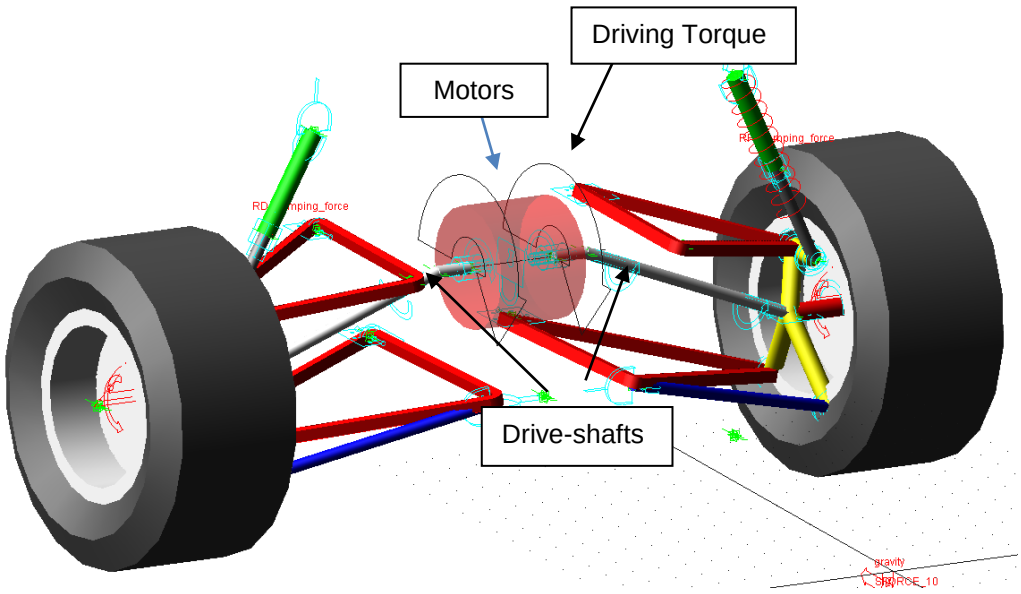

Figure 3-16 Modelling the driveline in ADAMS/View

There are some simulations required to retain the vehicle at a constant speed as in the following studies, because if the vehicle does not have any form of the driving torque, it will drive through the manoeuvres at a coasting condition using the momentum available from the initial velocity. Furthermore, even ignoring the rolling resistance and the aerodynamic drag force, the momentum of the vehicle will still lose because of the resistant element of the cornering forces, which is generated at the tyre during the manoeuvres. However, the means of modelling the driveline is to implement the driving torques to the driven wheels, then produce the traction at the contact patch; thus, the points for applying the driving torques on the driveline have been chosen at the two cylindrical joints. It is more like a real vehicle driven with electric motors, in which the torque generally outputs from the centric rotor of the electric motor.

The rotation of the two rear wheels is coupled to the rotation of the rotors of the electric motors, and the driving torque outputs are equally distributed to each of the drive-shafts as 50% of the torque. It can be considered as an ‘open differential’ mounted on the rear axle, which means the new driveline allows the rear wheel to rotate at different speeds during cornering, but only by applying the same torque on each of the driving wheels. Table 3-1 shows all bodies, joints and total DOFs have

been calculated by using a function in ADAMS, confirming the model has 15 DOFS and there are no redundant constraint equations.

Table 3-1 A list of all bodies, joints and DOFs

```
VERIFY MODEL: .Westfield_EV_VARIABLE_MF_TYRE

  15 Gruebler Count (approximate degrees of freedom)
  34 Moving Parts (not including ground)
   4 Cylindrical Joints
  14 Revolute Joints
  16 Spherical Joints
   5 Translational Joints
   2 Fixed Joints
   4 Hooke Joints
   2 Couplers

  15 Degrees of Freedom for .Westfield_EV_VARIABLE_MF_TYRE

There are no redundant constraint equations.


Model verified successfully
```

Before finishing this section to describe how to model the driveline, there is a method that needs to be represented. Namely, the driving torque acted on the drive-shafts can be modelled by using an existing TORQUE command in ADAMS/View. Thus, the torque can be controlled by using a function or subroutine in the TORQUE command that can be used to apply a control strategy for the vehicle dynamics or stability control to the driveline. For example, if the model runs at a ‘drifting’ condition, the torques from the driveline are deactivated, and the driveline is also able to produce equal torques on both the driving wheels to represent an ‘open differential’. It is a limitation of an open differential that the amount of total torque applied to both drive wheels depends on the side with the least traction. For example, when one wheel acts on a slippery surface, the torque applied to the other wheel would be the same as that on the slippery side. Thus, the total torque could be reduced and may be not enough for vehicle propulsion. In additional, the average of the rotational speed of the two driven wheels equals the input rotational speed of the drive shaft, and an increase in the speed of one wheel is balanced by a decrease in the speed of

the other. These characteristics can be represented by the function or subroutine associated with the torque to improve the control strategy of the driveline. Furthermore, even a more complex control strategy, such as torque vectoring control, can exploit this approach to implement all the control concepts or requirements into the driveline, and that will be discussed in Chapter 6.

3.4 Tyre modelling

The subject of extensive research, tyre modelling mainly focuses on how to model the forces and moments generated at the contact patch where the tyres touch the road surface. Pacejka and Sharp (1991) provided and developed the most common tyre model, which have been broadly used, and the tyre model can compromise the modelling of the tyres between the accuracy and complexity.

The research mainly focuses on a vehicle handling study, thus the project model is generally manoeuvring on a flat road surface. In general, the tyre model is used to create and model the forces and moments generating at the contact patch between the tyre and the road surface. These forces and moments will transfer through the suspension into the vehicle body. There are the three orthogonal forces and the three orthogonal moments that can be calculated by the tyre model at each wheel centre, controlling the vehicle body motion. Again, for the handling of the analysis, the calculation of the tyre model is mainly based on the longitudinal direction (driving and braking forces) and lateral forces, also including the formulation of rolling resistance and aligning moments. A flat 2D road file is used as a part of the model; furthermore it has the function to change the friction coefficient of the road surface to represent the various surface textures, namely dry, wet and ice conditions.

3.4.1 Modelling virtual tyre rig

The aim of modelling the tyre test rig is to provide a tool to integrate a given tyre model and its associated data set before using this with a vehicle simulation.

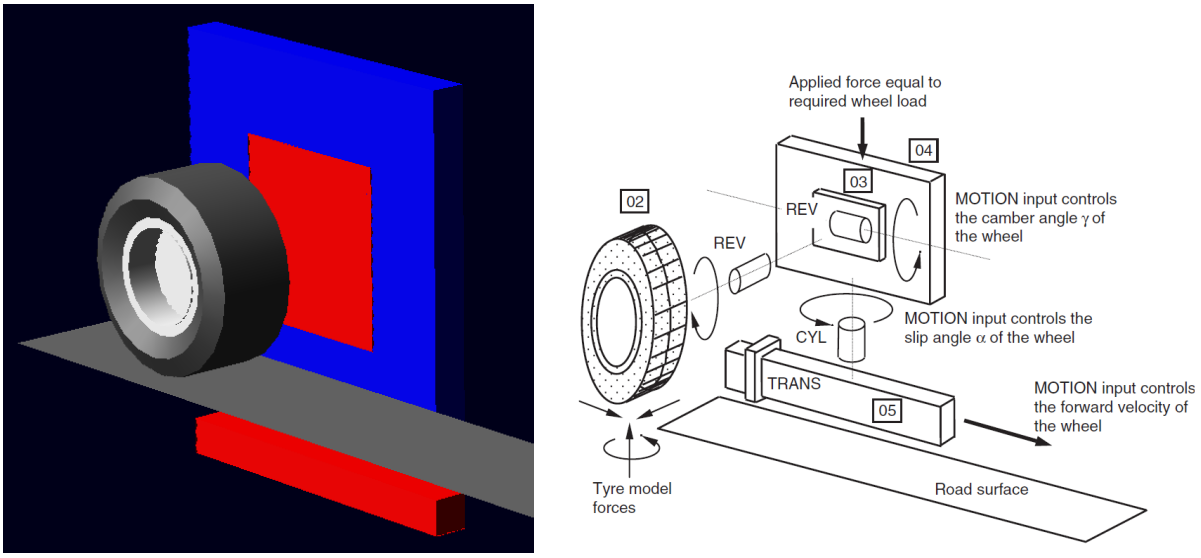

Figure 3-17 The tyre test rig model

The modelling of the tyre test machine is illustrated in Figure 3-17 and includes a tyre model that rolls forward on flat surface, representing the actual tyre interaction with a moving belt in a real experiment. In this model, the tyre model is attached to a 'test rig' model using a revolute joint, the axis of which is aligned with the spin axis of the wheel. A rotational motion can be applied to a cylindrical joint (aligned vertically) for which the rotation represents the side-slip angle on the tyre during the simulation. A vertical force can also be applied to the carrier part to represent the tyre load. For the parts and the joints used in this model, the overall system has only two degrees of freedom. These represent the spin motion of the tyre and the vertical movement of the wheel centre.

3.4.2 Tyre model for project vehicle

The tyre model used in extensive computing-based simulation is highly important when analysing dynamic behaviour. Because the Westfield Sportcars company cannot provide the particular parameters for modelling the given tyre as it is used on the project vehicle, an alternative approach involves an initial trial with the Fiala tyre model (Fiala, 1954). As is known, there are only ten input parameters that are required for creating the Fiala tyre model; this advantage can be directly correlated

to the characteristics of the tyre. Nevertheless, the major limitations of the tyre model include the following: a) the model does not have the ability to represent the combined situation, such as cornering and braking, or cornering and driving at the same time. b) Lateral force and aligning moment cannot be calculated as having a camber angle. c) When the tyre with the vertical load moves on the straight line, the variety of the cornering stiffness is not modelled.

Another suitable alternative approach is established to fulfil the requirements of the simulation. It is achieved by using the 'Magic Formula' tyre model (Bakker et al. 1986, 1989), of which the 'Magic Formula' tyre model is now most well-established, based on the work by Pacejka (Pacejka and Bakker, 1993). This model is a 'point follower' model, which uses an empirical mathematical form that can be shaped with a relatively small number of parameters to fit more or less any measured tyre dataset. The "point follower" term refers to the fact that the tyre is idealized as a single point of contact, which has aggregate forces and moments for the entire contact patch. This is the way that data is recorded on a typical tyre test machine and is completely suitable for smooth road handling calculations at low tyre slip angles. Because of the absence in the particular coefficients of the tyre model for the project vehicle, a set of standard data was used, as shown in Table 3-3. The coefficients need to be adjusted in a reasonable region within which the results from testing the tyre model on the rig can fulfil the expectations of this particular tyre model under the dynamic manoeuvring. Then, the tyre model has been tested on the virtual tyre test rig in ADAMS, and examination of the tyre results will be shown in the following section.

Table 3-1 A set data for tyre model

Pacejka Coefficients (89 Tyre Model Version)					
Lateral Coefficients		**Longitudinal Coefficient**		**Aligning Coefficient**	
a0	1.5	b0	2.37272	c0	2.298
a1	40	b1	-9.46	c1	-3.131
a2	1262	b2	1490	c2	-5.208
a3	2200	b3	130	c3	-1.347
a4	15	b4	276	c4	-5.404
a5	0.01399	b5	0.0886	c5	0.0
a6	-0.1026	b6	0.00402	c6	0.0
a7	0.11334	b7	-0.0615	c7	0.03651
a8	-0.01872	b8	1.2	c8	-0.2838
a9	-0.01151	b9	0.0299	c9	-1.864
a10	-0.08183	b10	-0.176	c10	-0.0515
a11	-14			c11	0.02864
a12	4.595			c12	-0.004203
a13	0.3496			c13	-0.1411
				c14	0.04018
				c15	-0.8838
				c16	-0.1855
				c17	0.3956

These coefficients of the tyre model will be used for all simulations in later Chapters. For these simulations, the tyre model was steered in a region of the slip angle and operated under four different vertical loads (1962N, 3924N, 5886N and 7848N). The examination of the tyre results is shown in Figure 3-18 and Figure 3-19; the results represent some curves for the lateral force and the self-aligning moment during the changes of the tyre slip angle. The results show that the tyre performed in an intended behaviour; nevertheless, the coefficients created in the tyre model were only modified to an approximate level. Further validation of the coefficients is needed to ensure that the data from the test rig model are as near the same as possible to the actual tyre characteristics, which has to be taken into account when examining all of the results generated from the simulations.

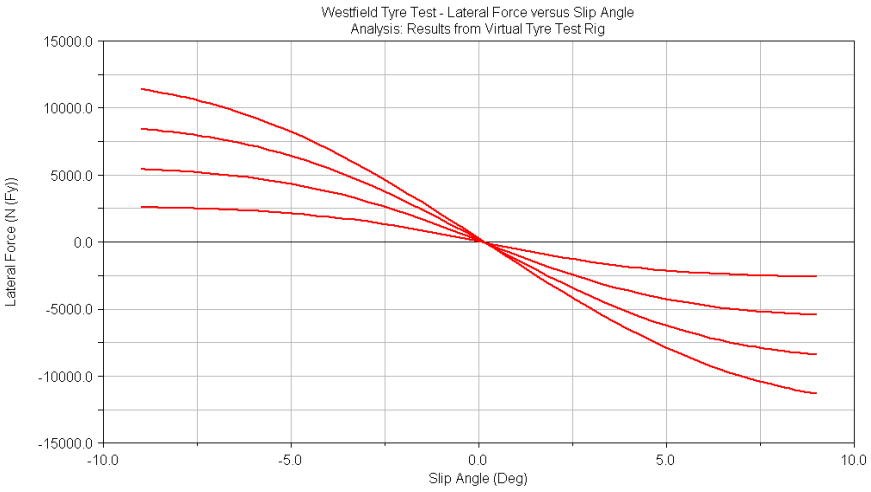

Figure 3-18 Lateral Force Vs Slip Angle tested on the Virtual Tyre Test Rig

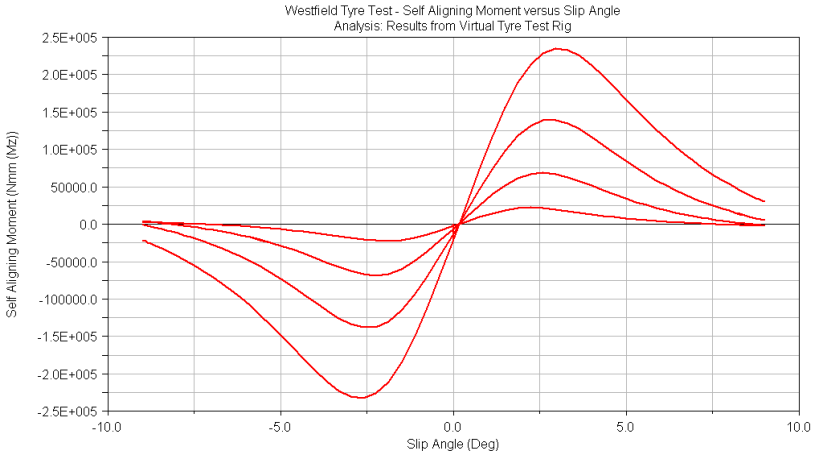

Figure 3-19 Self Aligning Moment vs Slip Angle

3.5 Conclusion

The project vehicle has been represented in detail, with the entire architecture of the given electric vehicle with RWD being included, and the components and the configuration of the new driveline also being introduced. The capacity of the twin electric motors could fulfil the requirements of the racing vehicle. The lightweight chassis and the wishbone suspension for the project vehicle were described.

Several sub-systems of the vehicle, for example the vehicle body, the suspension system and the driveline, have been modelled in ADAMS, and the audit was carried out to ensure the reliability of the model. Also, the aerodynamic effects were considered in this section. The driveline was able to produce the variable driving torque at the wheels, so that it could represent the different driving modes, such as the ‘open differential’ and the torque vectoring control. The ‘Magic Formula’ tyre model was added on the vehicle model, and also used with the virtual test rig model to examine characteristics of the tyre model in the intended behaviour due to modifying the coefficients of the tyre model.

4 Measurement and analysis of the virtual model

4.1 Introduction

When building a vehicle model in a computer-based environment, the accuracy of the simulation results relies on the accuracy of the model and the vehicle parameters used to build the model. Hence, there are several methods available to validate the vehicle model, such as kinematic studies and dynamic manoeuvres.

In order to verify the performance of the suspension system as modelled in Chapter 2, a range of characteristics will be determined through simulation of a quarter vehicle model. In this chapter it will be shown that the full vehicle model will be analysed in a number of ways that will provide information to support the following investigations. Also, the steady-state cornering manoeuvre will be used to define the basic driving characteristics of the vehicle model.

4.2 Kinematic analysis

The full vehicle model has been created in the previous chapter, where the arrangement of the suspension system consists of the typical linkages for the double-wishbone suspension to connect the wheels to the vehicle body. The interaction of the linkages restricts the wheel plane to undergoing combined translation and rotation. These motions are normally determined with respect to the vehicle body, so the following descriptions will explain the kinematic analysis of the wheel. For example, toe change for suspension linkages directly steers the front wheels and generates lateral force and yaw moment. Camber angle is a compensation angle to maintain the tyre perpendicular to the road surface when the vehicle body rolls. Half-track change influences the lateral velocity of the tyre contact patch via the roll rate. Hence, the slip angle of the tyre is affected, since the angle is defined as the arctangent of the lateral and longitudinal velocities; an increase in the lateral velocity directly increases the slip angle.

4.2.1 Quarter vehicle modelling

In this section, the basic function of the suspension system is represented from a functional perspective. The front suspension of the vehicle model has been built as one of the best-known suspension types, the so called ‘Double Wishbone system’, and also the double wishbone system has been created for the rear suspension. Using the software to analyse suspension geometry is now well established and will be discussed further in the next section of this chapter. The output from this type of analysis is mainly geometric and allows results such as the camber angle to be plotted graphically against the vertical wheel movement.

Modelling the quarter vehicle is discussed by using the existing double wishbone suspension system at the front axle. Basically, the suspension model uses the revolute joints to connect the upper and lower A-shape arms to the chassis as shown in Figure 4-1. Imparting a vertical motion to the suspension is achieved through a jack part that connects to the ground using a translational joint. Therefore, at the translational joint the applied motion moves the jack through a range of vertical movements that assumes the suspension moving between the bump and rebound positions. An in-plane joint is applied to link the jack to the wheel knuckle where the wheel centre is located. In addition, this joint only constrains the wheel centre at the top of the jack to move in the plane, but the wheel can still rotate or move in the lateral and longitudinal directions.

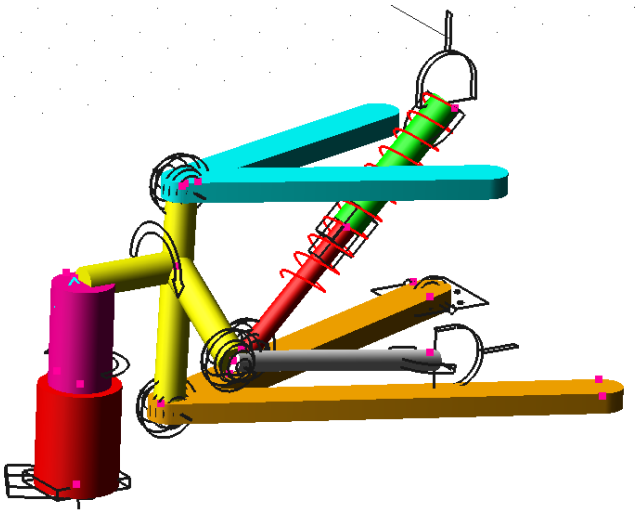

Figure 4-1 Modelling the front of the quarter project vehicle

Note that the resulting system model has a total of zero degrees of freedom. The movement in the system is due to the introduction of a user prescribed time dependant motion that accounts for one degree of freedom constrained from the system. The resulting analysis is kinematic. The introduction of one or more additional degrees of freedom would result in a dynamic analysis.

4.2.2 General approach for kinematic analysis

For a suspension system, the main function of a multi-body systems model is to simulate the geometric position and orientation when the suspension has a vertical movement between the full bump and full rebound positions (Blundell, 2004). When simulating the vertical motion, the output is only suitable for a kinematic or quasi-static analysis. As mentioned, the motion applied to the translational joint moves the wheel between the 60mm rebound and 60mm bump positions. This results in particular times for the movement, at 0.25 second for bump and at 0.75 second for rebound, which enables the present of the continuous and smooth animation of the movement cycles. The duration of the simulation time is 1 second with 100 output steps, which ensures the results are calculated over the full bump and rebound range. In ADAMS, a motion statement was used to move the translational joint during all the simulations.

The motion statement is shown below, where the total movement between bump and rebound is 120mm:

$$\mathrm{MOTION/01, JOINT} = 01, \mathrm{TRANS, FUNCTION} = 100 * \mathrm{SIN(TIME} * 360\mathrm{D)}$$

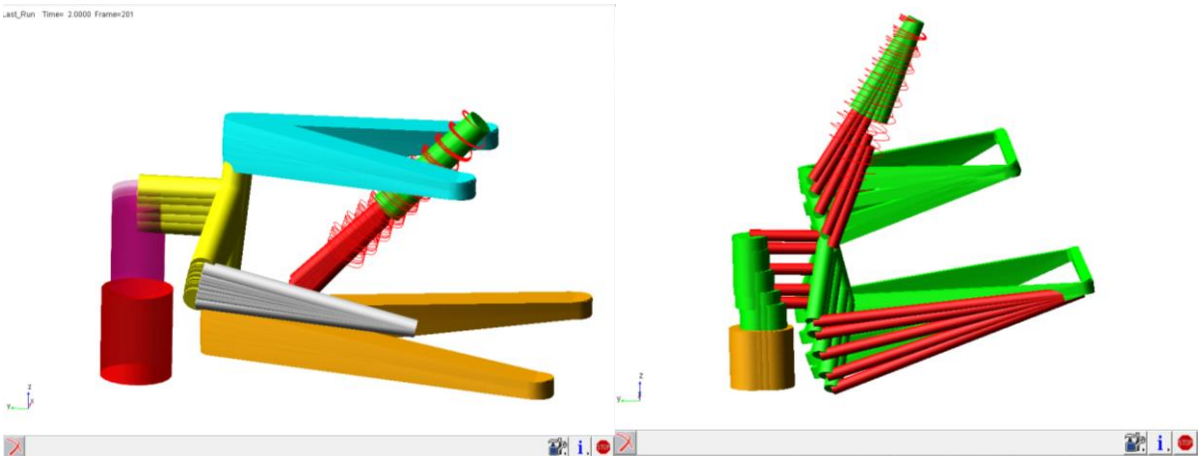

a) Front suspension b) Rear suspension

Figure 4-2 Kinematic simulation for suspension system

Something needs to be clarified at this stage in which the variable converts the time in seconds to degrees in the function that represent one cycle over 1 second during the simulation time. If implementing an asymmetric movement which involves different distances in the bump and rebound, the motion input needs a more complex function to operate in ADAMS.

4.2.3 Suspension measurements

Since ADAMS/View is general purpose multi-body dynamics simulation software, it does not have any specialized tools to measure the various vehicle parameters that need to be monitored and recorded to compare the performance of the vehicle. Hence the different variables to measure and monitor various parameters such as steering angle, camber angle and roll angle are created. The descriptions provided here will be limited to the most commonly calculated outputs. The outputs shown in Appendix 5 are for those plots that are normally used to compare simulation results with physical test data for validation of the virtual model in ADAMS.

Bump Movement: Measuring the wheel movement upwards in the positive vertical direction relative to the vehicle body.

Wheel Recession: Measuring the wheel movement rearwards in the positive longitudinal direction relative to the vehicle body.

Half-Track Change: Measuring the wheel movement outwards in the positive lateral direction relative to the vehicle body. All of these are shown in Figure 4-3

Figure 4-3. A model diagram for the WR, HTC and BM (Blundell. 2004)

Camber angle: This measurement uses two markers that are positioned at the wheel knuckle. The first marker (angle_wc) is situated at the wheel centre on the knuckle, and the second marker (angle_sa) is positioned on the axis of rotation of the wheel. The measure is defined in ADAMS by the equation as shown in Figure 4-4:

$$Camberangle = ATAN\frac{DZ(angle\_wc, angle\_sa)}{DY(angle\_sa, angle\_wc)}$$

Wheel Steer Angle: The road wheel steer angle is calculated using the same markers used to measure the camber angle. The steer angle measure is defined by the equation as shown in Figure 4-4:

$$Steerangle = ATAN\frac{DX(angle\_wc, angle\_sa)}{DY(angle\_sa, angle\_wc)}$$

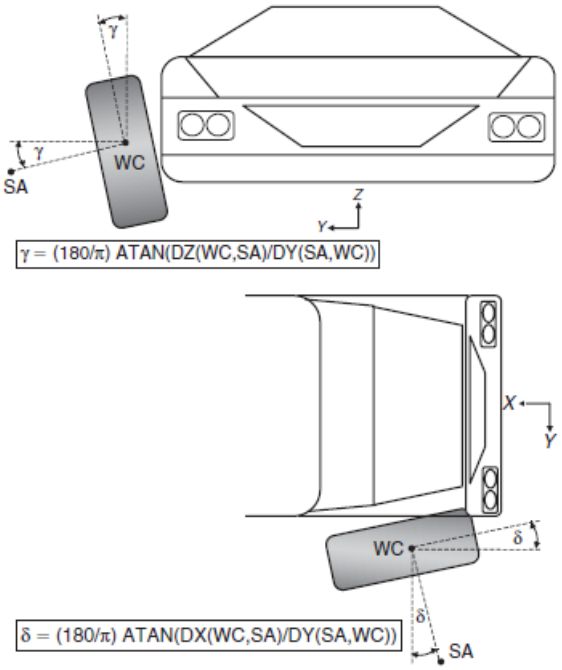

Figure 4-4. A diagram shows camber angle and steer angle

Castor Angle: The measurement of the castor angle is in degrees in the side elevation between the vertical and the steering axis. The points for measurement are located at the upper and lower ball joints of the suspension system connect. Thus, the angle is defined by the equation as shown in Figure 4-5:

$$Castorangle = ATAN\frac{DX(marker\_ub, marker\_lb)}{DZ(marker\_ub, marker\_lb)}$$

Suspension Trail: The suspension trail is the length in the longitudinal direction between intersection of the steering axis and the ground, and the wheel base wb which can be described as below:

$$Susptrail = DX(wb, lb) + DZ(lb, wb) * DX(ub, lb)/DZ(ub, lb)$$

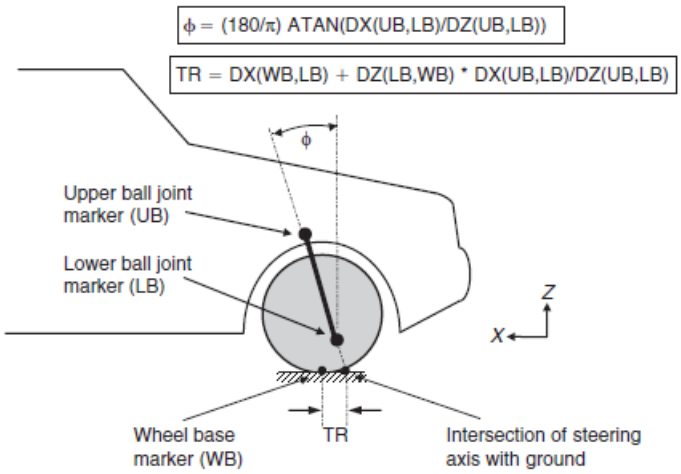

Figure 4-5. Calculation of castor angle and suspension trail

Steer Axis Inclination: The steer axis inclination is that the angle is measured at the front elevation between the vertical and the steering axis (from the upper ball joint to the lower ball joint). It can be explained by the equation below (see Figure 4-6):

$$SAI = ATAN(DY(LB, UB)/DZ(UB, LB))$$

Ground Level Offset: The ground level offset is the length in the lateral direction between intersection of the steering axis and the ground, and the wheel base (see Figure 4-6):

$$GLO = DY(wb, lb) - DZ(lb, wb) * (DY(lb, ub)/DZ(ub, lb)$$

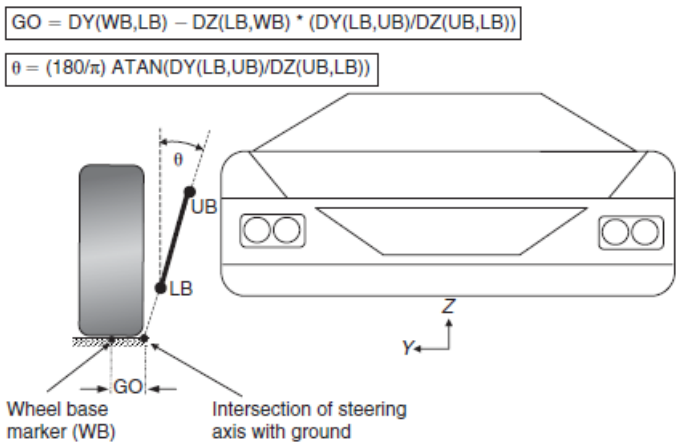

Figure 4-6 Calculation of steering axis inclination and ground level offset

4.3 Dynamic analysis

In the automotive industry, there is considerable focus on ride and handling where multi-body systems analysis is deployed to support design and analysis work. There are multiple sources of ride vibration which generally fall into two areas, namely road roughness and on-board sources. For vehicle dynamic analysis, the best starting point is to know the basic properties of a vehicle and its suspension system i.e. the motions of the body and axles. The body as a portion of the vehicle moves as an integral unit on the suspension. The suspension and wheels, as the un-sprung masses, move as a rigid body and impose excitation forces on the sprung mass. Thus, one must look into structural modes of vibration and resonances of the sub-system on the vehicle.

Before starting the computer-based simulation for dynamic analysis, manual calculations are necessary to introduce how to find the natural frequencies of the vehicle body and un-sprung between the suspension spring and the tyre spring. A quarter vehicle model with two degrees of freedom and the data to support the calculations is shown in Figure 4-7.

Figure 4-7 Two degrees of freedom quarter vehicle model (Blundell, 2004)

The un-damped natural frequencies f_b for the body and f_t for the un-sprung mass can be estimated using the following equations. Note that for the body an equivalent stiffness K is determined to represent the combined contribution of the road and tyre springs:

$$\mathrm{K} = \frac{K_s K_t}{K_s + K_t} \tag{4.1}$$

$$f_b = \frac{1}{2\pi}\sqrt{\frac{K}{m_b}} \tag{4.2}$$

$$f_t = \frac{1}{2\pi}\sqrt{\frac{K_s + K_t}{m_t}} \tag{4.3}$$

The modal solution uses numerical perturbation methods to estimate mass and stiffness matrices about an operating point before solving the eigenvalues in the normal fashion. For vehicle design, modal analysis is utilized to measure and analysis the dynamic response of vehicle structures when excited by multiple inputs.

4.3.1 Total degrees of freedom

Having introduced the modelling of the full vehicle model described in Chapter 3, the total degrees of freedom for this model need to be determined in the following section. For example, the vehicle body is a free floating rigid body in three-dimensional space so that it has six degrees of freedom. The vehicle body for the dynamic simulations does not have any connections directly to the ground, and is only connected to the suspension. To determine and understand the total degrees of freedom in the system, the Gruebler equation can be used as shown below:

$$Total\ DOF = 6 \times (numberof\ parts - 1) - (Numberof\ constraints) \tag{4.4}$$

For the vehicle model, it is necessary to verify the model size in terms of the degrees of freedom, and the calculation of the number of the DOF is based on the Greubler equation. Table 4-1 shows there are 6 degrees of freedom for the vehicle body, each of the four suspensions has only one translational degree of freedom in the vertical direction and one rotation degree of freedom exists for the wheel parts. This makes a total of 15 degrees of freedom for the entire model. Moreover, due to the model using the bushes on both the upper and lower wishbones, more DOFs are

introduced for each suspension system. Thus, the total DOFs of the full model is increased to 55.

Table 4-1 Total degrees of freedom for the model

a) Without bushes

Parts	DOF
Vehicle Body	6
Suspension System	4
Wheels	4
Steering System	1
Total	15

b) with bushes

Parts	DOF
Vehicle Body	6
Suspension System	44
Wheels	4
Steering System	1
Total	55

4.3.2 Dynamic model

In this case study, a dynamic model was established as shown in Figure 4-8, and it is considered good practice to examine the dynamic model for its eigenvalues to find the “Natural Frequencies” of the sprung and the unsprung mass. The model is assembled into its ‘Ride Rig’ configuration and the motion of the input rigs is set to zero. The approach used for the calculations in ADAMS is the so-called “small perturbation” method in which a small disturbance is introduced at each degree of freedom in order to construct stiffness and mass matrices, which are then solved in the traditional manner.

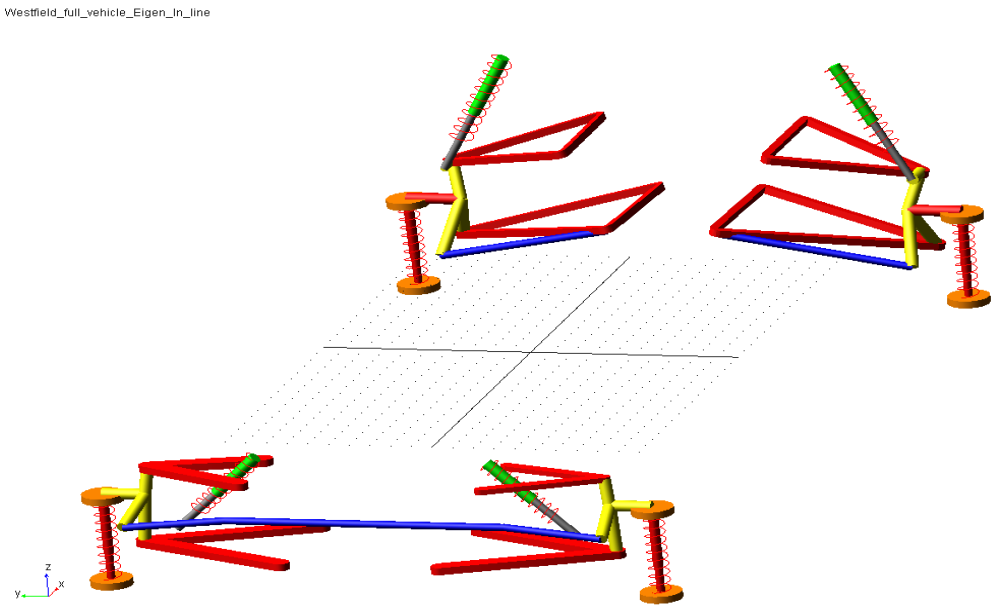

Figure 4-3 The dynamic model for modal solution

The dynamic model is essentially a basic version of the full vehicle model which only includes the suspension system and the vehicle body, thus reducing the total DOF to 10. The four tyres are replaced by a single spring unit that has the same stiffness as the tyre, and in-plane joints are added between the spring unit and the ground part to ensure that the unit is perpendicular to the ground, and also includes a planer constraint (x y direction) on the ground. The simulation runs in the dynamic mode for two seconds and examines the vehicle model to find the natural frequencies for each degree of freedom.

The results are shown in Table 4-2. The information includes: the sequential number of the mode that is predicted by the Eigen solution, natural frequencies corresponding to the modes, damping ratios for the modes and list the real and imaginary parts of the eigenvalue. The table of results from ADAMS/View produces ten modes of vibration for this full linkage vehicle model, and also includes the total number of the parts and the joints. Finally, the model is verified to show there are ten degrees of freedom for the model and no redundant constraint equations.

Table 4-2 Display of the eigenvalues in tabular form

```
                        EIGEN VALUES (Time = 2.0)

                        FREQUENCY UNITS: (Hz)

   MODE      UNDAMPED NATURAL        DAMPING
  NUMBER        FREQUENCY             RATIO              REAL                IMAGINARY

    1         3.980813E-002        5.657546E-004       -2.252163E-005  +/-   3.980812E-002
    2         8.600444E-002        4.355566E-001       -3.745980E-002  +/-   7.741788E-002
    3         1.784799E-001        7.101331E-001       -1.267445E-001  +/-   1.256619E-001
    4         1.408637E+000        4.436963E-002       -6.250071E-002  +/-   1.407250E+000
    5         2.478197E+000        2.935295E-002       -7.274238E-002  +/-   2.477129E+000
    6         3.527625E+000        5.002027E-003       -1.764528E-002  +/-   3.527581E+000
    7         1.774700E+001        5.292671E-001       -9.392904E+000  +/-   1.505754E+001
    8         1.787503E+001        5.353949E-001       -9.570202E+000  +/-   1.509729E+001
    9         1.894778E+001        5.710513E-001       -1.082016E+001  +/-   1.555451E+001
   10         1.914481E+001        5.788565E-001       -1.108210E+001  +/-   1.561124E+001
VERIFY MODEL: .Westfield_full_vehicle_Eigen

  10 Gruebler Count (approximate degrees of freedom)
  36 Moving Parts (not including ground)
   4 Planar Joints
   8 Revolute Joints
  16 Spherical Joints
   8 Translational Joints
   4 Convel Joints
   3 Fixed Joints
   8 Hooke Joints

  10 Degrees of Freedom for .Westfield_full_vehicle_Eigen

There are no redundant constraint equations.


Model verified successfully
```

The calculation for eigenvalues and eigenvectors can be done by using a function of ADAMS which can give a better understanding of the model's natural frequencies and mode shapes. After the calculation is complete, ADAMS can display in tabular form the Eigenvalues, in which the particular stability behaviour of the model depends on the existing real and imaginary parts of the eigenvalues, and the signs of the real parts and the different values of both parts. However, the model is a stable system in which all the real values are negative and the system has an imaginary part in which one pair of the values corresponds to each mode. In addition, each of the natural frequencies corresponds to the mode shapes that are the deformations of

the sprung mass and the un-sprung masses. Some explanations are shown in Table 4-3.

Table 4-3 Explanation of the natural frequencies at each mode

Mode	***Frequency***	***Comment***
1	0.0398 Hz	Body on rig stabilisation springs - Yaw
2	0.086 Hz	- Fore-aft
3	0.178Hz	- lateral
4	1.408Hz	Primary Ride 1 – Heave
5	2.478 Hz	Primary Ride 2 – Pitch
6	3.527 Hz	Primary Ride 3 – Roll
7	17.747Hz	Rear left wheel hop
8	17.875 Hz	Rear right wheel hop
9	18.94 Hz	Front left wheel hop
10	19.144Hz	Front right wheel hop

Moreover, in ADAMS the first six modes can be represented by animations of vibration for the vehicle body supported by the suspension systems as shown Figure 4-9. The animations give a better understanding of the response for the vehicle body at primary ride, for example, the natural frequency 0.0398 Hz at the first mode is calculated when the vehicle body is yawing. Reading the rest of the animations as shown below, the body movement and the natural frequency at each mode can be easily understood. However, the highest natural frequency of the sprung mass, around 3.5 Hz is found in the roll mode because the vehicle body is modelled as a single rigid body. This simplicity may give a large number for the torsional stiffness of the vehicle body structure in the roll mode. As is well known, the stiffness of the body structure is required for vehicle handling and drive performance; likewise, its effects on safety requirements are a major issue in the vehicle industry.

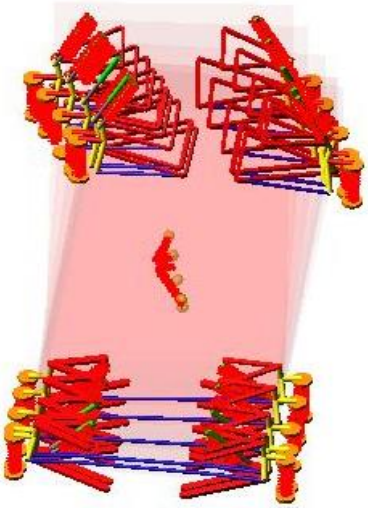

a) Mode_1 Yaw

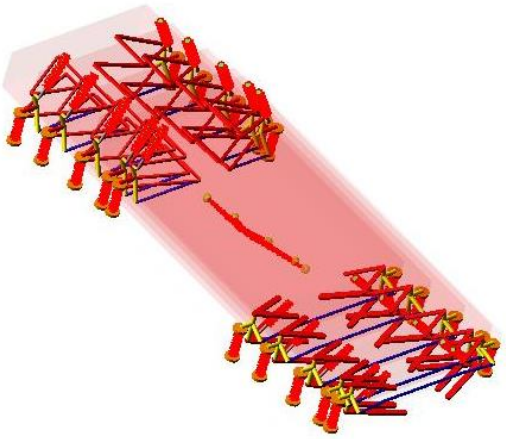

b) Mode 2 Fore-aft

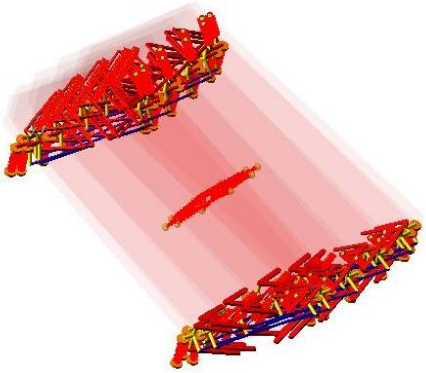

c) Mode 3 Lateral

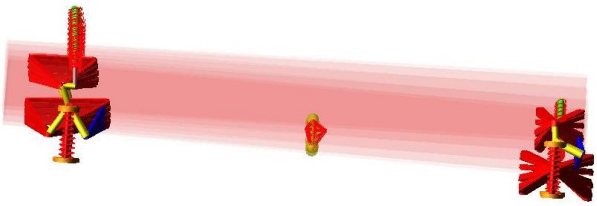

d) Mode 4 Heave

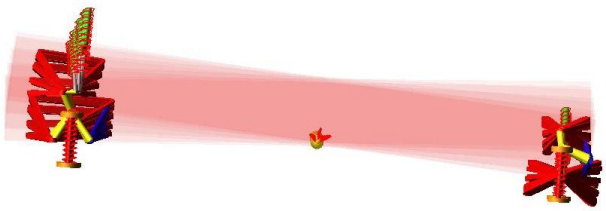

e) Mode 5 Pitch

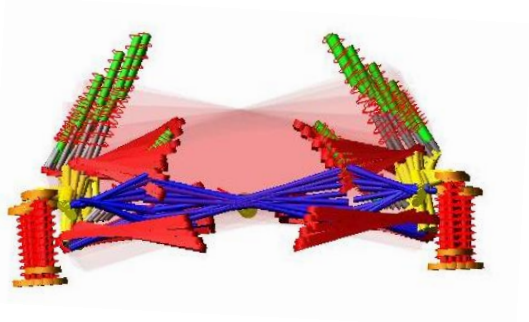

f) Mode 6 Roll

Figure 4-4 Animations of the modes at primary ride behaviour

In this model, the suspensions and the rigs are the un-sprung mass of the vehicle that is the second largest of the masses. In general, all un-sprung masses have the vertical hop mode that is excited by the road uneven inputs adding to the vibrations present on the vehicle. Thus, the four-wheel hop modes are sensibly positioned with respect to each other, and are represented in Figure 4-10. It can be seen that the natural frequencies are much higher than the sprung mass resonance, so that the sprung mass remains stationary during the wheel hop.

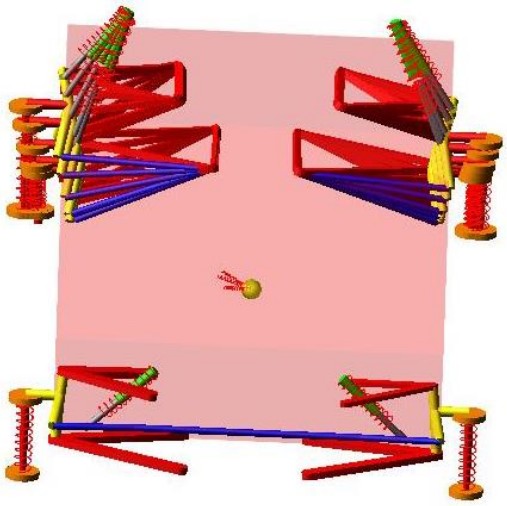

a) Wheel hop - Rear left

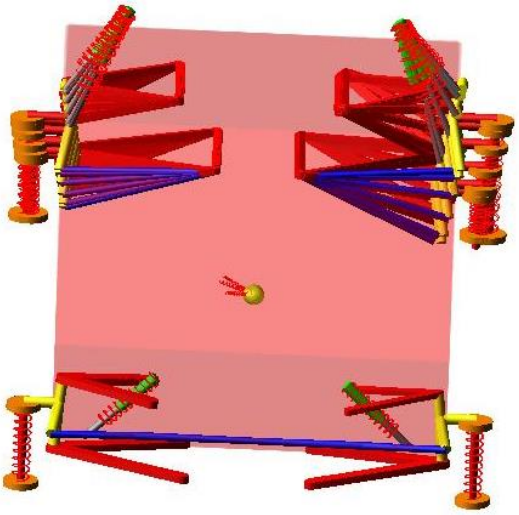

b) Wheel hop – Rear right

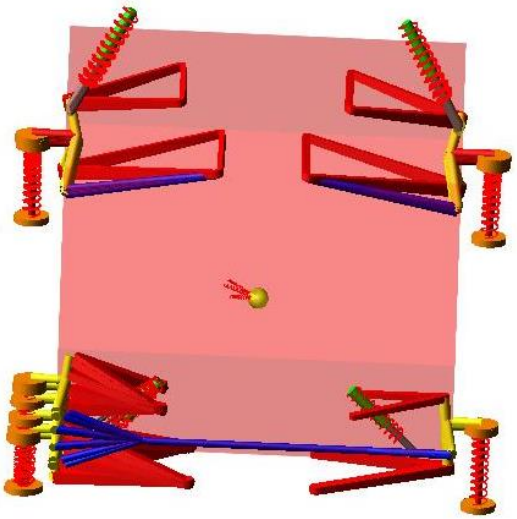

c) Wheel hop – Front left

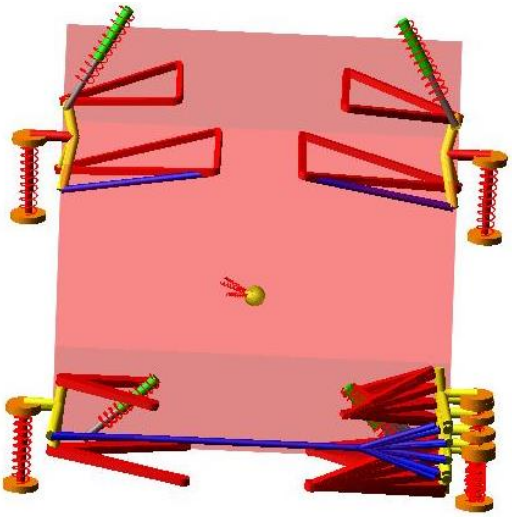

b) wheel hop – Front right

Figure 4-10 Animations of the modes at wheel hop behaviour

For a normal driving vehicle, the calculated frequency will be approximately 10 Hz. Friction in the suspension will increase the effective spring rate for small ride motions which in turn will increase the frequency to 12-15Hz. However, the wheel hop frequencies are high compared to those of the normal passenger car due to the track-racing nature of the vehicle, which means the vertical tyre stiffness and spring damper face are comparatively high, raising the wheel hop mode frequency. The purpose of kinematic and ride calculations are to check the virtual model has been built correctly using a Multi-body system for following analysis, i.e. the correct numbers of parts and the types of joints are being used in the model. Overall, the model behaves well dynamically and can be trusted for its intended 0-20Hz dynamic use in a numerical sense. However, in terms of representing real vehicle behaviour there is one important caveat – the roll stiffness distribution as modelled may be very different to the real roll stiffness distribution due to vehicle frame flexibility, about which no information was available.

4.4 Steady-State Handling analysis

The classical treatment of the behaviour of the vehicle model, that is called steady state cornering, is described out in this section. Steady state means the vehicle states are unchanging with time and speed as the vehicle travels on a constant radius circle. This treatment will be described in more detail; running the model around a circle with constant radius at a range of constant speeds, the increments in the speed should correspond to the increments in the lateral acceleration. Moreover, this approach is very practicable to perform and so it will be used for the basis of vehicle dynamic analysis in the following discussion.

4.4.1 Driver behaviour modelling – a ‘path following’ controller

Before starting the treatment, the first consideration of modelling the steering inputs is to represent the driver as part of the full vehicle system model. In this research,

the inputs to the steering wheel are designed with both open-loop and closed-loop control. The steering input with the open-loop control requires a time-dependent rotation that will be applied to the steering system. If applying a closed-loop control to the steering system, the aim is to adjust the input to produce the desired trajectory. However, the aim of the control method is to minimize the error that is the difference between the actual output and the desired output. In the literature, there are a variety of controller models suitable for modelling driver behaviour in existence. Some, such as ADAMS/Driver™ developed as part of the MSC.ADAMS modelling package, are very complete – others, such as the two-loop feedback control model are simpler (Blundell and Harty, 2004). Some researchers prefer to use a preview distance for controlling the trajectory of the vehicle, with an error of lateral deviation from the intended path. However, there is usually a difficulty associated with this since the lateral direction must be defined with respect to the vehicle. For 'normal' driving this type of model can produce acceptable results but for manoeuvres such as the ISO 3888 Lane Change the behaviour becomes unacceptably oscillatory particularly after the manoeuvre. An alternative method, used by the authors with some success for a variety of extreme manoeuvres, is to focus on the behaviour of the front axle. This model fits with driver's experience of driving at or near the handling limit, particularly on surfaces such as snow where large body slip angles highlight the mechanisms used in the driver's mind.

Ground Plane Velocity

The 'path following' controller model focuses on the behaviour of the front axle in which the principle of the control method is to determine the yaw rate error between the 'No-slip yaw rate' of the front axle and demanded yaw rate. The demanded yaw rate is the driver controlling the vehicle to follow the path as expected at a range of speed. The formulation used is described below. All subscripts x and y are in the vehicle reference frame.

In Figure 4-11, the ground plan velocity V_g is the given from the components V_x and V_y using

$$V_g = \sqrt{{V_x}^2 + {V_y}^2}$$

4.5

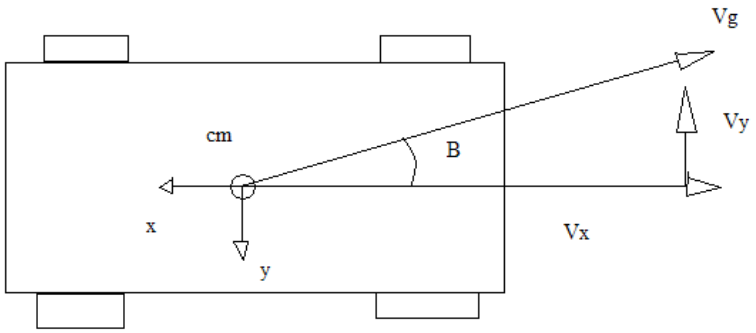

Figure 4-115 Explanation of Ground Plane Velocity

For the reference frame used here and as the vehicle moves forward, the signs of V_x and V_y are negative. A variable command is used to calculate V_g within the model to find out what the significance of the ground plane velocity is. The units of model work in mm and V_g will be set up in m. As the simplest start, the model will run for the steady state cornering, the driving torques will not act on this model and it only has an initial velocity on all parts, assuming the vehicle is in a coasting condition.

Demanded Yaw Rate

The demanded yaw rate ω_d is found from the forward velocity V_x and path curvature K using:

$$\omega_d = V_g K$$

4.6

$$K = \frac{1}{R}$$

4.7

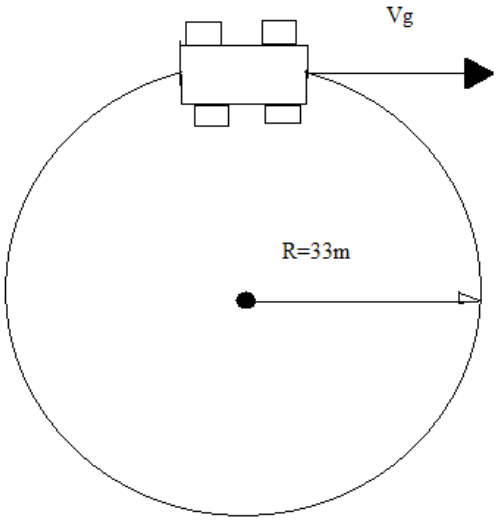

Figure 4-12 Explanation of Demanded Yaw Rate

For example, if the model runs at a 33m constant radius circle as shown in Figure 4-12, the path curvature K is K = 0.0303m^{-1}. So the demanded yaw rate can be easily calculated depending on the ground plane velocity of the model.

Path curvature and path length

The path curvature for a circle should be a constant value, but it needs some transition curves with varied radiuses to link path curvature from the straight line to the constant radius circle. This approach can avoid abrupt steering inputs while the vehicle model follows the desired path. The desired path curvature can be converted to a SPLINE command as used in ADAMS, shown in Figure 4-13. The X values are path lengths depending on vehicle speed, and Y values are path curvatures. Note that the value of the path curvature can be positive or negative, so it needs some definitions before the simulation. In this cornering scenario, when the path curvature is set up for a positive value the vehicle model turns to the left and the negative value makes the model turn to the right.

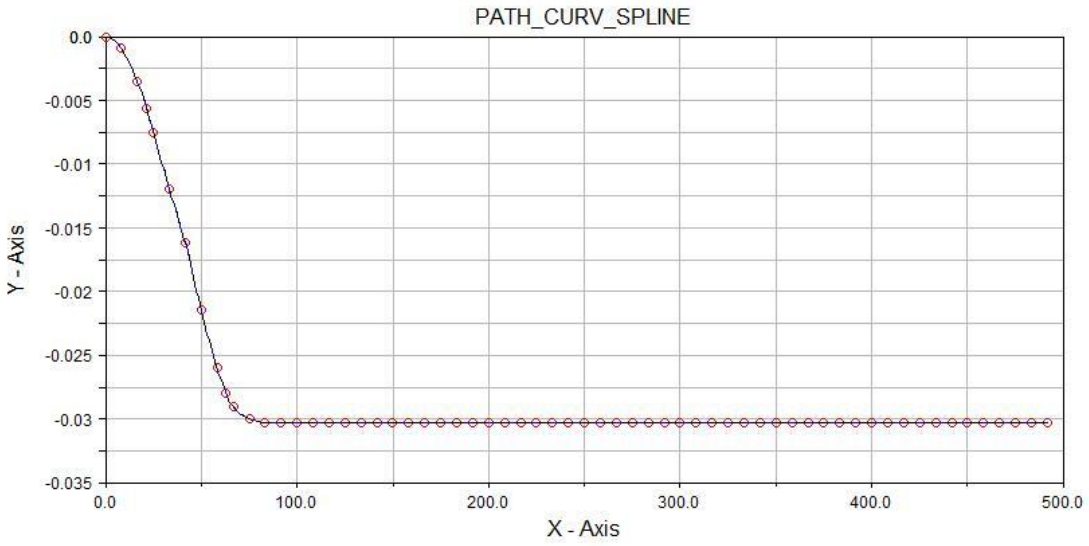

Figure 4-6 Path curvature for steady state cornering

However, the path curvature is determined and in order to simulate the model for a range of speeds, the path length corresponding to the different speeds is required. The path length is found by integrating the ground plane velocity of the vehicle to give a distance-travelled measurement. Using this measurement, the path curvature can be surveyed in the model.

Body Slip Angle β

The explanation for the body slip angle, which appeared in Figure 4-22, can be found from the velocities V_y and V_g using:

$$\beta = arcsin\left(\frac{V_y}{V_g}\right) \quad 4.8$$

A variable statement is built to convert the formula into ADAMS, thus the body slip angle of the vehicle body can be calculated when the model is cornering. The numerator requires the lateral velocity of the body V_y and the units set up in m/s. In

order to avoid having the denominator equal to zero, a correction factor has been added into the variable statement that can avert any the numerical failure. The effect of the factor is negligible.

Centripetal Acceleration A^p

First, the variables of lateral acceleration A_y and longitudinal acceleration A_x are created and calculated in the vehicle body axis system, the units set up in m/s^2. Then, the centripetal acceleration A^p is found from the components of acceleration A_x and A_y using

$$A^p = A_y \cos(\beta) + A_x \sin(\beta) \tag{4.9}$$

The Front Axle No-Slip Yaw Rate

The front axle no-slip yaw rate ω_{fNs} is found from the components of the centripetal acceleration A^p, the yaw acceleration $\alpha_{z,}$ the distance α, from the mass centre to the front axle and the ground plane velocity V_g using

$$\omega_{fNs} = \frac{A^p - \alpha\alpha_z}{V_g} \tag{4.10}$$

Yaw rate error

The yaw rate error ω_{err} is then found from the demanded yaw rate ω_d and the front axle no-slip yaw rate ω_{fns} using

$$\omega_{err} = \omega_d - \omega_{fns} \tag{4.11}$$

4.4.2 Driver behaviour modelling – a ‘survey’ controller

Before building the ‘survey’ controller, some basic knowledge of the vehicle driving characteristics during cornering needs to be mentioned. At the lowest speed, the performance of the actual vehicle corresponds very closely with the geometric yaw rate of the vehicle body. As vehicle speed rises, the lateral acceleration of the vehicle is increased so that the tyres must develop lateral forces, and slip angles are presented at each wheel. Due to the frictional limitations of the tyres, the vehicle cannot reach the geometric yaw rate for a large steering input. Thus, the characteristics of the vehicle are designed to have further modifications in which the yaw rate gain should be reduced even when the tyres are not saturated. Therefore, the over- or under-steer can be easily defined by the ratio of the geometric yaw rate and the actual yaw rate, i.e. if the ratio is greater than one, the vehicle is under-steering and when the vehicle is over-steering, the ratio is less than one,.

As is known, the tyre cornering force curve is treated as having linear, transitional and frictional regions, and the project racing model may operate in all of these regions. At the starting point, the response of the vehicle related to the driver control will be operated in the linear region, corresponding to the lateral acceleration of the vehicle body, which is about 0.3g (Milliken, 1995). Thus, a similar control method as the path-following controller is used in the survey controller model in which only the target behaviour differs slightly. The survey controller model still focuses on the behaviour of the front axle, but the aim is to control the lateral acceleration of the model at its linear region. Therefore, the target is set up for the body lateral acceleration at 0.3g so that it can be converted into ADAMS by using the SPLINE command. The SPLINE command represents the Y axis as target lateral acceleration depending on the X values – for simulation time, and the units are converted in *m*. Finally, the lateral acceleration can be found by using:

$$A_{error} = A^{p} - A_{target} \tag{4.12}$$

4.4.3 Steering torque input

The closed-loop driver model with the 'Path Following' and 'Survey' controllers will be applied to the vehicle model by using a typical PID controller. As one of the control technologies represented in the literature, the PID controller has the advantage by which it produces continuous output and there are no steps that are quite like the behaviour of a real driver. For example, when using the driver model with the path-following controller, the yaw rate error is minimized in three ways: a control effort is applied in proportion to the error, and then the error can be integrated and also differentiated. In the PID formulation, the integral and derivative terms can be represented by using DIF statements and variables in ADAMS. The controller theory section for Yaw Rate Error (YRE) is shown below

$$YRE = K_p * \omega_{err}(t) + K_i \int_0^t \omega_{err}(t)dt + K_d \frac{d}{dt}\omega_{err}(t) \quad 4.13$$

As stated, the simple steering system as modelled in the previous Chapter is using the steering rack connecting the steering column and the tie rods of the front suspension. The rotational motion of the steering column is related to the translational motion of the steering rack through the coupler joint. This coupler is based on a ratio where a degree of the steering column input generates the 0.18_{mm} translational motion of the steering rack. Therefore, the implementation of the control, as shown in Figure 4-28 is to apply the torque to the steering column and the 'driving' of the vehicle model follows the desired path.

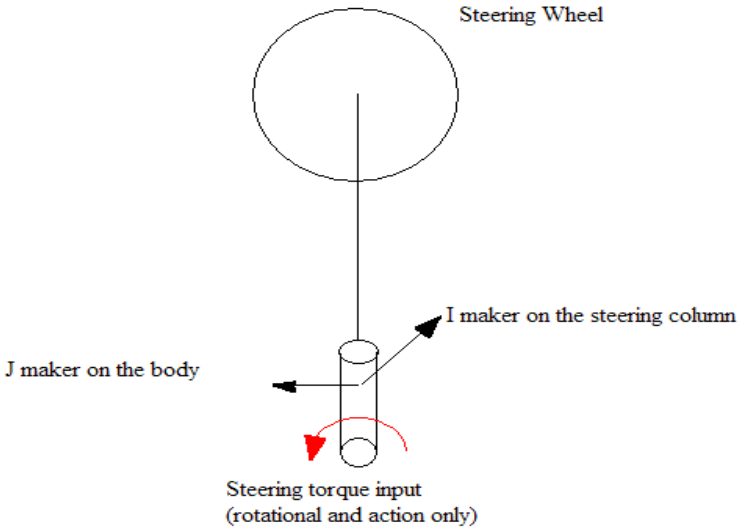

Figure 4-7 Steering torque acting on steering wheel

When the driver model implements the control signal on the steering wheel, the PID controller can modify the steering torque to minimize the yaw rate error. This is more like the behaviour of a real driver because when the yaw rate error increases the driver will apply more torque on the steering wheel to reduce the error and keep the vehicle on track. The SFORCE statement in ADAMS is used for implementation of the steering torque input as shown in Figure 4-29.

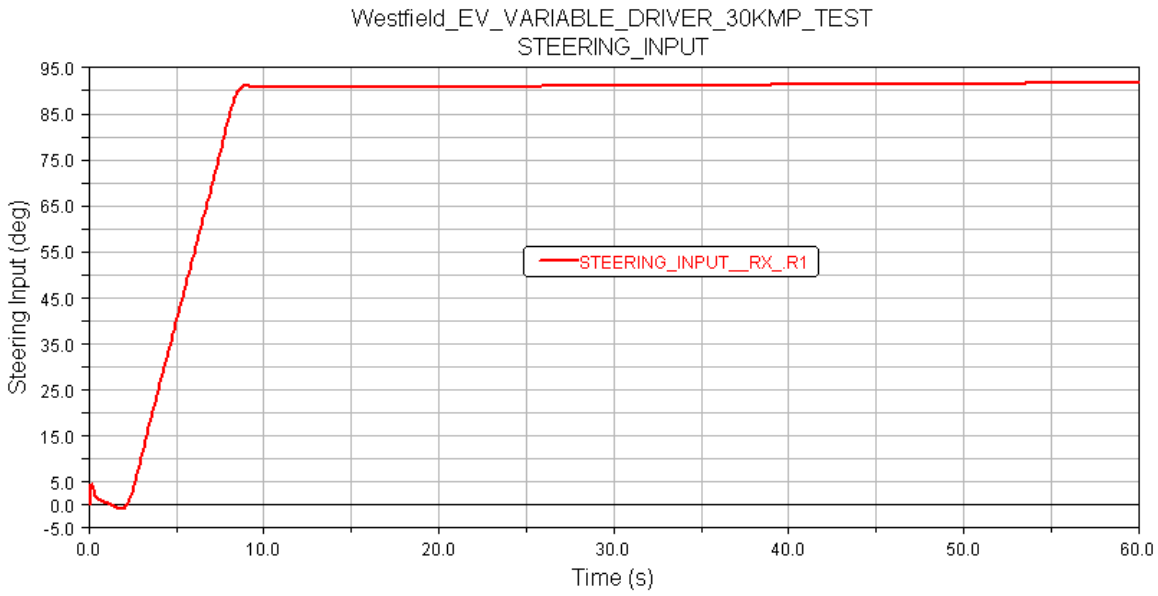

Figure 4-8 Steering input for the 'path following' model

4.5 Simulation results

4.5.1 Steady state cornering behaviour

The cornering behaviour of a vehicle is an important performance attribute that normally corresponds to the handling. There are three phases when a vehicle makes a turn into a corner, turn entry, steady-state cornering and turn exit. During the second phase, the radius of the path and velocity of the vehicle are constant. The Ackermann angle which is the average steer angle of the wheels, δ=L/R, can be found.

In the general steady state cornering manoeuvre, it is necessary to consider the relationships in Figure 4-30. The under-steer region requires more steer angle than the Ackermann angle to drive the vehicle in the desired circle. Similarly, the over-steer region has less steer angle compared to the Ackermann angle.

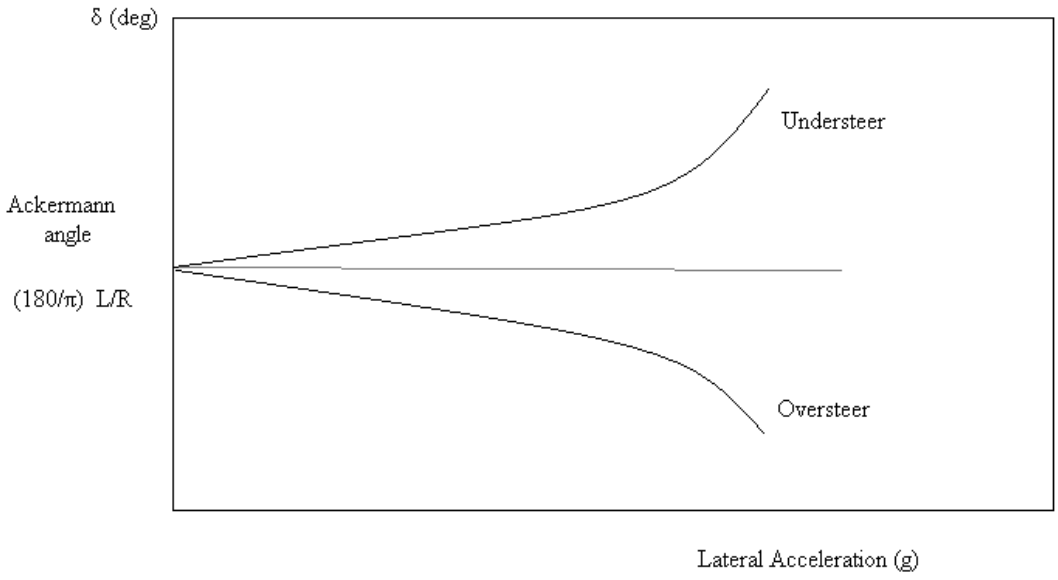

Figure 4-9 The explanation of Under-steer or Over-steer (Gillespie, 1992)

To determine the characteristics of the project vehicle, such as under-steer or over-steer, the constant radius turn test procedure, which is based on the British standard (ISO 4138), can be used. The procedure may be summarized as follows: for the first step, the model starts running at low speed to find the Ackermann angle

(86.3degree). Then, increasing speed in steps produces increments in lateral acceleration of typically 0.1g, and measures the steering inputs when the model runs in steady state cornering at each speed. Finally, the measurements can produce a graph as shown in Figure 4-31 that can indicate the project vehicle is understeering when turning the corner, and it also can provide the under-steer gradient K.

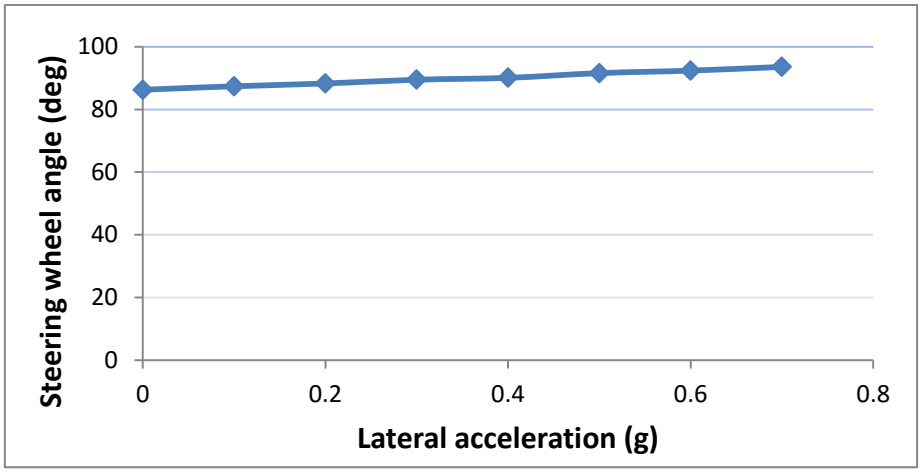

Figure 4-31 Determination of the project model

4.5.2 Path following behaviour

An initial comparative analysis of the actual and demanded driving behaviours is exhibited. As Figure 4-32 shows, the classical treatment based on steady state cornering verifies that the model can exactly follow the desired path during cornering by implementing the controlled steering torque on the steering column.

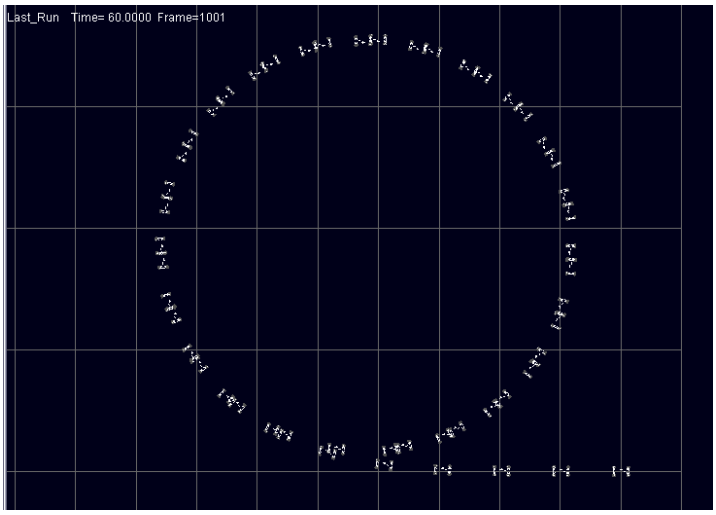

Figure 4-32 The model runs at the steady-state cornering

Moreover, the implementation of the closed-loop driver control with the PID controller provides the adjustable steering torques so that the yaw rate error can be minimized as shown in Figure 4-33.

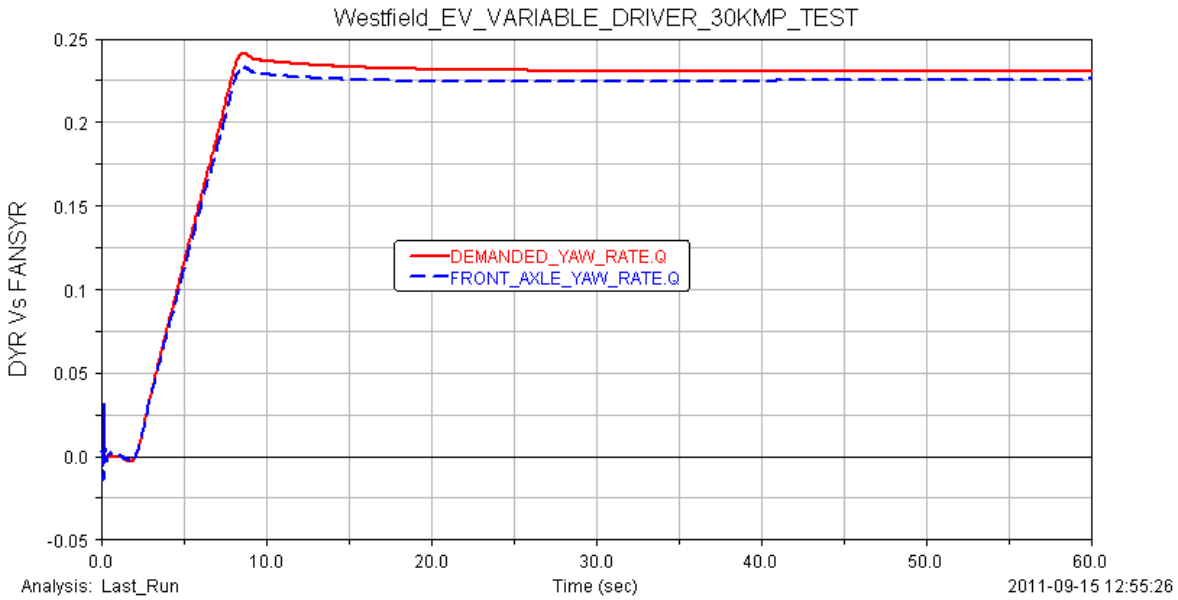

Figure 4-10 Demanded Yaw Rate Vs Front Axle No-Slip Yaw Rate

4.5.3 Vehicle linearity

In a process similar to that for the driver model with 'path following' controller, the 'survey' controller operates the vehicle model running at its linear region as shown in Figure 4-34. The linear steady-state control response characteristics are given as a series of ratios: curvature response, yawing velocity response and lateral acceleration response. As mentioned, the reason for steering the vehicle is to change the direction of the vehicle by developing the yaw rate. Thus, the notion of yaw rate gain which is a ratio of yaw rate to steer angle at the front wheels, becomes useful to describe the yaw velocity response to control inputs.

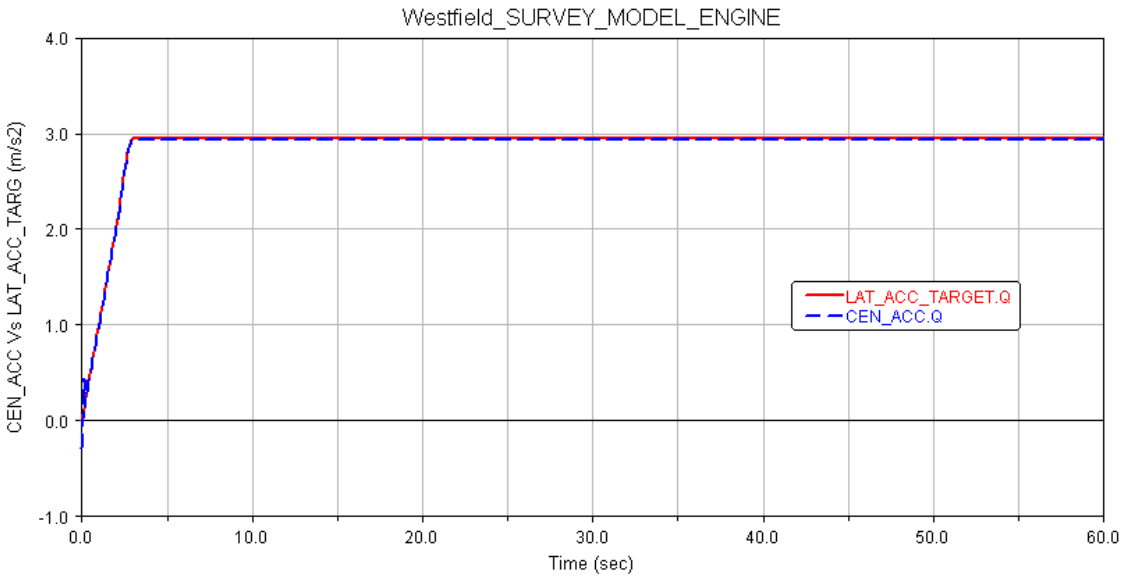

Figure 4-11 The vehicle lateral acceleration versus target lateral acceleration

Again, for vehicle stability and control, the basic characteristics of the vehicle need to be considered. If the response of the vehicle is less than what might have been expected, the term understeer is used. When the vehicle yaws more than expected, the term oversteer is used – the response of the vehicle exceeding what might have been expected. So far the approach for measuring the steering inputs to define the under- or oversteer has been discussed. Remaining with Newtonian friction to describe the behaviour of the tyres, one further fundamental point is worth establishing, which is the relationship between the yaw rate gains with forward velocity as shown in Figure 4-36. When the model is at low speed, the yaw rate gain is very close to the ideal yaw rate gain value, which means the response of the vehicle control is more like that of a natural steer vehicle. When the vehicle speed increases, the vehicle is unable to achieve the ideal yaw rate for large steering angles. The characteristics of the vehicle are performed to further reduce the yaw rate gain even when the tyres are not saturated. Furthermore, based on the vehicle characteristics, an authority envelope of torque vectoring control is carried out in Figure 4-36, so that the aim for the torque vectoring control which will be developed in this research is to control the vehicle behaviour close to its own characteristics when running at various conditions.

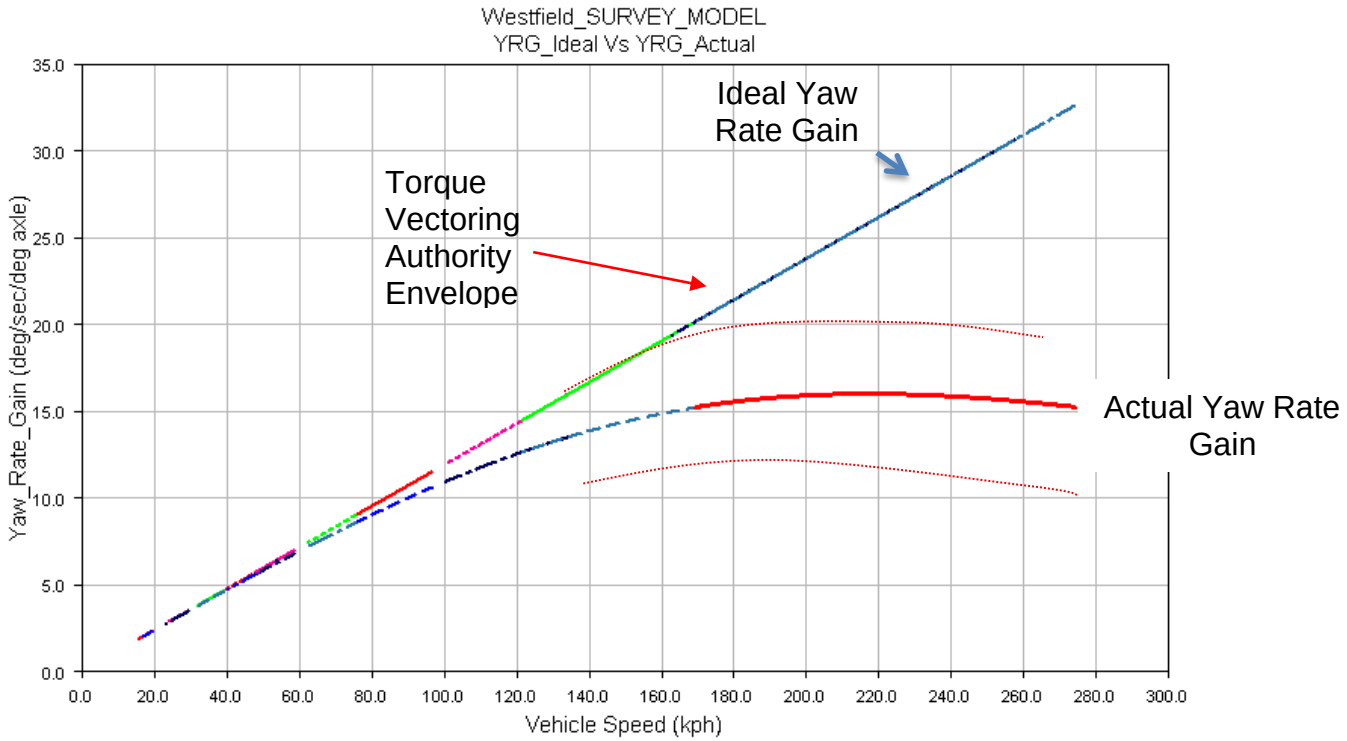

Figure 4-12 Yaw rate gain versus vehicle speeds

4.6 Conclusion

A summary of the simulation results was collected from these investigations to evaluate the overall characteristics of the project model during the different analyses. First, the characteristics of the suspension system have been determined by the kinematic analysis in which the results can be compared with the laboratory data from manufacturers to validate and refine the computer-based vehicle model.

Second, the dynamic analysis proved the model is a stable system with correct degrees of freedom, the natural frequencies at each mode being calculated and the animations clearly explaining the movement of the sprung and un-sprung mass. Also the influences of the natural frequencies at each mode were analysed.

Finally, the vehicle model ran for the characteristic driving manoeuvre - steady state cornering, and implementing the driver models with ‘path following’ and ‘survey’ controller to the full vehicle model was represented. Of most importance is the characteristic of the project vehicle which verified that the project vehicle is an under-

steer vehicle. Furthermore, Figure 4-23 for the yaw rate gain against the vehicle speed indicated that the aim of the further control strategy for active yaw control is to overcome all the variations, and then to dominate the vehicle running at its particular characteristics.

5. Comparison of architecture for electric vehicle

5.1 Introduction

For conventional vehicles, a main difference in architecture is the position of the Internal Combustion (IC) engine which can be located at the front, middle or rear of the vehicle. The type of mechanical driveline also is another important factor of vehicle architecture, such as Rear Wheel Drive (RWD) or All Wheel Drive (AWD). A novel architecture for electric vehicle driveline was a design that includes freedom to move the motors to a particular space in the vehicle, for example, mounting the motors within individual wheels. In addition, the electric motors can also be located in the middle of the chassis at the front, rear or both axles.

In recent year, the architecture of electric vehicle with in-wheel motors on the market has high driving efficiency, thus any other architecture may be neglected. Westfield Sportcars, a producer of in-line motors, has recommended a series of wide-ranging studies into the vehicle stability and driveability performances. Therefore, a comparison will be discussed in this chapter that includes ride comfort check and drivability check by using the ADAMS model. The discussion can provide a comprehensive overview of using in-wheel and in-line motors in this particular racing model.

5.2 Architecture of in-wheel motors vehicle

The change in the un-sprung mass significantly affects the ride and handling behaviour thus it is an important parameter. Many feasibility researches have been done broadly for in-wheel motors, some specific and detailed measures for the sizes of the effects in dynamics behaviours have been taken. The ride and handling performance from subjective and objective measures suggests that the modern development toolbox is easily capable of restoring dynamic performance. However, the advantages of the in-wheel motors in terms of packaging and vehicle dynamics control are of substantial interest to the vehicle dynamics community (Anderson and Harty 2010).

In recent years, a popular novel architecture of electric vehicle has developed by using electric motors mounted in driving wheel hubs that is effective in reducing the components of the entire traditional drivetrain. The higher driving efficiency of the powertrain can be improved which the fuel tank to wheel efficiency of the conventional powertrain is about 20% (Göschel and Burkhard, 2008), that of an electric vehicle with in-wheel motors amounts approximately 80% (Neudorfer, H and Binder, A, 2006).

Some new designs of suspension system with in wheel motor were published in last decades. First, Willberger and Ackerl (2010) designed an elementary model of intergraded suspension with in wheel motor as shown in Figure 5-1, which consisted of an electric motor, gear box and brake system. Eduardo and Rojas (2011) developed a single wheel suspension system to integrate entire demanded components together. The integration mainly considers in two aspects: first, if an electric motor will be integrated into an existing suspension system, the effect on the behaviour of the characteristic suspension parameters has to be minimized during the adjustment should reach the target behaviours of the vehicle handling. Moreover, it enables preventing any impact between suspension elements and the in-wheel motor. The modification bases on an original rear axle of Ford Focus 1999 suspension system, as mentioned, an electric motor and a gearbox are equipped into the wheel hub as the practical application example.

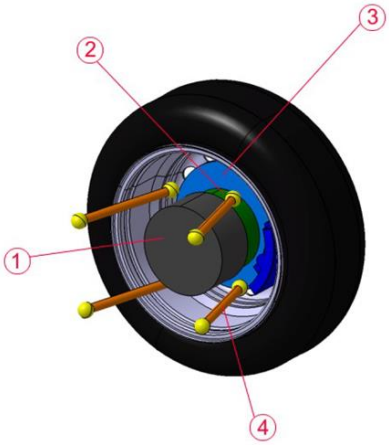

(a) Package design: 1. Electirc motor 2. Gearbox 3. Brake disc 4. Suspension arm (Willberger and Ackerl, 2010)

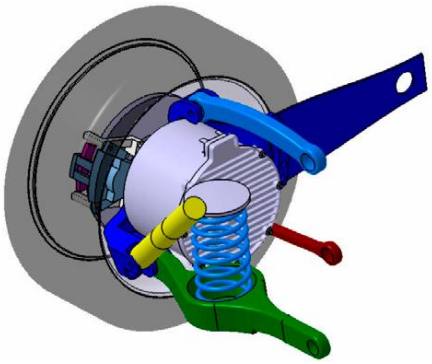

(b) Optimized suspension system for passenger vehicles with in-wheel motors (Eduardo and Rojas, 2011)

Figure 5-1 Different design of in-wheel motors

There are several different types of in-wheel motors in the literature mainly used for either pure and hybrid electric propulsion units in vehicles. The aim is to satisfy different demands of workloads depending on the uses of the vehicle. For current technologies, there are two motor types as asynchronous and synchronous machines can represent a realistic electrical drivetrain system due to assembly and cost reasons. The former has its advanced characteristics - robustness, simple construction and low costs is one of the most widely used electric motor and due to the compact design that the latter also has steadily developed in last decades. Willberger and Ackerl (2010) have done some comparisons in which they indicated that conclusively from a constructive point of view the synchronous motor has better characteristics concerning an application within an “on-demand” wheel hub scenario.

Furthermore, choosing the correct type of electric motor as used in the wheel hub depends on the velocity of vehicle, which the subsequent values can define the amplitudes of traction force acting on the driving wheels. The approach derived a prior analysis of different load requirements, that the desired torque has significant influence on the design of the in wheel motor. In fact, the in wheel motor has been required with high driving torque in a limited space, that means the in wheel motor may be redesigned due to individual diameter-length of the driving wheels for a given design torque. Moreover, the considerations under the geometric restrictions of the wheel hub should involve the viable gear radios, compact design of electric motor mounting in the wheel hub with the existing cooling issue and the braking system needs to modify in order to integrate the electric motor with a gearbox.

Figure 5-2 Protean Electric in-wheel motor

A more complex design is developed by a producer – Protean Electric, where the packaging is complicated by fitting a brake that the concept removed the traditional braking system in the wheel replacing by an inside out disc clearly shown in Figure 5-2 to preserve the track width and structural integrity of the suspension system. Due to a smaller rubbing surface of the brake disc and reducing bending moments, twin callipers are used to allow coupled friction forces, diametrically opposite from each other, to stop the vehicle. The symmetric braking force can avoid any large bending moments, air gap-closing forces and a lighter rotor results. Moreover, the size of wheel rim has been limited at least 18” to accept the motor but it is also important that the offset of the mounting flange allows the standard vehicle track and therefore steering geometry to be maintained (Whitehead, 2012). A simplified vehicle model for the architecture of the in-wheel motors is built by using the existing suspension system adds a dummy part on the wheel centre to simulate the in-wheel motors acting on the un-sprung mass as shown in Figure 5-3.

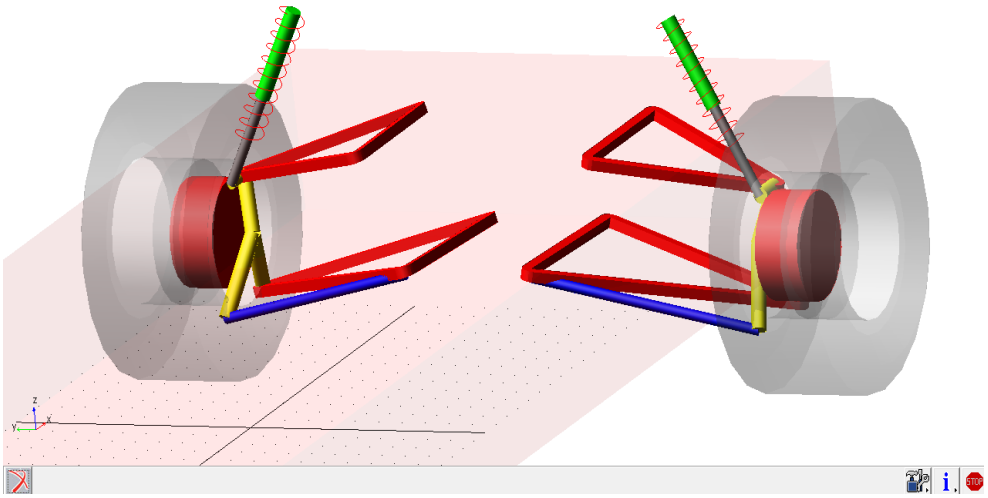

Figure 5-3 Architecture of in-wheel motors model

5.3 Modelling and validating of in-wheel motors vehicle

The ‘Ride Rig’ model used to test the dynamic behaviour of the vehicle model described was in the previous Chapter. This particular model has 10 degree of freedoms in total: the vehicle body has six degree of freedoms - three in rotational and three translational, and the suspensions each have one degree of freedom. The

tyre is represented by a single spring damper which has the same damping coefficient and vertical stiffness as the tyre.

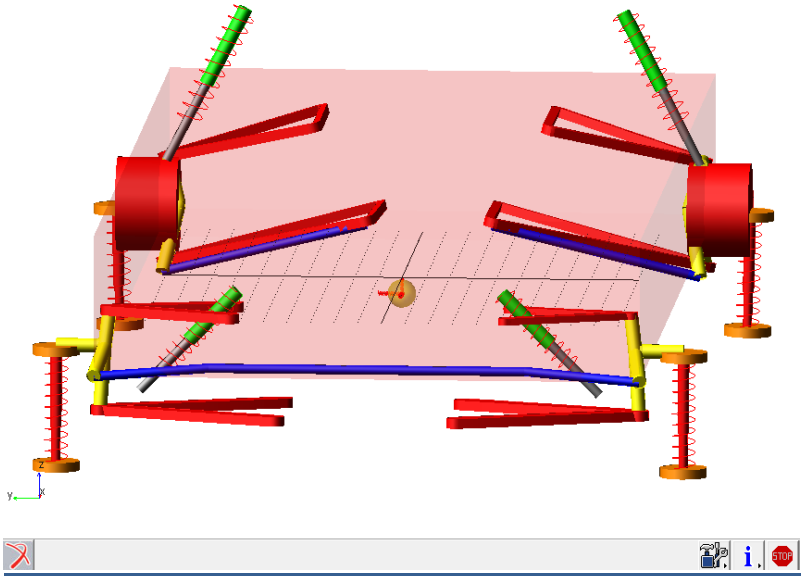

Figure 5-4 Westfield I-racer with in-wheel motors in ADAMS

Figure 5-4 shows the model built to represent the layout with in-wheel motors. In this model, the two motors connect from the middle of the rear axle to the individual rear wheel hubs. Thus the un-sprung mass is increased by 30 kg on the rear left and right sides. The simplified transmission system as modelled omits the driving shafts and constant velocity joint on both sides compared to the project vehicle model. Instead, the two electric motors are directly fitted at the centre of the wheel knuckles. It is good practice to examine the model for its eigenvalues to find the natural frequencies of the body and the suspensions. The model is assembled into its 'Ride Rig' configuration and the motion of the input jacks is set to zero. The approach used for the calculations in ADAMS is the so-called "small perturbation" method in which a small disturbance is introduced at each degree of freedom in order to construct the stiffness and mass matrices, which are then solved in the traditional manner.

Figure 5-5 shows a complete model used for handling simulation which includes the vehicle body, the suspension systems with a Pacejka tyre model and a closed-loop driver model. This is closer to the project vehicle model described in the previous chapter. Only the position of the electric motors is different. In order to check the

drivability and the stability for the model with in-wheel motors during the manoeuvres, the modification in the driveline is to move the application points for the driving torque from the middle of the axle to the wheel centre as shown in Figure 5-5. In this analysis, there is only an identical driving torque applying to each wheel that may be continuously produced even when the grip is lost between the road surface and the tyre. This means the model can progress beyond the point of vehicle spin out during a cornering manoeuvre.

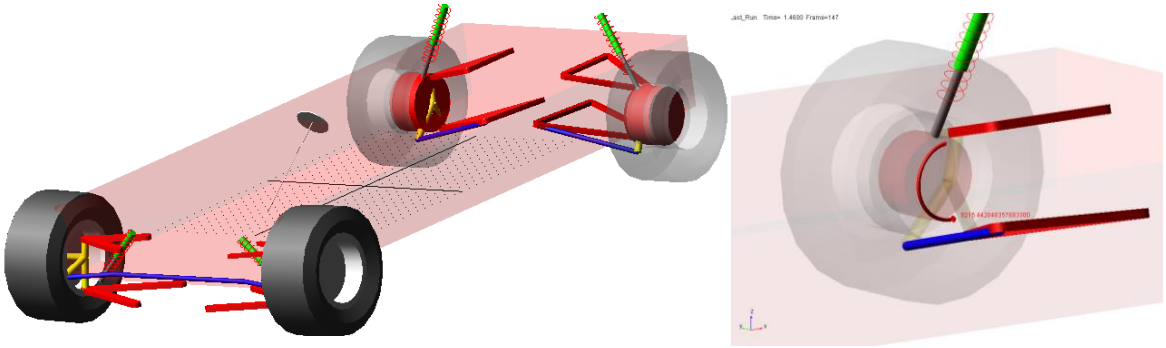

Figure 5-5 Model definition for in-wheel motors

5.4 Modelling architecture of in-line motors vehicle

The model for the vehicle with In-line motors is based on the basic model which is described in the previous Chapter. The basic model used for a kinematic check only has the suspensions and the vehicle body, where the vehicle body is clamped to the ground and the individual wheel centres have vertical stroke applied while the dampers and the tyres are absent. Modelling the vehicle with the in-line motors involves attaching the two electric motors and the drive-shaft to the rear axle. The inertia properties and mass for the additional parts are the same as the real components. More details were introduced and the model geometry is shown in Figure 5-5. In fact the architecture of the in-line motors vehicle model includes the characteristics of the conventional suspension. This means any modifications can be omitted thereby the costs of redesign and development will be reduced but the stability and durability is the same as the previous version.

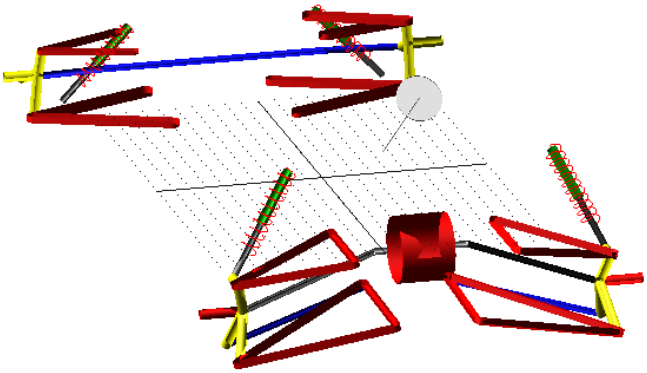

Figure 5-4 the model geometry of in-line motors for kinematic test

It is necessary to build a new model for the dynamic check because the driveline for the In-line motors vehicle was redesigned. The additional parts may change the structural stiffness and mass matrices. This can cause a small disturbance at each degree of freedom. Note that redesigning the driveline may have some flexibility to prevent substantial constraints between the multiple rigid bodies. Thus the driveline allows the drive-shaft to have some movement along the axle during ride height change. The weight distribution for the project vehicle is 50/50 and the additional masses from the electric motors can be balanced by mounting battery packages in the front of vehicle. Figure 5-6 shows the model still has 10 degree of freedoms due to the motors and the drive-shafts being attached to the vehicle body and rotating with the wheels. Thus no extra rotational and translational movement is required, again with the dampers and tyres absent.

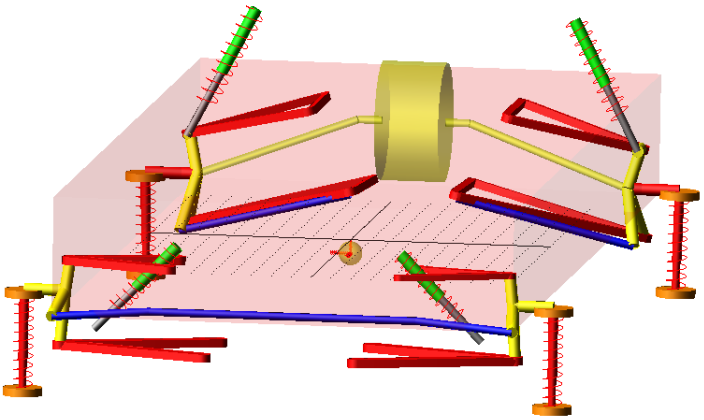

Figure 5-6 Dynamic check model for in-line motor

Figure 5-7 shows a completed model for a drivability check in which the dampers and tyres are now present. According to the configuration for the In-line motors vehicle model, the points for applying the driving torque move to the position where the motor and the drive shaft connect together. These retrofits to the architecture are intended to improve vehicle drive efficiency in which the new driveline has less mechanical components and a direct drive design. The efficiency of a conventional driveline is about 20% and an electric vehicle with in-wheel motors increases to approximately 80% depending on the driving cycle. However, the common architecture for in-wheel motors vehicles includes a shorter driveline than in-line motors vehicles, but requires major modifications to traditional suspensions to include the power source.

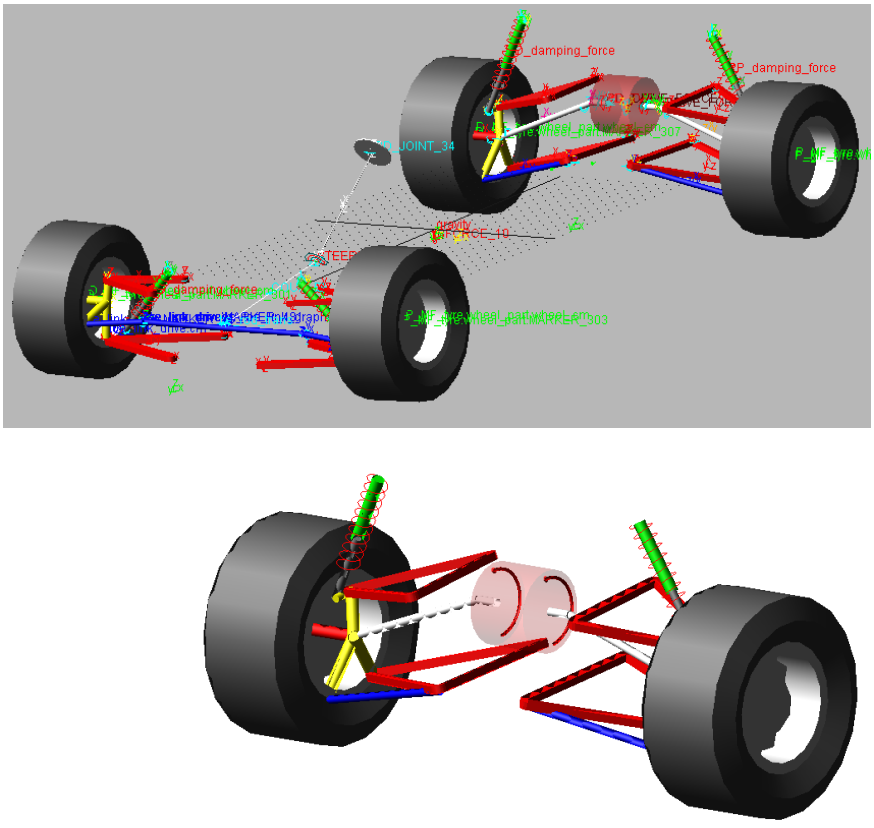

Figure 5-7 A full vehicle model for drivability check

5.5 Simulation Results

The results are carried out by simulating the ADAMS models in several examinations. Primary concerns with the additional mass on hub wheel centre are degraded road-holding and ride comfort. It is unacceptable to use a single measure in evaluating vehicle performance. Instead, there are a number of different indicators available to be considered as good practice. These indicators can be represented by using objective results, for example, numerical measures and data from predictive modelling or subjective review by an expert driver.

The performance of the ground vehicle dynamics can be broadly split into: ride, refinement, safety and driveability. The ride comfort is the capability of the vehicle to isolate disturbances and the refinement is the capability of the vehicle to reduce noise and vibration. The safety is the capability to drive and stop in emergency situations, and the last aspect is the driveability that is the agility of control response of the vehicle, for example, steering and braking in normal situations. The simulations focus on objective measurements and subjective analysis to review the influences on vehicle dynamic behaviours with additional un-sprung mass. Some subjective assessments will be reviewed to prove the results.

5.3.1 Analysis of ride comfort

Before starting analysis the simulation results, it is worth to review the function of subjective assessment that has been used in vehicle industry over decades. Subjective methods were first developed in the aircraft industry, where the Cooper rating scale was used to rate aircraft in terms of the ease or difficulty in completing specific tasks. A similar method used in vehicle industry is call “Vehicle Evaluation Rating” which the scale goes from 1 to 10- 1 is worst and 10is best. In practice, if a vehicle has been marked by grades 1 to 5, that means the vehicle is unable to sale on the market and unsuitable for further testing. A middle range of grades, such as scores 6 to 8, are used to denote vehicles that acceptable, mid-class and excellent. There are only skilled practitioners are available within the industry to acquire the subjective review of vehicles.

According to Anderson and Harty (2010) have tested a 2007 Model Year Ford Focus that was added 30kg additional mass to each wheel centre. This approach assumes rotating and non-rotating un-sprung masses in a way which broadly reflects the in-wheel motors. No other changes were made to the vehicle, which is to say no development was performed for the purpose of this exercise.

Subjective – Figure 5-8 shows the subjective result plot for ride evaluation. Some degradation can be found in the pitch control, small impact feel and large impact feel. Nothing in need of attention in the roll movement is described by the skilled practitioner.

Figure 5-8 Subjective results for ride testing (Anderson and Harty 2010)

Objective – As well as the subjective reviews carried out, objective measurements are made of ride comfort by using the in-line and in-wheel motors models that were built in previous section. The vehicle body is free and the platforms under wheels impart surface motion into the suspensions. The tyres represented by single spring damper and can separate from platforms under large inputs. The simulation runs at the dynamic mode for two second and to examine the vehicle models for their eigenvalues – Natural Frequencies at each degree of freedoms. The results show in Table 5-1. The information includes: sequential number of the mode that was predicted by the Eigen solution, natural frequency corresponding to the mode, damping ratio for the mode and list the real and imaginary part of the eigenvalue.

It is often true with passenger vehicles that the primary ride roll mode is at a higher frequency than the other two primary ride modes, since the anti-roll ("stabilizer") bars add a large amount of stiffness to the roll mode. Wheel hop frequencies are high compared to passenger car values but again the racing nature of the vehicle means the vertical tyre stiffness is relatively high, increasing up the wheel hop frequency. The four wheel hop modes are sensibly positioned with respect to each other, with the front modes, influenced by the steering gear mass.

Table 5-1 Display the eigenvalues in tabular form

EIGEN VALUES (Time = 2.0)

FREQUENCY UNITS: (Hz)

MODE NUMBER	UNDAMPED NATURAL FREQUENCY	DAMPING RATIO	REAL		IMAGINARY
1	4.918584E-002	5.093936E-001	-2.505495E-002	+/-	4.232607E-002
2	6.739976E-002	1.770735E-001	1.193471E-002	+/-	6.633468E-002
3	1.529638E-001	8.724846E-001	-1.334586E-001	+/-	7.474450E-002
4	1.389255E+000	7.546848E-002	-1.048450E-001	+/-	1.385293E+000
5	2.465433E+000	2.549324E-002	-6.285187E-002	+/-	2.464632E+000
6	3.487934E+000	4.726494E-003	-1.648570E-002	+/-	3.487895E+000
7	1.256368E+001	3.746509E-001	-4.706993E+000	+/-	1.164861E+001
8	1.268192E+001	3.809835E-001	-4.831601E+000	+/-	1.172547E+001
9	1.894751E+001	5.709073E-001	-1.081727E+001	+/-	1.555618E+001
10	1.914379E+001	5.787584E-001	-1.107963E+001	+/-	1.561174E+001

Table 5-2 Explanation of natural frequencies at each mode

Mode	***Frequency***	***Comment***
1-3	<0.2Hz	Body on rig stabilisation springs – fore-aft, yaw ,lateral
4	1.389 Hz	Primary Ride 1 – Heave
5	2.465 Hz	Primary Ride 2 – Pitch
6	3.487 Hz	Primary Ride 3 – Roll
7	12.56 Hz	Rear left wheel hop
8	12.68 Hz	Rear right wheel hop
9	18.94 Hz	Front left wheel hop
10	19.14 Hz	Front right wheel hop

The calculation for eigenvalues and eigenvectors can be performed using a function of ADAMS which provides a prediction of the model's natural frequencies and mode shapes. After the calculation is complete, ADAMS can display the Eigenvalues in tabular form and also plot complex Eigenvalues scatter as shown in Figure 5-9. Finding the stability of the system depends on the real and imaginary parts of the Eigenvalues, along with the positive or negative signs of the real parts and the difference of their values.

The system is unstable when the sign of the real part is positive, and its behaviour is more like an unstable oscillator. Comparatively, the system is stable when the real part is negative. To consider a more complex system, it is important to note that the system should has all real parts of the Eigenvalues with the negative values, and it is necessary condition to determine the system is stable. In additional, when the system is stable, the Eigenvalues should have the imaginary parts and that are not equal to zero. However, the model is a stable system in which the all real values are negative and the system has imaginary part that a pair of the values corresponds to the each mode.

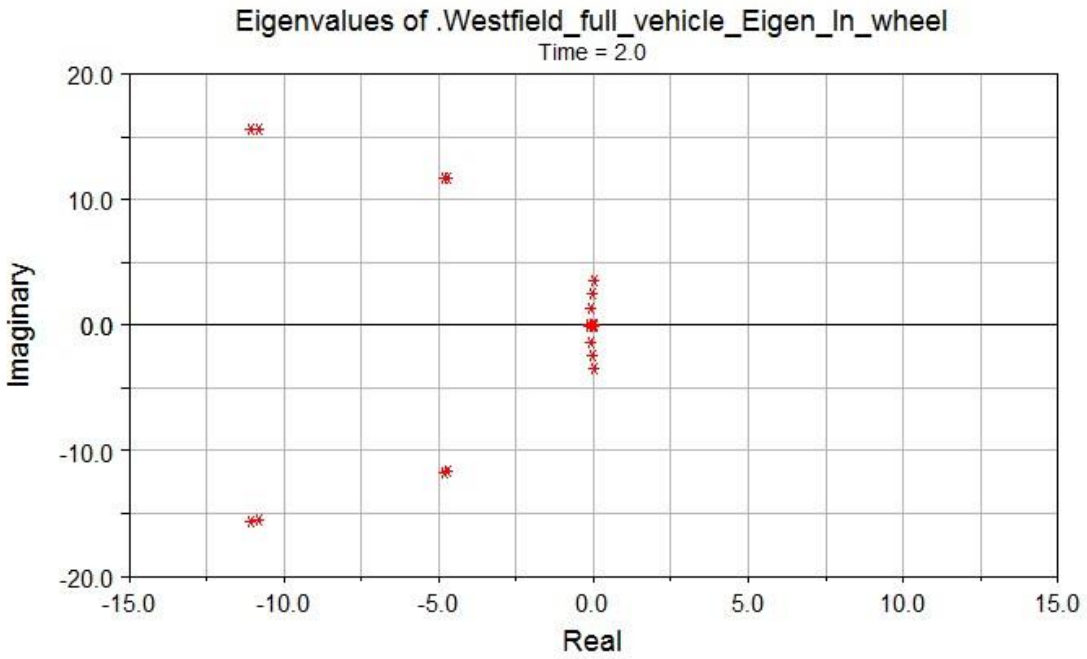

Figure 5-9 Eigenvalues for in wheel motors model

Animating the modes is able to give a better understanding of the deformations for the vehicle body and suspensions as shown in Figure 5-10. For example, the first animation is the body movement in fore-aft and then the second and third animations show the yaw and lateral movement. These three modes stay in very low frequencies. Start from the mode 4 is the animations for Primary Ride of the vehicle body in heave, pitch and roll, that can be seen the frequencies are increased at these modes and these changes should effect on the performance of the ride comfort as it is known in the vehicle dynamics field.

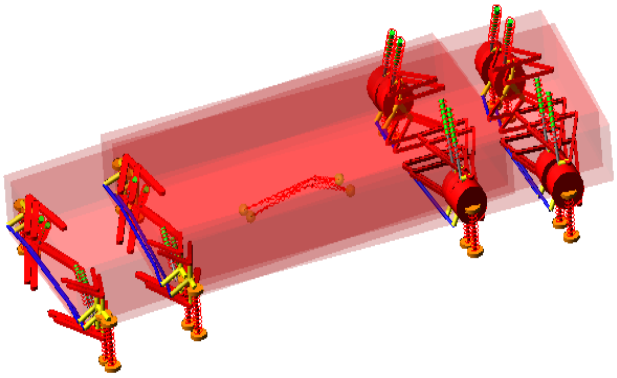

(a) Mode 1 Fore-aft (at 0.049185Hz)

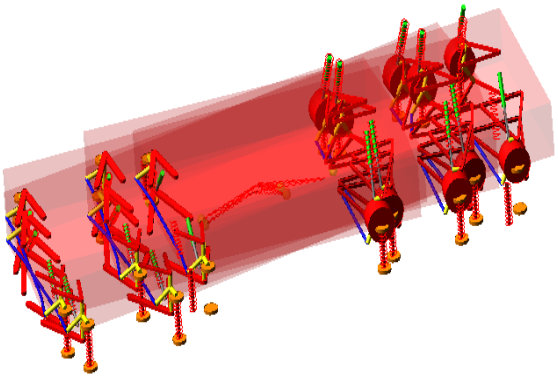

(b) Mode 2 Yaw (at 0.067399Hz)

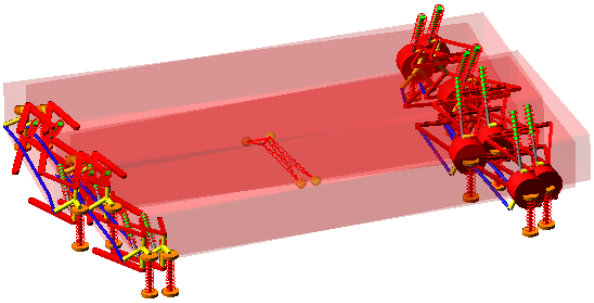

(c) Mode 3 Lateral (at 0.15296Hz)

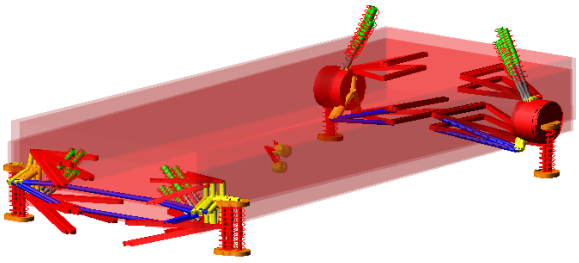

(d) Mode 4 Heave (at 1.3989Hz)

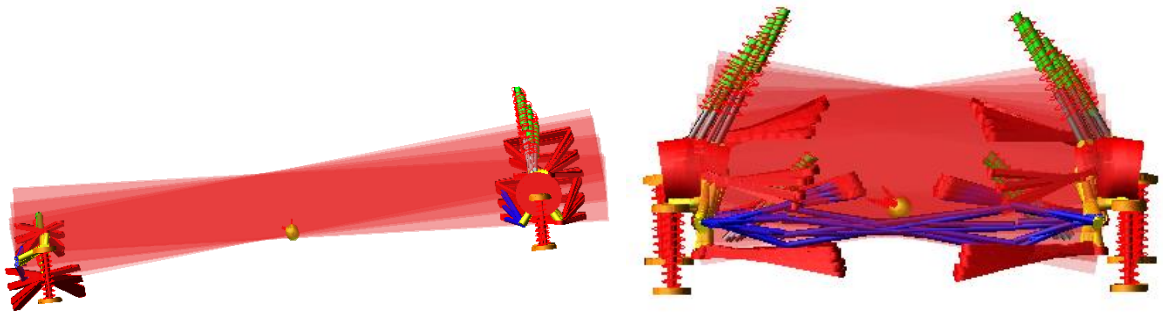

(e) Mode 5 Pitch (at 2.46543Hz) (f) Mode 6 Roll (at 3.48793Hz)

Figure 5-10 The animations for vehicle body

It is often true with racing vehicles that the roll mode of primary ride is at a higher frequency than other two primary ride modes, since the anti-roll bars add a large amount of stiffness to the roll mode. In addition, the vehicle body as modelled is built by using a single rigid body that may give large torsion stiffness for the vehicle structure in roll mode. As well as known, the stiffness of body structure is another open task to improve the vehicle handling and drive performance, likewise effects on safety requirements as a major issue in vehicle industry. Figure 5-11 shows the animations in wheel hop modes at front and rear suspensions.

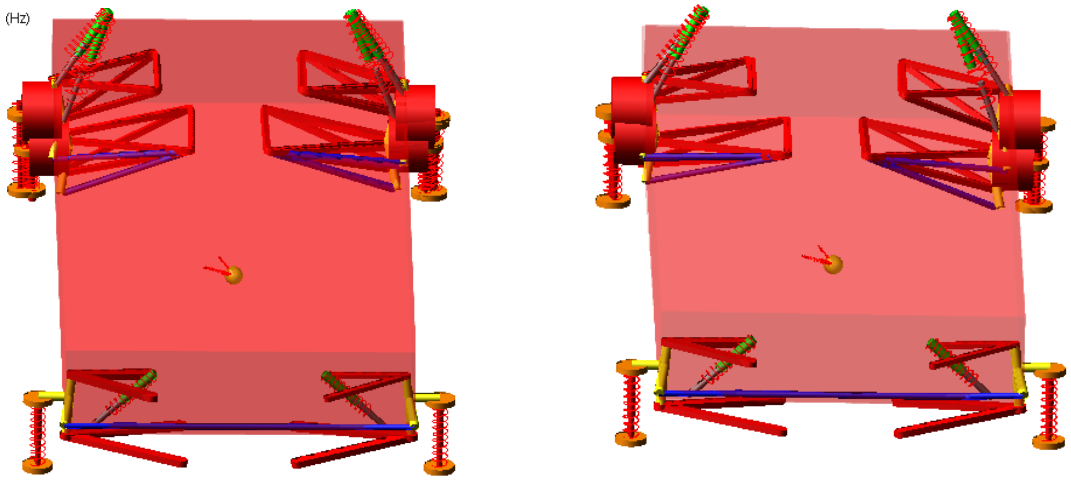

(a)Mode 7 Left wheel hop (at 12.563Hz) (b) Mode 8 Right wheel hop (at 12.681Hz)

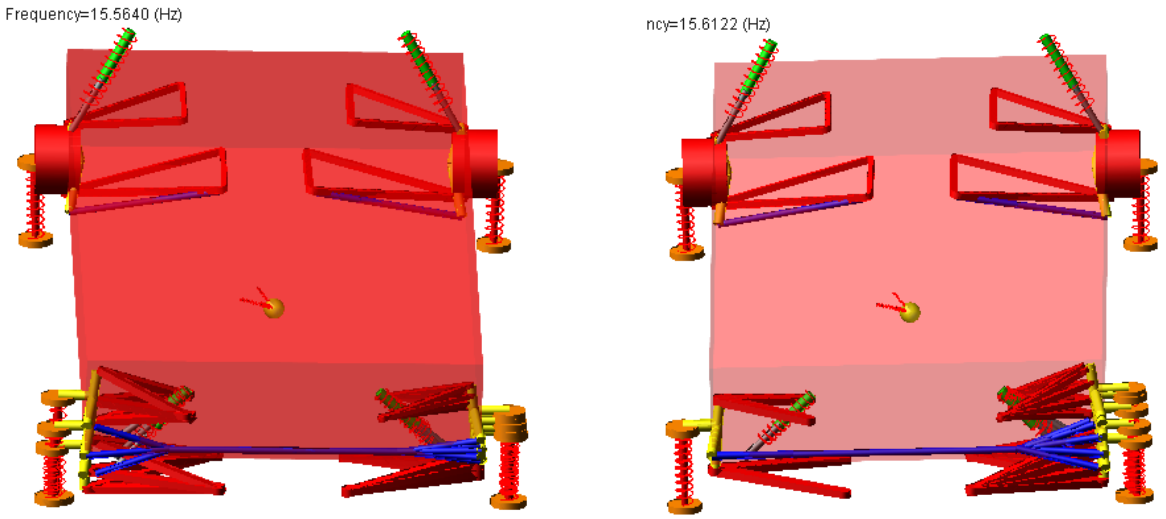

(c)Mode 9 Left wheel hop (at 18.947Hz) (d) Mode 10 Right wheel hop (at 19.143Hz)

Figure 5-11 Front wheel hop modes for in-wheel motors

The same procedure is used to simulate the in-line motors model in the ride comfort method. The table of the Eigenvalues and the plotting of the eigenvalues scatter are also carried out that the results are able to check how the frequencies at each mode effect on the ride performance and the model with new driveline is stable or unstable as shown in Table 5-3 and Figure 5-12. In tabular form, the modes for the in-wheel motors model have been checked by using the animations in which they have same the sequence as the in-wheel motors model, thus they can easily be compared.

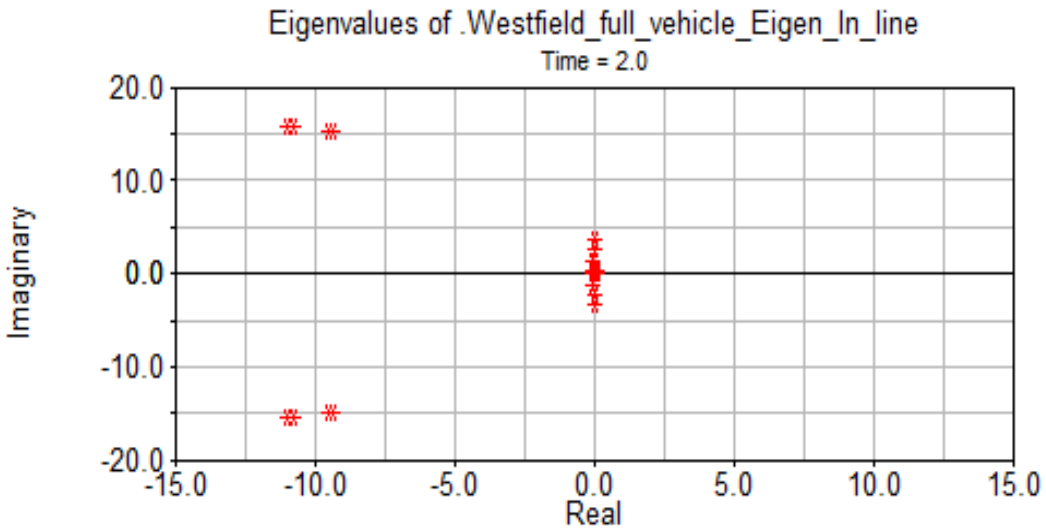

Figure 5-12 The plotting of Eigenvalues scatter for in-line motors model

Table 5-3 Natural Frequencies for in-line motors model

EIGEN VALUES (Time = 2.0)

FREQUENCY UNITS: (Hz)

MODE NUMBER	UNDAMPED NATURAL FREQUENCY	DAMPING RATIO	REAL		IMAGINARY
1	4.922365E-002	1.249780E-001	6.151871E-003	+/-	4.883771E-002
2	1.651381E-001	9.023115E-001	-1.490060E-001	+/-	7.118848E-002
3	7.644610E-002	3.578144E-001	-2.735351E-002	+/-	7.138481E-002
4	1.303363E+000	9.868148E-002	-1.286178E-001	+/-	1.297002E+000
5	2.485401E+000	1.802865E-002	-4.480842E-002	+/-	2.484997E+000
6	3.529858E+000	4.856114E-003	-1.714140E-002	+/-	3.529817E+000
7	1.777888E+001	5.305927E-001	-9.433341E+000	+/-	1.506985E+001
8	1.789426E+001	5.357963E-001	-9.587681E+000	+/-	1.510897E+001
9	1.893831E+001	5.697932E-001	-1.079092E+001	+/-	1.556327E+001
10	1.914463E+001	5.788755E-001	-1.108236E+001	+/-	1.561083E+001

Comparing the results of the objective measurement at the ride comfort check are carried out as shown in Figure 5-11 and the differences in the natural frequencies can be found between the two different architectures. For the in-line motors model, the natural frequencies at the mode 2 and mode 3 (i.e. the body motion in yaw and lateral direction) have very small variety comparing to the in-wheel motors model. The change is because of adding the in-line motors driveline effects on the stiffness and mass matrices of the vehicle body.

For the in-wheel motors model, the extra masses are attached on the suspensions merely, thus no influence on the natural frequency of the vehicle body. In addition, more decrease in the natural frequency occurs at the mode 7 and 8 (i.e. the wheel hop modes for the rear suspensions). As previously note, the reason for frequency reduction is due to the un-sprung mass being increased by integrating all the components into the wheel hub. However, the wheel-hop mode of vibration is reduced in frequency from around 17 Hz on the in-line motors model to around 12 Hz with in-wheel motors.

It is clear shown in Figure 5-11 (a), which the frequencies at the rear wheel hop modes are obviously different, and that should change the level of response, but not significant. There are no testing results to indicate that the vibrations of unsprung mass from 12 to 17Hz will produce more noisome, thus it may be summarized that the ride behaviour is not substantially changed by adding the masses on the wheel centre.

Table 5-4 Comparison of natural frequencies for in-line and in-wheel motors model

MODE NUMBER	UNDAMPED NATURAL FREQUENCY
1	4.918584E-002
2	6.739976E-002
3	1.529638E-001
4	1.389255E+000
5	2.465433E+000
6	3.487934E+000
7	1.256368E+001
8	1.268192E+001
9	1.894751E+001
10	1.914379E+001

(a) In-wheel motors

MODE NUMBER	UNDAMPED NATURAL FREQUENCY
1	4.922365E-002
2	1.651381E-001
3	7.644610E-002
4	1.303363E+000
5	2.485401E+000
6	3.529858E+000
7	1.777888E+001
8	1.789426E+001
9	1.893831E+001
10	1.914463E+001

(b) In-line motors

Nevertheless it is necessary to introduce another simulation for further ride comfort check in which an inspection in the vertical wheel hub acceleration will be needed to verify any influences of ride behaviour due to the additional masses. A typical method has developed by Blundell (2004) who defined a motion imparted to a jack part to represent inputs from the road surface, and a step function can also be used to describe a profile of speed bump as shown in Figure 5-13. Motion in translational applies on the jack to give the suspension an severe impact, and the result shows in Figure 5-14 over a large single disturbance the in-wheel motors model gives measurably poorer behaviour – higher and severe response, that can elucidate why the in-wheel motors vehicle provides lower score on subjective assessment.

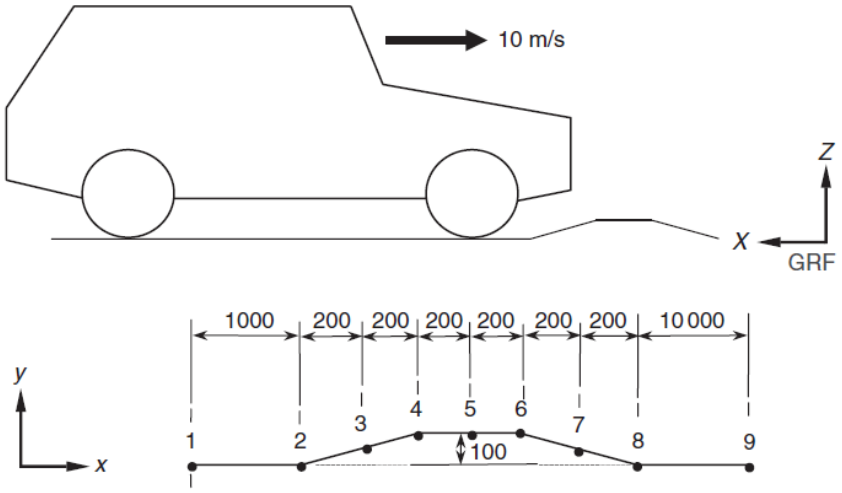

Figure 5-5 Road profile for speed bump (Blundell, 2004)

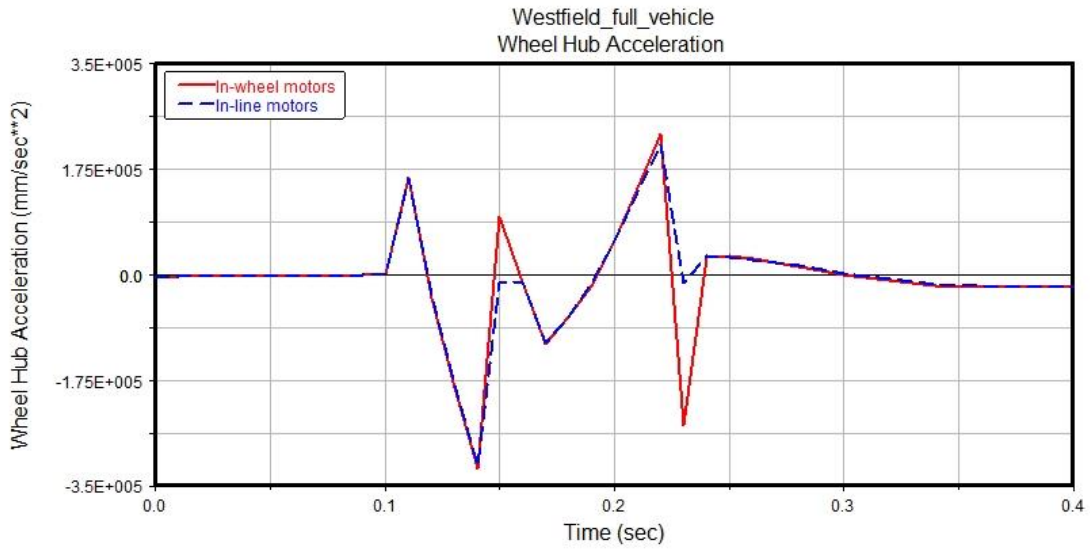

Figure 5-6 Measured results for wheel hub acceleration

5.3.2 Analysis of drivability check

As mentioned, it is very important to work out how the additional masses will effect on the drive safety and control performance of electric vehicles with different architectures. Reasonably, some reviews in subjective evaluations of real vehicle testing environment will be carried out as following, and therefore the driver sensitivity at the level of expert can define the response of the vehicle precisely and

give an authentic score in vehicle evaluation rating. The previous comparisons mainly focus on the ride comfort check with extra masses on the rear wheels, and that are very useful evidences to elucidate the advantages of architecture for in-line motors vehicle. More objective measurements in drivability will be accomplished still with more interested results.

Subjective – The subjective result of drivability check is shown in Figure 5-15, and the largest deficit concern is the effort in the steering in which becomes heavier under a large range of circumstances. The degradations obviously effect on the drivability of the in-wheel motors vehicle at obstacle avoidance and emergency turns, even need more efforts on parking. Nevertheless, the architecture for in-line motors vehicle has a typical or traditional chassis in which the drivability can be expected as same as a performed vehicle.

Figure 5-15 Subjective results of steering behaviour (Anderson and Hart, 2010)

Objective – The previous models for the drivability check are taken into the computer-based (ADAMS) simulation. The simulation consists of two manoeuvres: steady state cornering and double lane change. For first step, the analysis for steady state cornering is carried on a 40m radius course, and a closed-loop driver model uses PID controller in which strong emphasis on Integral gain gives the model accurate path following. The simulation starts with a speed of around 5kmh and the

driveline delivers equal torque to each wheel attempting to track a speed target. Speed ramps up at around 1kmh per second, substantially similar to the rate at which speed is applied in a normal constant radius test.

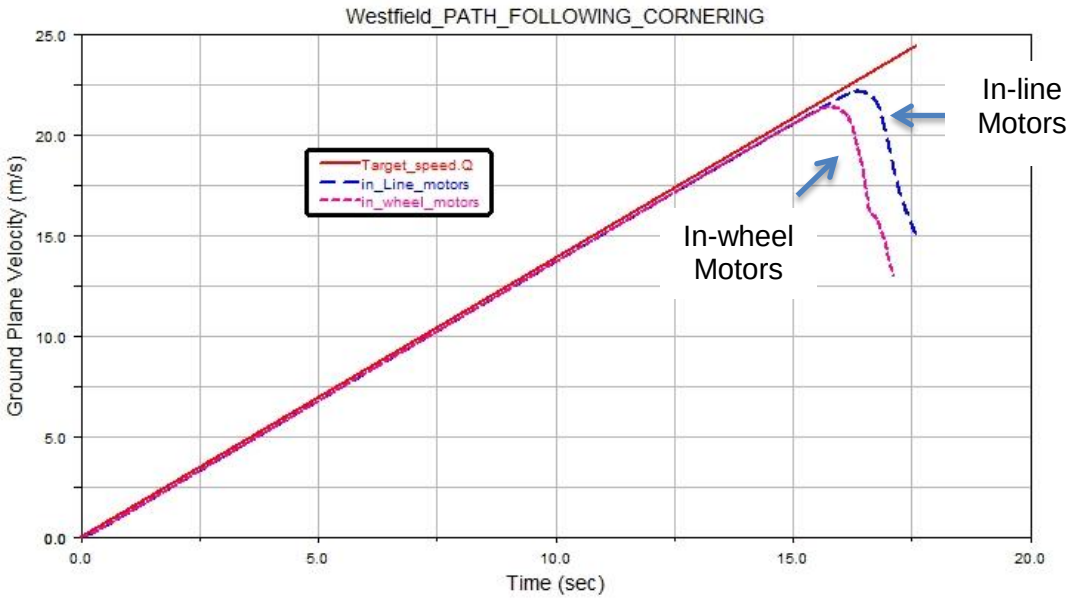

Figure 5-16 Ground plane velocity during steady state cornering

The analysis ends when the vehicle can no longer follow the line, either through tyre saturation or when the two inside wheels lift clear of the ground with an incipient rollover event. In the Figure 5-16, the both models tends to follow the target speed at the begin of the simulation, and then the model with in-wheel motors starts skidding due to the tyre saturation after simulation time16seconds, at 21m/s ground plane velocity. The model with in-line motors skids two second after this, at 22.5m/s. The validity of the Pacejka 89 equations collapse at high inclination angles and so the continued solution is of no interest.

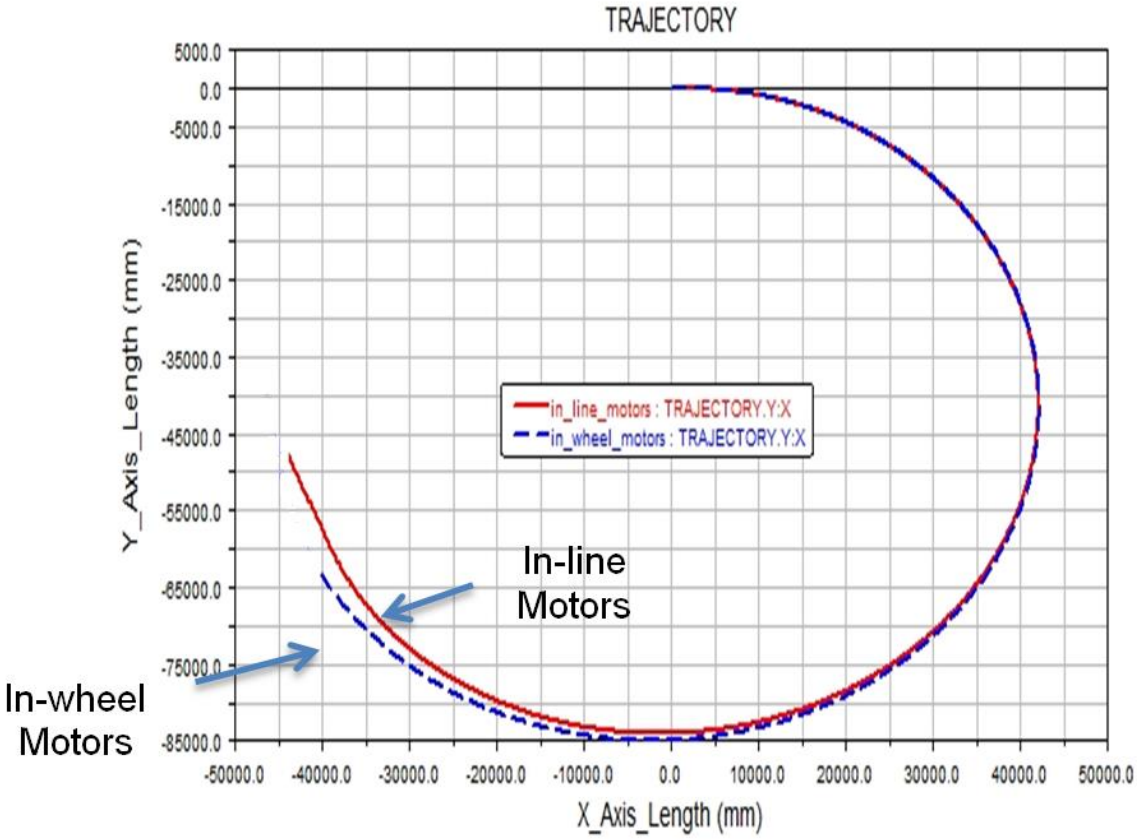

Figure 5-17 The trajectories at cornering

More effects can be seen in the trajectories at steady state cornering as shown in Figure 5-17. In side pushing effect of vehicle scenario, the model with in-wheel motors reaches the performance limits quicker and exhibits more understeer behaviour. The model with in-line motors induces extra yaw moment, helping the vehicle reduces understeer behaviour, thereby reducing the steering angle required. Figure 5-18 clearly shows that the centripetal acceleration is less with in-line motors.

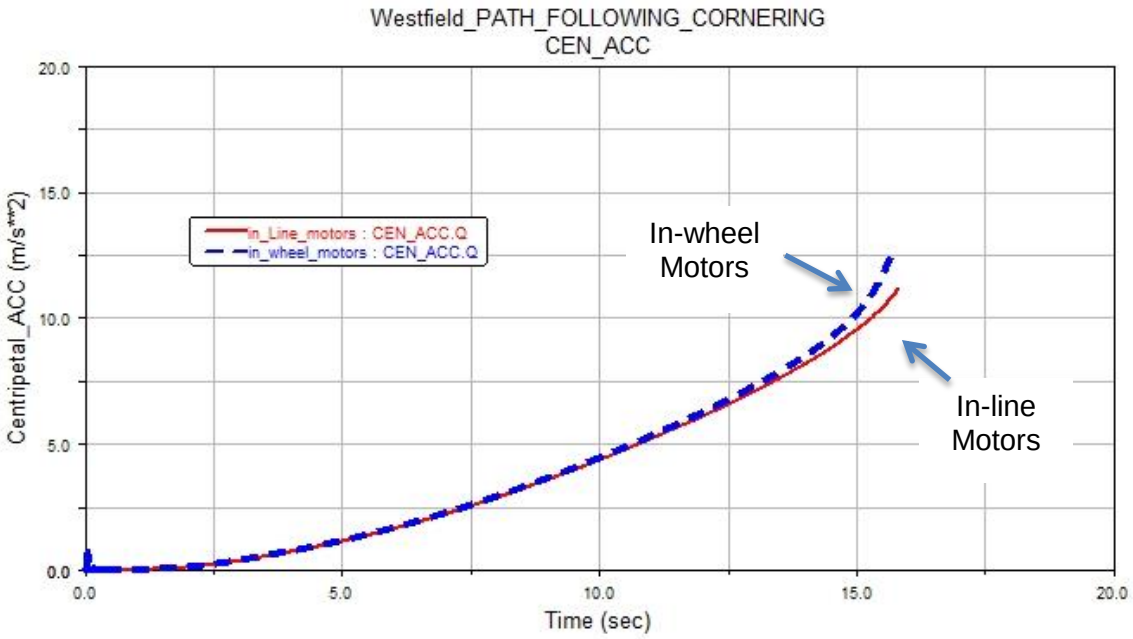

Figure 5-7 Testing results for centripetal acceleration of in-line and in-wheel motors

In the next step, the models will be taken into double lane change manoeuvre. The manoeuvre is essential a scaled version of ISO3888 lane change in its geometry, only the test protocol differs slightly. It consists of a defined zone in which the vehicle can take any path and reflects a real world avoidance manoeuvre within a finite width road. The vehicle must displace laterally by around 3.5m minimum and then return to its original path. The modification of the double lane change is intended to reflect maximum effort manoeuvring at highway speeds and the length and width of the manoeuvring zone are related to the vehicle proportions, as shown in Figure 5-19. Also the details for optimizations of double lane change will be discussed in the next Chapter.

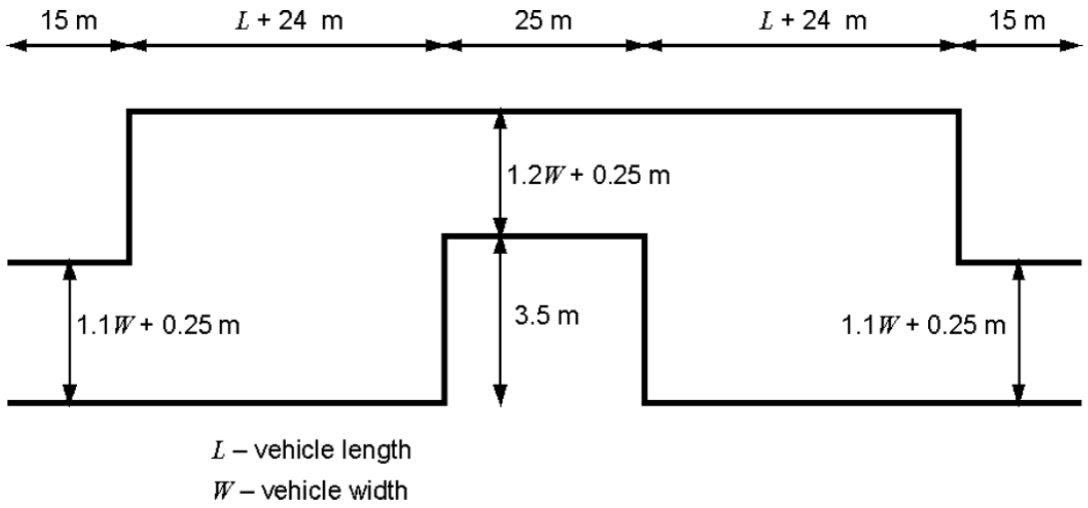

Figure 5-8 Double Lane Change Test Course

With real vehicle, the driver skill levels modify the performance of a given vehicle through the lane change substantially and so when comparing vehicles it is preferable to use a panel of drivers or at least a consistent driver. In the analysis the driver model is consistent and repeatable as well the closed-loop PID control gives the vehicle an accurate path following.

For the simulation, the both models are driven up to the manoeuvre start at 100km/h and the throttle released. The overrun condition is typically the most difficult in terms of stability. Although the vehicle loses speed as it enters the second of the two manoeuvres, it is typically unsettled dynamically and so the second transition is often the more problematic of the two. The maximum variation of yaw rate can be seen in the stage of centre correction and exit oscillations, there is that the increased angular velocity in yaw around 8 degree/s emerges an overshot at the peak values comparing to in-line motors model as shown in Figure 5-20. Also some influences of body slip angle are shown in Figure 5-21, which is important because it effectively grows the width of the vehicle. The changes are large enough to indicate the driver the vehicle will be lost control. The measurements based on computing simulations are broadly familiar with subjective assessments, which more evidences will be shown in next section to see somewhat worse results as expected.

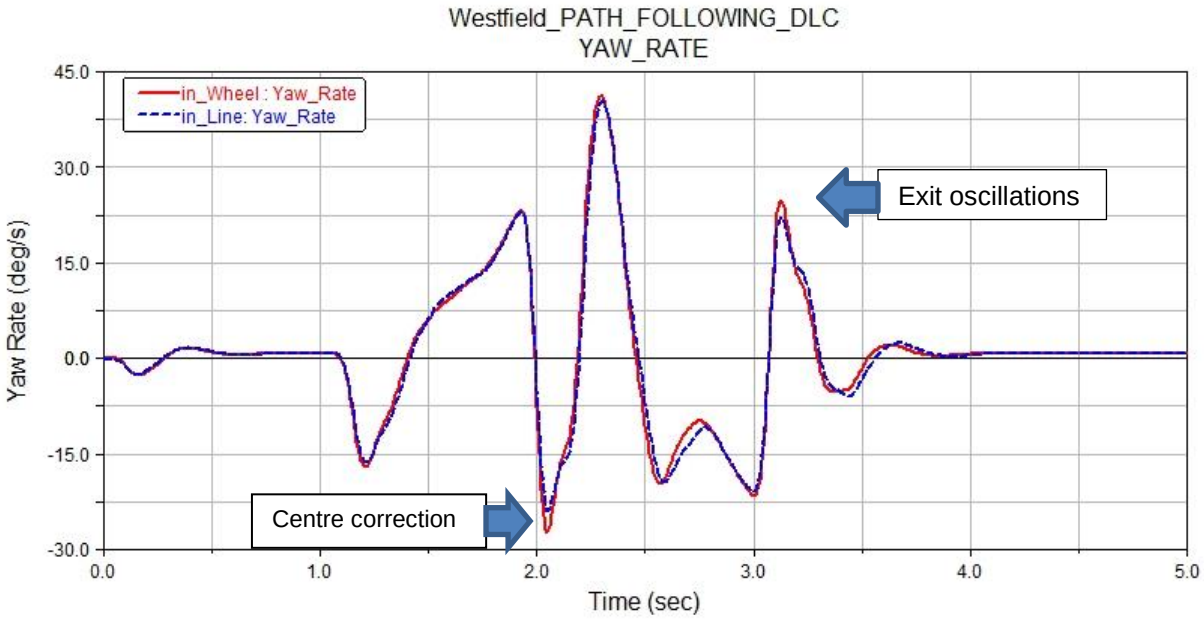

Figure 5-9 Comparison of yaw rate for in-line and in-wheel motors in DLC

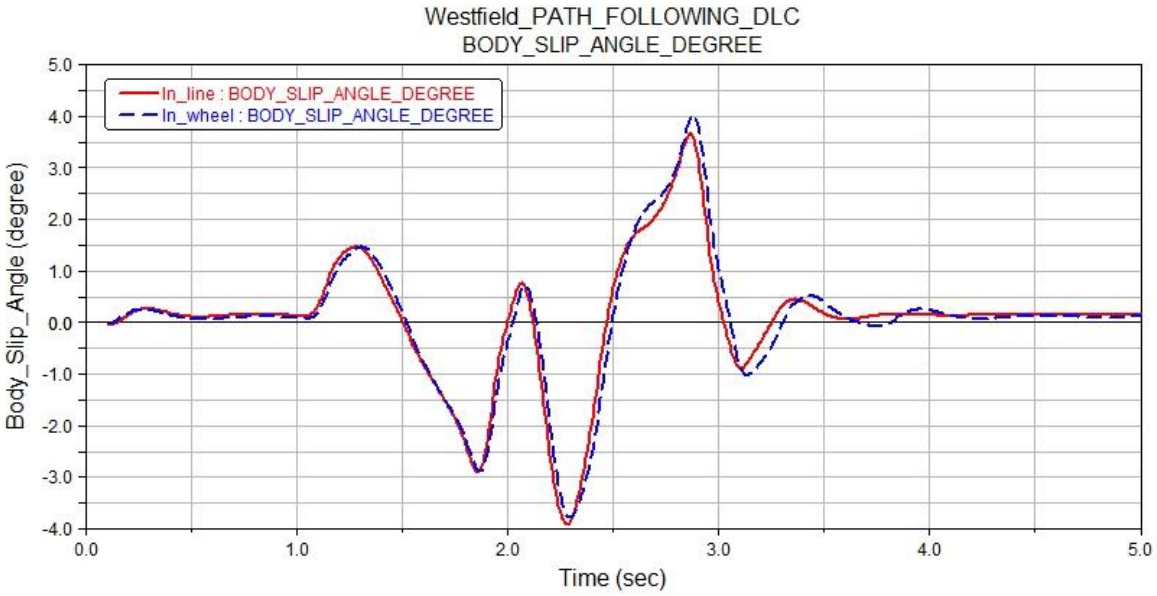

Figure 5-10 Comparison body slip angle for in-line and in-wheel motors in DLC

Considering driver steering motion inputs for both models, it can be seen in Figure 5-22, the model with the in-line motors has a large reduction about 10 degrees in first reversal and centre correction section, also a useful improvement in overall magnitude of steering angle inputs can be found. In addition, there is an improved quality to the steering traces in terms of smoothness and lack of reversals when the model with in-line motors. It may expect more significant differences in driveability

check when comparing the two architectures, nevertheless considering the change on in-wheel motor model is only to add 5% of the entire vehicle weight into the rear wheel centre and the extra weight is even less than a passenger.

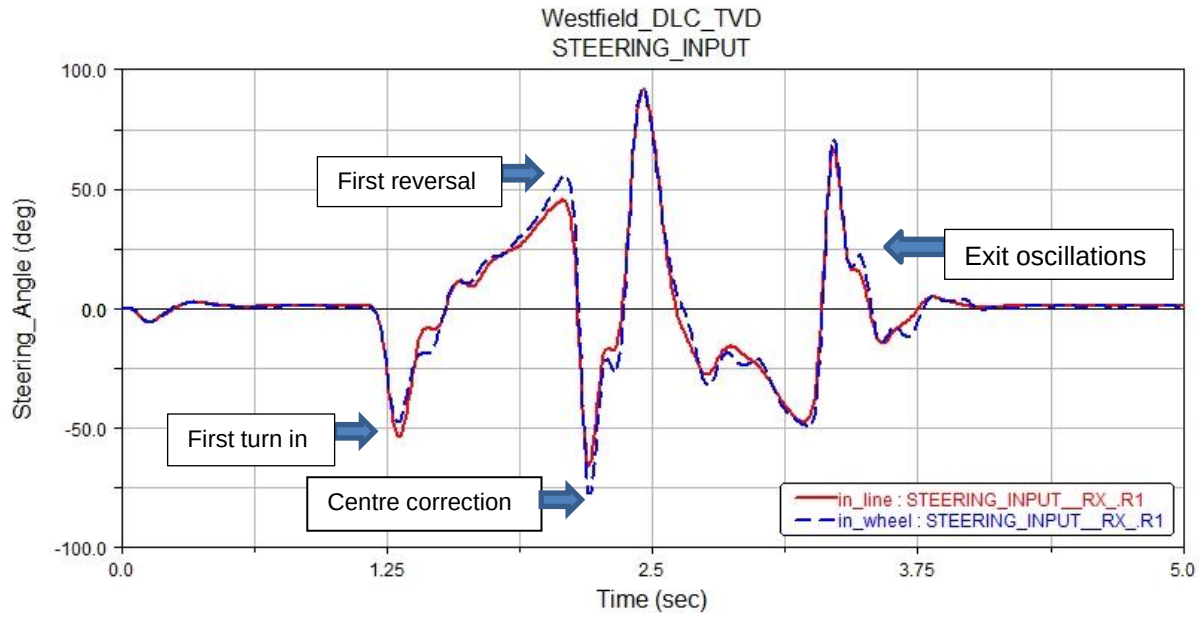

Figure 5-11 Comparison of steering angle for in-line and in-wheel motors in DLC

5.5 Conclusion

In this chapter, the vehicle architectures of in-wheel motor and in-line motor are introduced that the significant modifications of original suspension have been done to integrate all components of in-wheel motors, such as braking system, cooling system and electric motors, into the constraint volume at inside of the rim. Furthermore, the un-sprung mass is obvious increased for implementing in-wheel motors on a vehicle, and degraded ride and handling performance. Compare to the architecture of in-wheel motors vehicle, the in-line motors vehicle were required the minimum variations of suspension system thus is can remain the un-sprung masses and reduce redesign costs.

Objective measurements were carried out by using several computing simulation models in ADAMS, such as kinematic, dynamic and handling models. The aspects of simulation have been examined in detail and can be concluded thus the overall performance of ride comfort is demoted and the obvious impact of steering

behaviour emerge with testing the vehicle models in cornering and lane change manoeuvres. The effects on safety and driveability are required some variations in suspension component detail and increase in damping levels to restore agility.

Overall, developing the electric vehicle in next recent state the architecture of in-line motors vehicle can preserve the characteristics of conventional vehicle in high performance, and the redesign costs and efforts can be economized on improving capacity of electric motors and battery life. Moreover the good potential of individual wheel motor control can be implemented by using in-line wheel motors for substantial improvements in vehicle behaviour.

6 Torque vectoring system with in-line motors

6.1 Introduction

Active intelligent control systems for achieving vehicle stability and handling have been developed and implemented to enhance the driving safety and performance of the driving vehicle. Some enhancements, such as Active Steering Systems and Electronic Stability Programs, can help the driver to retain control of their vehicles when the grip between road surface and tyre is lost. In previous investigations, the ABS based Stability Control Systems are principal safety implement to accomplish the safety requirements under adverse road conditions. However, the vehicle speed is degraded while the Stability Control System implements braking force on four wheels individually to improve the correct position of the vehicle body. Moreover, the Torque Vectoring (TV) system can be designed to improve the vehicle handling qualities and avoid the vehicle speed decrease, or in other words the 'fun-to-drive' aspect. Thus, torque vectoring can be used to influence the driver experience.

In this chapter, the investigation focuses on developing and designing a novel TV control strategy that is called Optimal Driveline Control Strategy (ODCS). The ODCS involves three levels of control: Desired Dynamics Behaviours, Secondary Control and Advanced Torque Vectoring Control, more details of which will be represented in the following section. Reviewing the basic principles for TV control on the conventional driveline helps to understand how to implement those control strategies on the pure electric vehicle. The configuration of the ODCS algorithm is clearly shown in this chapter, and each level of control is explained in detail.

The project vehicle model with three different types of drivelines is taken into Computer-Based simulations. The results are carried out by running the vehicle model through the steady state cornering and lane change manoeuvres. The results for the vehicle model with ODCS are also compared against the conventional drivelines, such as Open and Limited Slip Differential, during which the vehicle speed is increased.

6.2 Basic principles

The conventional drivelines, such as Open Differential and Limited-Slip Differential, have been broadly used in the rear driving vehicles. The Open Differential allows the driving wheels to rotate at different speeds while giving the same driving torques on both wheels. The Limited-Slip Differential is designed to improve handling and stability while the vehicle turns into a corner, but a fixed kinematic relationship can only transfer the driving torques from the faster spinning wheel to the slower wheel (Mohan and Sharma, 2006). Thus, developing a Torque Vectoring system is required: first to retain the abilities of the open differential and limited slip differential, and then to incorporate a means to vary the kinematic ratio across the differential thus affecting the torque distribution between the wheels.

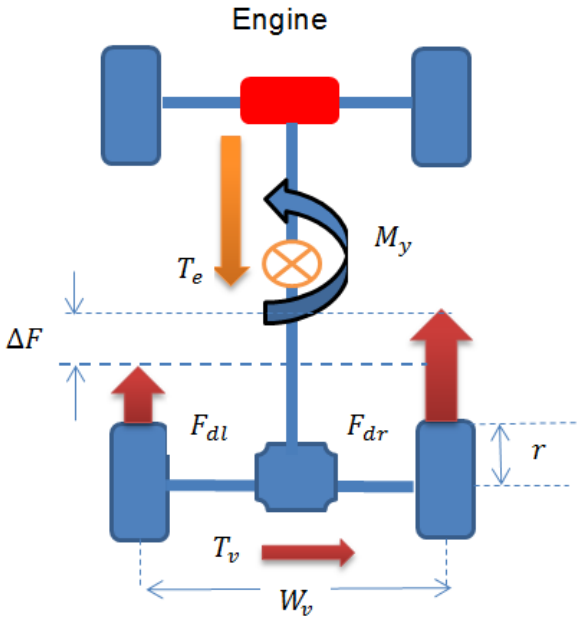

Figure 6-1 Definition of torque vectoring differential

$$F_{ldl} = (T_e/2 - T_v)/r \tag{6.2.1}$$

$$F_{ldr} = (T_e/2 + T_v)/r \tag{6.2.2}$$

$$\Delta F = F_{dr} - F_{dl} = 2T_v/r \tag{6.2.3}$$

$$M_y = \Delta F \times W_v/2 \tag{6.2.4}$$

Figure 6-1 shows a basic principle of TV applied to the rear axle when turning the vehicle left, the engaging clutches can transmit the engine torque T_e via the pro-shaft from left driving wheel to right side with transferring torque T_v. In addition, adding or subtracting the driving torques on the left and the right wheels give a difference ΔF on the longitudinal driving force. The difference ΔF generates additional yaw moment M_y to help the vehicle turn into the corner more easily.

Here is a good example in Figure 6.2.2 to show how to accomplish the requirements of TV by using a mechanism TV differential. The system includes planetary gears and slipping multi-plate wet clutches, which those components are controlled by electromechanical or electrohydraulic control systems (Li and Wu, 2011). In addition, the functions of TV system can be applied to all types of driving vehicles, such as Rear-Wheel-Drive (RWD), Front-Wheel-Drive (FWD), and Four-Wheel-Drive (4WD), which the device enables to be mounted on either front, rear or both axles to modify engine torque to each wheel. Closed-Loop Control is used in the system, thus the vehicle speed, wheel slip ratio, yaw rate error and other parameters have to be measured. The outputs from the measurements are used to modify the driving torques from an Internal Combustion engine.

Figure 6-2 Schematic of a mechanism torque-vectoring differential

(Mohan and Sharma, 2006)

Reviewing the schematic of a mechanism TV differential in Figure 6-2, the device uses stepped planets and sun gears meshing each other to provide for a differential action. The biasing gear-set is connected to the wet clutch as brakes that can slow down one side and speed up on the other side thereby allowing the driven vehicle to be turned. The secondary gears enable the reduction of the brake torque required to steer the vehicle, and thus increase the efficiency of the system.

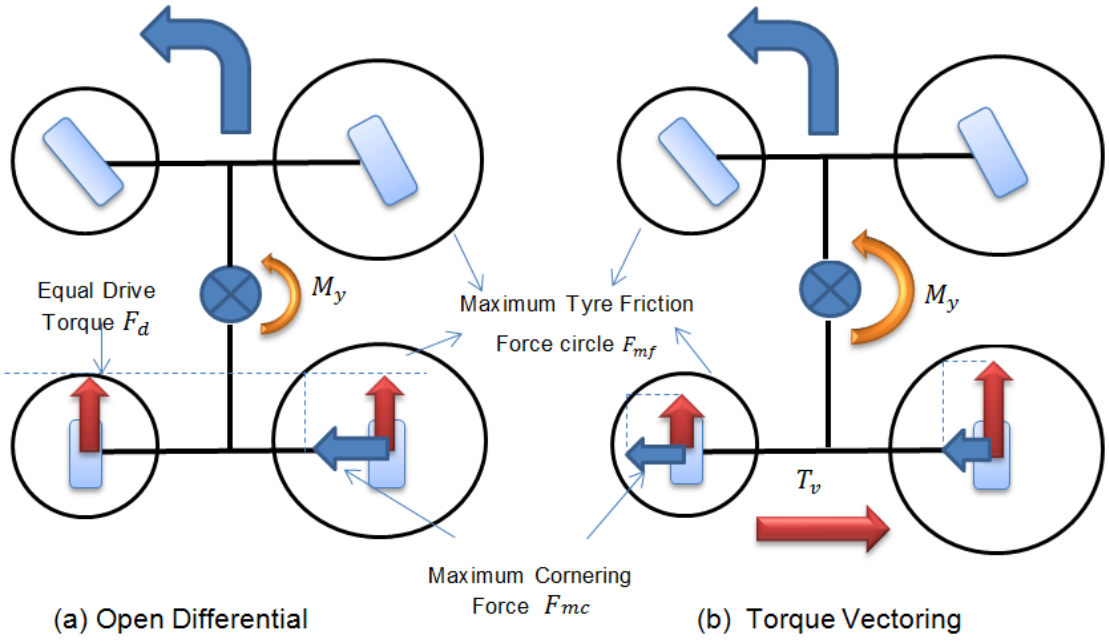

Figure 6-3 Explanations of the left-and-right torque vectoring

In order to explain how the functions of a TV system can be implemented on the project vehicle clearly, a schematic that shows the relationship between driving forces and maximum cornering forces is carried out in Figure 6-3. The project vehicle is pure electric vehicle with the Rear-Wheel-Drive, thus a mechanism driveline is replaced by a pair of electric motors at the middle of the rear axle where a differential is located. Moreover, the characteristics defined in the previous chapter indicate the project vehicle is under-steer and the weight distribution is 50/50 so the maximum friction circles are symmetric at the front and rear wheels when driving the vehicle in a straight line. According to the configurations of the project vehicle, only a Left-and-Right TV control has been considered in this research. The schematic shows that assuming the vehicle model is turning left, lateral acceleration causes the right wheel maximum friction circle to increase and the left wheel maximum friction circle to

decrease. If using a function of Open Differential on project vehicle, for example, the driving torques are identical at two rear wheels and only the right tyre generates cornering force F_{mc} because the maximum tyre friction force is bigger than the driving force. However, using a Left-and-Right TV configuration is possible to redistribute the engine torque between the two wheels, thus the left driving force will be $F_e - \Delta F/2$ and the right driving force is $F_e + \Delta F/2$, so that both the driving wheels generate the maximum cornering forces compared to the vehicle without TV control. The additional cornering force ΔF_c can be expressed as below:

$$\Delta F_c = F'_{lmc} + F'_{rmc} - F_{rmc} \tag{6.2.5}$$

So $$\Delta F_c = \sqrt{{F_{lmf}}^2 - \left(F_d - \frac{\Delta F}{2}\right)^2} + \sqrt{{F_{rmf}}^2 - \left(F_d + \frac{\Delta F}{2}\right)^2} - \left({F_{rmf}}^2 - {F_d}^2\right) \tag{6.2.6}$$

$F'_{lmc} and\ F'_{rmc}$: Left and right maximum cornering force with TV

F_{rmc}: Right maximum cornering force without TV

$F_{lmf} and\ F_{rmf}$: Left and right maximum tyre friction force

F_d: Driving force

Based on this formula, when the vectoring torque ΔF is applied, the additional cornering force ΔF_c will become a maximum value as shown below. It shows that the vectoring torque generates the additional cornering force.

$$\Delta F = F_d(F_{rmf} - F_d)/2(F_d + F_{rmf}) \tag{6.2.7}$$

In order to implement this concept into the handling and stability control of the project vehicle, a control strategy will be designed in the next section. Moreover, the promise of individual motor control shows good potential for substantial improvements in vehicle behaviour. It is worth mentioning, a mechanism TV differential is difficult to apply the vectoring torques to the driving wheels when the vehicle is on “throttle off” position. A solution has been found by adding electric equipment to the driving axle, thus enabling the extra propulsion forces to be

obtained. However, those issues will also be taken into account for creating a novel control strategy.

6.3 Optimal Driveline Control Strategy (ODCS)

An Optimal Driveline Control Strategy (ODCS) is designed and developed in this section. The aims of the control are to improve the project vehicle handling and lateral stability; thus, to achieve those requirements the design concepts will be based on the Left-and-Right TV control configuration and have three levels of control. The outputs from the control strategy can dominate the pair of electric motors individually.

A detailed diagram of the Optimal Driveline Control Strategy is exhibited in Figure 6-4, which consists of three levels: Desired Dynamics Behaviours, Secondary Control and Advanced Torque-Vectoring Control. The first level is created to define the operating scope and desired behaviours. The desired behaviours are able to be found according to the vehicle speed and path curvature calculation. The secondary control is created to implement the desired driving torques and yaw rate error correction for tracking the desired behaviours. The inputs from the upper levels should dominate the electric motors through the Advanced Torque Vectoring Control (ATVC). The use of ATVC level is to modify the vectoring torques and driving torques outputs, and some constraints are added to avoid wheel slip while accelerating or braking.

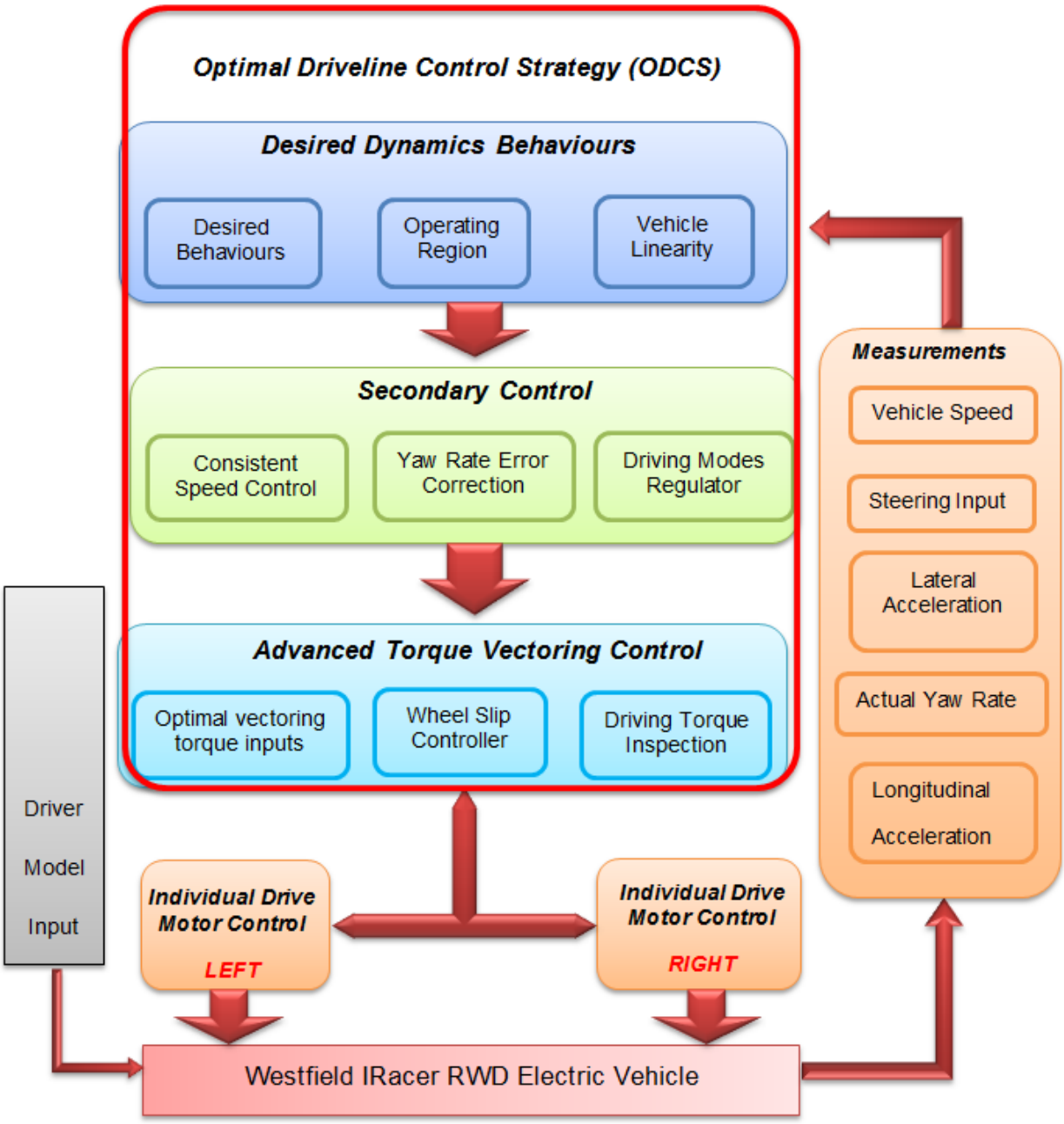

Figure 6-4 Schematic of Driveline Control Strategy (DCS)

In addition, a human driver model is required to simulate the project vehicle. The performance of a real vehicle, through road testing, can be modified by driver skill levels; so it is preferable to use a consistent driver when comparing the vehicles. Moreover, the aim of the DCS is to assist the driver to cope with the extreme driving scenarios even in the “throttle off” condition. However, an Open-Loop Driver model is used with the project vehicle to follow a desired path with consistent driving

performance. Thus the simulated results from the model with different driving configurations and vehicle speeds can be compared.

6.3.1 Definitions of Desired Dynamics Behaviour

Reference model definition

The primary requirement of the ODCS is to deliver desired dynamics behaviour in terms of the desired path, desired yaw rate, operating scope and vehicle linearity. The vehicle as modelled in the previous chapter will be taken into a steady state cornering manoeuvre for the first simulation. The yaw rate transfer function of the vehicle without TV control (the so-called “baseline vehicle”) can be obtained from the equations describing the lateral force and yaw dynamics of the single-track vehicle model (Milliken, 1995). Thus

$$\begin{aligned} J_z\dot{r} &= N_\beta\beta + N_r r + N_\delta\delta_\omega \\ mV(r+\dot{\beta}) &= \dot{Y_\beta}\beta + Y_r r + Y_\delta\delta_\omega \end{aligned} \tag{6.2.8}$$

In this equation, δ_ω is the mean steer angle of the front wheels. The stability derivatives can be expressed as a function of the front and rear cornering stiffnesses, i.e. C_F and C_R, respectively, as

$$Y_\beta = C_F + C_R;\quad Y_r = \frac{aC_F - bC_R}{V}\ ;\ Y_\sigma = -C_F$$

$$N_\beta = aC_F - bC_R;\ N_r = \frac{a^2C_F - b^2C_R}{V}\ ;N_\delta = -aC_F$$

These equations are correctly referred to as a 2-degree-of-freedom model; they are sometimes referred to as a ‘bicycle’ model but this description should not imply that the description may be suitable for two-wheeled vehicles.

The next hurdle to be crossed is the representation of the intended behaviour of the vehicle – the ‘reference’ states. Competition-developed lap simulation tools use a ‘track map’ based on distance travelled and path curvature. This representation allows the reference path to be of any form at all and allows for circular or crossing

paths to be represented without the one-to-many mapping difficulties that would be encountered with any sort of *y*-versus-*x* mapping. Integrating the longitudinal velocity for the vehicle gives a distance-travelled measure that shows it to be tolerably robust against drifting within simulation models. Using this measure, the path curvature can be surveyed in the vicinity of the model.

Some researchers favour the use of a preview distance for controlling the path of the vehicle, with an error based on the lateral deviation from the intended path. However, there is usually a difficulty associated with this since the lateral direction must be defined with respect to the vehicle. Failure to anchor the reference frame to the vehicle means that portions of the path approaching 90 degrees to the original direction of travel rapidly diverge to large errors. Projecting a preview line forward of the mass centre and located on the vehicle centre line is unsatisfactory due to the body slip angle variations. Either the proportional gain must be reduced to avoid pilot induced oscillation type behaviour, which leads to unsatisfactory behaviour through aggressive avoidance manoeuvres, or else some form of gain scheduling must be applied.

An alternative method, used here with some success for a variety of extreme manoeuvres, is to focus on the behaviour of the front axle. This model fits with the experience of drivers at or near the handling limit, particularly on surfaces such as snow where large body slip angles highlight the mechanisms used in the driver's mind. High performance driving coaches (Palmer, 1999) rightly concentrate on the use of a 'model' the driver needs in order to retain control in what would otherwise become stressful circumstances of non-linear vehicle behaviour and multiple requirements for control – typically vehicle orientation (body slip angle) and velocity (path control). Useful learning occurs on low grip environments that can be readily transferred across to high grip. In low grip environments, the extreme non-linearity of response of the vehicle can be explored at low speeds and with low stress levels, allowing the driver to piece together a model to be used within their own heads; it is then a matter of practise to transfer the lessons to a high grip environment. The same concepts can be used to explore the behaviour of a driver model within MSC.ADAMS.

Desired Yaw Rate

This section describes the methodology for the definition of desired yaw rate for the controller implemented on the vehicle model with nonlinear dynamics. A target under-steer characteristic is defined in terms of an analytical function relating the dynamic steering-wheel angle $\delta_{dyn} = \delta - \delta_{kin}$ (where δ is the actual steering-wheel angle, and δ_{kin} is the kinematic steering-wheel angle) to the lateral acceleration a_y. Therefore, Shibahata (1993) proposed a method based on the following three characteristic parameters: the under-steer gradient $Ku = \partial\delta_{dyn}/\partial a_y$; the threshold value a_y^*, which defines the upper limit of the linear part of the under-steer characteristic; and the maximum lateral acceleration achievable in trimmed conditions $a_{y,\,MAX}$. Thus

$$a_y = \frac{1}{Ku}\delta_{dyn}, \qquad if\ \delta_{dyn} < Kua_y^*$$

$$a_y = a_yMAX + \left(a_y^* - a_yMAX\right) \times e\,\frac{Kua_y^* - \delta_{dyn}}{\left(a_yMAX - a_y^*\right)Ku}, \qquad if\,\delta_{dyn} \geq Kua_y^*$$

Where $a_y, MAX = a_y, MAX(\mu,\, a_x)$, and $a_y^* = a_y^*(\mu,\, a_x)$. The terms K, a_y^*, and a_yMAX can be chosen according to the control design requirements. In particular, the same value of Ku at different values of the longitudinal acceleration have been considered, to achieve the compensation of the variation of the under-steer gradient in traction and braking conditions. Following Shibahata (1993), the steady-state value of the desired yaw rate is given by

$$\omega_d = \frac{a_y}{V} = VK$$

$$K = 1/R$$

All equations allow the generation of the desired yaw rate as a function of vehicle speed, steering-wheel angle, longitudinal acceleration, and friction coefficient at the tyre-road contact. At the starting point, finding a desired path for testing the vehicle model under dynamics manoeuvres, i.e. steady state cornering and double lane change, is important and it can be defined by using path curvature K. The analysis starts when the vehicle runs on a 33m diameter circle, and then a desired yaw rate can be calculated by using the expression above.

The path curvature for a circle should be a constant value, but it needs some transition curvatures with varied radius to link path curvature from the straight line to the constant radius circle. The approach can avoid abrupt steering inputs while the vehicle model traces the desired path. The desired path curvature can be converted to a SPLINE command as used in ADAMS, as shown in Figure 6-5. The X values are path lengths depending on vehicle speed, and Y values are path curvatures. A human driver model as motioned in Chapter 4 will apply a torque on the steering wheel to drive the vehicular model; the inputs from the driver model are corresponding to the path curvature (SPLINE) commends.

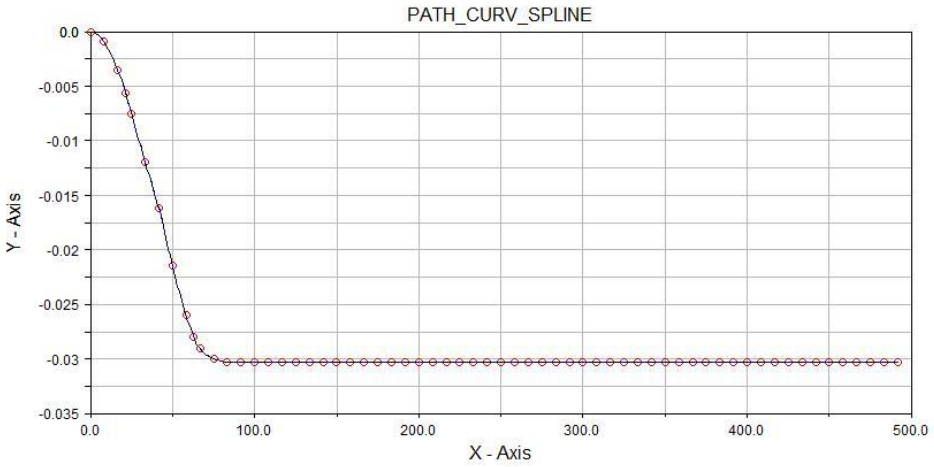

Figure 6-5 Path curvature spline in ADAMS for cornering

It is tempting to draw the lane change path as a series of connected arcs – the treatment of O'Hara, (2005) is typical - but this does not reflect the reality of a driver's inputs, which are observed to be somewhat fluid and continuous during a high effort lane change without the dwell periods a series of arcs would imply. An improvement might be to view the path as a "cosine ramp" of the form. L is the wheel base of the project vehicle. The length of the entrance section is rescaled and the path of "cosine ramp" lane change is created in Figure 6-7

$$Y = \frac{3.5}{2}\left(1 - \cos\left(\frac{X\pi}{24+L}\right)\right) \tag{6.3.1}$$

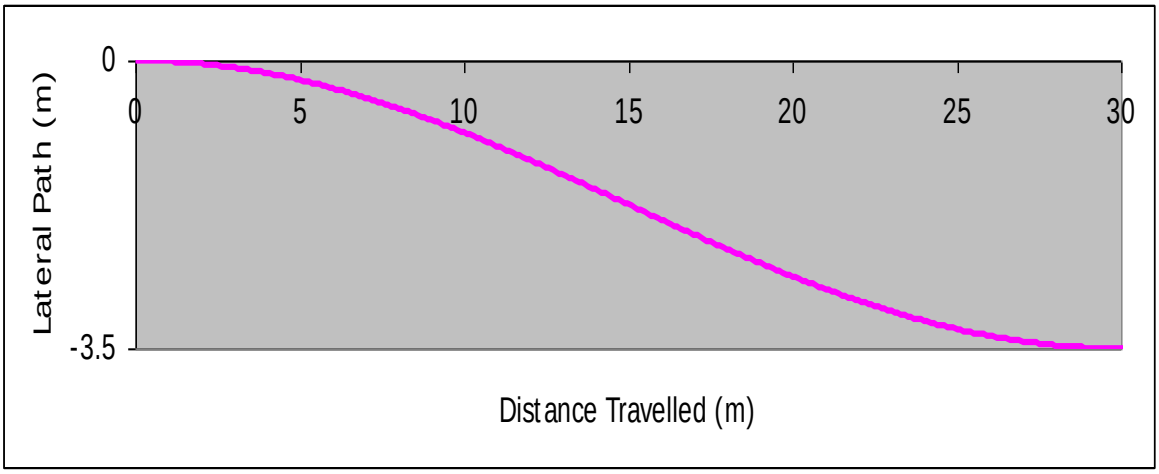

Figure 6-6 Cosine ramp lane change path visualisation

When considering the task in detail, it is noted that the mid-section is wider than the vehicle. When the position of the vehicle is fractionally away from the very edge of the entrance gate, it is necessary to tune the relative length of the turn-in and turn-out sections and to run out to the very widest part of the path available. Further slight modification to the exact form is made to make it continuously differentiable as shown in Figure 6-8. If this “optimized cosine” form is compared with the initial cosine form, a substantial reduction in centripetal acceleration is realised as shown in Figure 6-9.

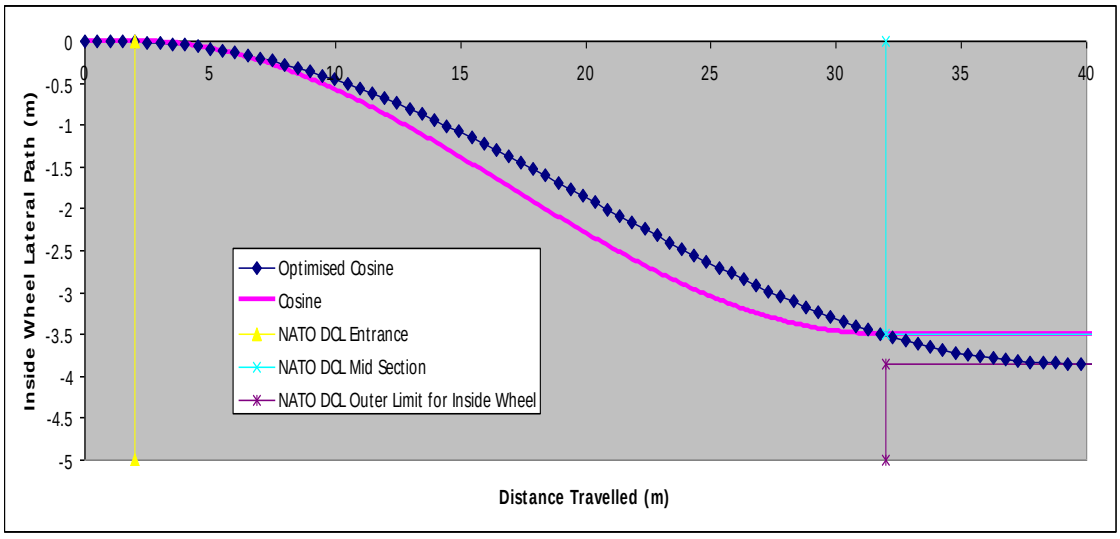

Figure 6-7 Optimized lane change path with the behaviours of real driver

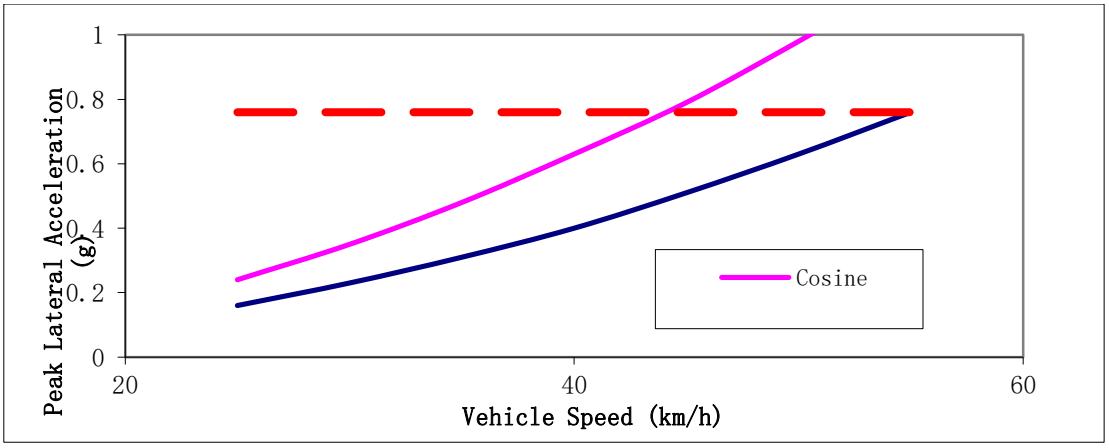

Figure 6-8 Comparison of the lateral acceleration for cosine and optimised lane change path

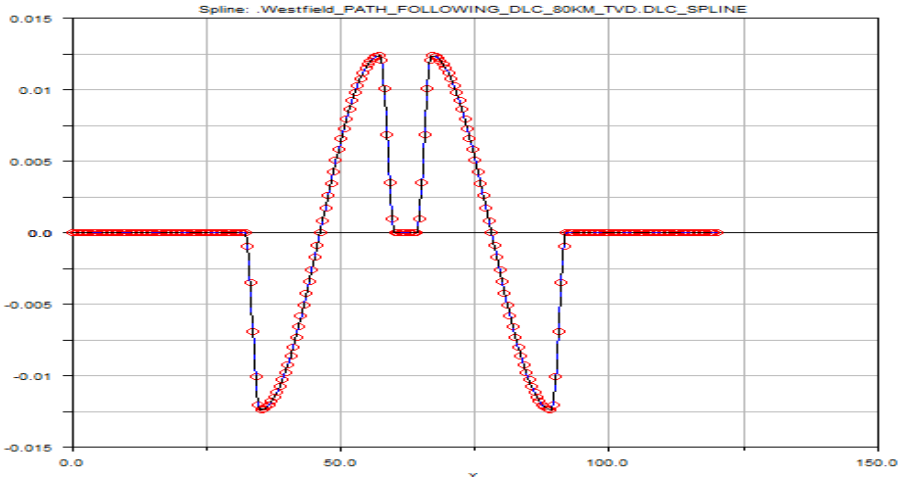

Figure 6-9 Path curvature of lane change

By using the same calculation as the cornering manoeuvre, Figure 6-10 shows that the path curvature for the double lane change is created and then it can be converted to a SPLINE command. Thus, the desired yaw rate and lateral acceleration can be found. A comparison can be made between a theoretical value and a base vehicle simulation at 30 km/h and shows that even at this speed the response is being limited by the dynamics of the vehicle; nevertheless there is broad agreement as shown in Figure 6-11.

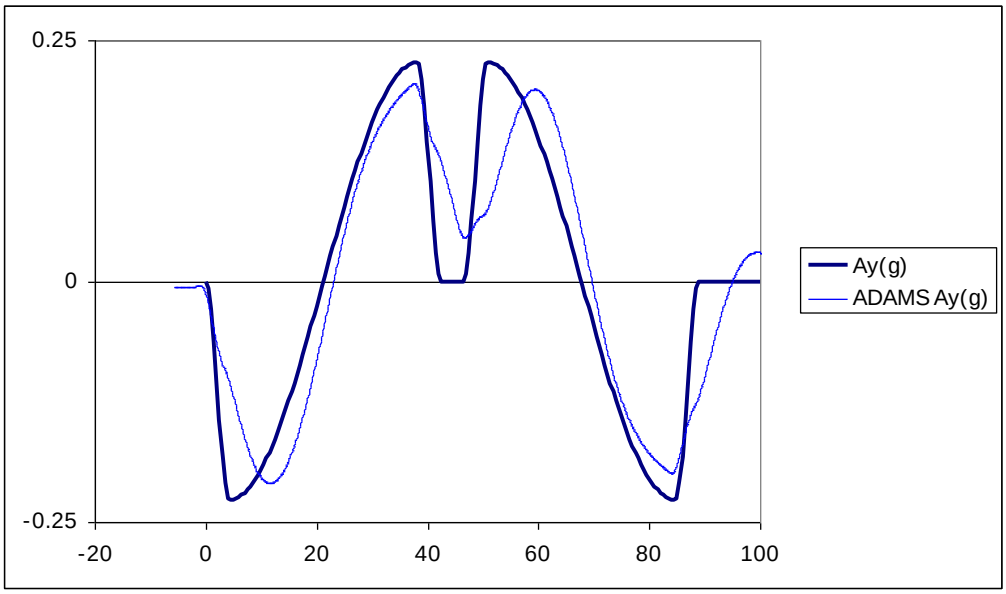

Figure 6-10 Comparison of desired and actual lateral acceleration

An actual double lane change protocol calls for an increase in vehicle speed until the driver is no longer able to complete the manoeuvre; the outcome from the test is the highest speed at which the driver can repeatedly complete the manoeuvre. For this simulation, the vehicle model runs from low speed 40 km/h to a high speed that is close to the physical limitation of the vehicle model. Repeated iterations are made to discover the optimal performance of the vehicle model that should be improved by Driveline Control Strategy. Nevertheless, the reported vehicle behaviour is to complete the manoeuvre at 110 km/h so that the lateral acceleration starts to exceed the control region of the TV system. The ODCS is no longer to fulfil the safety requirements, therefore the manoeuvre approaches an emergency stage requiring the vehicle to reduce the speed to control its motion and diminish the kinetic energy of the vehicle body by normal use of the braking or stability control system.

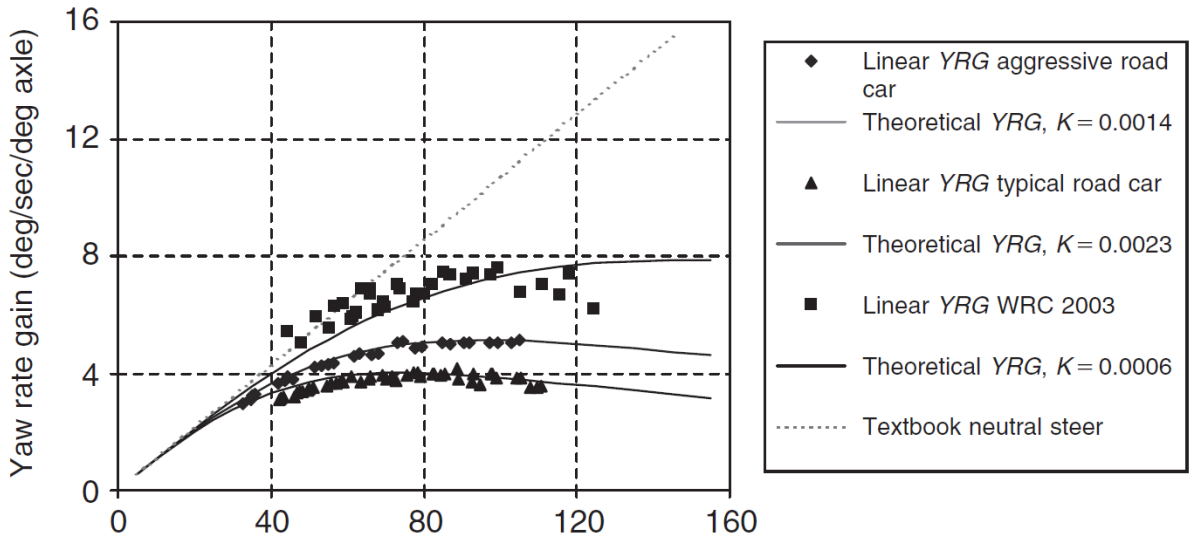

Figure 6-11 Yaw Rate Gain (YRG) for three different vehicles (Blundell and Harty, 2004)

Normally, the vehicles need to be designed to reduce the Yaw Rate Gain (YRG) at high speed to ensure the drivers still control the vehicle when faced with emergency evasive manoeuvres. For typical road vehicles, the characteristics of the vehicle are performed to have further modifications to reduce the yaw rate gain even when the tyres are not saturated. These modifications are very different between different demands as shown in Figure 6-12, in which all three vehicles are under-steer in their linear regions, but yet the racing vehicle tends to increase yaw rate gain at higher speed thus improving dynamic control performance for expert drivers because it is closer to neutral steer. Reviewing the YRG characteristics for the WRC 2003 car, some linear YRG points are very close, and are even over the neutral steer line when the vehicle speed is around 50km/h. Moreover, the linear YRG points are substantially decreased while the vehicle speed is over 100km/h.

Based on the YRG characteristics for racing vehicles, the TV control should dominate the YRG of the project vehicle model close to their theoretical YRG curve. Therefore, Figure 6-13 represents an operating region for the TV system in this research. The theoretical YRG curve for the project vehicle was calculated in the Chapter 4. Because of the characteristics being very close to the neutral steer when the speed is below 80km/h, the use of TV control should maintain the model in its own characteristics and prevent a bulk over-steer. The actual YRG may have a large

drop as shown while the vehicle speed is raised, thus The TV control is also required to dominate the actual YRG approaching the theoretical curve.

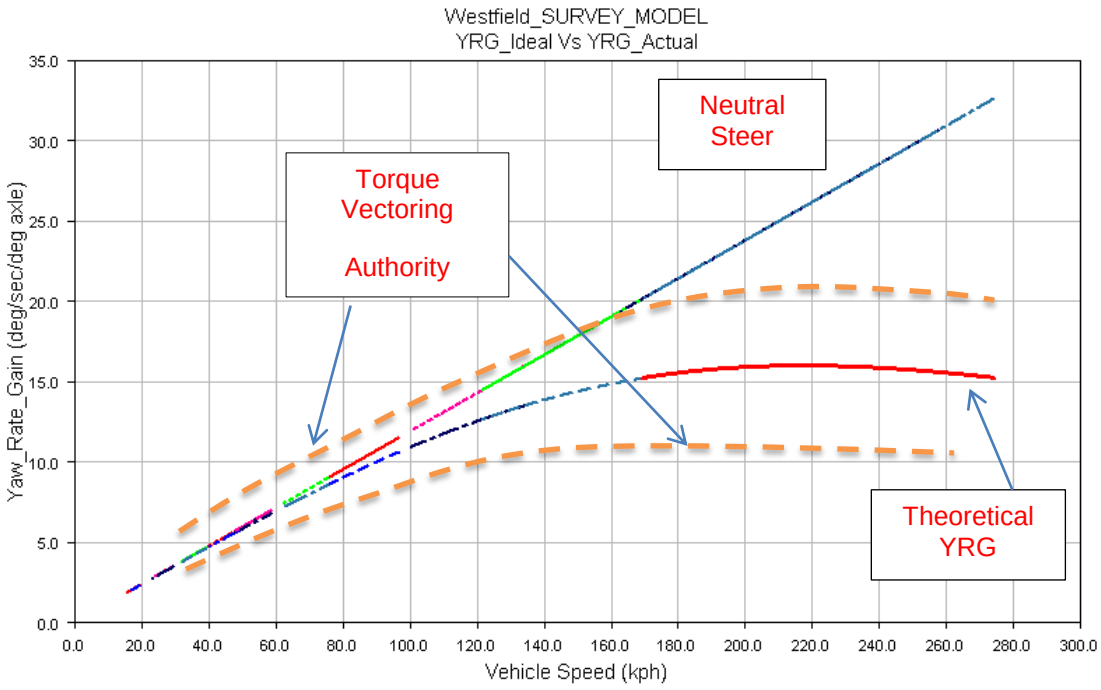

Figure 6-12 Explanation of torque vectoring authority envelope

In Figure 6-13, the YRG for neutral steer and the theoretical YRG of the project model can be calculated by using the equations below:

$$YRG_{neutral} = {}^{V}/_{L} \tag{6.3.4}$$

$$YRG_{theo} = {}^{\omega_g}/_{\delta} \tag{6.3.5}$$

V: Vehicle speed

L: Vehicle length

Note that the over-steer and ω_g: Geometric yaw rate ly known by a ratio of the geometric yaw rate and wheel steer angle as shown in the equation 6.3.5. If the ratio is more than 1, the vehicle is under-steer and if the ratio is less than 1, the vehicle is over-steer.

6.3.2 Secondary Control

The aim of secondary control design is to control the vehicle model tracking the desired dynamics, which consists of the aspects of vehicle speed control, yaw rate correction and control modes regulator. Rolling resistance and aerodynamic drag forces are applied on this vehicle model, thus the vehicle speed is lost and also the vehicle loses momentum during the resistant of the tyre cornering forces. Modelling a speed compensation controller is required to offset the vehicle speed and the inputs for the controller are dependent on the difference in the vehicle speed that is measured between the ground plane velocity and the speed of the vehicle model. Another controller for yaw rate correction is designed to minimise the difference between the desired and the actual yaw rate. The outputs from this controller have a substantial effect on the vectoring torques control. Finally, a regulator is added into the Secondary Control to switch the Optimal Driveline Control Strategy (ODCS) between the driving modes.

Speed Compensation (SC) Controller

In this simulation, a constant velocity of the vehicle needs to be maintained. Therefore, a simple method of applying torque to the driven wheels is explained in this section. The secondary control includes a Speed Compensation (SC) Controller as part of the traction system, which means the torques are impart to the road wheels and then produce tractive driving forces at the tyres. The ground plane velocity as a reference speed can be calculated by using equation 6.3.6.

$$V_g = \sqrt{V_x^2 + V_y^2} \tag{6.3.6}$$

Hence, the tractive driving torques from the SC controller depend on the maximum driving torques from the pair of electric motors, and the difference between the ground plane velocity V_g and longitudinal velocity V_x of the vehicle model as shown in equation 6.3.7

$$T_d = T_{max} * \left(V_g - |V_x|\right) \tag{6.3.7}$$

Based on ground reference frame, the direction of the velocity V_x is negative so using an absolute value for the velocity V_x is necessary to ensure the driving torques outputs in positive, which means the positive value gives the vehicle model a tractive torque and the negative value may cause the vehicle to slow down. Note that the maximum torque T_{max} as output from the electric motors may produce large instant tractive forces at the driven wheels when starting the simulation. It is necessary to modify the torque T_{max} to prevent the driving wheels slipping when the simulation starts at different initial speeds. Therefore, an optimal output from the SC controller will be taken into account in the third level of the ODCS.

Yaw Rate Error Correction (YREC)

The path curvatures for steady state cornering and lane change were detected in the first level of the ODCS and hence the Desired Yaw Rate ω_d is found from the Path Curvature K and forward velocity V_g using:

$$\omega_d = V_g * K \tag{6.3.8}$$

To apply the equation 6.3.8 to the simulation software, it needs to find out the path length when the vehicle model runs at various speeds. Calculating the path length is simply to integrate the ground plane velocity V_g as shown below.

$$L_p = \int_0^t f(V_g)dt$$

6.3.9)

The body slip angle β can be computed by using the equation 6.3.10 based on the velocities of V_y and V_g.

$$\beta = arcsin\left(\frac{V_y}{V_g}\right)$$

3.10)

Hence, the variables of lateral acceleration A_y and longitudinal acceleration A_x are created and calculated in the vehicle body axis system. The units are set up in m/s^2. As follows, the centripetal acceleration A^p is given from the components of acceleration A_x and A_y using

$$A_p = A_y \cos(\beta) + A_x \sin(\beta) \tag{6.3.11}$$

The front axle no-slip yaw rate ω_{fns} is found from the components of the centripetal acceleration A_p, the yaw acceleration α_z, the distance α, and the ground plane velocity V_g using

$$\omega_{fns} = \frac{A_p - \alpha\alpha_z}{V_g} \tag{6.3.12}$$

Eventually, the yaw rate error ω_{err} is then found from the desired yaw rate ω_d and the front axle no-slip yaw rate ω_{fns} using

$$\omega_{err} = \omega_d - \omega_{fns} \tag{6.3.13}$$

The yaw rate correction uses a close-loop control to monitor the vehicle body position and minimise the yaw rate error. In general, a controller, such as the PID controller, is required to be assembled into the close-loop control. It is broadly used in control theory; and the advantage of the PID controller is that it can produce continuous output, and it has no steps. It consists of three terms:

- The term of 'P' provides a proportional output to reduce the current error value and multiplying a gain value can K_p adjust the proportional response.
- The term of 'I' contributes to the response proportional to both the magnitude and duration of the error. In the PID controller, the integral gives the

accumulated compensation from the previous correction and counts the total of instantaneous error over time. Thus, the error can be minimized by multiplying a gain value K_i and that will be added to the controller output.

- The derivative is the 'D' item of the PID controller in which the derivative of the error is calculated by determining the slope of the error over time, and the derivative gain K_d can adjust the rate of change.

In the ideal parallel form, the controller theory section for Yaw Rate Error Correction (YREC) is shown below:

$$YRC = K_p * \omega_{err}(t) + K_i \int_0^t \omega_{err}(t)dt + K_d \frac{d}{dt}\omega_{err}(t) \tag{6.3.14}$$

Driving Modes Regulator

When simulating a vehicle model in manoeuvres, the use of several driving modes enables determining the differences in vehicle dynamics handling and driving performance. Therefore, the project vehicle is set up for three driving modes as known: free rolling, driving with a differential, and TV control. The free rolling mode is when the vehicle model is coasting through the manoeuvres without any propulsion forces and only frictional force acts between road surface and tyre. The second driving mode is to apply the use of an open differential to the model driveline to produce an even torque at the driving wheels. The developed TV control is the third driving mode in which the TV control should retain the function of the Open Differential and Limited-Slip Differential, and it also has the ability to modify the driving torque. Thus, a regulator has been designed to switch the SC controller and YREC controller on/off between the driving modes automatically. In addition, when the SC controller is off, the vehicle model does not have any propulsion forces at the driving wheels. With this status, as mentioned, it is difficult for the mechanical driveline to have the vectoring torque while retaining the position of the vehicle. Nevertheless, the regulator can still force the ODCS to implement its function to

control the motors while the vehicle is turning; thus the vehicle enables having the continuous vectoring torques at the driving wheels. To explain the use of the regulator clearly, Table 6-1 shows how it switches between the driving modes.

Table 6-1 The schematic of control modes

Control Modes	Driving Modes	Speed Control	Yaw Rate Error Correction
1	Coasting	*Deactivate*	*Deactivate*
2	Open Diff	*Activate*	*Deactivate*
3	Torque Vectoring	*Deactivate/Activate*	*Activate*

6.3.3 Advanced Torque Vectoring Control (ATVC)

In the previous section, the desired tractive driving forces from the speed compensation and the desired yaw rate are determined. The inputs from the secondary control level should be applied to the vehicle model through an Advanced Torque Vectoring Control (ATVC) level. The ATVC is designed for the last level of the ODCS and in order to modify the inputs from the previous control level. The aim of this level should satisfy the conditions below.

- ✓ Modifying the traction force for speed compensation
- ✓ Optimizing the vectoring torque for yaw rate correction
- ✓ Inspecting the driving efficiency

Modifying the traction force for speed compensation

In general, a speed compensation controller is derived to minimize the difference between the ground plane speed and actual speed. The difference in the speed can be modified by multiplying a constant gain T_{max}. Normally the gain value is simply set up for the maximum driving torque from the electronic motors; nevertheless, this

simplicity of the adjustment can cause some issues, such as longitudinal wheel slip, when the vehicle runs at different speeds.

As a complex method, optimization can help and improve the overall design of the product. If the process has a good design in early stage, the design cycle can be shorted. In general, an optimization problem is described as a problem to minimize or maximize an objective function over a selection of design variables, while satisfying various constraints on the design and state variables of the system. The objective function is normally represented by a numerical form of the quality, or stability of the model. The aim for modifying the traction force for speed compensation decides that the optimization chooses to find the maximum torque of the traction as shown in Equation 6.3.15. The optimal value of this formula corresponds to the best design possible that can give the optimal driving torques for the speed compensation. Design variables can be thought of as the Ground Plane Velocity for this design problem. The Ground Plane Velocity can be altered to define the design results. In this study, the changes in the vehicle speed should result in changes to the driving torque.

$$J_d = \left(\min_{T \in (0,750)} f((T_{opt}), V_g) \right) * (V_g - |V_x|) \tag{6.3.15}$$

T_{opt}: Optimal torque for speed compensation

V_g: Ground plane velocity

The difference in the vehicle speed can be minimized by multiplying an optimum gain value T_{opt} as shown in Equation 6.3.16. Constraints are boundaries that directly or indirectly eliminate unacceptable issues, thus a constraint for wheel slip is created to keep the wheel slip ratio at driving wheels below a limit valueS_{limit}. The constraint only is applied when the actual wheel slip ratio S_w is over the limitation; it also can be explained by using the formula as below:

$$J_d = \begin{Bmatrix} \min\limits_{T\in(0,750)} f((T_{opt}), V_g) & if \;\; S_w \;\leq S_{limit} \\ 0 & if \;\; S_w \;> S_{limit} \end{Bmatrix} * (V_g - |V_x|) \quad (6.3.16)$$

However, the ATVC is able to produce the optimized driving torque J_d under the constraint to compensate the speed. In this calculation, the design variable is set up for the Ground Plane Velocity V_g, thus the amplitude of the optimized torque J_d depends on two variables: the Ground Plane Velocity and the speed compensation.

Optimizing the vectoring torque for yaw rate error correction

A considerable change in yaw rate with vehicle speed can be perceived by the driver as inconsistent vehicle behaviour during in normal driving conditions. To make the vehicle behave more predictable, the TV control can be used (at least partially) to compensate the variation of the yaw rate. However, the outputs from secondary control are not precise enough and, thus, cannot provide a-priori definable amount of vectoring torque.

The inputs from the yaw rate correction at the secondary control level should be applied to the project model through the ATVC. As is known, the terms of the PID controller can give a precise and rapid response in the yaw rate correction, but it is still necessary to tune the gain values for the proportional, integral and derivative terms. In general, the gain values are modified manually and are closely related to the amplitude of the vectoring torque. Due to the variation in the vehicle speed, the gain values over all the simulations are required in order to modify the amplitude automatically. This means that the optimal vectoring torque inputs are able to adjust the position of the vehicle body to reach the desired dynamic behaviours in any conditions.

Performance Index

In this paper the parallel PID controller is used as below;

$$K_{PID}(s;p) = k_P + \frac{k_i}{s} + k_D s = \omega_{err}\left(1 + \frac{1}{\tau I s} + \tau D s\right); \quad p = (k_p \;\; k_i \;\; k_d)^T \quad (6.3.17)$$

where, ki and kd is the proportional, integral, and derivative gain, respectively. The parallel PID controller can have complex zeros, which we have observed can result in several peaks for the magnitude of sensitivity function in the frequency domain.

In this paper, one of the most popular ways of quantifying controller performance is used here is the integrated absolute error (IAE)

$$IAE(p) = \int_0^{t_f} |\omega_{err}(t;p)|dt \tag{6.3.18}$$

when subjecting the system to a disturbance. Both of input and output disturbances are taken into account and chosen the weighted cost function,

$$J(p) = 0.5\big(\varphi_{out} IAE_{out}(p) + \varphi_{in} IAE_{in}(p)\big) \tag{6.3.19}$$

Where both terms are weighted equally with 0.5 to get a good balance. The φ_{out} and φ_{in} are scaling factors from IAE-optimal PID controllers for a step load change on the input and output, respectively.

Many methods have proven efficient and effective in special fields of application. Such as Simplex method (Dantzing, 1963) in linear programming problems, Conjugate gradient method (Reeves, 1964) and Quasi-Newton method (Broyden, 1967) in Non-linear Programming problems with no constraints, and Convex simplex method (Zangwill, 1967) and Reduced gradient methods (Wolfe, 1976) in Non-linear programming with linear constraints, etc. Researchers devote their effort to extend these methods to wider application. The Generalized Reduced Gradient method has been developed and proven to be one of the efficient and effective methods for the Non-linear Programming problem with Non-linear constraints.

Based on the description of the optimization problem using the mathematical language, the objective function (i.e. the gain values) is minimized over the selection of the design variables. Various algorithms are available for finding a solution to an optimization problem, thus the Generalized Reduced Gradient (GRG) algorithm that is provided with Adams/View has been used in this study. This algorithm requires a range of the limitation for the design variables.

The basic concept of GRG method entails linearizing the Non-linear objective and constraint functions at a local solution with Taylor expansion equation. Then, the concept of reduced gradient method is employed which divides the variable set into two subsets of basic variables and the concept of implicit variable elimination to express the basic variable by the non-basic variable. Finally, the constraints are eliminated and the variable space is deduced to only non-basic variables. The proven efficient method for non-constraints nonlinear programming problems is involved to solve the approximated problem and then the next optimal solution for the approximated problem should be found. The process repeats again until it fulfils the optimal conditions.

$$\textit{Minimize } J(p) = 0.5\left(\varphi_{out} IAE_{out}(p) + \varphi_{in} IAE_{in}(p)\right)$$

$$\textit{Subject} \quad h_i(p) = 0 \quad i = 1, \dots, m$$

$$pl_k \leq \ p_k \leq pu_k \ \ k = 1, \dots, n$$

Function $J(p)$ and $h_i(p) = 0 \quad i = 1, \dots, m$ are continuous and differentiable in the domain region $\{pl_k \leq \ p_k \leq pu_k \ \ k = 1, \dots, n\}$. First of all, the linearizing process at a local feasible solution $p_1$for the objective and constraint functions is performed as follows.

$$\tilde{f}(p, p_1) = f(p_1) + \nabla f(p)(p - p_1) \tag{6.3.20}$$

Since p_1 is a feasible solution for the original problem, it must be a feasible solution for the approximate problem, implying that

$$\widetilde{h_i}(p, p_1) = h_i(p_1) + \nabla h_i(p_1)(p - p_1) = 0 \quad i = 1, \dots, m \quad \text{and}$$

$$\nabla h_i(p_1)(p - p_1) = 0 \quad i = 1, \dots, m \tag{6.3.21}$$

If p_1 is an optimal solution, the gradient of objective function must be zero, implying that,

$$\frac{\partial \tilde{f}}{\partial p} = \frac{\partial \tilde{f} \partial p}{\partial p \partial p_1} + \frac{\partial \tilde{f}}{\partial p_1} = 0 \tag{6.3.22}$$

This equation is normally referred to as the reduced gradient. If the reduced gradient at the point p_1 equal to a zero vector then it also satisfies the Lagrange stable point conditions (Wild, 1971)

The next step is using equation (6.3.22) to calculate the gradient for the basic variable. Consider the boundary condition for the variable and take an adequate modification as follows

$$\bar{d} = \begin{cases} -\nabla\tilde{f} & if\ \nabla\tilde{f} > 0\ and\ \bar{p} - \bar{pl} > \varepsilon \\ -\nabla\tilde{f} & if\ \nabla\tilde{f} < 0\ and\ \bar{p}u - \bar{p} > \varepsilon \\ 0 & Otherwise \end{cases} \quad (6.3.23)$$

Checking the optimal condition, if $\left|\bar{d}\right| < \varepsilon$ then stop, otherwise, modify $\bar{d}$ to construct the searching direction d. Checking the feasibility in which if at least one constraint violates the feasibility condition, use the Newton method to pull the solution back to the feasible region and then change the basis.

Inspecting the driving efficiency

The inspection of the driving efficiency should be taken into account in the ATVC. In this stage, some constraints at the driving wheels should be under consideration. For example, checking the maximum driving force during the simulation is not exceeding the capacity of electric motors; also monitoring the driving force is not over the maximum friction circle of the tyre at the varied vertical loads. When the speed compensation control and the torque vectoring control operate at the same time, the total driving torque is accumulating to approach the maximum limitation. Thus, the function of the inspection is not only required to monitor the amount of the driving torque, but also to check the torque at the rear wheels individually, because the torque vectoring control may apply the different torques at each wheel.

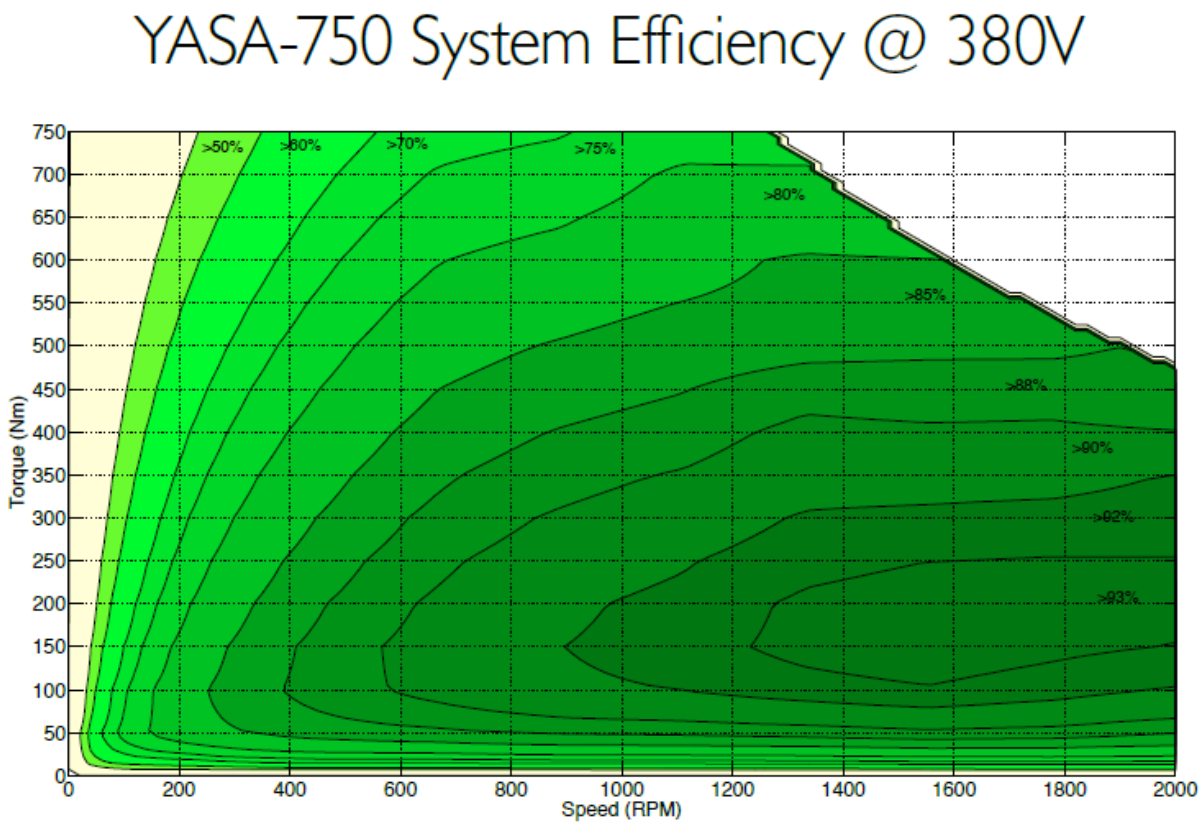

Figure 6-13 Motor efficiency map

The limitation of the friction circle can be defined at each driving wheel based on the current load and friction coefficient, which also represents the boundary of the resultant horizontal force available at that wheel, hence the maximum friction torque $T_{max.f}$ can be found as below:

$$\left|\begin{matrix}T_{dl}\\T_{dr}\end{matrix}\right| \leq r * \mu * F_h = T_{max.f} \tag{6.3.24}$$

Furthermore, Figure 6-14 is a motor efficiency map that shows the characteristics of the given electric motor - the torque outputs versus the motor revolution speed. Hence, during the simulation, the maximum motor torque $T_{max.m}$ outputs correspond to the revolution speed, which is restricted, based on the motor efficiency map. Finally, the limitations can be described as below:

$$\left|\begin{matrix}T_{dl}\\T_{dr}\end{matrix}\right| \leq T_{max.m} \quad (6.3.25)$$

where, T_{dl} and T_{dr} are required driving torques at the left and right driving wheels in which the torques are restricted by the limitations of the wheel friction circle and the capacity of the electric motors.

6.4 Simulation results

In order to detect how successfully the ODCS can improve the vehicle dynamic performance, the project model will be taken into two typical computer-based simulations - steady state cornering and double lane change manoeuvres. The project model with three driving modes has been modelled in the previous chapters. Results are now generated to investigate the performance of the ODCS in the project vehicle. The results are also compared against the project vehicle with the two conventional driving modes.

The first driving mode is that the model runs only at its initial speed, which means no driving torque is applied to the wheels, so it is called ‘Coasting’. It represents the original driveability of the project vehicle based on its own characteristics of the settings. The second driving mode represents an open or limited-slip differential that is commonly used in rear drive vehicles. Finally, the third mode is the project model with the Optimal Driveline Control Strategy (ODCS).

6.4.1 Steady state cornering

The early work of vehicle dynamics experts, such as Olley, Milliken and Segel, developed the classical treatment of the behaviour of a vehicle and they have documented in several textbooks dealing with the subject. As following, the classical treatment will be summarized by a consideration based on the steady state of the project vehicle model.

However, the treatment of the behaviour of the project vehicle is based on steady state cornering simulation. Steady state is the condition in which, if the hand wheel remains stationary, all the vehicle states – speed, yaw rate, path curvature and so on

– remain constant. In this simulation, a traditional evaluation method is used that involves running the vehicle model through the defined circle at a range of constant speeds. The variation of the vehicle speed will cause the increments in lateral acceleration. This approach is easily performed in a practice and so it will be used for the basis of the following discussion as shown in Figure 6-15

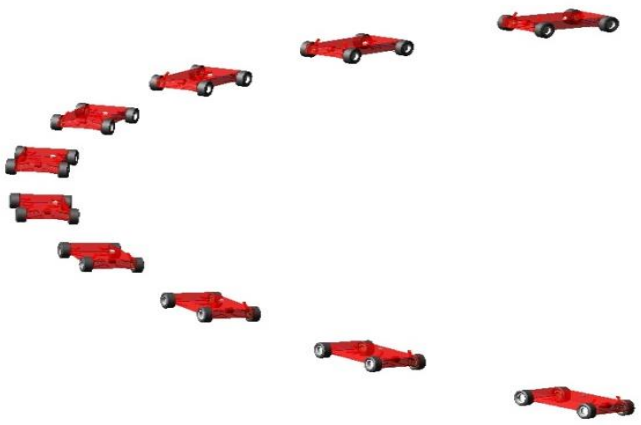

Figure 6-14 Vehicle model at steady state cornering

The minimum radius available in normal driving is the turning circle (Blundell and Harty, 2004). The coefficient of friction between tyres and road determine the turning circle and better starting point for this treatment is at low speed. Thus, the speed compensation controller can be examined as shown in Figure 6-16, where it can be seen a constant speed is produced during the cornering.

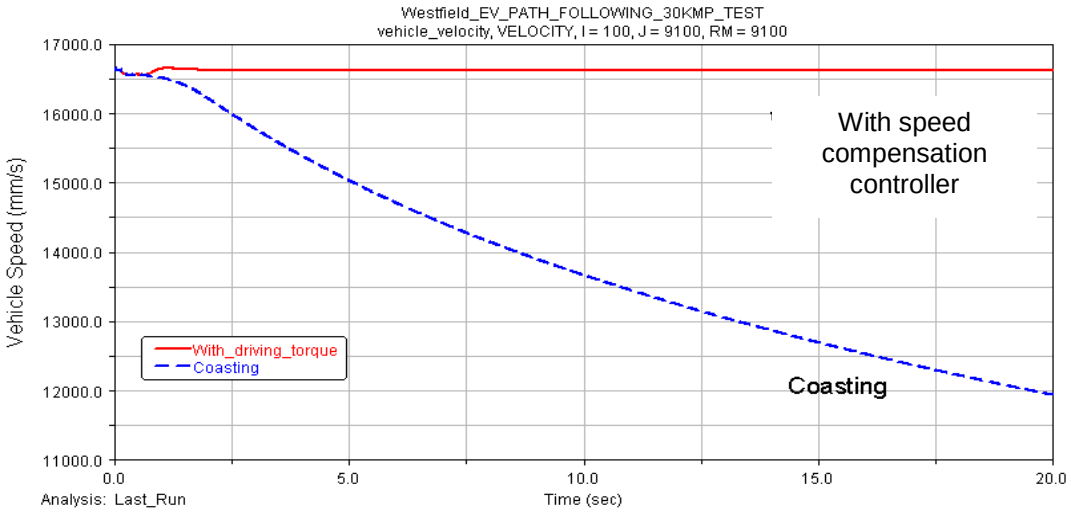

Figure 6-15 Speed compensation with driving torque

There are three trajectories represented in Figure 6-17, of which the outer line is the trajectory of the model in the coasting, and the middle trajectory is the model that runs with the open differential. The third line is the trajectory of the model with the ODCS that produces a function of limited-slip differential in which is closest to the desired path.

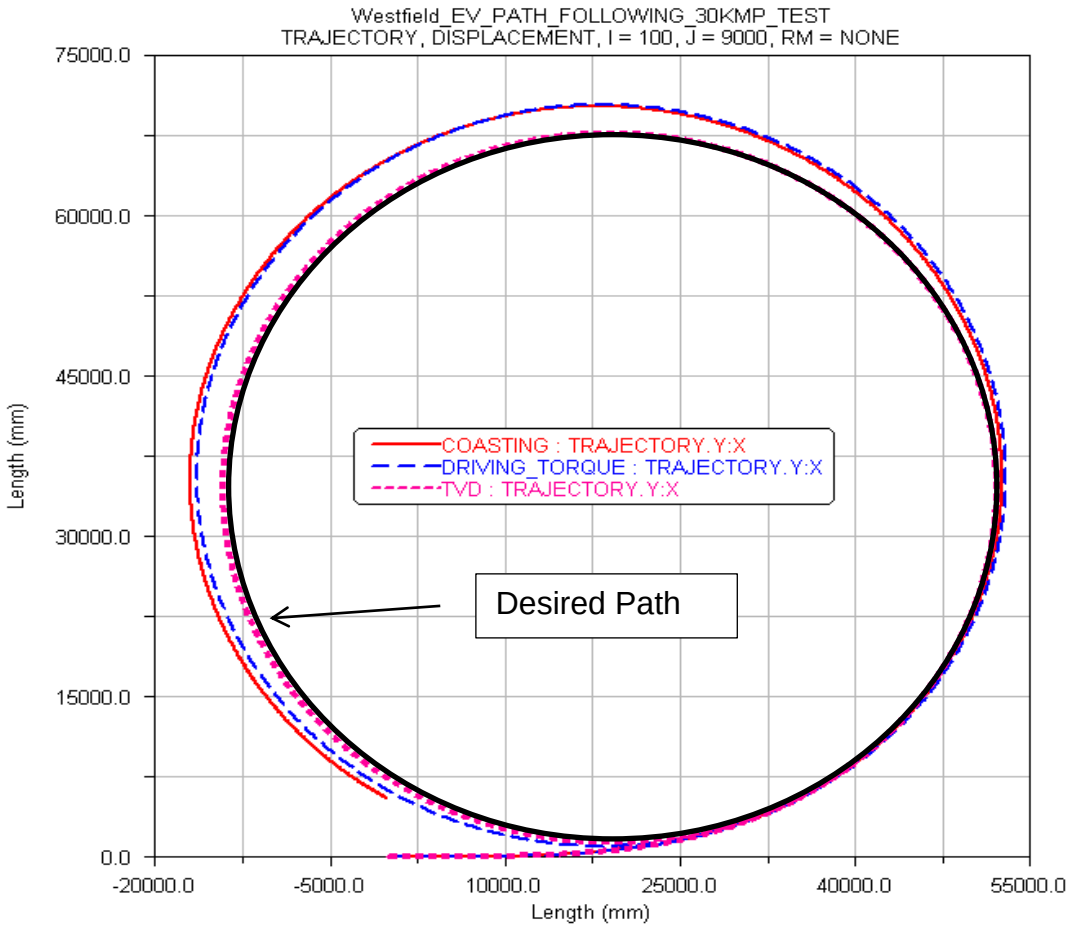

Figure 6-16 Trajectory of vehicle at coasting, with driving torque and TV

The trajectory of the model in the coasting indicated that because there are no the torques that were applied to the wheels, thus the model lost speed and exhibited more understeer behaviours. There is a similar scenario, which has appeared on the model with the open differential. When the identical torque was applied to the driving wheels, it could retain the speed but there was no significant improvement on the cornering performance, only a constant speed being given. Because the ODCS is required to have the capacities of the open and limited-slip differential, the scenario of the third trajectory is more like the model running with the limited-slip differential.

The ODCS can transfer torque along the rear axle in which the difference in the driving torque between the left and right wheels produces more yaw moment to make the model turn more easily, to have less under-steer behaviour, and to run with the exact desired trajectory.

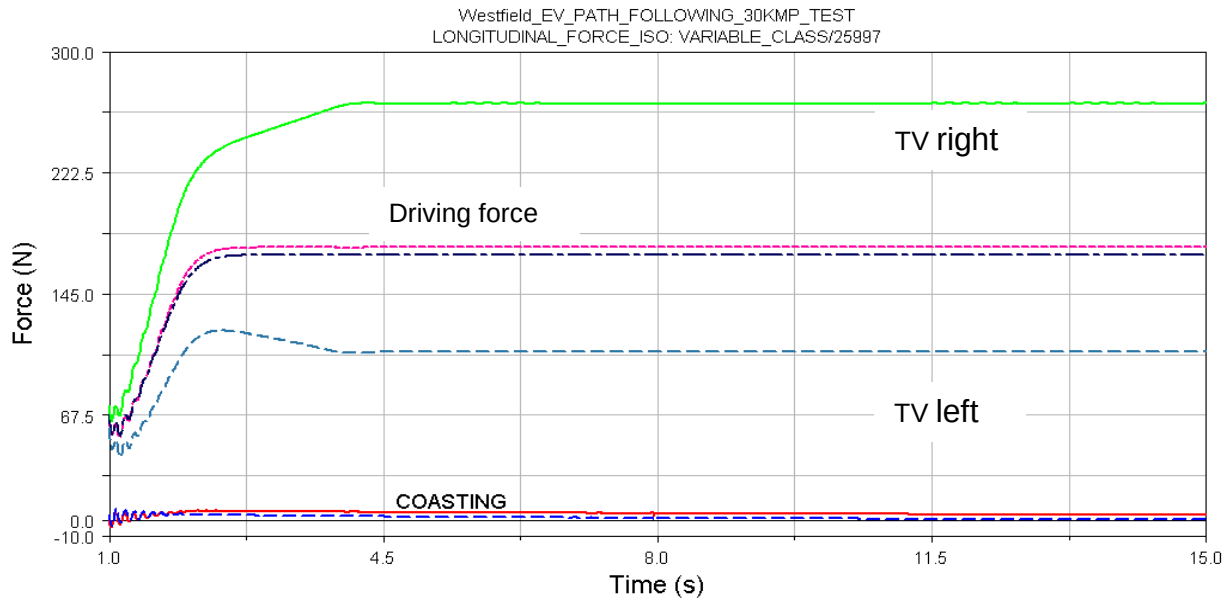

Figure 6-17 Longitudinal driving forces for rear driving wheels

The measurements of the longitudinal driving force at the rear wheels are clearly shown in Figure 6-18. The model in the coasting has none of the driving force, and the open differential produces the identical driving force that is slightly different due to the various vertical loads at the tyre. However, the ODCS can provide the required driving force at each wheel, and the force is directly controlled by the PID controller and adjusted by the ATVC. Also, it can be seen that the terms of the PID controller produce the outputs value to reach the target proportionally around two seconds; and then it makes some adjustment of the driving force outputs. The adjustment is due to the desired trajectory needing some transition curvatures with varied radius to link the path curvature from the straight line to the constant radius circle. After 4 seconds, the model has the constant driving force for turning the circle with the constant radius.

The effects on the yaw rate correction are presented in Figure 6-19. There are four lines for describing the yaw rates of the different driving modes. The first top line is the desired yaw rate, and the second line just below the desired yaw rate is the yaw rate of the model with ODCS. The third line from the top is the model with the open differential, and the bottom line is the model in the coasting condition. Obviously, the model with the ODCS has the best result in the cornering manoeuvre. In the ODCS, the PID controller for the yaw rate correction can reduce the error between the desired and the actual yaw rate, and then the integral term can accelerate the movement of the actual yaw rate towards the desired yaw rate and eliminate the residual steady-state error that occurs from the previous proportional term. Finally, the derivative response improves the settling time and stability of the control. It is worth mentioning that a high proportional gain results in a large change of the output, i.e. if the proportional gain is too high, the vehicle can become unstable. In contrast, a small proportional gain produces a small output response to a large input error, if the value is too low, the effects on control may not enable the enhancement of the dynamics performance. Thus, the function of the ATVC level can solve those issues when the PID controller is activated.

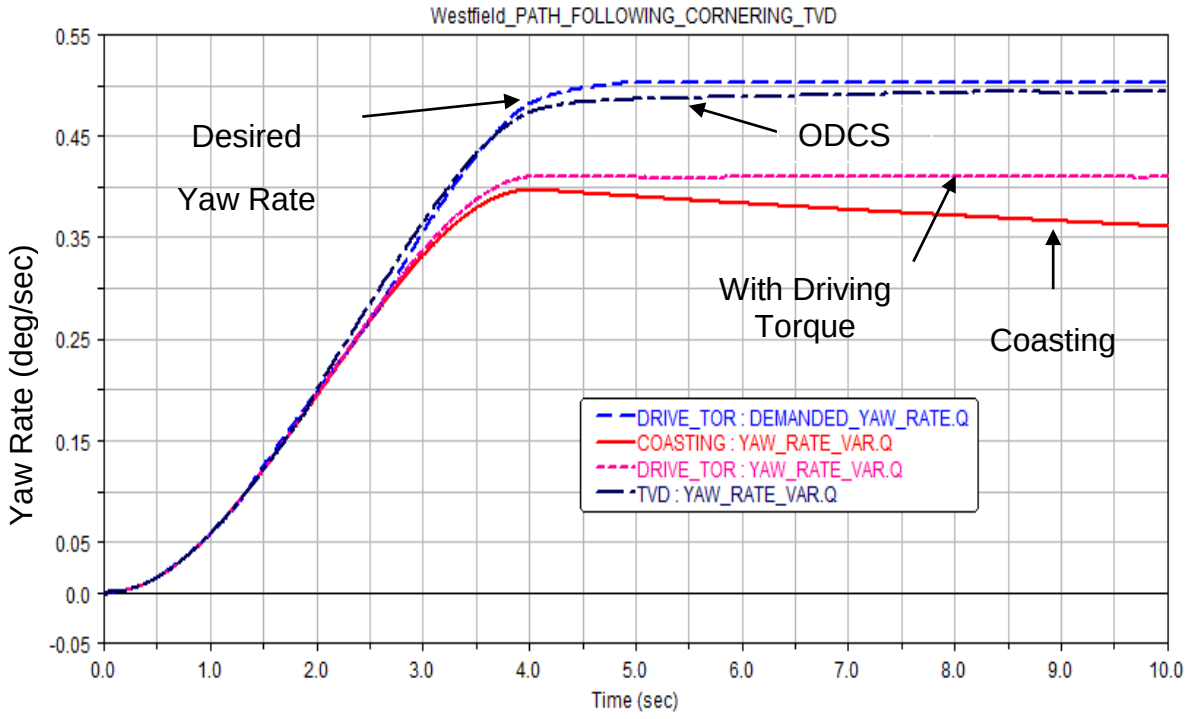

Figure 6-18 Comparison of Yaw rate correction

6.4.2 Double lane change

The double lane change consists of a defined zone in which the vehicle can take any path and it reflects a real world avoidance manoeuvre within a finite width road. The vehicle must displace laterally by around 3.5m minimum and then return to its original path. The length and width of the manoeuvring zone are related to the vehicle's proportions, so that the dimensions of the project vehicle with 2.69m in length and 1.54m in width are used to define a new section for the simulation.

With real vehicles, the performance of the given vehicle through the lane change can be substantially modified with driver skill levels and so when comparing vehicles it is preferable to use a panel of drivers or at least a consistent driver. In this analysis, the open-loop driver model is consistent and repeatable as it applies a steering torque to steer the vehicle model following the desired path; although there is no guarantee it accurately reflects the performance of real drivers. When real drivers complete the manoeuvre, they experiment noticeably with the exact trajectory over several attempts. This driver model is unable to learn from its previous experiences but some modification of the intended trajectory is worth mentioning as shown in the previous section.

The actual protocol of double lane change calls for an increase in vehicle speed until the driver is no longer able to complete the manoeuvre; the outcome from the test being the highest speed at which the driver can repeatedly complete the manoeuvre. For this exercise, the model starts to run at 40km/h and the speed continually accumulates to a higher speed of 110km/h at which point the ODCS is no longer able to improve the dynamics behaviour. In general, when an under-steer vehicle is taken to frictional limits where it is no longer possible to increase lateral acceleration, the vehicle will follow a path with a radius larger than intended. So that the ODCS can produce more turning or yaw moment on the vehicle's body, more driving torque should be applied to the outer wheel and less torque to the inner wheel. The explanation is shown in Figure 6-20.

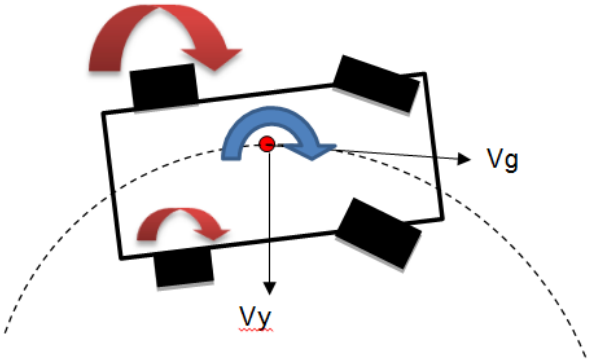

Figure 6-19 Explanation of torque vectoring control at 40km/h

The project model is driven up to the manoeuvre start and the ‘throttle’ released; the overrun condition is typically the most difficult in terms of stability. Although the model loses speed as it enters the second of the two manoeuvres, it is typically unsettled dynamically and so the second transition is often the more problematic of the two. The aim of the first run is to test what the ‘original’ dynamics behaviour of the model in the coasting condition is; it is also to check how the ODCS can improve the driveability of the model in the ‘throttle off’ condition. In Figure 6-21, the results in the yaw rate are compared, showing a large error between the yaw rate of the model in the coasting condition and desired yaw rate; nevertheless, the ODCS is able to minimize the error.

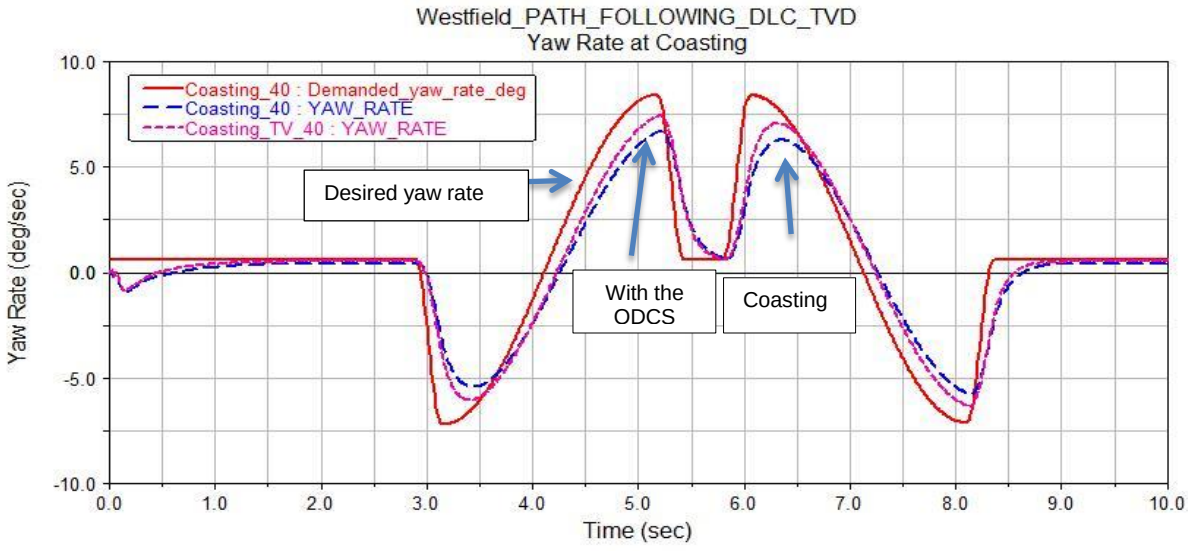

Figure 6-20 Comparisons of Yaw rate without the speed controller

In the second run, the speed controller is switched on to give the model traction force. Similar results can be found in Figure 6-22 in which the ODCS can still make the improvement in the yaw rate error correction.

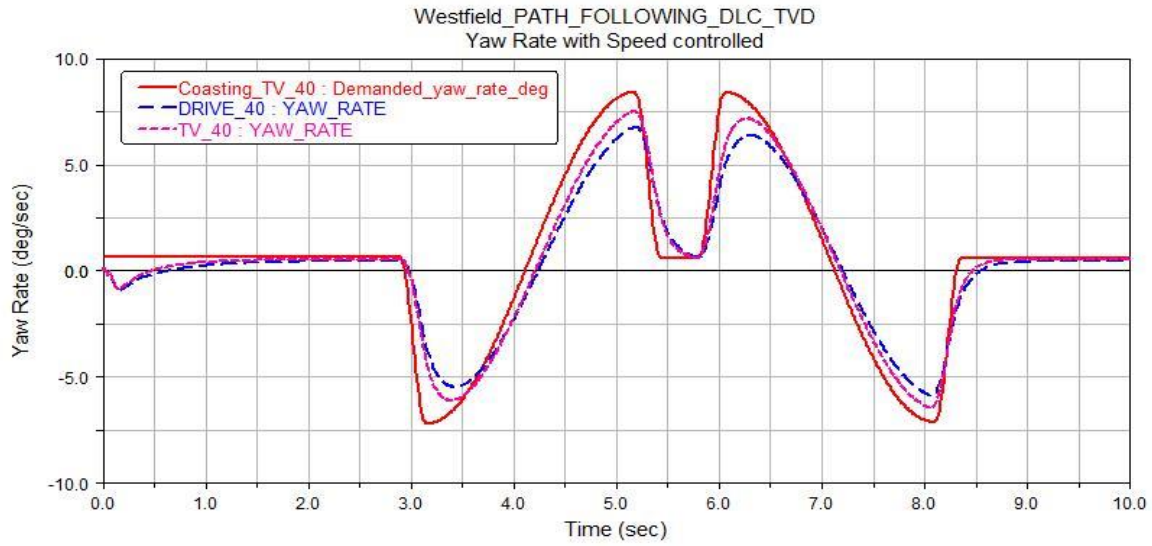

Figure 6-21 Yaw rate with speed controlled

In terms of stability, reducing the body slip angle is important because it effectively produces the width of the vehicle, and because it stores energy in the “pendulous” yaw mode of vibration possessed by the running vehicle. For ordinary drivers the storage of energy in this mode is problematic to understand and control. Figure 6-23 represents a comparison of the body slip angle for the model with the different driving mode. In the coasting mode, the vehicle body exhibits the largest body slip angle compared to the other two modes, and the body slip angle can be reduced somewhat when the model runs with the driving torque. It is clear to see that the body slip angle diminishes as the model runs with the ODCS; furthermore, the clear improvement in the driveability can be seen throughout the trace.

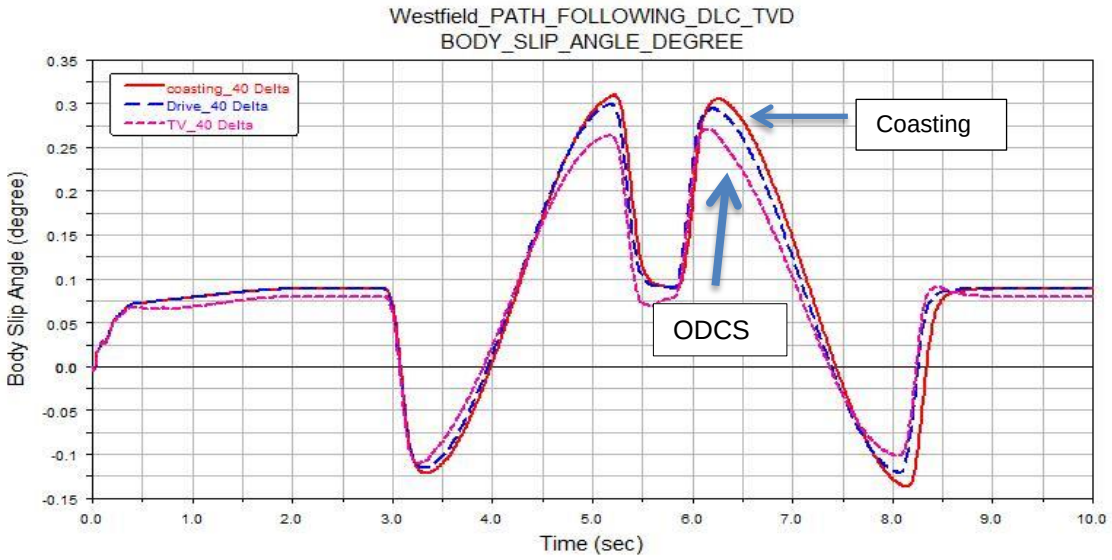

Figure 6-22 Body slip angle for the different driving mode

At the low speed, the use of the ODCS is more like the function of a limited-slip differential by which means the torque can only be transferred from the fast wheel to the slower one. When the simulation continues with an increase in the vehicle speed to 60 km/h, it should focus attention on the yaw moment of the vehicle body. Less yaw moment is needed, otherwise the vehicle will become over-steer, by which means it becomes dynamically unstable with a tendency to spin out. In this case, the ODCS is able to produce more torque on the inner wheel and less torque on the outer wheel, and thus the yaw moment can be reduced. The explanation is shown in Figure 6-24.

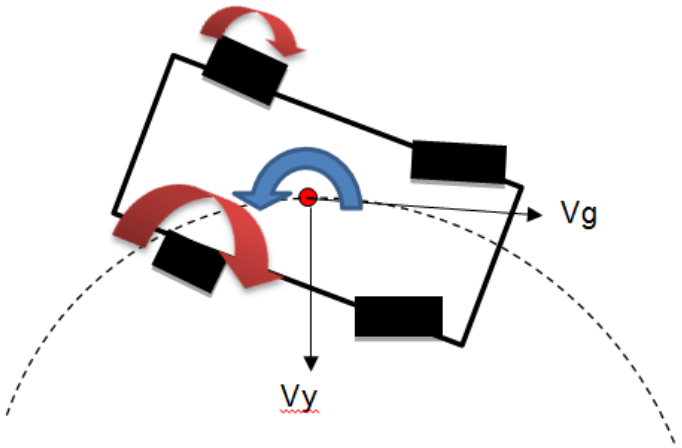

Figure 6-23 Explanation of torque vectoring control at 60km/h

Figure 6-25 represents the comparison of the yaw rate as the model runs with the speed controlled. The yaw rate of the model with the identical torque overruns at the first turn-in and exit oscillation section, and the model using the ODCS has some improvements on those sections. There are similar results which can be found in Figure 6-26 when the model runs at the 'throttle' released condition. Moreover, reduction in the body slip angle is clear evidence to prove that the ODCS enables the enhancement of the driveability of the model, as shown in Figure 6-27.

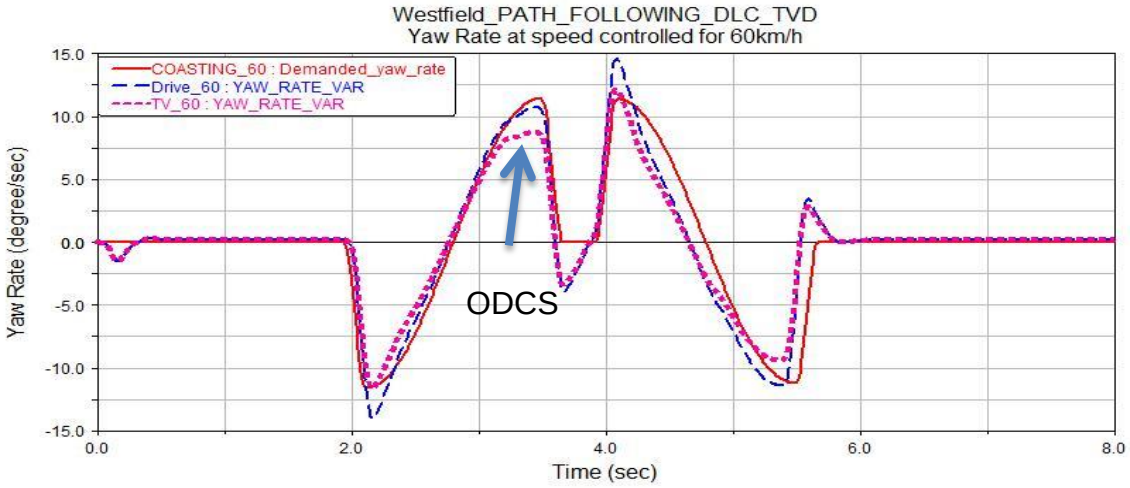

Figure 6-24 Variations of yaw rate with the speed controlled at 60 km/h

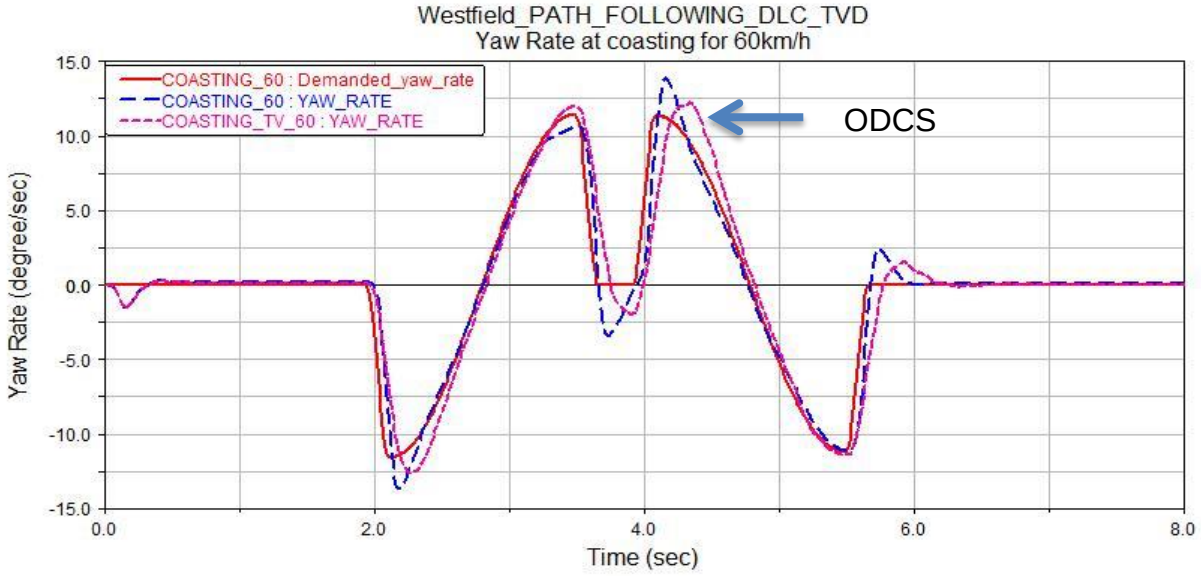

Figure 6-25 Yaw rate variations at 60 km/h

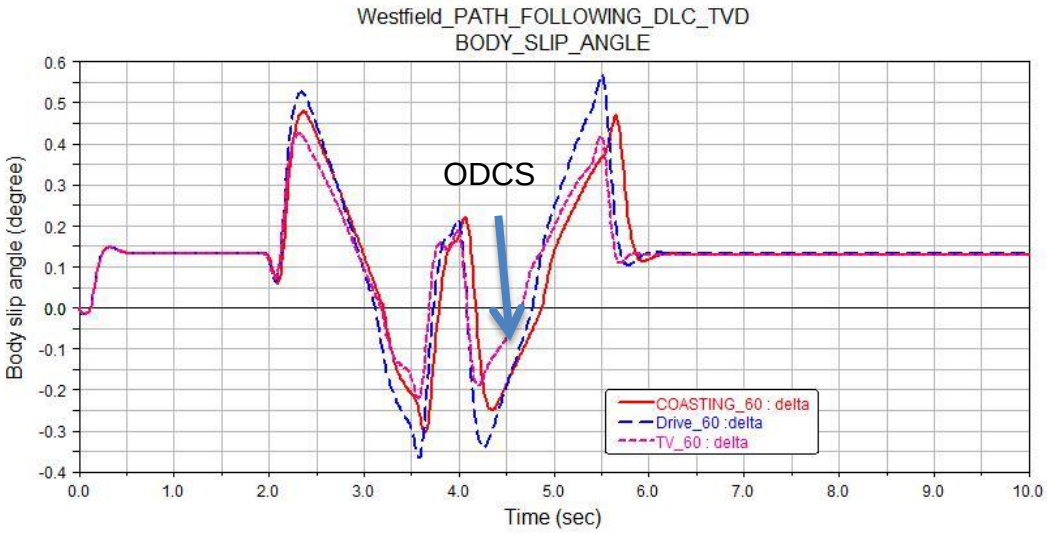

Figure 6-26 Variations of body slip angle at 60 km/h

The simulation is continued and the model is driven up to 100km/h and lateral acceleration is about 0.65g. Figure 6-28 to 6-30 clearly show that there are some improvements that can still be seen in the yaw rate and the body slip angle when using the ODCS, but there are no substantial effects on the driveability. Due to the high lateral acceleration, the model tends to be in accident-avoidance stage. Thus, it needs to use the brakes to reduce the kinetic energy of the vehicle and to minimize the wheel load variation for maximum grip and control. However, the limitation in the lateral acceleration is the boundary for the operating region of the ODCS at high speed.

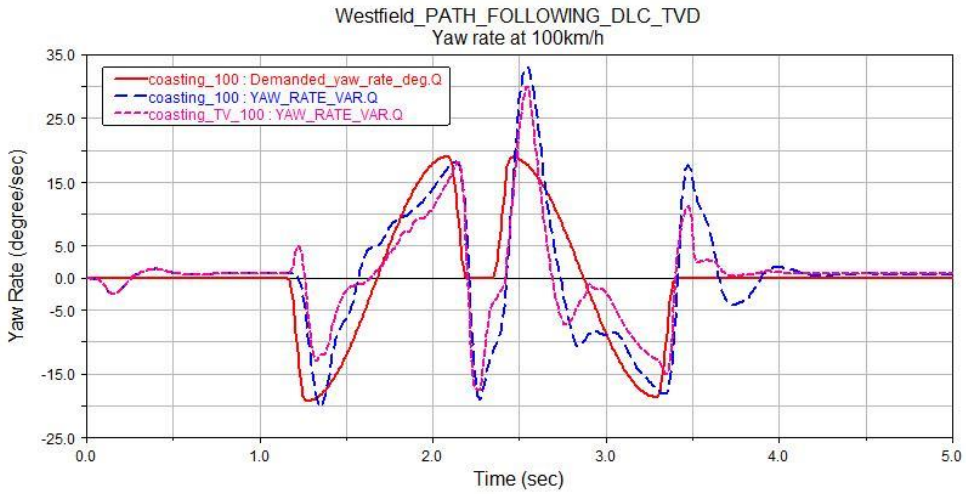

Figure 6-27 Yaw rate variation at 100km/h

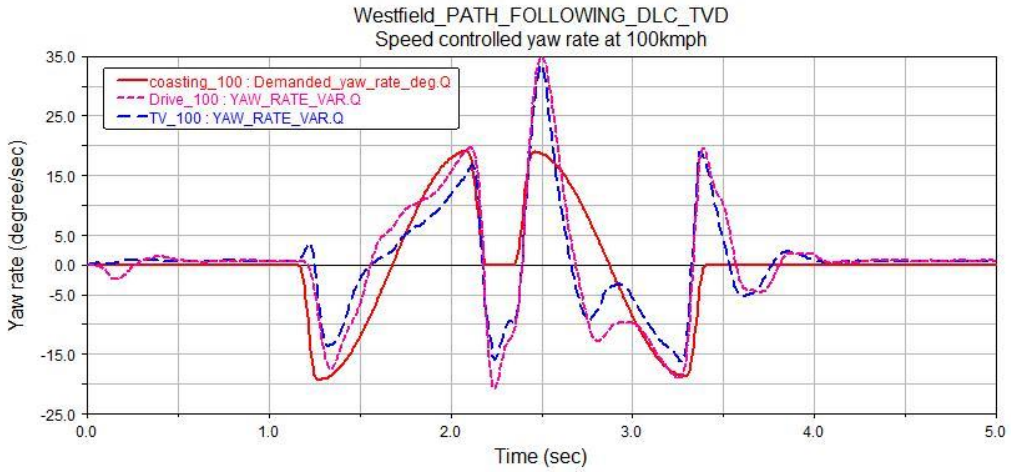

Figure 6-28 Yaw rate variation with the speed controlled at 100km/h

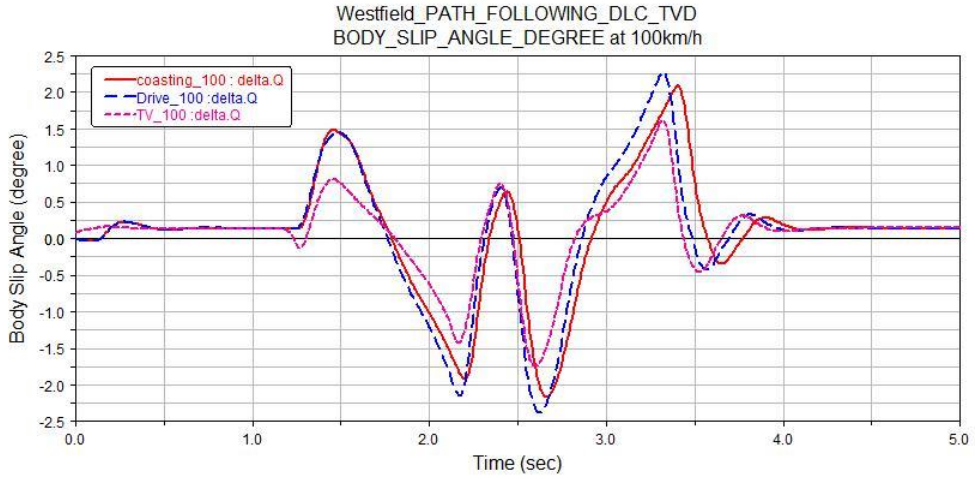

Figure 6-29 Comparison of body slip angles at 100km/h

6.5 Conclusion

Based on the basic principles of torque vectoring control, the example was carried out to explain how the mechanical TV control improves the vehicle driveability. As is known, re-allocating the driving torque on the rear wheel results in substantial influence on the control of the yaw moment.

There are several promising outcomes from this work listed below; these must be interpreted in the context of the design approach used.

- The Optimal Driveline Control Strategy (ODCS) for RWD EVs equipped with an in-line motor at the rear wheels and the independent motor control has been designed to enhance vehicle driveability and yaw stability.

- The ODCS involves three parts: the desired dynamics behaviours, the secondary control and the advanced torque vectoring control (ATVC). The use of all levels has been introduced in detail, so that the desired dynamics behaviours have been found to define the operating region and retain the vehicle linearity. In order to track the desired dynamics, the secondary control has been designed that can modify the traction force then to minimize the yaw rate error and retain the vehicle speed. Since the inputs from the secondary control should be applied to the electric motor through the ATVC, the ATVC has been developed to map the secondary control inputs to the electric motors.

- The simulation results with the proposed driving control have been compared to those with the two types of other driving modes in order to verify the performance of the proposed speed control and the proposed optimal torque vectoring algorithm. It has been shown from simulation results that the vehicle driveability and yaw stability can be significantly improved at the same time or individually compared to the other driving modes.

- Driving control algorithms for alternative types of electric drive system, such as a 4WD system with independently driven in-line motors, will be investigated in the future.

7. Conclusions and future work

7.1. Summary and conclusions

Overall, the thesis has shown that there are worthwhile performance advantages available through improved torque vectoring control strategy for the project vehicle. For example, this thesis has shown that the novel Optimal Driveline Control Strategy (ODCS) for the rear-wheel-drive electric vehicles has some performance advantages over the conventional drivelines which have been used successfully. For example, in the project vehicle model, the new driveline with the ODCS has better driveability performance than the model with the open or limited-slip differential. In addition, research in this thesis has shown that the electric vehicle with the architecture of the in-line motors can result in significant improvements in overall performance compared with the electric vehicle with the in-wheel motors.

In Chapter 2, previous work on the improvement of vehicle dynamics and the direct yaw control strategies are reviewed. With the rise of awareness of sustainable development, interest in the electric vehicles has increased rapidly over recent years, from the viewpoint of both industry and academic. Research and development efforts have been focused on developing new concepts and low cost systems, but this has proved difficult primarily because of high battery costs. Historically, the role of active yaw control in the overall development of vehicle dynamics control technology has commonly been focused. Active steering control and braking-based stability control have actually played the main crucial roles in controlling the yaw moment of vehicles and ensuring good safety, driveability and manoeuvrability. It is concluded that it has been an area of rapidly changing technology over the past decade. But perhaps more importantly, this is certain to continue over the next decade.

In Chapter 3, the project vehicle has been represented in detail, with the entire architecture of the given electric vehicle with RWD being included, and the components and the configuration of the new driveline also being introduced. The capacity of the twin electric motors could fulfil the requirements of the racing vehicle. The lightweight chassis and the wishbone suspension for the project vehicle were

described. Several sub-systems of the vehicle, for example the vehicle body, the suspension system and the driveline, have been modelled in ADAMS, and the model audit was carried out to ensure the reliability of the model. Also, the aerodynamic effects were considered in this section. The driveline was able to produce the variable driving torque at the wheels, so that it could represent the different driving modes, such as the ‘open differential’ and the torque vectoring control. The ‘Magic Formula’ tyre model was added to the vehicle model, and also used with the virtual test rig model to examine characteristics of the tyre model in the intended behaviour due to modifying the coefficients of the tyre model.

The analysis of the full vehicle model was presented in Chapter 4. A summary of the simulation results was collected from these investigations to evaluate the overall characteristics of the project model during the different analyses. First, the characteristics of the suspension system have been determined by the kinematic analysis in which the results can be compared with the laboratory data from manufacturers to validate and refine the computer-based vehicle model.

Second, the dynamic analysis proved the model is a stable system with correct degrees of freedom, the natural frequencies at each mode being calculated and the animations clearly explaining the movement of the sprung and unsprung mass. Also the influences of the natural frequencies at each mode were analysed. Finally, the vehicle model ran for the characteristic driving manoeuvre - steady state cornering, and implementing the control signal from the driver model with ‘path following’ and ‘survey’ controller on the steering system was represented. Of most importance is the fact that the characteristics of the project vehicle can be defined. Furthermore, Figure 4-23 for the yaw rate gain against the vehicle speed indicated that the aim of the further control strategy for active yaw control is to overcome all the variations, and then to dominate the vehicle running at its particular characteristics.

In chapter 5, the vehicle architectures of in-wheel motors and in-line motors are introduced, and the significant modifications of original suspension have been made to integrate all components of in-wheel motors, such as the braking system, cooling system and electric motors, into the constrained volume at the inside of the rim. Furthermore, the un-sprung mass is obviously increased for implementing in-wheel

motors on a vehicle, and degrades ride and handling performance. Compared to the architecture of the in-wheel motors vehicle, the in-line motors vehicle required the minimum variations of the suspension system, thus it can retain the un-sprung masses and reduce redesign costs.

Objective measurements were carried out by using several computing simulation models in ADAMS, such as kinematic, dynamic and handling models. The aspects of simulation have been examined in detail and it can be concluded that the overall performance of ride comfort is degraded, and that the obvious impact of steering behaviour emerges with testing the vehicle models in cornering and lane change manoeuvres. The effects on safety and driveability require some variations in suspension component detail and increases in damping levels to restore agility.

Overall, developing the electric vehicle in its next state the architecture of the in-line motors vehicle can preserve the characteristics of a conventional vehicle with high performance; also, the redesign costs and efforts can be economized by improving the capacity of the electric motors and battery life. Moreover the benefits of individual wheel motor control can be implemented by using in-line wheel motors for substantial improvements in vehicle behaviour.

Based on the basic principles of torque vectoring control, an example was carried out to explain how the mechanical torque vectoring control improves the vehicle driveability. As stated, re-allocating the driving torque on the rear wheel results in substantial influences on the control of the yaw moment. There are several promising outcomes from this work listed below; these must be interpreted in the context of the design approach used.

The Optimal Driveline Control Strategy (ODCS) for RWD EVs equipped with an in-line motor at the rear wheels and the independent motor control has been designed to enhance vehicle driveability and yaw stability. The ODCS involves three parts: the desired dynamics behaviours, the secondary control, and the advanced torque vectoring control (ATVC). The use of all levels has been introduced in detail, so that the desired dynamics behaviours have been found to define the operating region and to retain the vehicle linearity. In order to track the desired dynamics, the secondary

control has been designed so that it can modify the traction force to minimize the yaw rate error and retain the vehicle speed. Since the inputs from the secondary control should be applied to the electric motor through the ATVC, the ATVC has been developed to map the secondary control inputs to the electric motors.

The simulation results with the proposed driving control have been compared to those with the other two types of driving modes in order to verify the performance of the proposed speed control and the proposed optimal torque vectoring algorithm. It has been shown from simulation results that the vehicle driveability and yaw stability can be significantly improved at the same time or individually compared to the other driving modes. Driving control algorithms for alternative types of electric drive system, such as a 4WD system with independently driven in-line motors, will be investigated in the future.

A procedure for the optimal PID controller design and evaluation of torque-vectoring controller for fully electric vehicles has been presented. The results, obtained for a vehicle with in-line motors, demonstrate the effectiveness of torque-vectoring control in tuning vehicle response. This is achieved through a set of reference dynamics vehicle response in conditions of constant and variable vehicle velocities. For implementation of this torque vectoring control system, the optimal PID controller allows to evaluate the feed forward map of the control yaw moment, as a function of measured and estimated quantities, for a given set of vehicle and tyre parameters.

The analysis of the optimal PID control criteria shows that energy-based cost functions provide marginal benefit in the selection of the individual wheel torque distribution. In contrast, performance index based on driving torque output allow a smooth variation of the wheel torques for all achievable lateral accelerations and yield.

Overall, the novel aspects of the work are: defining the characteristics and linearity of the project vehicle using a novel consideration of yaw rate gain; the design and development the Optimal Driveline Control Strategy (ODCS); the analysis and modelling the ODCS in the vehicle and the comparison of the results with conventional drivelines. The conclusions of the research are in-line with the original

aim and objectives. The overall performance benefits of equipping the project vehicle with the new control strategy have been predicted to offer significant benefits in the dynamic control over typical driving manoeuvres.

7.2. Future work

Future work could focus on other potential benefits of vehicle dynamic control, for instance, the driveability of an electric vehicle with individual four-wheel control. Also, the types of subjective assessments that are used to assess driveability, for example, the stop-start condition, the feel of acceleration or deceleration, the control pedal response and feel, and the body slip rate control could be investigated. It is clear there exists a research opportunity to investigate how the objective numerical measures are relative to the subjective assessments of expert assessors, and the effects of different architectures on drivability.

Another potential benefit of the dynamic control for the electric vehicles which could be investigated, is whether it is possible to downsize the motor and also reduce the weight while maintaining acceleration ability in the limited times.

The simulation in this research suggests that the idea of using an optimal control strategy in an electric vehicle will improve the driveability performance. In future work, a four-wheel drive model could be taken into consideration and a more complex control strategy for individual wheel control will be developed. The research could also be focused on attempting to quantify both driving efficiency gains and driveability improvements.

Bibliography

Ackermann J, J. G. (1995). Linear and Nonlinear Controller Design for Robust Automotive Steering. *IEEE Transactions on Control Sytems Technology, Vol.3,No.1,1995, pp. 132-143*.

al., J. C. (2005). Torque Vectoring Driveline: SUV-based Demonstrator and Practical Actuation Technologies. *SAE Internationa*.

Andrés Eduardo Rojas Rojas, H. N. (2010). Comfort and Safety Enhancement of Passenger Vehicles with In-Wheel Motors. *SAE International*.

Andrés Eduardo Rojas Rojas, H. N. (2011). Mechanical Design of In-Wheel Motor Driven Vehicles with Torque-Vectoring. *SAE International*.

Andrés Eduardo Rojas Rojas, H. N. (2011). Mechanical Design of In-Wheel Motor Driven Vehicles with Torque-Vectoring. *SAE International*.

Andrés Eduardo Rojas Rojas, H. N. (2011). Mechanical Design of In-Wheel Motor Driven Vehicles with Torque-Vectoring,. *SAE International*.

Assadian, F. &. (2005). A comparison of yaw stability control strategies for the active differential. *In IEEE ISIE. Dubrovnik, Croatia.*

Babik, B. (2006). Advanced Technology and Energy Strategies, General Motors.

Bo¨rner, M. &. (2006). Model-based detection of critical driving situations with fuzzy logic decision making. *Control Engineering Practice, 14(5),527*.

C Ghike, T. S. (2009). Integrated control of wheel drive–brake torque for vehicle-handling enhancement. *Proceedings of the Institution of Mechanical Engineers, Part D: Journal of Automobile Engineering*.

Chan, C. C. (2001). Modern electric vehicle technology, Oxford University Press.

Cheli, F. M. (2005). A new control strategy for a semi-active differential (Part I),. *16th IFAC World Congress.*

Colombo, D. (2005). Active differential technology for yaw moment control. *In sixth all wheel drive congress. Austria: Gratz.*

Cong Geng, L. M. (2009). Direct Yaw-Moment Control of an In-Wheel-Motored Electric Vehicle Based on Body Slip Angle Fuzzy Observer. *IEEE TRANSACTIONS ON INDUSTRIAL ELECTRONICS, VOL. 56, NO. 5,*.

Edoardo Sabbioni, L. K. (2010). On the Impact of the Maximum Available Tire-Road Friction Coefficient Awareness in a Brake-Based Torque Vectoring System. *SAE International*.

Edoardo Sabbioni, L. K. (2010). On the Impact of the Maximum Available Tire-Road Friction Coefficient Awareness in a Brake-Based Torque Vectoring System. *SAE International*.

ExxonMobil. (2007). New Outlook for Energy: A View to 2030. Texas, ExxonMobil.

F. Assadian, M. H. (2008). Development of a Control Algorithm for an Active Limited Slip Differential. *Loughborough University / Society of Automotive Engineers of Japan (JSAE)*.

F. Cheli, M. P. (2006). Development of a new control strategy for a semi-active differential for a high-performance vehicle. *Vehicle System Dynamics - VEH SYST DYN 01/2006; 44:202-215.* .

G. Kaiser, F. H. (2011). Torque Vectroing with a feedback and feed forward controller - applied to a through the road vehicle. *IEEE Intelligent Vehicle Symposium*.

Gaspar, P. S. (2005). Reconfigurable control structure to prevent the rollover of heavy vehicles. *Control Engineering Practice, 13(6), 699.*

Gerd Kaiser, F. H. (2011). Torque Vectoring with a feedback and feed forward controller - applied to a through the road hybrid electric vehicle. *IEEE*.

Gerhard, J. L.-C. (2005). Robust yaw control design with active differential and active roll control systems. *In 16th IFAC world congress. Prague, Czech Republic.*

Gillespie, T. D. (1992). *Fundamentals of Vehicle Dynamics.* SAE International.

Göschel, B. (2008). Ausgewählte Kapitel der Verbrennungskraftmaschinen: Alektrifizierung Antrieb. *Institute for Internal Combustion Engines and Thermodynamics, Graz University of Technology*.

Harty, M. B. (2004). *Multibody Systems Approach to Vehicle Dynamics.* Elsevier's Science and Technology Rights Department.

Hirsch, R. L. (2005). Peaking of World Oil Production: Impacts, Mitigation & Risk Management.

Husain, I. (2003). Electric and hybrid vehicles; design fundamentals., CRC Press.

Ikushima, Y. a. (1995). "A Study on the Effects of the Active Yaw Moment Control,". *SAE Technical Paper 950303, 1995, doi:10.4271/950303.*

IME. (2009). Brochure for Integrating Technologies for Low Carbon. Integrating Technologies for Low Carbon, Norfolk, Institution of Mechanical Engineers.

Inoue, K. S. (2007). Effect of the Right-and-left Torque Vectoring System in Various Types of Drivetrain. *SAE International*, 2007-01-3645.

IPIECA. (2004). Transportation and climate change: opportunities, challenges and longterm strategies. AN IPECA workshop, Baltimore, USA.

J.C. Wheals, M. D. (2006). Design and Simulation of a Torque Vectoring™Rear Axle. *SAE International*.

Johann Willberger, M. A. (2010). Motor Selection Criteria and Potentials of Electrified All Wheel Drive Concepts for Passenger Cars by Add-on Wheel Hub Motors on the Rear Axle. *SAE International*.

Johann Willberger, M. A. (2010). Motor Selection Criteria and Potentials of Electrified All Wheel Drive Concepts for Passenger Cars by Add-on Wheel Hub Motors on the Rear Axle. *SAE International*.

Johann Willberger, M. A. (2010). Motor Selection Criteria and Potentials of Electrified All Wheel Drive Concepts for Passenger Cars by Add-on Wheel Hub Motors on the Rear Axle. *SAE International* .

John Feltman, J. G. (2006). Mechatronic Torque Vectoring System with Enhanced Controllability for Augmenting the Vehicle Agility and Safety. *SAE International*.

Jonathan C. Wheals, H. B. (2004). Torque Vectoring AWD Driveline: Design, Simulation, Capabilities and Control. *SAE International ISBN 0-7680-1319-4*.

Jonathan C. Wheals, H. B. (2004). Torque Vectoring AWD Driveline: Design,Simulation, Capabilities and Control. *SAE International*.

Juyong Kang, Y. k. (2012). Control Allocation based Optimal Torque Vectoring for 4WD Electric Vehicle. *SAE International*.

Kakalis L., C. F. (2010). n the impact of the maximum available tire-road friction coefficient awareness in a brake-based torque vectoring system. . *In SAE International Congress and Exposition, SAE Paper 2010-01-0116.*

Kang, J. k. (2012). Control Allocation based Optimal Torque Vectoring for 4WD Electric Vehicle. *SAE Technical Paper 2012-01-0246*.

Kim, D.-H. J. (2007). "Optimal brake torque distribution for a four-wheel drive hybrid electric vehicle stability enhancement." . *Proc. IMechE, Part D: J Automobile Engineering vol. 221: 1357-1366.*

Kiumars Jalali, K. B. (2008). Design of an Advanced Traction Controller for an Electric Vehicle Equipped with Four Direct Driven In-Wheel Motors. *SAE International*.

Kiumars Jalali, T. U. (2012). Development of a Fuzzy Slip Control System for Electric Vehicles with In-wheel Motors. *SAE International*.

Kohen, P. &. (2004). Active steering—the BMW approach towards modern steering technology. . *In SAE Technical Paper No.2004-01-1105.*

Kroppe, J. P. (2004). Dana Torque Vectoring Differential Dynamic Trak. *SAE International*.

Larminie, J. a. (2003). Electric vehicle technology explained. West Sussex, England, J. Wiley.

Lifu Li, Z. (2011). Study on Torque Vectoring Differential for Vehicle Stability Control via Hardware Hardwarein-. *IEEE*.

M Milehins, C. C. (2010). Handling behaviour of a TTR hybrid electric vehicle with independent rear wheel torque control. *In: AVEC10*.

Martyn Anderson, D. H. (2011). Unsprung Mass with In-Wheel Motors - Myths and Realities. *SAE International* .

Milliken, W. a. (1995). *Race car vehicle dynamics.* Society of Automotive Engineers, Inc .

Mokhiamar, O. &. (2002). Active wheel steering and yaw moment control combination to maximize stability as well as responsiveness during quick lane change for active vehicle handling safety. *Proceedings of the Institution of Mechanical Engineers Part D, Journal of Automobile Engineering, 216(1), 115–124.*

Motoki Shino, M. N. (2001). Yaw-moment control of electric vehicle for improving handling and stability. *Society of Automotive Engineers of Japan, Inc. and Elsevier Science B.V.*

Neudorfer, H., Binder, A., & Wicker, N. (2006). Analyse von Unterschiedlichen Fahrzyklen fur den einsatz von Elektrofahrzeugen . *E&I 123 no 7-8 p,352-360*.

O'Hara, S. R. (2005). VEHICLE PATH OPTIMIZATION OF EMERGENCY LANE CHANGE MANEUVERS FOR VEHICLE SIMULATION.

Pacejka, H. a. (1991). Shear force generation by pneumatic tyres in steady state conditions: a review of modelling aspects. *Vehicle System Dynamics, 20, pp. 121–176, 1991.*

PINTO, L. A. (2011). YAW MOTION CONTROL OF A VEHICLE. *International Patent Cooperation Treaty*.

Qin Liu, G. K. (2011). Two-Degree-of-Freedom LPV Control for a through-the-Road Hybrid Electric Vehicle via Torque Vectoring. *IEEE*.

Randall, B. P. (2009). Electric cars - are they really 'green'? Low-carbon vehicles 2009, London, Institution of Mechanical Engineers.

Resta, F. G. (2005). A new control strategy of a semi-active differential (Part II). *the 16th IFAC WORLD CONGRESS.*

Sawase, K. U. (2007). Effect of the Right-and-left Torque Vectoring System in Various Types of Drivetrain. *SAE Technical Paper 2007-01-3645, 2007, doi:10.4271/2007-01-3645.*

Sawase, T. K. (2012). Classification and analysis of electric Classification and analysis of electricpowered. *Proceedings of the Institution of Mechanical Engineers, Part D: Journal of Automobile Engineering*.

Sharma, S. K. (2006). Torque Vectoring Axle and Four Wheel Steering: A Simulation Study of Two Yaw Moment Generation Mechanisms. *SAE International*.

Sharma, S. K. (2006). Torque Vectoring Axle and Four Wheel Steering: A Simulation Study of Two Yaw Moment Generation Mechanisms. *SAE International*.

Sharma, S. K. (2006). Torque Vectoring Axle and Four Wheel Steering: A Simulation Study of Two Yaw Moment Generation Mechanisms. *SAE International*.

Sienel, A. J. (1993). Robust Yaw and Damping of Cars with Front and Rear Wheel Steering. *IEEE Transactions on Control Systems Technology, Vol.1,No.1,1993,pp.15-20*.

Taehyun Shim, G. A. (n.d.). Autonomous vehicle collision avoidance system using path planning and model-predictive-control-based active front steering and wheel torque control. *Proceedings of the Institution of Mechanical Engineers, Part D: Journal of Automobile Engineering*.

Taeyoung Lee, J. K. (2010). Integration of Longitudinal and Lateral Human Driver Models for Evaluation of the Vehicle Active Safety Systems. *SAE International*.

van Zanten, A. T. (1995). VDC, the vehicle dynamics control system of bosch. *In SAE Technical Paper No. 95759.*

van Zanten, A. T. (2000). Bosch ESP systems: 5 years of experience. *In SAE Technical Paper No. 2000-01-1633.*

Vilaplana, M. A. (2005). Control of yaw rate and sideslip in 4-wheel steering cars with actuator constraints. *Lecture Notes in Computer Science, (vol. 3355, pp.201–222). Berlin: Springer.*

Whitehead, A. (2012). IN-WHEEL ELECTRIC MOTORS. *The Packaging and Integration Challenges Senior Mechanical Systems Engineer Protean Electric Ltd, UK*, p. 15.

Wu, L. L. (2011). Study on Torque Vectoring Differential for Vehicle Stability Control via Hardware-in-Loop Simulation. *IEEE 978-1-61284-486-2/111*.

YASA motor. (2014). Retrieved from http://www.yasamotors.com/technology

Zhang, Y. H. (2006). "Performance modelling and optimization of a novel multi mode hybrid powertrain.". *Trans. ASME, J. Mech. Design 128(1): 79-89*.

Appendix

Appendix 1 Westfield vehicle model for kinematic analysis (part of the model)

```
!------------------------- Default Units for Model -------------------------!
defaults units  & length = mm  &angle = deg  & force = newton    mass = kg  &time = sec
defaults units  & coordinate_system_type = cartesian  & orientation_type = body313
!------------------------ Default Attributes for Model ------------------------!
defaults attributes  & inheritance = bottom_up  &icon_visibility = on   grid_visibility = off  &
size_of_icons = 20.0  & spacing_for_grid = 1000.0
!------------------------------ Adams/View Model ------------------------------!
model create  &model_name = Westfield_Front_Drive_Kin_rig
model attributes   model_name = Westfield_Front_Drive_Kin_rig  & size_of_icons = 20.0
view erase
-------------------------------- Materials ---------------------------------!
material create  & material_name = .Westfield_Front_Drive_Kin_rig.steel  & adams_id = 1
&youngs_modulus = 2.07E+005  &poissons_ratio = 0.29  & density = 7.801E-006
!-------------------------------- Rigid Parts -------------------------------!
! Create parts and their dependent markers and graphics
!---------------------------------- ground ----------------------------------!
! ****** Ground Part ******
defaults model  &part_name = grounddefaults coordinate_system  &
default_coordinate_system = .Westfield_Front_Drive_Kin_rig.ground
! ****** Markers for current part ******
marker create  &
marker_name = .Westfield_Front_Drive_Kin_rig.ground.m_wheel_centre_ground   adams_id = 2  &
location = -1167.999, 663.971, 0.0  & orientation = 0.0d, 0.0d, 0.0d
marker attributes  &marker_name = m_wheel_centre_ground  &size_of_icons = 20.0 marker create
&marker_name
 = .Westfield_Front_Drive_Kin_rig.ground.MARKER_57  & adams_id = 57  & location = -1269.8,
336.933, -96.75  &orientation = 186.7030013032d, 79.0487029613d, 0.0
marker create  &marker_name
= .Westfield_Front_Drive_Kin_rig.ground.Body_FD_Lower_wish_rev_joint_maker  & adams_id = 42
&  location = -1026.439, 190.41, -135.4  & orientation = 269.7809583075d, 90.0d, 0.0d
marker create  &marker_nam
= .Westfield_Front_Drive_Kin_rig.ground.MARKER_55  & adams_id = 55  &location = -1183.751,
279.455, 121.4  &orientation = 0.0d, 0.0d, 0.0d
marker create   marker_name
 = .Westfield_Front_Drive_Kin_rig.ground.MARKER_63  adams_id = 63  &
location = -1183.751, 279.455, 121.4  &orientation = 178.4831821016d, 136.0112734674d, 0.0d
marker create  &marker_name
 = .Westfield_Front_Drive_Kin_rig.ground.MARKER_99  & adams_id = 99  &
location = -1277.559, 290.911, 74.56  &orientation = 270.1944385707d, 90.0d, 90.0d
marker create  &marker_name
= .Westfield_Front_Drive_Kin_rig.ground.MARKER_80  & adams_id = 80
  location = -1167.999, 663.971, -50.0  & orientation = 0.0d, 0.0d, 0.0d

marker create  & marker_name
 = .Westfield_Front_Drive_Kin_rig.ground.ground_wheel_base  &adams_id = 88  & location = -
1167.999, 663.971, -266.0  &orientation = 0.0d, 0.0d, 0.0d
marker create  &marker_name
= .Westfield_Front_Drive_Kin_rig.ground.MARKER_108  &adams_id = 108  &location = -1167.999,
663.971, -200.0  &orientation = 0.0d, 0.0d, 0.0d
part create rigid_body mass_properties  part_name= .Westfield_Front_Drive_Kin_rig.ground
&material_type = .Westfield_Front_Drive_Kin_rig.steel

! ****** Points for current part ******
```

```
point create  &point_name = .Westfield_Front_Drive_Kin_rig.ground.upper_wishbone_outer_ball_joint
& location = -1158.169, 551.78, 74.5point attributes  &point_name = upper_wishbone_outer_ball_joint
& size_of_icons = 20.0
!
point create  &point_name
= .Westfield_Front_Drive_Kin_rig.ground.upper_wishbone_inner_Rear_joint  &location = -1085.433,
291.563, 74.5 point create  &
point_name= .Westfield_Front_Drive_Kin_rig.ground.upper_wishbone_inner_Front_joint  &location =
-1277.559, 290.911, 74.56
point attributes  & point_name = upper_wishbone_inner_Front_joint  &size_of_icons = 20.0 point
create  &
point_name = .Westfield_Front_Drive_Kin_rig.ground.POINT_25  & location = -1050.0, 350.0, 0.0
point create  & point_name = .Westfield_Front_Drive_Kin_rig.ground.lower_wishbone_outer_ball_joint
& location = -1177.704, 570.758, -135.4
point attributes   point_name = lower_wishbone_outer_ball_joint  &size_of_icons = 20.0

!----------------------------- FD_Upper_wishbone -----------------------------
defaults coordinate_system  &default_coordinate_system = .Westfield_Front_Drive_Kin_rig.ground
part create rigid_body name_and_position  &part_name
= .Westfield_Front_Drive_Kin_rig.FD_Upper_wishbone  & adams_id = 8  &
 location = 0.0, 0.0, 0.0  & orientation = 0.0d, 0.0d, 0.0d
part create rigid_body initial_velocity  &
   part_name = .Westfield_Front_Drive_Kin_rig.FD_Upper_wishbone  &vx = -2.7778E+004
defaults coordinate_system  & default_coordinate_system
= .Westfield_Front_Drive_Kin_rig.FD_Upper_wishbone

! ****** Markers for current part ******
marker create  &marker_name = .Westfield_Front_Drive_Kin_rig.FD_Upper_wishbone.MARKER_98
&adams_id = 98
location = -1277.559, 290.911, 74.56  &
orientation = 270.1944385707d, 90.0d, 90.0
marker create  & marker_name = .Westfield_Front_Drive_Kin_rig.FD_Upper_wishbone.MARKER_35
adams_id = 35  &
 location = -1085.433, 291.563, 74.56  &
 orientation = 65.4081991848d, 0.0d, 0.0

!----------------------------- FD_Lower_wishbone -----------------------------!
defaults coordinate_system  &default_coordinate_system = .Westfield_Front_Drive_Kin_rig.ground
part create rigid_body name_and_position  & part_name
= .Westfield_Front_Drive_Kin_rig.FD_Lower_wishbone  &
adams_id = 7  & location = 0.0, 0.0, 0.0  & orientation = 0.0d, 0.0d, 0.0d

part create rigid_body initial_velocity  & part_name
= .Westfield_Front_Drive_Kin_rig.FD_Lower_wishbone  &vx = -2.7778E+004
defaults coordinate_system  &default_coordinate_system
= .Westfield_Front_Drive_Kin_rig.FD_Lower_wishbone
! ****** Markers for current part ******
marker create  & marker_name = .Westfield_Front_Drive_Kin_rig.FD_Lower_wishbone.MARKER_30
 adams_id = 30  &
 location = -1177.704, 570.758, -135.4  &
 orientation = 291.6877938567d, 0.0d, 0.0d
marker create  &marker_name= .Westfield_Front_Drive_Kin_rig.FD_Lower_wishbone.MARKER_31
&adams_id = 31  &
   location = -1026.439, 190.41, -135.4  &
   orientation = 291.6877938567d, 0.0d, 0.0d
marker create  &marker_name = .Westfield_Front_Drive_Kin_rig.FD_Lower_wishbone.cm  &
adams_id = 43  &
   location = -1179.1194902269, 380.878555804, -135.4  &
   orientation = 179.2773770674d, 90.0000000007d, 89.9999999907d
```

```
marker create  &marker_name = .Westfield_Front_Drive_Kin_rig.FD_Lower_wishbone.MARKER_32
adams_id = 32  &
  location = -1177.704, 570.758, -135.4  &
  orientation = 291.6877938567d, 0.0d, 0.0d
marker create  &
  marker_name = .Westfield_Front_Drive_Kin_rig.FD_Lower_wishbone.MARKER_33  &
  adams_id = 33  &
  location = -1334.311, 191.587, -135.4 orientation = 291.6877938567d, 0.0d, 0.0

marker create  & marker_name
= .Westfield_Front_Drive_Kin_rig.FD_Lower_wishbone.FD_Lower_wish_rev_joint_marker
&adams_id = 41  &
location = -1026.439, 190.41, -135.4  &
orientation = 269.7809583075d, 90.0d, 0.0d
!

marker create  &
  marker_name = .Westfield_Front_Drive_Kin_rig.FD_Lower_wishbone.lower_wishbone_ball_joint  &
  adams_id = 47  &
  location = -1177.704, 570.758, -135.4  &
  orientation = 0.0d, 0.0d, 0.0d
!
marker create  &
  marker_name = .Westfield_Front_Drive_Kin_rig.FD_Lower_wishbone.MARKER_70  &
  adams_id = 70  &
  location = -1178.278, 486.142, -92.79  &
  orientation = 0.0d, 0.0d, 0.0d
!
part create rigid_body mass_properties  &
  part_name = .Westfield_Front_Drive_Kin_rig.FD_Lower_wishbone  &
  mass = 2.497681221  &
  center_of_mass_marker =   &
                    .Westfield_Front_Drive_Kin_rig.FD_Lower_wishbone.cm  &
  ixx = 5.130318723E+004  &
  iyy = 3.158268078E+004  &
  izz = 1.984539051E+004  &
  ixy = 0.0  &
  izx = 0.0  &
  iyz = 0.0
! ****** Graphics for current part ******

geometry create shape link  &
  link_name = .Westfield_Front_Drive_Kin_rig.FD_Lower_wishbone.LINK_19  &
  i_marker = .Westfield_Front_Drive_Kin_rig.FD_Lower_wishbone.MARKER_30  &
  j_marker = .Westfield_Front_Drive_Kin_rig.FD_Lower_wishbone.MARKER_31  &
  width = 40.0  &
  depth = 20.0
!

geometry create shape link  &
  link_name = .Westfield_Front_Drive_Kin_rig.FD_Lower_wishbone.LINK_20  &
  i_marker = .Westfield_Front_Drive_Kin_rig.FD_Lower_wishbone.MARKER_32  &
  j_marker = .Westfield_Front_Drive_Kin_rig.FD_Lower_wishbone.MARKER_33  &
  width = 40.0  &

  depth = 20.0

part attributes  &
  part_name = .Westfield_Front_Drive_Kin_rig.FD_Lower_wishbone  &
  color = MAIZE  &
  name_visibility = off
```

```
!---------------------------------- upright ----------------------------------!

defaults coordinate_system  &
   default_coordinate_system = .Westfield_Front_Drive_Kin_rig.ground
!
part create rigid_body name_and_position  &
   part_name = .Westfield_Front_Drive_Kin_rig.upright  &
   adams_id = 4  &
   location = 0.0, 0.0, 0.0  &
   orientation = 0.0d, 0.0d, 0.0d
part create rigid_body initial_velocity  &
   part_name = .Westfield_Front_Drive_Kin_rig.upright  &
   vx = -2.7778E+004
!
defaults coordinate_system  &
   default_coordinate_system = .Westfield_Front_Drive_Kin_rig.upright

! ****** Markers for current part ******

marker create  &
   marker_name = .Westfield_Front_Drive_Kin_rig.upright.MARKER_34  &
   adams_id = 34  &
   location = -1167.999, 663.971, 0.0  &
   orientation = 0.0d, 90.0d, 0.0d
!

marker create  &
   marker_name = .Westfield_Front_Drive_Kin_rig.upright.m_upright_CG  &
   adams_id = 17  &
   location = -1167.999, 561.269, 0.0  &
   orientation = 0.0d, 0.0d, 0.0d
!

marker attributes  &
   marker_name = m_upright_CG  &
   size_of_icons = 20.0
!
marker create  &
   marker_name = .Westfield_Front_Drive_Kin_rig.upright.m_upright_graphics  &
   adams_id = 18  &
   location = -1177.704, 570.758, -135.4  &
   orientation = 45.8285909785d, 7.391038812d, 313.9325193345d
!
marker attributes  &
   marker_name = m_upright_graphics  &
   size_of_icons = 20.0
!

marker create  &
   marker_name = .Westfield_Front_Drive_Kin_rig.upright.m_upright_graphics2  &
   adams_id = 19  &
   location = -1298.093, 577.671, -49.847  &
   orientation = 82.8141733619d, 69.1856027052d, 272.5651822746d
```

Appendix 2 Westfield model for Eigen solution (part of model)

```
!-------------------------- Default Units for Model --------------------------!
defaults units  &
   length = mm  &
```

```
   angle = deg  &
   force = newton  &
   mass = kg  &
   time = sec
!
defaults units  &
   coordinate_system_type = cartesian  &
   orientation_type = body313
!
!------------------------ Default Attributes for Model ------------------------!
defaults attributes  &
   inheritance = bottom_up  &
   icon_visibility = on  &
   grid_visibility = off  &
   size_of_icons = 20.0  &
   spacing_for_grid = 1000.0
!
!------------------------------- Adams/View Model -------------------------------!
model create  &
   model_name = Westfield_full_vehicle_Eigen
!
model attributes  &
   model_name = .Westfield_full_vehicle_Eigen  &
   size_of_icons = 20.0
!
view erase
!--------------------------------- Data storage ---------------------------------!
data_element create variable  &
   variable_name = .Westfield_full_vehicle_Eigen.YAW_RATE_VAR  &
   adams_id = 25136  &
   initial_condition = 0.0  &
   function = ""
!
data_element create spline  &
   spline_name = .Westfield_full_vehicle_Eigen.SPLINE_G686  &
   adams_id = 1000  &
   comments = "DAMPER SPLINES", "G686 WESTFIELD 3742078"  &
   x = -2000.0, -840.995, -800.995, -760.995, -720.995, -680.995, -660.995,  &
      -580.995, -520.995, -460.995, -420.995, -380.995, -340.995, -300.995,  &
      -270.995, -240.995, -228.995, -207.995, -192.887, -174.38, -161.916,  &
      -144.542, -128.301, -113.57, -98.84, -85.998, -71.268, -57.293,  &
      -43.696, -27.455, -15.746, 0.0, 15.746, 27.455, 38.408, 47.851,  &
      53.894, 64.092, 75.045, 83.354, 90.153, 100.728, 112.059, 122.257,  &
      130.944, 140.765, 152.096, 161.16, 167.959, 176.646, 184.2, 193.265,  &
      204.974, 214.974, 224.974, 234.974, 244.974, 254.974, 264.974,  &
      274.974, 284.974, 294.974, 304.974, 314.974, 380.0  &
   y = 2000.0, 1186.0, 1156.0, 1126.0, 1096.0, 1066.0, 1036.0, 1006.0, 976.0,  &
      946.0, 916.0, 886.0, 856.0, 826.0, 796.0, 766.0, 736.0, 706.522,  &
      670.29, 634.058, 606.884, 570.652, 525.362, 498.188, 461.956, 434.782,  &
      389.493, 362.319, 317.029, 262.681, 226.449, 0.0, -280.797, -452.899,  &
      -625.0, -778.986, -878.623, -996.377, -1105.073, -1195.652, -1277.174,  &
      -1385.87, -1494.565, -1603.261, -1702.899, -1802.536, -1938.406,  &
      -2028.986, -2110.507, -2255.435, -2391.304, -2536.232, -2726.449,  &
      -2926.0, -3126.0, -3326.0, -3526.0, -3726.0, -3926.0, -4126.0,  &
      -4326.0, -4526.0, -4726.0, -4926.0, -8000.0  &
   linear_extrapolate = no
!
data_element attributes  &
   data_element_name = .Westfield_full_vehicle_Eigen.SPLINE_G686  &
   visibility = off
```

```
!
data_element create spline  &
  spline_name = .Westfield_full_vehicle_Eigen.SPLINE_West_1  &
  adams_id = 2000  &
  comments = "WESTFIELD 1"  &
  x = -1000.0, -273.24, -262.24, -251.24, -240.24, -229.24, -218.24,  &
     -207.24, -196.287, -182.689, -170.603, -157.006, -143.031, -130.189,  &
     -118.858, -104.128, -87.131, -78.067, -69.002, -58.048, -41.807,  &
     -29.343, -16.124, 0.0, 16.124, 35.764, 48.606, 60.315, 70.135, 80.333,  &
     90.153, 101.484, 110.549, 120.369, 131.7, 144.919, 157.383, 174.38,  &
     186.089, 197.797, 206.484, 216.0, 226.0, 236.0, 250.0, 267.0, 520.0  &
  y = 2400.0, 750.0, 720.0, 690.0, 660.0, 630.0, 600.0, 588.768, 570.652,  &
     534.42, 507.246, 498.188, 461.956, 434.782, 416.667, 371.377, 335.145,  &
     317.029, 289.855, 262.681, 199.275, 153.985, 108.696, 0.0, -63.406,  &
     -217.391, -326.087, -434.783, -525.362, -625.0, -724.638, -824.276,  &
     -896.739, -969.203, -1068.841, -1186.594, -1277.174, -1422.102,  &
     -1530.797, -1630.435, -1702.899, -1772.0, -1870.0, -1970.0, -2100.0,  &
     -2200.0, -5000.0  &
  linear_extrapolate = no
!
data_element attributes  &
  data_element_name = .Westfield_full_vehicle_Eigen.SPLINE_West_1  &
  visibility = off
!
data_element create spline  &
  spline_name = .Westfield_full_vehicle_Eigen.SPLINE_West_2  &
  adams_id = 3000  &
  comments = "WESTFIELD 2"  &
  x = -1000.0, -272.995, -251.995, -239.995, -228.995, -215.995, -201.952,  &
     -187.222, -170.603, -156.628, -142.653, -131.322, -118.103, -104.883,  &
     -92.041, -81.088, -71.268, -60.692, -50.117, -38.03, -25.944, -15.746,  &
     0.0, 15.746, 25.566, 36.52, 47.473, 53.894, 60.315, 68.624, 79.955,  &
     90.153, 99.973, 109.793, 119.613, 128.678, 137.743, 149.829, 159.65,  &
     170.603, 180.423, 192.51, 206.484, 212.484, 231.0, 251.0, 272.0,  &
     1000.0  &
  y = 1448.5058131529, 601.0, 584.0, 551.0, 519.0, 498.188, 489.13, 461.956,  &
     434.782, 407.609, 380.435, 353.261, 326.087, 298.913, 271.739,  &
     235.507, 217.391, 190.217, 163.043, 135.869, 108.696, 90.58, 0.0,  &
     -36.232, -63.406, -90.58, -117.754, -135.87, -181.16, -217.391,  &
     -280.797, -344.203, -407.609, -471.015, -543.478, -606.884, -670.29,  &
     -751.812, -806.16, -878.623, -951.087, -1032.609, -1114.131, -1210.0,  &
     -1290.0, -1410.0, -1580.0, -6756.1418342369  &
  linear_extrapolate = no
!
data_element attributes  &
  data_element_name = .Westfield_full_vehicle_Eigen.SPLINE_West_2  &
  visibility = off
!
data_element create spline  &
  spline_name = .Westfield_full_vehicle_Eigen.LEFT_TURN_SPLINE  &
  adams_id = 7000  &
  x = 0.0, 8.333, 16.666, 21.5, 24.999, 33.332, 41.665, 49.998, 58.331,  &
     63.0, 66.664, 74.997, 83.33, 91.663, 99.996, 108.329, 116.662,  &
     124.995, 133.328, 141.661, 149.994, 158.327, 166.66, 174.993, 183.326,  &
     191.659, 199.992, 208.325, 216.658, 224.991, 233.324, 241.657, 249.99,  &
     258.323, 266.656, 274.989, 283.322, 291.655, 299.988, 308.321,  &
     316.654, 324.987, 333.32, 341.653, 349.986, 358.319, 366.652, 374.985,  &
     383.318, 391.651, 399.984, 408.317, 416.65, 424.983, 433.316, 441.649,  &
     449.982, 458.315, 466.648, 474.981, 483.314, 491.647  &
  y = 0.0, 0.0, -1.0E-003, -2.7575744042E-003, -5.05E-003, -1.01E-002,  &
```

```
      -1.515E-002, -2.02E-002, -2.4997042955E-002, -2.7618766292E-002,  &
      -2.9065236397E-002, -2.9969280214E-002, -3.03E-002, -3.03E-002,  &
      -3.03E-002, -3.03E-002, -3.03E-002, -3.03E-002, -3.03E-002,  &
      -3.03E-002, -3.03E-002, -3.03E-002, -3.03E-002, -3.03E-002,  &
      -3.03E-002, -3.03E-002, -3.03E-002, -3.03E-002, -3.03E-002,  &
      -3.03E-002, -3.03E-002, -3.03E-002, -3.03E-002, -3.03E-002,  &
      -3.03E-002, -3.03E-002, -3.03E-002, -3.03E-002, -3.03E-002,  &
      -3.03E-002, -3.03E-002, -3.03E-002, -3.03E-002, -3.03E-002,  &
      -3.03E-002, -3.03E-002, -3.03E-002, -3.03E-002, -3.03E-002,  &
      -3.03E-002, -3.03E-002, -3.03E-002, -3.03E-002, -3.03E-002,  &
      -3.03E-002, -3.03E-002, -3.03E-002, -3.03E-002, -3.03E-002,  &
      -3.03E-002, -3.03E-002, -3.03E-002  &
   linear_extrapolate = yes
!
data_element attributes  &
   data_element_name = .Westfield_full_vehicle_Eigen.LEFT_TURN_SPLINE  &
   visibility = off

!---------------------------------- Materials ----------------------------------
material create  &
   material_name = .Westfield_full_vehicle_Eigen.steel  &
   adams_id = 1  &
   youngs_modulus = 2.07E+005  &
   poissons_ratio = 0.29  &
   density = 7.801E-006
!------------------------------- Rigid Parts --------------------------------!
!
! Create parts and their dependent markers and graphics
!
!----------------------------------- ground -----------------------------------!
! ****** Ground Part ******
defaults model  &
   part_name = ground
defaults coordinate_system  &
   default_coordinate_system = .Westfield_full_vehicle_Eigen.ground
! ****** Markers for current part ******
marker create  &
   marker_name = .Westfield_full_vehicle_Eigen.ground.m_wheel_centre_ground  &
   adams_id = 2  &
   location = -1167.999, 663.971, 0.0  &
   orientation = 0.0d, 0.0d, 0.0d
!
marker attributes  &
   marker_name = .Westfield_full_vehicle_Eigen.ground.m_wheel_centre_ground  &
   size_of_icons = 20.0
!
marker create  &
   marker_name = .Westfield_full_vehicle_Eigen.ground.MARKER_150  &
   adams_id = 150  &
   location = 1163.586, 399.311, 419.149  &
   orientation = 0.0d, 0.0d, 0.0d
!
marker create  &
   marker_name = .Westfield_full_vehicle_Eigen.ground.ground_wheel_base  &
   adams_id = 200  &
   location = 1169.081, 663.971, -266.0  &
   orientation = 0.0d, 0.0d, 0.0d
!
marker create  &
   marker_name = .Westfield_full_vehicle_Eigen.ground.MARKER_292  &
```

```
   adams_id = 292  &
   location = 1163.586, -399.311, 419.149  &
   orientation = 0.0d, 0.0d, 0.0d
!
marker create  &
   marker_name = .Westfield_full_vehicle_Eigen.ground.MARKER_342  &
   adams_id = 342  &
   location = -1334.311, 191.587, -255.4  &
   orientation = 0.0d, 0.0d, 0.0d
!
marker create  &
   marker_name = .Westfield_full_vehicle_Eigen.ground.MARKER_369  &
   adams_id = 369  &
   location = 993.63, 134.002, -255.4  &
   orientation = 0.0d, 0.0d, 0.0d
!
marker create  &
   marker_name = .Westfield_full_vehicle_Eigen.ground.MARKER_404  &
   adams_id = 404  &
   location = -1269.8, 336.933, -33.12  &
   orientation = 0.0d, 0.0d, 0.0d
!
marker create  &
   marker_name = .Westfield_full_vehicle_Eigen.ground.aero_drag_marker  &
   adams_id = 405  &
   location = -1.00964, 0.0, -33.7444  &
   orientation = 0.0d, 0.0d, 0.0d
!------------------------------- upright_drive -------------------------------!
defaults coordinate_system  &
   default_coordinate_system = .Westfield_full_vehicle_Eigen.ground
!
part create rigid_body name_and_position  &
   part_name = .Westfield_full_vehicle_Eigen.upright_drive  &
   adams_id = 13  &
   location = 0.0, 0.0, 0.0  &
   orientation = 0.0d, 0.0d, 0.0d
!
part create rigid_body initial_velocity  &
   part_name = .Westfield_full_vehicle_Eigen.upright_drive  &
   vx = 0.0
!
defaults coordinate_system  &
   default_coordinate_system = .Westfield_full_vehicle_Eigen.upright_drive
!
! ****** Markers for current part ******
!
marker create  &
   marker_name = .Westfield_full_vehicle_Eigen.upright_drive.MARKER_86  &
   adams_id = 86  &
   location = -1158.169, 551.78, 74.56  &
   orientation = 226.0112237762d, 169.6160562249d, 46.4838491772d
!
marker create  &
   marker_name = .Westfield_full_vehicle_Eigen.upright_drive.cm  &
   adams_id = 103  &
   location = -1188.6920986753, 576.0213355289, -21.7272633248  &
   orientation = 278.3869741337d, 153.2999544485d, 183.8203841601d
!
marker create  &
   marker_name = .Westfield_full_vehicle_Eigen.upright_drive.MARKER_87  &
```

```
   adams_id = 87  &
   location = -1167.999, 561.269, 0.0  &
   orientation = 225.6447517964d, 174.2755531549d, 45.7879283968d
!
marker create  &
   marker_name = .Westfield_full_vehicle_Eigen.upright_drive.MARKER_88  &
   adams_id = 88  &
   location = -1298.093, 577.671, -49.847  &
   orientation = 82.8141733619d, 69.1856027052d, 272.5651822746d
!
marker create  &
   marker_name = .Westfield_full_vehicle_Eigen.upright_drive.MARKER_89  &
   adams_id = 89  &
   location = -1167.999, 561.269, 0.0  &
   orientation = 180.0d, 90.0d, 180.0d
!
marker create  &
   marker_name = .Westfield_full_vehicle_Eigen.upright_drive.MARKER_91  &
   adams_id = 91  &
   location = -1158.169, 551.78, 74.56  &
   orientation = 0.0d, 0.0d, 0.0d
!
marker create  &
   marker_name = .Westfield_full_vehicle_Eigen.upright_drive.MARKER_93  &
   adams_id = 93  &
   location = -1177.704, 570.758, -135.4  &
   orientation = 0.0d, 0.0d, 0.0d
!
marker create  &
   marker_name = .Westfield_full_vehicle_Eigen.upright_drive.MARKER_94  &
   adams_id = 94  &
   location = -1298.093, 577.671, -49.847  &
   orientation = 0.0d, 0.0d, 0.0d
!
marker create  &
   marker_name = .Westfield_full_vehicle_Eigen.upright_drive.MARKER_504  &
   adams_id = 504  &
   location = -1167.999, 663.971, 0.0  &
   orientation = 0.0d, 90.0d, 0.0d
!
part create rigid_body mass_properties  &
   part_name = .Westfield_full_vehicle_Eigen.upright_drive  &
   mass = 7.027406137  &
   center_of_mass_marker = .Westfield_full_vehicle_Eigen.upright_drive.cm  &
   ixx = 2.7196645587E+004  &
   iyy = 2.4214601705E+004  &
   izz = 1.1083130452E+004  &
   ixy = 0.0  &
   izx = 0.0  &
   iyz = 0.0
!
! ****** Graphics for current part ******
!
geometry create shape cylinder  &
   cylinder_name = .Westfield_full_vehicle_Eigen.upright_drive.CYLINDER_41  &
   adams_id = 41  &
   center_marker = .Westfield_full_vehicle_Eigen.upright_drive.MARKER_86  &
   angle_extent = 360.0  &
   length = 75.8014750582  &
   radius = 15.0  &
```

```
   side_count_for_body = 20  &
   segment_count_for_ends = 20
!
geometry create shape cylinder  &
   cylinder_name = .Westfield_full_vehicle_Eigen.upright_drive.CYLINDER_42  &
   adams_id = 42  &
   center_marker = .Westfield_full_vehicle_Eigen.upright_drive.MARKER_87  &
   angle_extent = 360.0  &
   length = 136.0786101707  &
   radius = 15.0  &
   side_count_for_body = 20  &
   segment_count_for_ends = 20
!
geometry create shape cylinder  &
   cylinder_name = .Westfield_full_vehicle_Eigen.upright_drive.CYLINDER_43  &
   adams_id = 43  &
   center_marker = .Westfield_full_vehicle_Eigen.upright_drive.MARKER_88  &
   angle_extent = 360.0  &
   length = 140.2790000285  &
   radius = 15.0  &
   side_count_for_body = 20  &
   segment_count_for_ends = 20
!
geometry create shape cylinder  &
   cylinder_name = .Westfield_full_vehicle_Eigen.upright_drive.CYLINDER_44  &
   adams_id = 44  &
   center_marker = .Westfield_full_vehicle_Eigen.upright_drive.MARKER_89  &
   angle_extent = 360.0  &
   length = 102.702  &
   radius = 15.0  &
   side_count_for_body = 20  &
   segment_count_for_ends = 20
!
part attributes  &
   part_name = .Westfield_full_vehicle_Eigen.upright_drive  &
   color = YELLOW  &
   name_visibility = off
```

Appendix 3 Optimal driveline control strategy in ADAMS

```
!---------------------------- Function definitions ----------------------------!

constraint modify motion_generator  &
   motion_name = .Westfield_PATH_FOLLOWING_CORNERING_TVD.STEERING_MOTION  &
   function = "STEP(TIME,0,0,4,-80D)"
!
data_element modify variable  &
   variable_name = .Westfield_PATH_FOLLOWING_CORNERING_TVD.VARIABLE_20000  &
   function = "0.4"
!
data_element modify variable  &
   variable_name = .Westfield_PATH_FOLLOWING_CORNERING_TVD.VARIABLE_21000  &
   function = "1.247E-9"
!
data_element modify variable  &
   variable_name = .Westfield_PATH_FOLLOWING_CORNERING_TVD.VARIABLE_22000  &
   function = "573300"
!
data_element modify variable  &
   variable_name = .Westfield_PATH_FOLLOWING_CORNERING_TVD.VARIABLE_23000  &
```

```
  function                                                                    =
"VX(.Westfield_PATH_FOLLOWING_CORNERING_TVD.ground.aero_drag_marker,.Westfield_PAT
H_FOLLOWING_CORNERING_TVD.vehicle_body.aero_drag_force,.Westfield_PATH_FOLLOWING
_CORNERING_TVD.vehicle_body.aero_drag_force)"
!
data_element modify variable  &
  variable_name = .Westfield_PATH_FOLLOWING_CORNERING_TVD.VARIABLE_24000  &
  function                                                                    =
"VY(.Westfield_PATH_FOLLOWING_CORNERING_TVD.ground.aero_drag_marker,.Westfield_PAT
H_FOLLOWING_CORNERING_TVD.vehicle_body.aero_drag_force,.Westfield_PATH_FOLLOWING
_CORNERING_TVD.vehicle_body.aero_drag_force)"
!
data_element modify variable  &
  variable_name = .Westfield_PATH_FOLLOWING_CORNERING_TVD.VARIABLE_25000  &
  function = "1000.0"
!
data_element modify variable  &
  variable_name
= .Westfield_PATH_FOLLOWING_CORNERING_TVD.GROUND_PLANE_VELOCITY  &
  function                                                                    =
"((VX(.Westfield_PATH_FOLLOWING_CORNERING_TVD.vehicle_body.MARKER_9000,.Westfield_
PATH_FOLLOWING_CORNERING_TVD.ground.MARKER_100)**2+VY(.Westfield_PATH_FOLLOW
ING_CORNERING_TVD.vehicle_body.MARKER_9000,.Westfield_PATH_FOLLOWING_CORNERIN
G_TVD.ground.MARKER_100)**2)**0.5)/1000"
!
data_element modify variable  &
  variable_name = .Westfield_PATH_FOLLOWING_CORNERING_TVD.PATH_LENGTH  &
  function = "DIF(.Westfield_PATH_FOLLOWING_CORNERING_TVD.DIFF_path_length)"
!
data_element modify variable  &
  variable_name  =  .Westfield_PATH_FOLLOWING_CORNERING_TVD.DEMANDED_YAW_RATE
&
  function                                                =                   "-
VARVAL(.Westfield_PATH_FOLLOWING_CORNERING_TVD.GROUND_PLANE_VELOCITY)*AKIS
PL(VARVAL(.Westfield_PATH_FOLLOWING_CORNERING_TVD.PATH_LENGTH),0,.Westfield_PAT
H_FOLLOWING_CORNERING_TVD.PATH_CURV_SPLINE)"
!
data_element modify variable  &
  variable_name = .Westfield_PATH_FOLLOWING_CORNERING_TVD.BODY_SLIP_ANGLE  &
  function                                                                    =
"ASIN((VY(.Westfield_PATH_FOLLOWING_CORNERING_TVD.ground.MARKER_100,.Westfield_P
ATH_FOLLOWING_CORNERING_TVD.vehicle_body.MARKER_9000,.Westfield_PATH_FOLLOWIN
G_CORNERING_TVD.vehicle_body.MARKER_9000)/1000)/(VARVAL(.Westfield_PATH_FOLLOWIN
G_CORNERING_TVD.GROUND_PLANE_VELOCITY)+0.00001))"
!
data_element modify variable  &
  variable_name = .Westfield_PATH_FOLLOWING_CORNERING_TVD.LAT_ACC  &
  function                                                                    =
"ACCY(.Westfield_PATH_FOLLOWING_CORNERING_TVD.ground.MARKER_100,.Westfield_PATH
_FOLLOWING_CORNERING_TVD.vehicle_body.MARKER_9000,.Westfield_PATH_FOLLOWING_C
ORNERING_TVD.vehicle_body.MARKER_9000)/1000"
!
data_element modify variable  &
  variable_name = .Westfield_PATH_FOLLOWING_CORNERING_TVD.LONG_ACC  &
  function                                                                    =
"ACCX(.Westfield_PATH_FOLLOWING_CORNERING_TVD.ground.MARKER_100,.Westfield_PATH
_FOLLOWING_CORNERING_TVD.vehicle_body.MARKER_9000,.Westfield_PATH_FOLLOWING_C
ORNERING_TVD.vehicle_body.MARKER_9000)/1000"
!
data_element modify variable  &
```

```
  variable_name = .Westfield_PATH_FOLLOWING_CORNERING_TVD.CEN_ACC  &
  function                                                    =                                                    "-
(VARVAL(.Westfield_PATH_FOLLOWING_CORNERING_TVD.LAT_ACC)*COS(VARVAL(.Westfield
_PATH_FOLLOWING_CORNERING_TVD.BODY_SLIP_ANGLE)))+(VARVAL(.Westfield_PATH_FOL
LOWING_CORNERING_TVD.LONG_ACC)*SIN(VARVAL(.Westfield_PATH_FOLLOWING_CORNER
ING_TVD.BODY_SLIP_ANGLE)))"
!
data_element modify variable  &
  variable_name  =  .Westfield_PATH_FOLLOWING_CORNERING_TVD.FRONT_AXLE_YAW_RATE
&
  function          =          "-(VARVAL(.Westfield_PATH_FOLLOWING_CORNERING_TVD.CEN_ACC)-
WDTZ(.Westfield_PATH_FOLLOWING_CORNERING_TVD.ground.MARKER_100,.Westfield_PATH
_FOLLOWING_CORNERING_TVD.vehicle_body.MARKER_9000,.Westfield_PATH_FOLLOWING_C
ORNERING_TVD.vehicle_body.MARKER_9000)*(DX(.Westfield_PATH_FOLLOWING_CORNERING
_TVD.vehicle_body.MARKER_9000,.Westfield_PATH_FOLLOWING_CORNERING_TVD.vehicle_bo
dy.MARKER_139,.Westfield_PATH_FOLLOWING_CORNERING_TVD.vehicle_body.MARKER_9000
)/1000))/(VARVAL(.Westfield_PATH_FOLLOWING_CORNERING_TVD.GROUND_PLANE_VELOCI
TY)+0.00001)"
!
data_element modify variable  &
  variable_name = .Westfield_PATH_FOLLOWING_CORNERING_TVD.YAW_RATE_ERROR  &
  function                                                                                                    =
"VARVAL(.Westfield_PATH_FOLLOWING_CORNERING_TVD.DEMANDED_YAW_RATE)-
VARVAL(.Westfield_PATH_FOLLOWING_CORNERING_TVD.FRONT_AXLE_YAW_RATE)"
!
data_element modify variable  &
  variable_name
= .Westfield_PATH_FOLLOWING_CORNERING_TVD.YAW_RATE_ERROR_INTEGARL  &
  function = "DIF(.Westfield_PATH_FOLLOWING_CORNERING_TVD.DIFF_YRE_integral)"
!
data_element modify variable  &
  variable_name = .Westfield_PATH_FOLLOWING_CORNERING_TVD.YAW_RATE_GAIN  &
  function                                                                                                    =
"VX(.Westfield_PATH_FOLLOWING_CORNERING_TVD.ground.MARKER_100,.Westfield_PATH_F
OLLOWING_CORNERING_TVD.vehicle_body.MARKER_9000,.Westfield_PATH_FOLLOWING_CO
RNERING_TVD.vehicle_body.MARKER_9000)/2337.0"
!
data_element modify variable  &
  variable_name = .Westfield_PATH_FOLLOWING_CORNERING_TVD.YAW_RATE_VAR  &
  function                                                                                                    =
"WZ(.Westfield_PATH_FOLLOWING_CORNERING_TVD.ground.MARKER_100,.Westfield_PATH_F
OLLOWING_CORNERING_TVD.vehicle_body.MARKER_9000)"
!
data_element modify variable  &
  variable_name = .Westfield_PATH_FOLLOWING_CORNERING_TVD.PI_CONTROLLER  &
  function                                                                                                    =
"VARVAL(.Westfield_PATH_FOLLOWING_CORNERING_TVD.YAW_RATE_ERROR)*100000+VAR
VAL(.Westfield_PATH_FOLLOWING_CORNERING_TVD.YAW_RATE_ERROR_INTEGARL)*1000"
!
data_element modify variable  &
  variable_name = .Westfield_PATH_FOLLOWING_CORNERING_TVD.DRIVE_TORQUE  &
  function                                                                                                    =
"STEP(TIME,0.5,0,1,500*(abs(.Westfield_PATH_FOLLOWING_CORNERING_TVD.VEH_LON_VEL)-
VX(.Westfield_PATH_FOLLOWING_CORNERING_TVD.ground.MARKER_100,.Westfield_PATH_FO
LLOWING_CORNERING_TVD.vehicle_body.MARKER_9000,.Westfield_PATH_FOLLOWING_COR
NERING_TVD.vehicle_body.MARKER_9000)))"
!
data_element modify variable  &
  variable_name = .Westfield_PATH_FOLLOWING_CORNERING_TVD.TVD_Pass  &
```

```
  function                                                                    =
"IF(VARVAL(.Westfield_PATH_FOLLOWING_CORNERING_TVD.CEN_ACC):0,0,VARVAL(.Westfiel
d_PATH_FOLLOWING_CORNERING_TVD.DRIVE_TORQUE)-
VARVAL(.Westfield_PATH_FOLLOWING_CORNERING_TVD.PI_CONTROLLER))"
!
data_element modify variable  &
  variable_name = .Westfield_PATH_FOLLOWING_CORNERING_TVD.TVD_Drive  &
  function                                                                    =
"IF(VARVAL(.Westfield_PATH_FOLLOWING_CORNERING_TVD.CEN_ACC):0,0,VARVAL(.Westfiel
d_PATH_FOLLOWING_CORNERING_TVD.DRIVE_TORQUE)+VARVAL(.Westfield_PATH_FOLLO
WING_CORNERING_TVD.PI_CONTROLLER))"
!
part modify equation differential_equation  &
  differential_equation_name
= .Westfield_PATH_FOLLOWING_CORNERING_TVD.DIFF_path_length  &
  function                                                                    =
"VARVAL(.Westfield_PATH_FOLLOWING_CORNERING_TVD.GROUND_PLANE_VELOCITY)"
!
part modify equation differential_equation  &
  differential_equation_name
= .Westfield_PATH_FOLLOWING_CORNERING_TVD.DIFF_YRE_integral  &
  function = "VARVAL(.Westfield_PATH_FOLLOWING_CORNERING_TVD.YAW_RATE_ERROR)"
!
force modify direct single_component_force  &
  single_component_force_name
= .Westfield_PATH_FOLLOWING_CORNERING_TVD.FD_damping_force  &
  function                                                    =                 "-
CUBSPL(VR(.Westfield_PATH_FOLLOWING_CORNERING_TVD.FD_Lower_damper_drive.MARKE
R_56,.Westfield_PATH_FOLLOWING_CORNERING_TVD.FD_Upper_damper.MARKER_55),0,.West
field_PATH_FOLLOWING_CORNERING_TVD.SPLINE_G686)"
!
force modify direct single_component_force  &
  single_component_force_name
= .Westfield_PATH_FOLLOWING_CORNERING_TVD.FP_damping_force  &
  function                                                    =                 "-
CUBSPL(VR(.Westfield_PATH_FOLLOWING_CORNERING_TVD.FP_upper_damper_pass.MARKE
R_124,.Westfield_PATH_FOLLOWING_CORNERING_TVD.FP_Lower_damper_pass.MARKER_125
),0,.Westfield_PATH_FOLLOWING_CORNERING_TVD.SPLINE_G686)"
!
force modify direct single_component_force  &
  single_component_force_name
= .Westfield_PATH_FOLLOWING_CORNERING_TVD.RP_damping_force  &
  function                                                    =                 "-
CUBSPL(VR(.Westfield_PATH_FOLLOWING_CORNERING_TVD.RP_lower_damper.MARKER_366,
.Westfield_PATH_FOLLOWING_CORNERING_TVD.RP_lower_damper.MARKER_296),0,.Westfield_
PATH_FOLLOWING_CORNERING_TVD.SPLINE_G686)"
!
force modify direct single_component_force  &
  single_component_force_name
= .Westfield_PATH_FOLLOWING_CORNERING_TVD.RD_damping_force  &
  function                                                    =                 "-
CUBSPL(VR(.Westfield_PATH_FOLLOWING_CORNERING_TVD.RD_lower_damper.MARKER_154,
.Westfield_PATH_FOLLOWING_CORNERING_TVD.RD_Upper_damper.MARKER_153),0,.Westfield
_PATH_FOLLOWING_CORNERING_TVD.SPLINE_G686)"
!
force modify direct single_component_force  &
  single_component_force_name
= .Westfield_PATH_FOLLOWING_CORNERING_TVD.SFORCE_10  &
  function                                                                    =
"SIGN(1,VARVAL(.Westfield_PATH_FOLLOWING_CORNERING_TVD.VARIABLE_23000))*((VARV
```

```
AL(.Westfield_PATH_FOLLOWING_CORNERING_TVD.VARIABLE_20000)*VARVAL(.Westfield_PA
TH_FOLLOWING_CORNERING_TVD.VARIABLE_21000)*VARVAL(.Westfield_PATH_FOLLOWING
_CORNERING_TVD.VARIABLE_22000)*(VARVAL(.Westfield_PATH_FOLLOWING_CORNERING_T
VD.VARIABLE_23000)**2))/(2*VARVAL(.Westfield_PATH_FOLLOWING_CORNERING_TVD.VARIA
BLE_25000)+0.1E-20))"
!
force modify direct single_component_force  &
  single_component_force_name
= .Westfield_PATH_FOLLOWING_CORNERING_TVD.RD_DRIVE_TORQUE  &
  function = "VARVAL(.Westfield_PATH_FOLLOWING_CORNERING_TVD.DRIVE_TORQUE)"
!
force modify direct single_component_force  &
  single_component_force_name = .Westfield_PATH_FOLLOWING_CORNERING_TVD.RD_TVD  &
  function       =       "IF((VARVAL(.Westfield_PATH_FOLLOWING_CORNERING_TVD.CEN_ACC)-
2.943):0,0,STEP(TIME,0,0,4.5,1)*",  &
          "(VARVAL(.Westfield_PATH_FOLLOWING_CORNERING_TVD.DRIVE_TORQUE)",  &
          "-VARVAL(.Westfield_PATH_FOLLOWING_CORNERING_TVD.PI_CONTROLLER)))"
!
force modify direct single_component_force  &
  single_component_force_name = .Westfield_PATH_FOLLOWING_CORNERING_TVD.RP_TVD  &
  function       =       "IF((VARVAL(.Westfield_PATH_FOLLOWING_CORNERING_TVD.CEN_ACC)-
2.943):0,0,STEP(TIME,0,0,4.5,1)*",  &
          "(VARVAL(.Westfield_PATH_FOLLOWING_CORNERING_TVD.DRIVE_TORQUE)",  &
          "+VARVAL(.Westfield_PATH_FOLLOWING_CORNERING_TVD.PI_CONTROLLER)))"
!
force modify direct single_component_force  &
  single_component_force_name
= .Westfield_PATH_FOLLOWING_CORNERING_TVD.RP_DRIVE_TORQUE  &
  function = "VARVAL(.Westfield_PATH_FOLLOWING_CORNERING_TVD.DRIVE_TORQUE)"
```

Appendix 4 'Optimised Cosine' path curvature for double lane change

Optimised Cosine		
	Max	0.403298928
	0.012378754	
		Instant Centre vehicle frame
Xcv	curvature	Ay(g)
0	0	0
0.5	-0.000417955	-0.013620573
1	-0.001615372	-0.052642757
1.5	-0.003430534	-0.11179639
2	-0.005618293	-0.183092446
2.5	-0.00788318	-0.256901999
3	-0.00991931	-0.323256658
3.5	-0.011451691	-0.373194859
4	-0.012273368	-0.399972172
4.5	-0.012375451	-0.403298928
5	-0.012349041	-0.402438268
5.5	-0.012296278	-0.400718784
6	-0.012217274	-0.398144146
6.5	-0.012112198	-0.394719849
7	-0.011981273	-0.390453199

7.5	-0.01182478	-0.385353303
8	-0.011643052	-0.379431043
8.5	-0.011436477	-0.372699058
9	-0.011205497	-0.365171715
9.5	-0.010950603	-0.356865077
10	-0.01067234	-0.34779687
10.5	-0.010371302	-0.337986448
11	-0.010048131	-0.327454746
11.5	-0.009703516	-0.316224239
12	-0.009338194	-0.304318893
12.5	-0.008952944	-0.291764115
13	-0.008548587	-0.278586698
13.5	-0.008125988	-0.264814763
14	-0.007686047	-0.2504777
14.5	-0.007229704	-0.235606105
15	-0.006757932	-0.220231715
15.5	-0.006271739	-0.204387339
16	-0.005772161	-0.18810679
16.5	-0.005260265	-0.171424812
17	-0.004737144	-0.154377005
17.5	-0.004203913	-0.136999749
18	-0.003661711	-0.119330129
18.5	-0.003111695	-0.101405852
19	-0.002555038	-0.08326517
19.5	-0.001992928	-0.064946797
20	-0.001426566	-0.046489823
20.5	-0.000857159	-0.027933638
21	-0.000285923	-0.009317841
21.5	0.000285923	0.009317841
22	0.000857159	0.027933638
22.5	0.001426566	0.046489823
23	0.001992928	0.064946797
23.5	0.002555038	0.08326517
24	0.003111695	0.101405852
24.5	0.003661711	0.119330129
25	0.004203913	0.136999749
25.5	0.004737144	0.154377005
26	0.005260265	0.171424812
26.5	0.005772161	0.18810679
27	0.006271739	0.204387339
27.5	0.006757932	0.220231715
28	0.007229704	0.235606105
28.5	0.007686047	0.2504777
29	0.008125988	0.264814763
29.5	0.008548587	0.278586698
30	0.008952944	0.291764115
30.5	0.009338194	0.304318893
31	0.009703516	0.316224239
31.5	0.010048131	0.327454746
32	0.010371302	0.337986448
32.5	0.01067234	0.34779687
33	0.010950603	0.356865077
33.5	0.011205497	0.365171715
34	0.011436477	0.372699058
34.5	0.011643052	0.379431043
35	0.01182478	0.385353303
35.5	0.011981273	0.390453199
36	0.012112198	0.394719849

36.5	0.012217274	0.398144146
37	0.012296278	0.400718784
37.5	0.012349041	0.402438268
38	0.012375451	0.403298928
38.5	0.012273368	0.399972172
39	0.011451691	0.373194859
39.5	0.00991931	0.323256658
40	0.00788318	0.256901999
40.5	0.005618293	0.183092446
41	0.003430534	0.11179639
41.5	0.001615372	0.052642757
42	0.000417955	0.013620573
42.5	0	0
43	0	0
43.5	0	0
44	0	0
44.5	0	0
45	0	0
45.5	0	0
46	0	0
46.5	0	0
47	0.000417955	0.013620573
47.5	0.001615372	0.052642757
48	0.003430534	0.11179639
48.5	0.005618293	0.183092446
49	0.00788318	0.256901999
49.5	0.00991931	0.323256658
50	0.011451691	0.373194859
50.5	0.012273368	0.399972172
51	0.012375451	0.403298928
51.5	0.012349041	0.402438268
52	0.012296278	0.400718784
52.5	0.012217274	0.398144146
53	0.012112198	0.394719849
53.5	0.011981273	0.390453199
54	0.01182478	0.385353303
54.5	0.011643052	0.379431043
55	0.011436477	0.372699058
55.5	0.011205497	0.365171715
56	0.010950603	0.356865077
56.5	0.01067234	0.34779687
57	0.010371302	0.337986448
57.5	0.010048131	0.327454746
58	0.009703516	0.316224239
58.5	0.009338194	0.304318893
59	0.008952944	0.291764115
59.5	0.008548587	0.278586698
60	0.008125988	0.264814763
60.5	0.007686047	0.2504777
61	0.007229704	0.235606105
61.5	0.006757932	0.220231715
62	0.006271739	0.204387339
62.5	0.005772161	0.18810679
63	0.005260265	0.171424812
63.5	0.004737144	0.154377005
64	0.004203913	0.136999749
64.5	0.003661711	0.119330129
65	0.003111695	0.101405852

65.5	0.002555038	0.08326517
66	0.001992928	0.064946797
66.5	0.001426566	0.046489823
67	0.000857159	0.027933638
67.5	0.000285923	0.009317841
68	-0.000285923	-0.009317841
68.5	-0.000857159	-0.027933638
69	-0.001426566	-0.046489823
69.5	-0.001992928	-0.064946797
70	-0.002555038	-0.08326517
70.5	-0.003111695	-0.101405852
71	-0.003661711	-0.119330129
71.5	-0.004203913	-0.136999749
72	-0.004737144	-0.154377005
72.5	-0.005260265	-0.171424812
73	-0.005772161	-0.18810679
73.5	-0.006271739	-0.204387339
74	-0.006757932	-0.220231715
74.5	-0.007229704	-0.235606105
75	-0.007686047	-0.2504777
75.5	-0.008125988	-0.264814763
76	-0.008548587	-0.278586698
76.5	-0.008952944	-0.291764115
77	-0.009338194	-0.304318893
77.5	-0.009703516	-0.316224239
78	-0.010048131	-0.327454746
78.5	-0.010371302	-0.337986448
79	-0.01067234	-0.34779687
79.5	-0.010950603	-0.356865077
80	-0.011205497	-0.365171715
80.5	-0.011436477	-0.372699058
81	-0.011643052	-0.379431043
81.5	-0.01182478	-0.385353303
82	-0.011981273	-0.390453199
82.5	-0.012112198	-0.394719849
83	-0.012217274	-0.398144146
83.5	-0.012296278	-0.400718784
84	-0.012349041	-0.402438268
84.5	-0.012375451	-0.403298928
85	-0.012273368	-0.399972172
85.5	-0.011451691	-0.373194859
86	-0.00991931	-0.323256658
86.5	-0.00788318	-0.256901999
87	-0.005618293	-0.183092446
87.5	-0.003430534	-0.11179639
88	-0.001615372	-0.052642757
88.5	-0.000417955	-0.013620573
89	0	0
89.5	0	0
90	0	0
90.5	0	0
91	0	0
91.5	0	0
92	0	0
92.5	0	0
93	0	0
93.5	0	0
94	0	0

94.5	0	0
95	0	0
95.5	0	0
96	0	0
96.5	0	0
97	0	0
97.5	0	0
98	0	0
98.5	0	0
99	0	0
99.5	0	0
100	0	0

Appendix 5 Tables of the front and rear suspension hard points

Table 0-1 Front suspension hard points

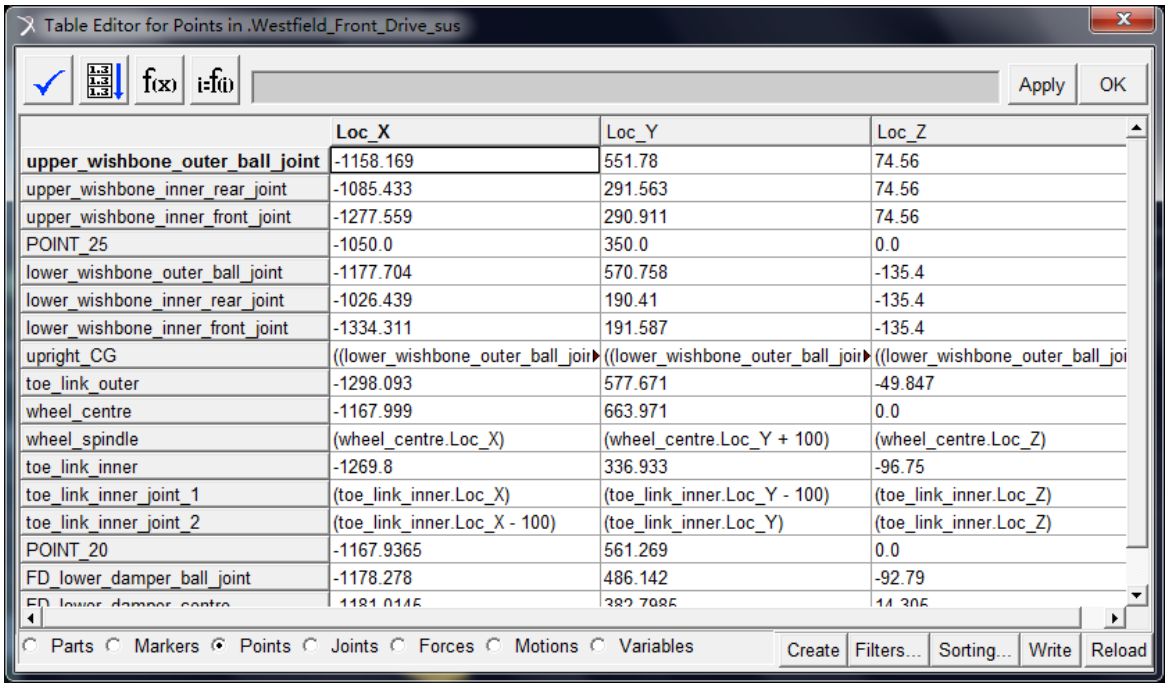

Table 0-2 Rear suspension hard points

Table Editor for Points in .Westfield_Rear_Drive_sus

Apply OK

	Loc_X	Loc_Y	Loc_Z
upper_wishbone_outer_ball_joint	1210.084	565.758	96.639
upper_wishbone_inner_rear	1352.26	253.875	177.206
upper_wishbone_inner_front_joint	1068.462	253.594	180.481
lower_wishbone_outer_ball_joint	1254.081	571.367	-130.826
lower_wishbone_inner_rear_joint	1358.474	133.455	-18.293
lower_wishbone_inner_front_joint	993.63	134.002	-16.586
upright_CG	((lower_wishbone_outer_ball_joi	((lower_wishbone_outer_ball_joi	((lower_wishbone_outer_ball_jo
toe_link_outer	1076.185	568.722	-131.798
wheel_centre	1169.081	669.944	-0.309
wheel_spindle	(ground.wheel_centre.Loc_X)	(ground.wheel_centre.Loc_Y + 1	(ground.wheel_centre.Loc_Z)
toe_link_inner	993.63	134.002	-16.586
toe_link_inner_joint_1	(toe_link_inner.Loc_X)	(toe_link_inner.Loc_Y - 100)	(toe_link_inner.Loc_Z)
toe_link_inner_joint_2	(toe_link_inner.Loc_X - 100)	(toe_link_inner.Loc_Y)	(toe_link_inner.Loc_Z)
Upright_centre	1169.408719	539.9905573	-3.772425769
RD_lower_damper_ball_joint	1149.544	565.215	96.624
RD_lower_damper_centre	1156.565	482.263	257.8865
Body_RD_Upper_damper_ball_joint	1163.686	399.311	419.149

Parts Markers Points Joints Forces Motions Variables

Create Filters... Sorting... Write Reload

Appendix 5 Measurement outputs from the front and rear suspension system

All Figures show the outputs for the front suspension characteristics based on the quarter car model that has been built in the previous section.

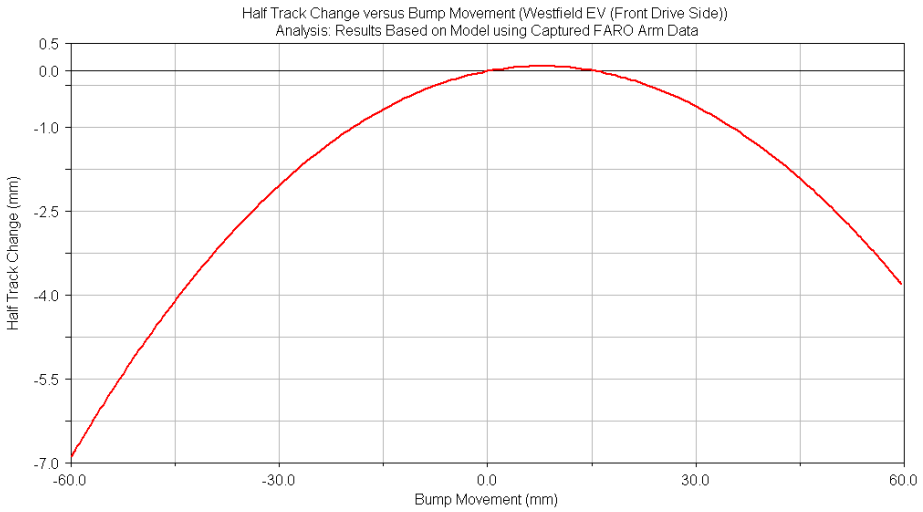

Figure 1 Half Track Change Vs Bump Movement (Front)

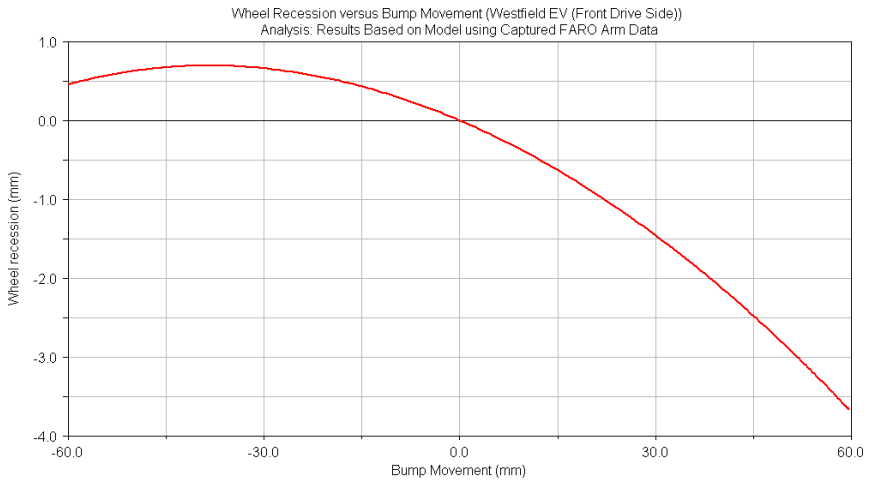

Figure 2 Wheel Recession Vs Bump Movement (Front)

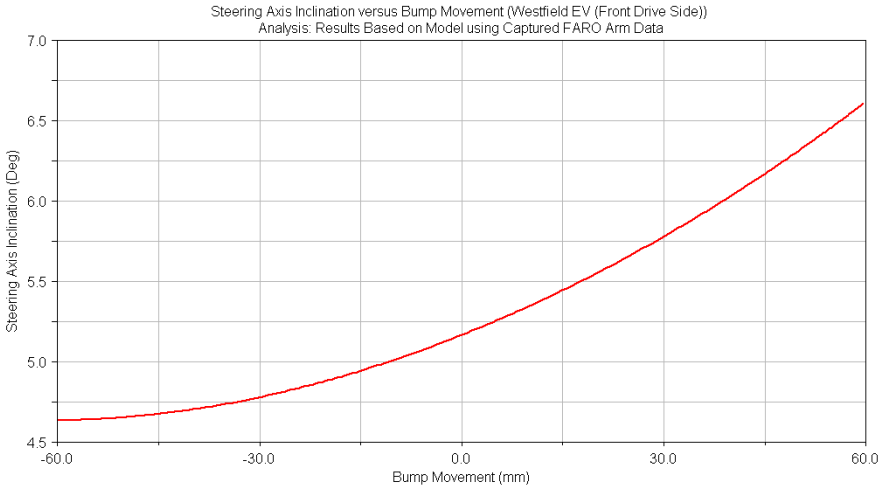

Figure 3 Steering Axis Inclination Vs Bump Movement (Front)

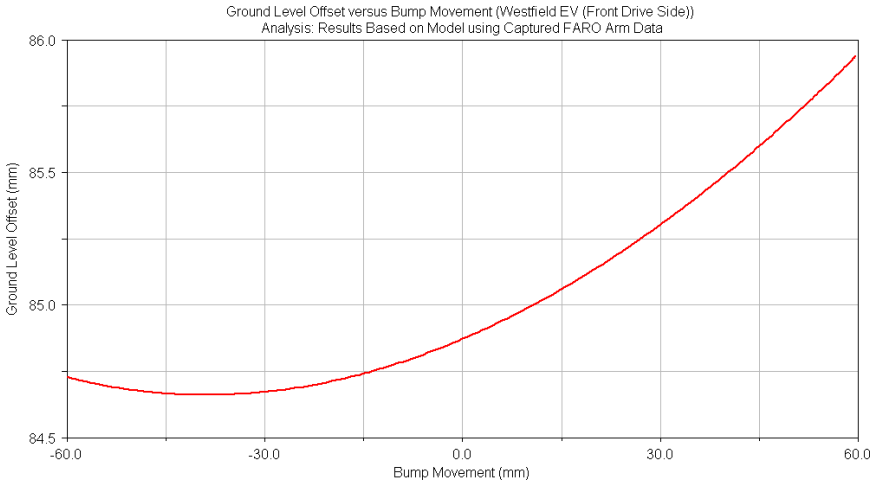

Figure 4 Ground Level Offset Vs Bump Movement (Front)

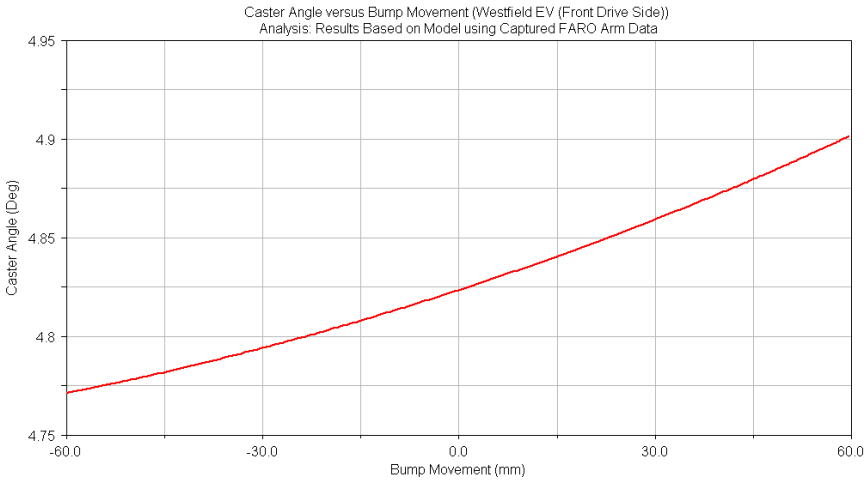

Figure 5 Castor Angle Vs Bump Movement (Front)

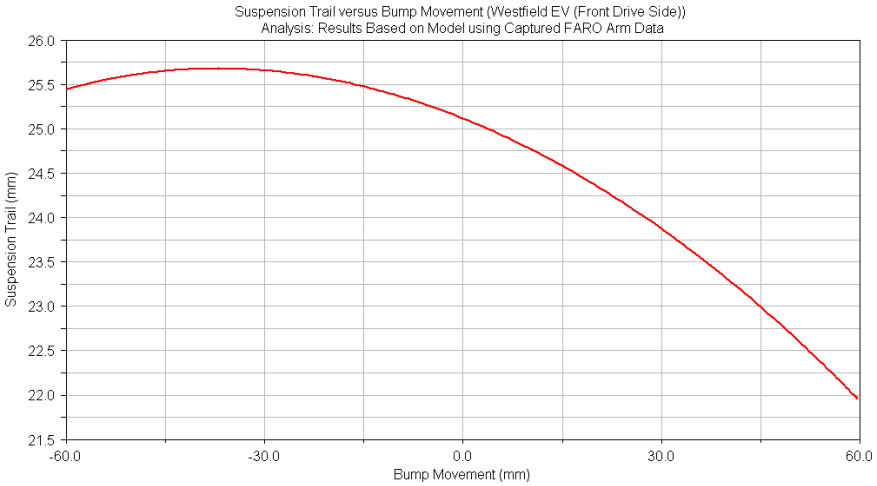

Figure 6 Suspension Trail Vs Bump Movement (Front)

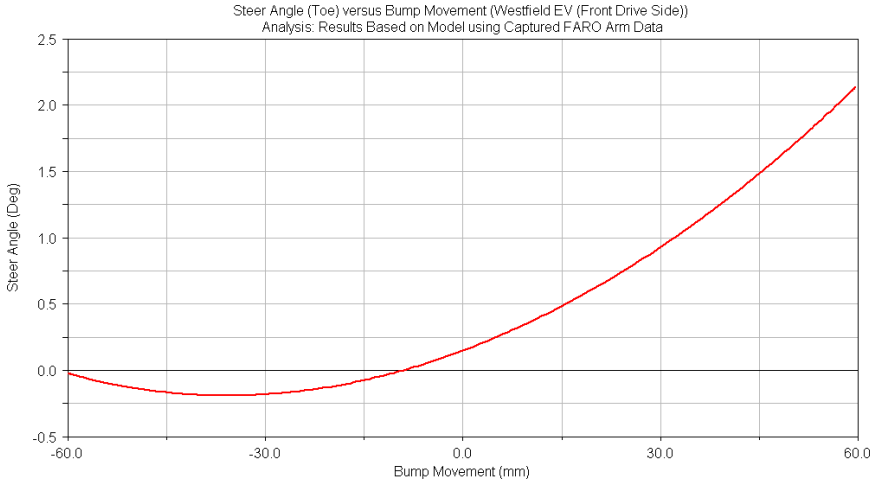

Figure 7 Steer Angle Vs Bump Movement (Front)

Figures show the outputs for the rear suspension characteristics based on the quarter car model that has been built in the previous section.

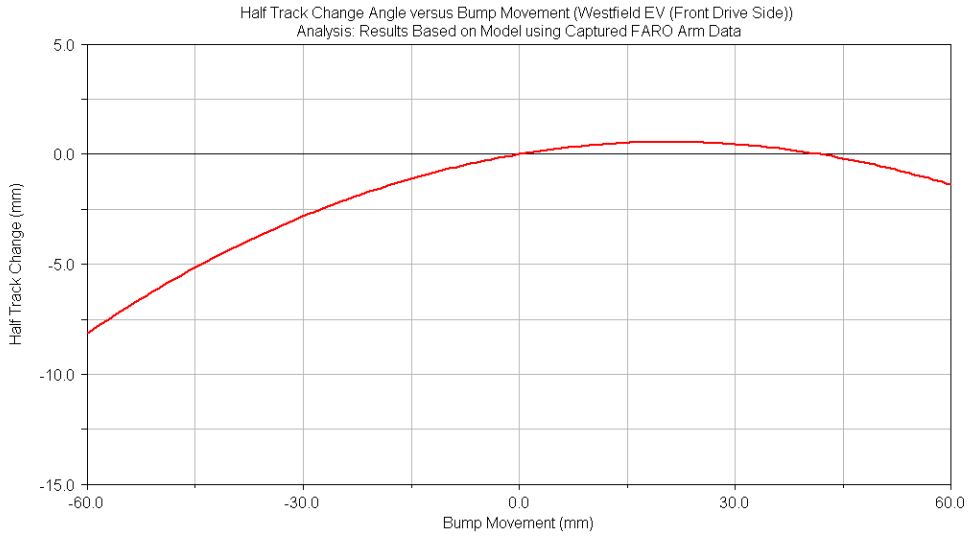

Figure 9 Half Track Change Vs Bump Movement (Rear)

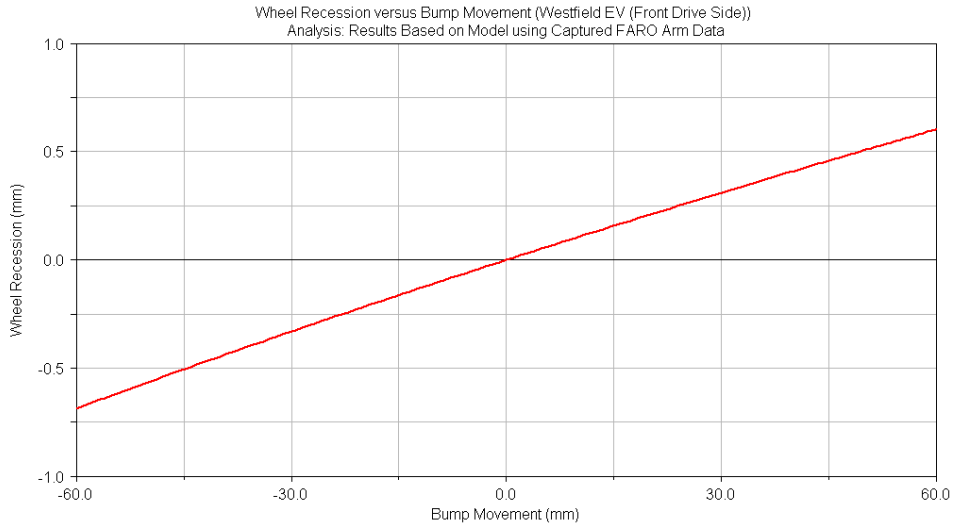

Figure 10 Wheel Recession Vs Bump Movement (Rear)

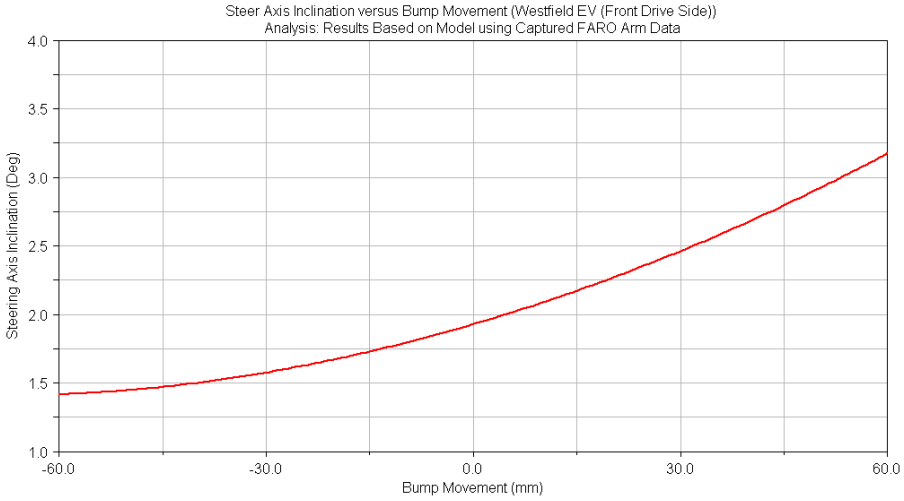

Figure 11 Steer Axis Inclination Vs Bump Movement (Rear)

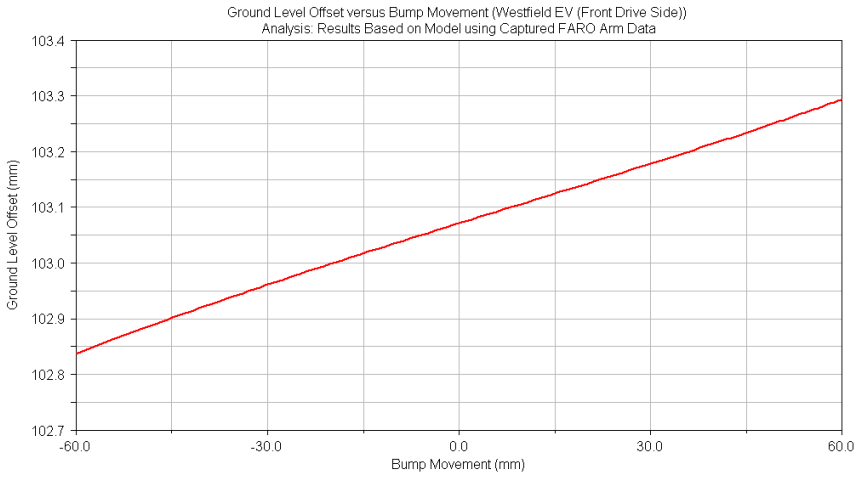

Figure 12 Ground Level Offset Vs Bump Movement (Rear)

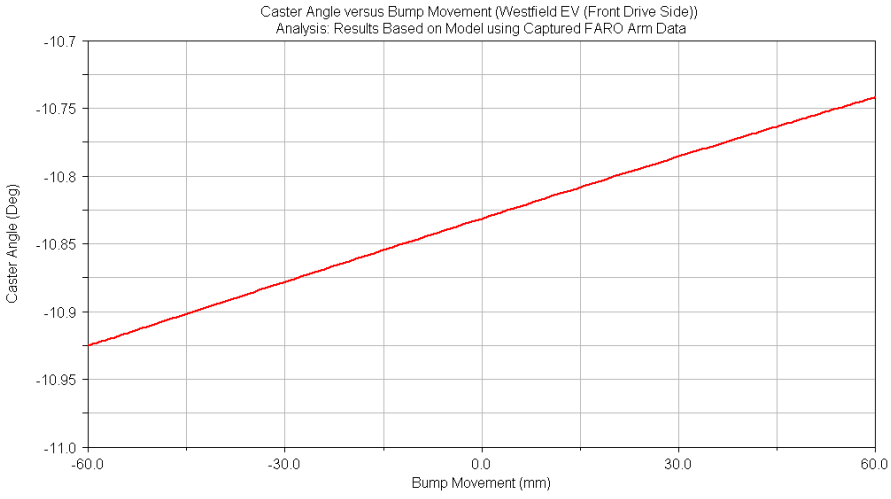

Figure 13 Castor Angle Vs Bump Movement (Rear)

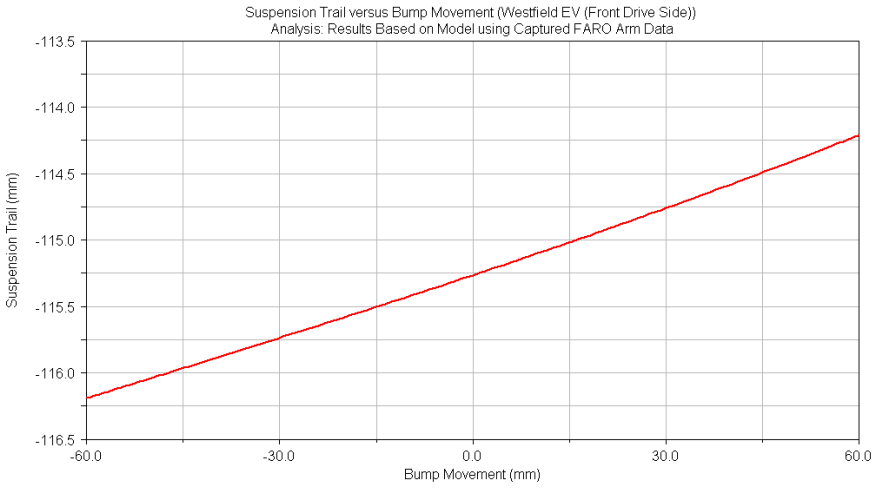

Figure 14 Suspension Trail Vs Bump Movement (Rear)

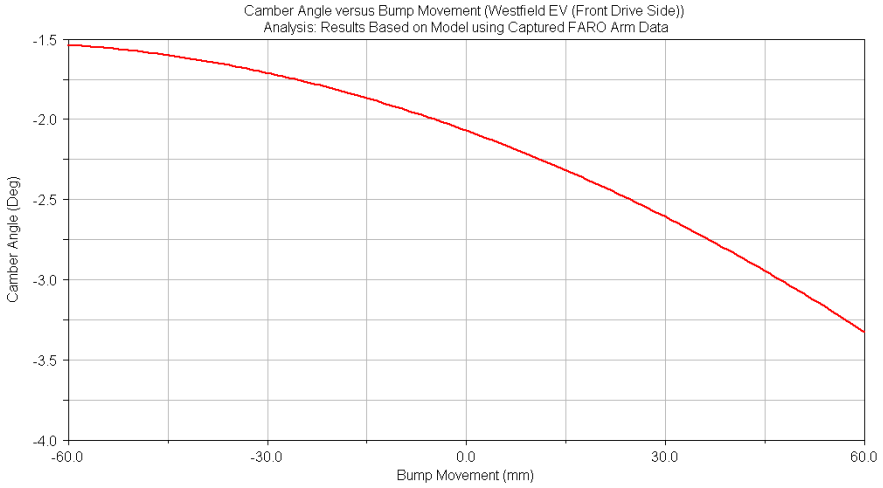

Figure 15 Camber Angle Vs Bump Movement (Rear)

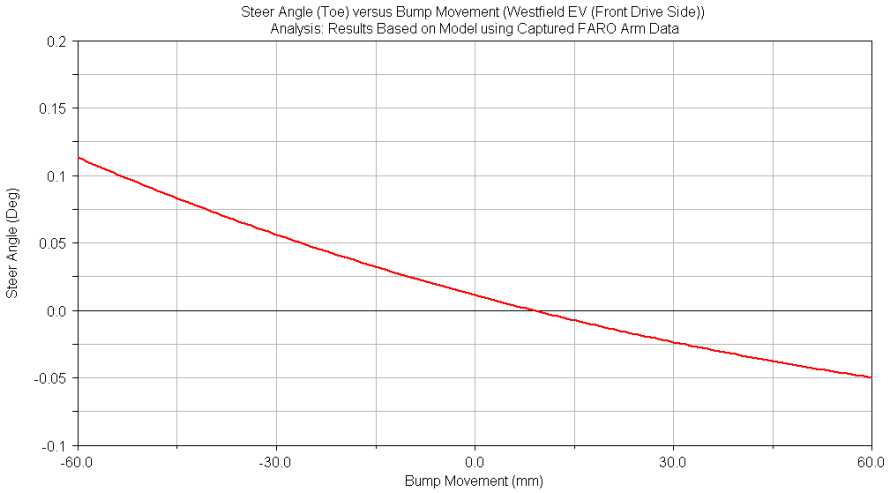

Figure 16 Steer Angle Vs Bump Movement (Rear)